UNIVERSITY OF OKLAHOMA

GRADUATE COLLEGE

# FLOW STRUCTURE EFFECTS ON TURBULENT TRANSPORT USING COMPUTATIONS

A DISSERTATION

SUBMITTED TO THE GRADUATE FACULTY

in partial fulfillment of the requirements for the

Degree of

DOCTOR OF PHILOSOPHY

By
LE KIEU OANH PHAM
Norman, Oklahoma
2023

FLOW STRUCTURE EFFECTS ON TURBULENT TRANSPORT USING COMPUTATIONS

A DISSERTATION APPROVED FOR THE

SCHOOL OF SUSTAINABLE CHEMICAL, BIOLOGICAL AND MATERIALS ENGINEERING

BY THE COMMITTEE CONSISTING OF

Dr. Dimitrios V. Papavassiliou, Chair

Dr. Liangliang Huang

Dr. Ramkumar N.Partharasathy

Dr. Edgar A.O'Rear

Dr. Bin Wang

*To my beloved family-my parents, my husband, my son, my cousin, my sisters, my aunts who supported me and stood by me.*

## Acknowledgements

Firstly, I would like to express my deepest gratitude to my advisor Prof. Dimitrios V. Papavassiliou for his support and guidance during the time I worked with him. It was a great fortune for me when I got the chance to pursue a Doctorate degree at the University of Oklahoma and became a member in the research group of my advisor. My advisor is very supportive and generous that makes me feel comfortable when working with him. He gave me useful advice and created favorable conditions so that I could do research during the time I had baby and COVID-19. I am also grateful for his patience when we got stuck in research and helped me to deal with problems.

Secondly, I sincerely appreciate my committee members, Dr. Liangliang Huang, Dr. Ramkumar N.Partharasathy, Dr. Edgar A.O'Rear, Dr. Bin Wang for their comments and incites that contribute to improving my work. I want to thank the support of Supercomputing Center for Education & Research (OSCER) and the Texas Advanced Computing Center through XSEDE with allocation CTS-090025. I gracefully acknowledge the financial support of the National Science Foundation (Grant No. CBET-1803014).

Finally, I am thankful to my research group colleagues and friends for your discussion and willingness to share experiences and knowledge with me.

# TABLE OF CONTENTS

**LIST OF FIGURES** ........ **viii**

**LIST OF TABLES** ........ **xv**

**ABSTRACT** ........ **xvi**

**CHAPTER 1: INTRODUCTION** ........ **1**

1.1 Turbulent flow ........ 1

1.2 Hydrodynamic stress on von Willebrand Factor in turbulent flow ........ 8

1.2.1 von Willebrand Factor under shear stress in turbulent flow ........ 8

1.2.2 vWF under extensional stress in turbulent flow ........ 14

1.2.3 Critical shear and extensional stress for the unravelling of vWF ........ 17

1.3 Helicity and Dissipation and Coherent structures ........ 23

1.3.1 Helicity and dissipation rate ........ 25

1.3.2 Helicity and coherent structures ........ 28

**CHAPTER 2: METHODOLOGY** ........ **35**

2.1 Direct Numerical Simulation (DNS) ........ 35

2.2 Lagrangian Scalar Tracking (LST) ........ 39

**CHAPTER 3: COMPUTATIONS OF THE SHEAR STRESSES DISTRIBUTION EXPERIENCED BY PASSIVE PARTICLES AS THEY CIRCULATE IN TURBULENT FLOW: A CASE STUDY FOR VWF PROTEIN MOLECULES.** ........ **43**

3.1 Methodology and parameter ........ 43

3.2 Results and Discussion ........ 48

3.2.1 Transitional Poiseuille-Couette flow ........ 48

3.2.2 Fully turbulent Poiseuille flow ........ 55

3.3 Conclusions ........ 60

**CHAPTER 4: DISTRIBUTION AND HISTORY OF EXTENSIONAL STRESSES ON VWF SURROGATE MOLECULES IN TURBULENT FLOW** ........ **63**

4.1 Methodology and parameter ........ 63

4.2 Results and discussion ........ 64

4.2.1 Transitional Poiseuille-Couette flow ........ 64

4.2.2 Fully developed turbulent Poiseuille flow ........ 68

4.2.3 Conclusions ........ 73

**CHAPTER 5: HELICITY AND DISSIPATION CORRELATION IN ANISOTROPIC TURBULENT FLOW FIELDS. .......... 76**
5.1 Methodology and Parameters .......... 76
5.2 Results and Discussion .......... 80
5.2.1 Eulerian mean of helicity in Poiuseuille and Couette flow .......... 80
5.2.2 The average position of particles at various release position and Sc numbers .......... 82
5.2.3 Autocorrelation of helicity and dissipation in Poiseuille and Couette flow at different $\boldsymbol{Sc}$ number .......... 83
5.2.4 Cross correlation of helicity and dissipation rate conditioned on kinetic energy .......... 85
5.2.5 Correlation of helicity and dissipation of particle moving farthest and closest .......... 88
5.2.6 Lagragian timescale as a function of source for dispersion .......... 90
5.3 Conclusions .......... 99
**CHAPTER 6: THE ROLE OF HELICITY IN TURBULENT TRANSPORT AND COHERENT STRUCTURES. .......... 101**
6.1 Methodology and Parameters .......... 101
6.2 Results and Discussion .......... 103
6.2.1 Helicity and verical velocity .......... 103
6.2.2 Helicity and vorticity .......... 109
6.2.3 Helicity distribution conditioned on Reynold stress quadrants .......... 112
6.2.4 Helicity and Q-criterion .......... 117
6.2.5 Helicity and eigenvetors of rate of strain tensor .......... 123
**CHAPTER 7: CONCLUSIONS AND FUTURE WORKS .......... 133**
7.1 Conclusions .......... 133
7.2 Future works .......... 135
**APPENDIX A: INVESTIGATE THE COUETTE FLOW USING DIRECT NUMERICAL SIMULATION .......... 137**
**REFERENCES .......... 142**

## LIST OF FIGURES

Figure 1.1 Schematic representation of local instantaneous flow patterns in turbulent flow in a pipe [7]. ..... 2

Figure 1.2 Turbulent eddies in a plane mixing layer subjected to periodic forcing [8]. ..... 2

Figure 1.3(A) Schematic illustration of vWF's domains. (B) Possible mechanism of flow-induced conformational change [96]. ..... 9

Figure 1.4 Dynamic conformational change of VWF under shear [100]. ..... 11

Figure 1.5 Illustration of the change of vWF in shear and elongational flow [89]. ..... 11

Figure 1.6 This figure from ref. [133] indicates that the folding-unfolding of the vWF on the surface of platelets depends on the shear stress values and a molecule unfolding on a surface has interactions and forces causing it is not a reversible process – it depends on the history of the stress that is experienced by the vWF molecule. ..... 19

Figure 1.7 The prediction of unfolding of vWF subjected to shear. This is a copy of Fig. 4 from ref. [98] where the inverse proportionality of shear rate (and thus shear stress) with time of exposure is evident for the unfolding of vWF. Unfolding of vWF is not the same as degradation. The experiments that Antaki used to validate his work actually proves that vWF is not degraded. ..... 21

Figure 1.8 The Table 2 in ref. [135] provide data for averaged exposure time required to unravel a globular vWF multimer for varied elongational rate. ..... 21

Figure 1.9 This is a plot of the logarithm of the elongational rate vs the logarithm of the exposure time using the data from Table 2 in ref.[135]. The straight line indicates the validity of a power law model. Strain rate is in $s^{-1}$ and exposure time is in seconds. The values in that Table are shown, in Figure 1.8. ..... 22

Figure 2.1 Plane channel flow configuration [225]. ..... 42

Figure 2.2 Plane Couette flow configuration[225]. .................................................................... 42

Figure 3.1 Average position of the vWF markers in the Poiseuille-Couette velocity field at each time step. Results for particles released within the viscous wall layer (Yo = 3 and 5), within the buffer region (Yo = 15) and at the center of the channel (Yo =80) are presented. Each point in the figure is the average of position of all particles per a release position at each time step. ............ 49

Figure 3.2 Sample trajectories of individual vWF markers in the Poiseuille-Couette velocity field. Examples of particles released at Yo = 3 (yellow circle), Yo 5(red circle), Yo = 15 (green start), Yo = 80 (pink star) are shown........................................................................................... 50

Figure 3.3 Magnitude of shear stress as a function of time for vWF particles injected at different initial locations. The abscissa in dimensionless viscous parameters and in dimensional units is shown. The critical shear stress is 5 Pa as in Ref [86] ................................................................ 51

Figure 3.4 Average of actual shear stresses. The abscissa in dimensionless viscous parameters in dimensional units is shown. One can adjust the dimensional stress axis at the same Re by considering a new channel width with a new corresponding mean velocity to recalculate $\tau_w$ and $u^*$, and using the dimensionless values presented. ..................................................................... 51

Figure 3.5 Distributions of shear stress on vWF particles at different times in viscous wall units. (A) Cloud released at the channel bottom wall, (B) release at the edge of the viscous wall subregion (Yo = 5), (C) release within the buffer region (Yo = 15) and (D) release at the channel center. . 53

Figure 3.6 Distributions of the shear stress history for vWF particles at different times in viscous wall units. (A) Cloud released at the channel bottom wall, (B) release at the edge of the viscous wall subregion (Yo = 5), (C) release within the buffer region (Yo = 15) and (D) release at the channel center. ......................................................................................................................... 55

Figure 3.7 Average vWF position in fully-developed Poiseuille turbulent flow. Results for particles released within the viscous wall layer (Yo = 1.5 and 5), within the logarithmic layer (Yo = 75) and at the center of the channel (Yo = 300) are presented. Each point in the figure is the average position of all particles per release position at each time step. .................................................. 56

Figure 3.8 Trajectories of particles released in a Poiseuille flow field. Examples of particles released at Yo = 1.5 (blue circles), Yo = 5 (yellow circles), Yo = 10 (green stars), Yo = 75 (red stars), Yo = 300 (pink star dot). ........................................................................................ 57

Figure 3.9 Magnitude of the shear stress as a function of time for vWF particles released at different initial locations in fully turbulent flow. The abscissa in dimensionless viscous parameters and in dimensional units is shown. ........................................................................................ 58

Figure 3.10 Distributions of shear stress on vWF particles at different times in viscous wall units. (A) Cloud released at the channel bottom wall, (B) release within the viscous sublayer (Yo = 1.5), (C) release within the buffer region (Yo = 15) and (D) release at the channel center. ................ 59

Figure 3.11 Distributions of the shear stress history for vWF particles at different times in viscous wall units. (A) Cloud released at the channel bottom wall, (B) release within the viscous wall subregion (Yo = 1.5), (C) release within the buffer region (Yo = 15) and (D) release at the channel center. ........................................................................................ 60

Figure 4.1 The magnitude of the extensional stress as a function of the channel height in the x, y, z directions in Poiseuille-Couette flow. These are averaged values of Eulerian velocity fields... 64

Figure 4.2 Mean of the absolute value of extensional stress for particles released at different positions in the Poiseuille-Couette flow field over time. The dark blue line represents the critical stress of 1.2 Pa for the case modeled herein. ........................................................................ 65

Figure 4.3 Probability density function for the extensional stress components in x, y, z directions of particles released at $Y_0$ = 0, 5, 15, 80 at different time instances Poiseuille-Couette flow field. The green line represents the critical stress of 1.2 Pa for the case modeled herein. .................... 67

Figure 4.4 Probability density function of the extensional stress histories in x, y, z, directions for particles released at different positions at $t^+$=300 and 600 in the Poiseuille-Couette flow field. . 68

Figure 4.5 Eulerian average of the absolute value of the extensional stress as a function of the distance from the wall in plane Poiseuille flow. Since the Poiseuille flow channel is symmetric across the center place at $y^+$=300, only the bottom half of the stress profile is presented. .......... 69

Figure 4.6 Average of the absolute value of the extensional stress on vWF model particles released at different positions in the Poiseuille flow field. The solid straight line at 1.2 Pa indicates the critical extensional stress. ........................................ 70

Figure 4.7 The probability density function for the extensional stress components in x, y, z directions of particles released at Yo=1.5, 15, 75, 300 at different time instances Poiseuille flow field. The solid green line depicts the critical stress value for vWF deformation. ....................... 71

Figure 4.8 The PDF of the extensional stress histories in x, y, z, directions for particles released at different positions at $t^+$=150 and 300 in the Poiseuille flow field. ............................................. 73

Figure 5.1 The Eulerian mean of the absolute values of fluctuating helicity density ($|H'| = |\boldsymbol{u}'.\boldsymbol{\omega}'|$) for (a) Poiseuille flow and (b) for Couette flow. Mean absolute value of the relative helicity density ($|h'| = |cos\theta'|$) calculated as a function of distance from the wall for (c) Poiseuille flow and (d) Couette flow. ........................................ 81

Figure 5.2 The average position of particles at release positions Yo =1.5, 3, 5, 75 of Couette flow and Poiseuille flow at various $Sc$ number. Couette flow (a) $Sc$=0.7, (b) $Sc$ =6, (c) fluid particle; Poiseuille flow (d) $Sc$ =0.7, (e) $Sc$ =6, (f) fluid particle. ........................................ 83

Figure 5.3 The autocorrelation of relative helicity density $h' = cos\theta'$for Poiseuille flow and Couette flow at (a) $Sc$ = 0.7, (b) $Sc$ = 6 and (c) fluid particles. The symbol P on the legend represents results for Poiseuille flow and the symbol C represents Couette flow. ....................... 84

Figure 5.4 The Pearson cross-correlation between the relative helicity density $h' = cos\theta'$and the dissipation for Poiseuille flow and Couette flow at (a) $Sc$=0.7, (b) $Sc$= 6, (c) fluid particles...... 86

Figure 5.5 The Pearson cross-correlation between $\epsilon$ and absolute value of $h'$ for Poiseuille flow and Couette flow at different $Sc$: (a) $Sc$ =0.7, (b) $Sc$ =6, (c) fluid particles. ............................... 87

Figure 5.6 Profiles of the autocorrelation of $h'$ with time, $h'\_h'$; the autocorrelation of dissipation with time, $\epsilon\_\epsilon$ ; the Pearson cross-correlation between $h'$ and dissipation $h'\_\epsilon$ ; and the Pearson cross-correlation of the absolute value of $|h'|$ with dissipation, a$h'_\epsilon$. The correlations for the 25%

of the particles that were found to be the farthest from the wall at $t^+$=100 are shown in the top raw: (a) $Sc$ = 0.7, (b) $Sc$ = 6, (c) fluid particles. The correlations for the 25% of the particles that were found to be the closest to the wall at $t^+$=100 is shown in the bottom raw: (d) $Sc$ = 0.7, (e) $Sc$ = 6, (f) fluid particles. The particles that were released at Yo = 3 for both Poiseuille and Couette flow. ........................................................................................................................................ 89

Figure 5.7 The Lagrangian timescale as a function of source elevation for dispersion in the y-direction for different $Sc$ number and types of flow where the vertical axis is timescale and the horizontal axis is $Yoh$ ($Y0$ is the initial position of release particles) for the relative helicity density $h' = cos\theta'$ (h'_h') and velocity from prior results (v_v, from ref [167]) for Couette flow at (a) $Sc$ = 0.7, (b) $Sc$ = 6, (c) fluid particles and for Poiseuille flow at (d) $Sc$ = 0.7, (e) $Sc$ = 6 and (f) fluid particles. ........................................................................................................................ 91

Figure 5.8 The distribution of relative helicity density $h' = cos\theta'$ conditional on high (left column) at (a) Yo = 3, (b) Yo = 10, (c) Yo =15, (d) Yo =75 and low dissipation (right column) at (e) Yo =3, (f) Yo = 10, (g) Yo = 15, (h) Yo =75 at $t^+$=100 for Poiseuille and Couette flow. For both Couette and Poiseuille flow, the high dissipation is more than 8 times and 10 times the average dissipation respectively, and the low dissipation is less than 0.25 times the average dissipation.................. 93

Figure 5.9 The distribution of relative helicity density $h' = cos\theta'$at various times for a release position at Yo = 1.5, 3, 5, 75 of Poiseuille flow with Sc = 0.7, 6, and fluid particles. Columns correspond to Sc and rows to positions of release. ...................................................................... 94

Figure 5.10 The distribution of relative fluctuating helicity density $h' = cos\theta'$at various times for release position Yo = 1.5, 3, 5, 75 for Couette flow with Sc = 0.7, 6, and fluid particles. Columns correspond to Sc and rows to positions of release. ...................................................................... 95

Figure 5.11 Joint PDF of relative helicity density $h' = cos\theta'$and fluctuating dissipation for all particle of Poiseuille flow for different $Sc$ numbers at time $t^+$=100. .......................................... 97

Figure 5.12 Joint PDF of relative helicity density $h' = cos\theta'$and fluctuating dissipation for all particle of Couette flow for different $Sc$ numbers at time $t^+$=100. ............................................. 98

Figure 6.1 JPDF of relative helicity density $h' = cos\theta'\ and$ vertical velocity v′ of all particles, at time $t^+$=100 for Poiseuille flow at *Sc* = 0.7, 6 and fluid particles. Rows correspond to different location of marker release in the y direction, indicated by the value of $Y_0$, shown in the plots, and columns correspond to markers of different *Sc*, as indicated at the top of the figure................ 105

Figure 6.2 JPDF of relative helicity density $h' = cos\theta'$and vertical velocity v′ of all particles, at time $t^+$=100 for Couette flow at Sc = 0.7, 6 and fluid particles. Rows correspond to different location of marker release in the y direction, indicated by the value of $Y_0$, shown in the plots, and columns correspond to markers of different *Sc,* as indicated at the top of the figure................ 106

Figure 6.3 JPDF of relative helicity density $h' = cos\ \theta'$ and vertical velocity v′ at $t^+$=100 for only the 25000 particles in Poiseuille flow that are the closest to the channel wall (a) *Sc* = 0.7, (b) *Sc* = 6 and (c) fluid particles and for the 2,500 particles that are the farthest from the wall (d) *Sc* = 0.7, (e) *Sc* = 6 and (f) fluid particles in Poiseuille flow from initial position $Y_0$ = 3. ........................ 108

Figure 6.4 JPDF of relative helicity density $h' = cos\ \theta'$ and vertical velocity v′ at $t^+$=100 for only the 25000 particles in Couette flow that are the closest to the channel wall (a) *Sc* = 0.7, (b) *Sc* = 6 and (c) fluid particles and for the 2,500 particles that are the farthest from the wall (d) *Sc* = 0.7, (e) *Sc* = 6 and (f) fluid particles in Poiseuille flow from initial position $Y_0$ = 3.............................. 108

Figure 6.5 the JPDF of relative helicity density $h' = cos\ \theta'$ and the cosine of vorticity in the normal direction cos$\omega$ of all particles and Poiseuille flow at $t^+$=100. Rows correspond to different locations of marker release in the y direction, indicated by the value of $Y_0$, shown in the plots, and columns correspond to markers of different *Sc,* as indicated at the top of the figure. ...............................110

Figure 6.6 the JPDF of relative helicity density $h' = cos\ \theta'$ and cosine of vorticity in the normal direction cos$\omega$ of all particles and Couette flow at $t^+$=100. Rows correspond to different locations of marker release in the y direction, indicated by the value of $Y_0$, shown in the plots, and columns correspond to markers of different *Sc,* as indicated at the top of the figure. ...............................111

Figure 6.7 Conditional distribution of relative helicity density $h' = cos\ \theta'$ for particles within each of the 4 quadrants of Reynolds stress (u′v′) at $t^+$=100. Rows correspond to different locations of marker release in the y direction, indicated by the value of $Y_0$, shown in the plots, and columns correspond to markers at different Reynolds stress quadrants at time $t^+$ =100. The type of low, Poiseuille or Couette, is indicated by P or C respectively and the *Sc* is also indicated in the figure legends for each curve. ........................................................................................................113

Figure 6.8 The contour plot of velocity field and the particles with their relative helicity density magnitude at yz plane at $254\,\Delta x \le x \le 256\,\Delta x$ time t=100$^+$ for Poiseuille flow at various *Sc* numbers (a) *Sc* = 0.7, (b) *Sc* = 6 and (c) fluid particles. The center of the channel is at y = 0 and the bottom wall is at y = -300. .......................................................................................115

Figure 6.9 Vector plot of velocity field with the particles and their relative helicity density magnitude on a yz plane. The particles shown are for $254\,\Delta x \le x \le 256\,\Delta x$ at time t=100$^+$ for Couette flow at various *Sc* numbers (a) *Sc* = 0.7, (b) *Sc* = 6 and (c) fluid particles. The center of the channel is at y = 0 and the bottom wall is at y = -300. .......................................................116

Figure 6.10 The autocorrelation coefficient for the Q values as a function of time for Poiseuille and Couette flow (indicated as P and C on the legend) at various *Sc* numbers and for different positions of particle release (a) *Sc* = 0.7, (b) *Sc* = 6, (c) fluid particles. ....................................119

Figure 6.11 The correlation of Q values with time for particles conditional on their location relative to the wall at time $t^+$ = 100: (a) The 25% of all particles that are closer to the wall, (b) 25% of particles that are the farthest from their initial position at $Y_0$ = 3 for Poiseuille and Couette flow and for various *Sc* numbers. ........................................................................................ 121

Figure 6.12 The distribution of relative helicity density $h'$ conditioned for Q > 0 for Poiseuille and Couette flow at various *Sc* numbers and for release positions (a) $Y_0$ = 1.5, (b) $Y_0$ = 3, (c) $Y_0$ = 5, (d) $Y_0$ = 75 at time $t^+$=100. .................................................................................................. 122

Figure 6.13 The average value of the second largest eigenvalues β of strain rate tensor for Poiseuille and Couette flows at various $Sc$ numbers and release positions. .............................. 125

Figure 6.14 Distribution of relative helicity density $h'$ conditioned on $\beta > 0$ at various position of release (a) $Y_0$ =1.5, (b) $Y_0$ =3, (c) $Y_0$ =5 and (d) $Y_0$ =75 and $Sc$ numbers............................ 126

Figure 6.15 Cross correlation between absolute value of relative helicity $h' = cos\theta'$ and absolute value of the cosine between vorticity and the eigenvectors of the rate of strain tensor, cos(ω, $\boldsymbol{e}_i$). $\boldsymbol{e}_i$ with i=1-3 corresponds to eigenvectors with eigenvalues α>β>γ, for Poiseuille flow and various *Sc* numbers. ........................................................................................................................ 127

Figure 6.16 Cross correlation between absolute value of relative helicity $h' = cos\theta'$ and absolute value of the cosine between vorticity and the eigenvectors of the rate of strain tensor, cos(ω, $\boldsymbol{e}_i$). $\boldsymbol{e}_i$ with i=1-3 corresponds to eigenvectors with eigenvalues α>β>γ, for Couette flow and various *Sc* numbers. ........................................................................................................................ 128

Figure 6.17 Cross correlation between the absolute value of relative helicity $h' = cos\theta'$ and absolute value of cosine between vorticity and eigenvectors cos(ω, $\boldsymbol{e}_i$). $\boldsymbol{e}_i$ with i=1-3corresponds to eigenvectors of eigenvalues α > β > γ) for the 25% of particles that are located closer and farther from the initial position $Y_0 = 3$ for Couette and Poiseuille flows at various $Sc$ numbers. .......... 130

## LIST OF TABLES

Table 1.1 Literature review of critical shear and extensional stresses for the deformation of vWF, cells, and capsules. ........................................................................................................ 18

Table 4.1 The simulation parameters for Poiseuille and Poiseuille-Couette flows. ..................... 63

# ABSTRACT

Turbulent flow is the most typical flow in various fields such as biological, chemical and industrial applications and atmospheric phenomena. The main goal of this research is to investigate the fundamental effects of the very large-scale structures of turbulence on convective transport and the effects of the interplay between molecular diffusion and flow structure on turbulent transport. Applying Lagrangian computations in conjunction with direct numerical simulations for turbulent flow in channel and Couette flow, it could explore the effects of the very large-scale turbulent fluid motions on scalar transport and determine the mechanism by which they contribute to transport. From that we can develop a predictive model for turbulent scalar transfer and control this.

One of our applications is the effect of turbulent flow in cardiovascular devices such as blood pumps, ventricular assist devices (VADs) and even heart valves. According to clinical findings, VAD patients often suffer from acquired von Willebrand disease after VAD implantation. Indeed, the von Willebrand Factor protein is susceptible to supraphysiological shear stress and extensional stress which leads to the conformational change of vWF. Apart from that, the detailed measurement of stresses in a hemodynamic velocity field is difficult, especially in-situ for turbulent flow conditions. In such cases, the use of computational methods has become critical for both the probing of the hemodynamic conditions and for device design. Therefore, recognizing advantages of Direct Numerical Simulation (DNS) and Lagrangian Scalar Tracking (LST) we applied it to the case of vascular assist devices and indicate (i) the development of a numerical methodology for obtaining the history of the stresses on vWF molecules as they move in a flow field; (ii) the detailed calculation of shear and extensional stress statistical distributions on the vWF molecules showcasing the importance of the tails of the distributions in addition to average values; and (iii) the investigation of the importance of the flow field configuration and of the location of vWF injection on the distribution of stresses over time. This study's contribution is

the statistical data for hydrodynamic stress on vWF along the trajectories of protein particles that could contribute to design the medical devices and reduce the cost of experiments.

The second application is to investigate the role of helicity in turbulent transport in channel and Couette flow and the interplay between helicity with scalar transport and coherent structures. Helicity is also important for understanding the relationship between coherent structures and turbulent kinetic energy. There has been a hypothesis that coherent structures at different scales are associated with regions in which helicity is large and dissipation of turbulent kinetic energy is low. Low dissipation means that these coherent structures could survive for a long time leading to significant impacts on the flow. In this study, Direct Numerical Simulation (DNS) of turbulent Poiseuille and Couette flow were used in combination with Lagrangian Scalar Tracking (LST) at various Schmidt numbers of 0.7, 6 and infinite (i.e., fluid particles), and the friction Reynolds number for both simulations was 300 to probe the correlation between helicity and dissipation, and the role of helicity in the regions of coherent structures in anisotropic turbulence. Our Lagrangian Scalar Tracking could provide the fluid velocity at each marker location with time. From these data, one can compute turbulent kinetic energy dissipation, vorticity, and helicity along these trajectories. The autocorrelation coefficients, the cross-correlation coefficients and the joint probability density function are employed to investigate the relation between helicity and dissipation, and helicity and vorticity and with the vertical velocity in the Lagrangian framework. In addition, conditional statistics for scalar markers are evaluated in flow regions of high dissipation or coherent structure regions based on vortex identification criteria. In addition, scalar markers that dispersed most or least in the flow field were also calculated to provide more evidence for the role of helicity in transport in turbulent flow.

# CHAPTER 1: INTRODUCTION

## 1.1 Turbulent flow

Turbulent flow has been known as the most common flow in industrial applications and atmospheric phenomena. The random motion of the flow could affect fluid mixing and interaction with solid surfaces (friction, heating, and pollutant dispersion) [1]. Turbulent flows could be encountered almost everywhere, for example, atmospheric and ocean currents, discharge of pollutants, oil transport in pipelines, flow through pumps and turbines, and the flow in boat wakes and around aircraft wing tips. Turbulent flows are characterized mainly by unsteadiness, vorticity, three dimensionality, dissipation, wide spectrum of scales, and large mixing rates [2] [3]. In addition, turbulent flow is highly irregular, random, chaotic, and exhibits multiscale flow conditions with a wide range of time and length scales [4]. In blood flow, these characteristics can cause harmful effects because of significant fluctuations in shear stresses and pressure. There has been evidence showing that turbulence effects are important to red blood cell damage causing hemolysis, which is enhanced when cells are exposed to turbulent stresses [5].

Turbulent fluid motion includes many interacting coherent structures commonly referred to as ‘eddies’. In particular, large energy containing eddies play an active role in the flow dynamics [6]. Vortex stretching is an important mechanism in a turbulent flow. The cascade process is a continuous transport of energy from mean flow to large eddies, from these large eddies to a series of increasingly smaller eddies. The smaller eddies are influenced by the strain rate imposed by the large eddies and are continually stretched. The smallest eddies dissipate the kinetic energy into thermal energy by viscous effects. The smallest eddy size, termed as the Kolmogorov scale, decreases with increasing Reynolds number. The largest eddy size depends on the flow configuration and is usually approximately as large as the size of the domain [2]. Illustrations of turbulent flow pattern and eddies are shown in Figures 1.1 and 1.2.

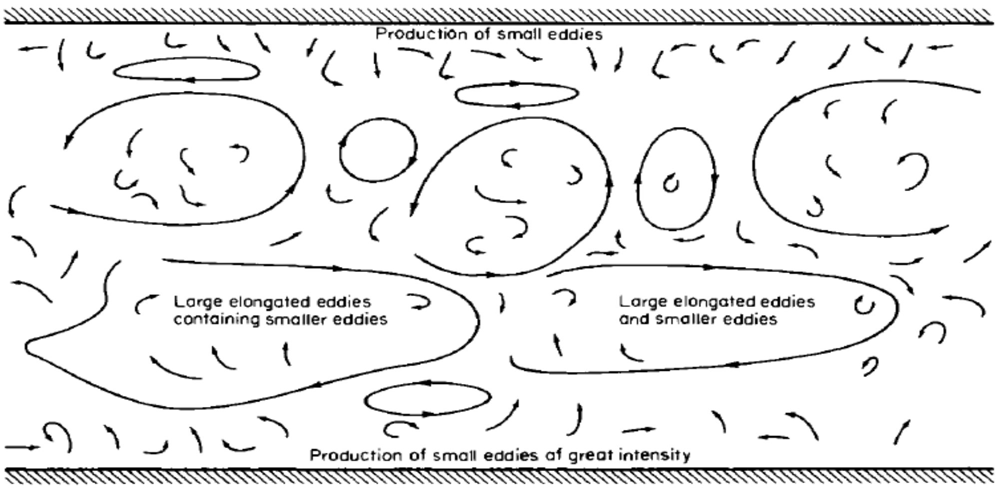


Figure 1.1 Schematic representation of local instantaneous flow patterns in turbulent flow in a pipe [7].

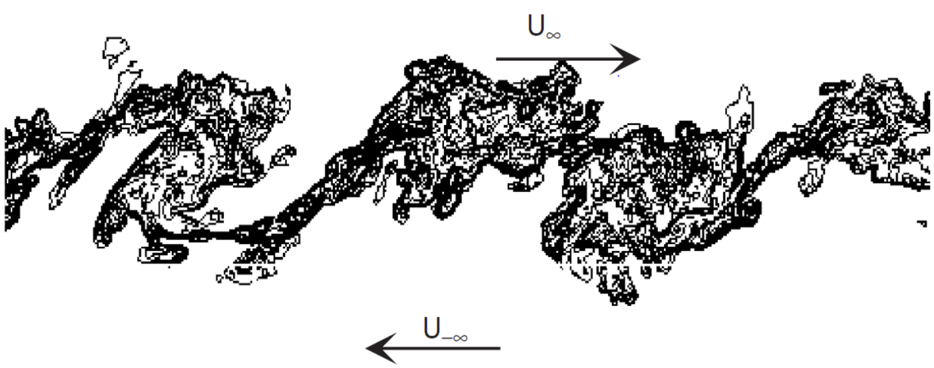


Figure 1.2 Turbulent eddies in a plane mixing layer subjected to periodic forcing [8].

With the fast development of computing systems, turbulent flows have been investigated using high fidelity numerical methods and results have been reported by many researchers [6, 9-14]. Wall-bounded turbulent flows at high Reynolds numbers have been an active area of research for many years. Many challenges remain in theory, scaling, physical understanding, experimental techniques, and numerical simulations [15-19]. Canonical wall-bounded flows have been studied e.g. the flat-plate boundary layer [20-23], pipe [24, 25], and channel flows [21, 26-29]. Simulations of wall-bounded turbulent flows are necessary in identifying physical processes occurring in near-wall turbulence, since the entire velocity field (and its derivatives and time series) are available for detailed analysis [30]. The behavior of fluctuations of the wall flow variables in a turbulent boundary flow or in a turbulent channel flow have been attractive topics in applications of drag, noise and heat transfer [31, 32]. Previously, the presence of large structures has been investigated and it is expected that comprehensive knowledge concerning the dynamics of these large energetic structures might be useful to model and control high Reynolds number wall-bounded flows [23].

Two simple canonical configurations of wall-bounded flow are Poiseuille and Couette flow [33]. Poiseuille flow is the pure pressure-driven fluid motion in channels with fixed walls, while Couette flow is the pure shear-driven motion of a fluid between walls that are moving relative to each other [34, 35]. Typical applications of pure Couette flow and combined Couette-Poiseuille flows are found in turbulent bearing films in lubrication technology, stratified two-phase flows and the flow between a tunnel wall. Because of the difficulties of achieving fully developed plane flow in a long channel with a moving wall in the case of Couette flow, experiments on this type of flow are limited [36]. In turbulent Couette flow, it has been revealed that the central part of the channel contains large-scale low- and high-speed regions extending over a very long streamwise distance [37]. Note also that a fully developed plane Couette flow has a constant shear stress across the entire channel that are averaged over time. The existence of a non-zero mean shear rate, and associated turbulence production at the center of the channel, gives a significantly different character to the flow in this region, as compared to pressure-driven channel flow [14, 38, 39]. The main issue of Couette flow is the existence of long and wide structures, which have been found experimentally and numerically that need large computational boxes to capture these structures making the study of this flow much more computationally expensive than turbulent Poiseuille flow [40]. (Our simulations of Couette flow for the frictional Reynolds number $Re_\tau = 450$ have converged and the data for the stationary state is illustrated through mean velocity, turbulent stresses and turbulent intensities that are described in appendix A).

In addition to the structure of turbulent flow, turbulent transport plays a crucial role in many important engineering and scientific applications, such as indoor air quality, motorway/railway tunnel ventilation, atmospheric pollutant dispersal, contaminant mixing in oceans and rivers, the spreading of airborne contaminants in enclosed environments, material and food processing, pneumatic transport, fluidized beds, slurry flows, or sediment transport [41-44]. Turbulent transport is dominant at relatively large scales (called production and inertial range scales) and due to the effects of viscosity, becomes weak at the small scales (the dissipation scales) [45]. Predicting the dynamics of a scalar advected by a turbulent flow is an important contribution in many applications. The temperature field, the concentration of chemical species or a level-set function to capture the interface in multiphase flows could be described by the scalar field [46]. One of the main difficulties for turbulent transport prediction lies in the intrinsic multi-scale nature of turbulence: depending on their size and density, particles will interact with structures of the carrier flow at different time and spatial scales [47]. On the other hand, the transport and mixing of passive components by turbulent flows are prevalent in environmental and industrial applications. [48]. Many chemical engineering processes in aqueous solutions are carried out at high Reynolds numbers and prediction of such processes is very challenging because the reaction rate depends on large scale features, such as stirring motions, geometry of the mixing device, etc., and on the distribution of the mixture fraction on the smallest scales [49].

Understanding and prediction of heat and mass transfer between a solid boundary and a turbulent fluid flow are important topics in many engineering problems. Many studies have been dedicated to the experimental investigation of this problem at various Reynolds (*Re*) and Schmidt (*Sc*) or Prandtl numbers (*Pr*) [50]. In the problem of mass transfer by fluid flow, the Schmidt number can range from order of unity (or less) for gaseous substances in air, to hundreds for salinity in water, and to thousands for color dyes in water [51]. Mass transfer with high-Schmidt number is important because it is related to the very common case of slightly soluble gases diffusing in liquids. Studying high $Sc$ number is more difficult in comparison to the case of heat or mass transfer at low or moderate $Pr$ or $Sc$ number because the diffusive sublayer lies entirely into the viscous sublayer, meaning that mass transfer efficiency is controlled by turbulent motions present very close to the wall [50].

The friction Reynolds number is defined based on friction velocity $u_\tau = \sqrt{\frac{\tau_w}{\rho}}$ (where $\rho$ , $\tau_w$ is the density of the fluid and the mean shear stress at the wall), the kinematic viscosity $\nu$ and $h$ is half of channel width [52-54]:

$$Re_\tau = \frac{u_\tau h}{\nu} \tag{1-2}$$

The Prandtl number $Pr$ is defined as [55, 56]:

$$Pr = \frac{\nu}{\alpha} \tag{1-3}$$

$\alpha$ is molecular thermal diffusivity.

The Schmidt number is defined as [57, 58]:

$$Sc = \frac{\nu}{D} \tag{1-4}$$

*D* is the molecular diffusivity.

With the significance of turbulent transport and the remaining challenges for this field of studies, there has been a lot of effort to investigate different aspects of transport in turbulent flow. Cazalboua et al. [59] modelled the turbulent diffusion of quantities such as the turbulent kinetic energy and its dissipation rate in outer part of wall bounded flow [59]. Isabelle et al. [50] studied mass transfer through the solid boundary of a turbulent channel flow using large-eddy simulation for Schmidt numbers $Sc$=1, 100, and 200 [50]. Chakravarthy et al. [45] employed the linear eddy model to investigate effects of molecular diffusion on turbulent scalar mixing [45]. Henning et al. [60] explored the consequences for the motion of passive tracers, based on a continuum model for the micro swimmer velocity field [60]. Yeung et al. [61] studied the dynamics of turbulent scalar transport in direct numerical simulations by solving the advection-diffusion equation in the presence of a uniform mean scalar gradient [61]. Using Direct Numerical Simulation (DNS), the turbulence structure and passive scalar (heat) transport in plane Couette flow at Reynolds number equal to 3,000 were also studied by Liu et al. [41]. The results showed that the total (turbulent and viscous) shear stress and total (turbulent and conductive) heat flux were constant throughout the channel [41]. To investigate the transport of scalars by turbulent flows with different shear stresses, Debusschere et al. [62] applied DNS to passive heat transfer in a plane channel and Couette flow. The simulations showed that streamwise vortices play a significant role in near wall heat transfer for both flows [62]. Pedro et al. [63] theoretically analyzed the transport of a passive scalar within a turbulent plane channel flow when the $Sc$ number associated to the molecular diffusivity of the passive scalar was a large number [63]. The application of computational fluid dynamics (CFD) using Reynolds-averaged Navier–Stokes equations (RANS) model to turbulent flows with mass transfer to estimate the turbulent scalar flux assuming the gradient diffusion hypothesis with the definition of the turbulent Schmidt number was carried out by Tominaga et al. [64]. Florian et al.

performed DNS of passive scalar transport in low Reynolds number turbulent channel flow at Schmidt numbers up to $Sc$ =49. This study showed the statistical quantities of the turbulent channel flow with mass transport and a scaling for the mean scalar field [65]. Ybarra et al. considered turbulent diffusion of a passive scalar with a large-Schmidt number ($Sc \gg 1$) in the viscous sublayer of a turbulent channel flow [66]. Yacine et al. also studied the turbulent flow in electrochemical reactors for scalar mixing with the implementation of a passive scalar transport equation into a hybrid spectral/finite element code [67]. Wang et al. investigated turbulent transport of momentum and scalars over an urban canopy using the quadrant analysis technique [68]. Rasthofer et al. extended multifractal subgrid-scale modeling within a variational multiscale method to (Large Eddy Simulation) LES of passive-scalar mixing in turbulent incompressible flow [69]. Watanabe et al. studied the mixing of reactive species at a high Schmidt number ($Sc \approx 600$) near the turbulent/nonturbulent interface is investigated in a planar liquid jet with a chemical reaction [70]. Pirozzoli et al. studied passive scalars in turbulent plane channels at high Reynolds number from 500 to 4000 [71] and Geert et al. [72] also applied DNS for passive scalar transport in plane turbulent channel flow subject to spanwise system rotation at $Re$=20000 and for wider range of rotation number Ro to obtain understanding of turbulent heat and mass transfer in rotating wall-bounded flow [72]. Mohaghar et al. [73] studied scalar power spectra and turbulent scalar length scales of high-Schmidt-number passive scalar fields in turbulent boundary layers [73]. A two-scale simulation modeling approach applied by Ranjan et al. [74] for its ability to model passive scalar transport and mixing in a wall-bounded fully developed turbulent channel flow (at $Re_\tau$= 395) at two different $Sc$ numbers (1 and 4) [74]. Bec et al. [75] studied the transport of long, flexible fibers in turbulent channel flow sample non-linear variation of the fluid velocity along their length. They provided an illustration for instantaneous distribution of fibers, the near wall alignment and tumbling [75].

Generally, studying turbulent transport is a subject that contributes significantly to the development of engineering and natural applications. However, this is a challenging problem for high Reynolds number. Our study objectives are to take advantage of supercomputers to simulate and model large scale motions at large Reynold numbers utilizing on our internal code with some modifications, investigate the transport in turbulent flow applied in medical applications, and examine the interactions between flow structures in turbulent regions and their relation to turbulent transport. We expect that our contribution could provide necessary data and evidence to investigate the effects of flow structure on the mechanism of scalar transfer from the wall and its interplay with quadratic invariant terms such as helicity and dissipation.

## 1.2 Hydrodynamic stress on von Willebrand Factor in turbulent flow

### 1.2.1 von Willebrand Factor under shear stress in turbulent flow

Blood pumps, ventricular assist devices (VADs) and even heart valves generate blood flow conditions that are not typical for blood flow in the cardiovascular system [76-79]. The non-physiological conditions generated as blood flows through mechanical devices including turbulence lead to red blood cell (RBC) damage, known as hemolysis, because of shear and extensional stresses [80-85] and to changes of the von Willebrand Factor protein [80, 86-90].

The blood multimeric protein Von Willebrand factor (vWF), which has a very high molecular weight, plays an important role in the primary haemostatis [91]. Protein vWF includes three A domains: vWF-A1 could recognizes the platelet GpIba receptor under shear, vWF-A2 is cleaved by ADAMTS13 and regulate protein size in circulation, and vWF-A3 is the primary binding partner for collagen on the denuded endothelium (as seen in Figure 1.3) [92]. vWF circulates in inactive globular form in blood flow, a conformational change to extended form is caused by sufficient mechanical forces. This extension exposes 3 domains of vWF. The A1 domain mediates binding to the platelet GPIB-α and integrin $\alpha_{IIb}\beta_3$ receptors. The cryptic $Tyr^{1605}$-$Met^{1606}$ cleavage site is exhibited in the A2 domain, and the binding to collagen is mediated by A3 domain. Turbulent flow facilitates cleavage of vWF causing vWF functionally deficient. When vWF exposed to turbulent flow, the platelet adhesion on vWF decrease and vWF activity even before severe structural changes such as loss of HMWM are detected [93]. The vWF initiates the formation of a hemostatic plug, which can adhere to the surface of a damaged blood vessel through a binding mechanism to collagen and simultaneous binding to platelets in the blood [94]. The resulting disease is known as the von Willebrand syndrome (vWS) [95] which can cause blood clotting irregularities and sometimes internal bleeding, especially to patients with cardiovascular implants.

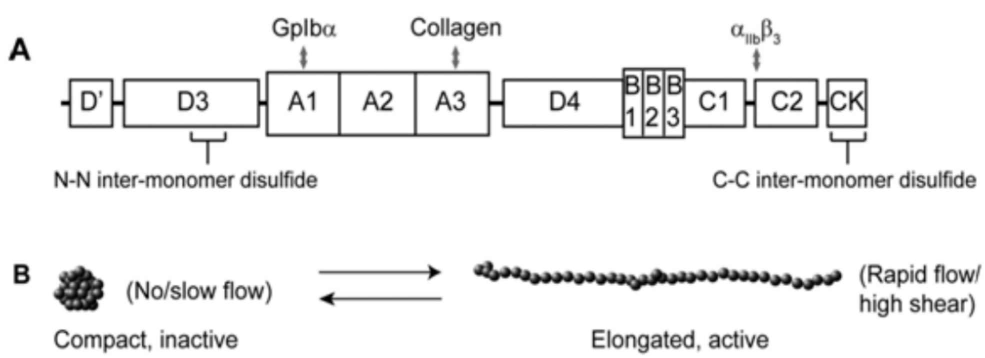


Figure 1.3(A) Schematic illustration of vWF's domains. (B) Possible mechanism of flow-induced conformational change [96].

The overall shape of vWF is dynamic and dependent on the type of flow in circulation. vWF multimers have overall compact, bird's nest shape. Above the critical shear stress, hydrodynamic drag overcomes the attractive forces between monomers within each concatemers, and vWF free in flow elongates and tumbles and there have been dynamic changes in each tumbling cycle. In elongational flow, concatemer extension will increase and prolonged compared to shear flow (as shown in Figures 1.4 and 1.5) [86, 94, 97-99].

Measurement of wall shear stress fluctuations has been a difficult issue because it is associated with the spatial resolution and frequency response of the probe and also with heat conduction to the wall [31]. Schneider suggested that a single vWF multimer forms a compact or collapsed structure like a folded protein. This is different to a regular protein, all repeating units are attracted to each other most likely without any sequence-specific binding preference, assuring the reversible character of the transition.  Changing the monomer size cause the drastic changes in critical shear rate [100]. In Rack et al. [101] experiments in microfluidic channels and computations (mainly 2D) were utilized to explore the vWF adhesion in the red blood cell free layer (RBC-FL) close to the vessel walls. While the margination of the vWF through the RBC-FL and its adhesion to the vessel wall were examined, and the importance of the stretching of the vWF between a globular form and an elongated form were explored, the authors appreciated the difficulty of conducting 3D computations that would connect the molecular behavior at the protein level to the hydrodynamic flow field.

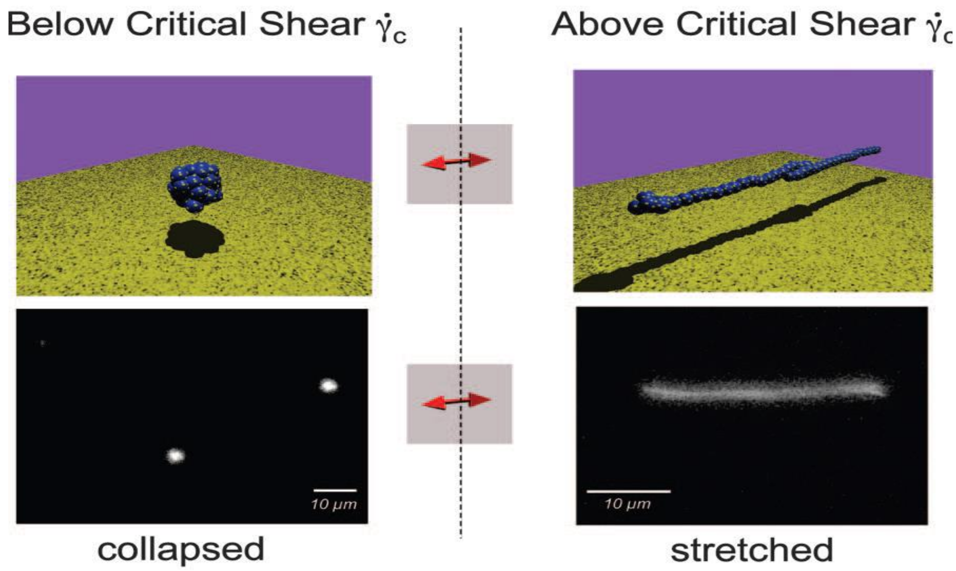


Figure 1.4 Dynamic conformational change of VWF under shear [100].

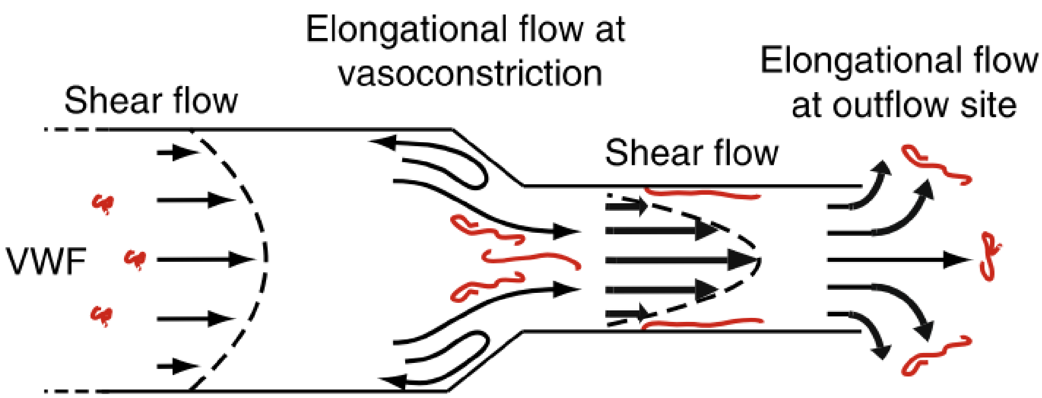


Figure 1.5 Illustration of the change of vWF in shear and elongational flow [89].

The behavior of the vWF as a sphere has been adopted by others, e.g., Gogia et al. [92] and Sharifi & Bark [86]. vWF is a multimer which contains several identical subunits and its function in primary hemostasis is strictly related to its multimer size. Svenja et al. provided evidence to show that the size distribution of recombinant and physiological vWF multimers is exponential [102]. Kania et al. predicted transition rates for going from a globule to an unraveled state of vWF in elongation flow using Weighted Ensemble Brownian dynamic (WEBD) simulations. The distribution of transition rate follows a lognormal distribution. The mean transition rate increases with the increment in strain rate [94]. Carlo et al. carried out experiment to separate the effects of shear stress alone and ADAMTS-13 in the presence of shear stress on vWF degradation. At a given shear stress, the main mechanism of vWF degradation was caused by ADAMTS-13. When the purified vWF protein underwent the supraphysiologic shear stress in the absence of ADAMTS-13, vWF multimers degraded into smaller multimers but not smallest vWF degradation fragments [103]. Santamaria et al. [104] carried out molecular dynamics (MD) simulations to study how shear-driven vWF activation and deactivation occurs. It was found that under equilibrium conditions the vWF A1 and A2 domains bind to each other, with the A2 domain specifically targeting the GPIba binding site in the A1 domain, thus blocking the binding of GPIba to vWF. A stretching force was needed to detach the two domains and unblock the GPIa binding site. However, a stronger stretching force can also unfold the A2 domain and cause protein degradation. Based on findings such as those in [104, 105], Belyaev [99] explored the interactions of the vWF subunits using coarse-grained computations, which are less detailed than MD but are necessary if one wants to explore the behavior of large molecules that are difficult (or even unfeasible) to simulate with MD. The vWF was modeled using the finitely extensible nonlinear elastic (FENE) potential that connected the domains of the vWF as beads with springs, and the surrounding fluid was modeled with the lattice Boltzmann method. Conformational changes of the vWF under hydrodynamic stress could be obtained, but the simulations were focused on the investigation of what happens to one vWF molecule as one changes the applied stresses by employing a specified pull on the molecule, or a specified shear stress. Wang et al. also demonstrated that a simple mechanical bead spring model can be used to predict the global conformational changes of tethered vWF. They showed that increasing chain length or MW could decrease the threshold shear rate because the biomechanical response of vWF change when the chain length, tether point location and the number of tethering location condition change [106]. Aleksey et al. studied the conformations of the vWF dimer in thermalized Lattice Boltzmann (LB) fluid with and without externally imposed shear stress. This study suggested that interdomain forces can regulate the shape and size of vWF multimers, rather than just mechanical properties [99]. Baldauf et al. used molecular dynamics simulations to examine whether tensile stress in vWF under shear flow activates the vWF A2 domain for cleavage by ADAMTS13 [107]. Morabito et al. use Brownian molecular dynamics simulation to examine the internal dynamics and biomechanical response of vWF multimer under shear flow. They examine the dynamic behavior of hydrodynamic forces acting on A2 domains as a function of shear rate and multimer length, as well as position of an A2 domain along multimer contour [108].

The effect of laminar, transitional and turbulent flow on vWF cleavage by ADAMTS13 was performed by vane rheometer by Bortot et al. [93]. Cleavage and nearly full digestion of vWF was shown in the turbulent flow. Meanwhile, there is no detection of cleavage for samples exposed in laminar and transitional flow. This simulation gives explanations for the effect of nonphysiological flows on vWF cleavage [93]. Antaki et al. introduced a continuum model of vWF unfolding which is developed within framework of multi-constituent model of platelet-mediated thrombosis. Although this model could be employed in numerical simulations of vWF mediated thrombosis or vWF degradation in complex geometries, there has been a considerable challenge to extend the model to 3D arbitrary flow and turbulent flows. Sharifi et al. applied scission theory to provide understandings in flow that produce large extensional forces on vWF resulting domain unfolding and exposure of cryptic site for cleavage through a metalloproteinase. Their findings can be applied in designing blood contact medical devices by providing hemodynamic limits to these devices that can otherwise lead to acquired von Willbrand syndrome. As mentioned in

Sharifi's paper, turbulent flow condition may enhance vWF cleavage due to increased mixing, collisions, high instantaneous shear stress or through the interaction of turbulent eddies [97].

### 1.2.2 vWF under extensional stress in turbulent flow

Apart from RBCs, there have been other microparticles that are affected by extensional stress in a flow field, such as synthetic, liquid filled capsules that are suspended in hyperbolic extensional flow. Experimental results have demonstrated that capsule deformation is a function of the strain rate for an extensional flow generated in a four-roll mill [109]. Other results have provided information to the extent that entomopathogenic nematodes were damaged during flow through an abrupt contraction, a predominately extensional flow regime [110]. Turning the focus back on vWF, when arterioles are cut, both the shear and elongational flow components increase with the elongational flow component selectively increasing at the site of rupture. After that, the flow would decrease with subsequent vasoconstriction that leads to a decrease of shear rate. Meanwhile, the elongational flow would increase precisely at the site of vasoconstriction hence it plays an utmost important role in hemostasis [86]. Therefore, studying the behavior of vWF under extensional flow is quite necessary since there are strong indications that unraveling the multimer vWF is more impactful in extensional flow than in pure shear flow. Table 1.1 is a collection of data from the literature regarding the critical elongational stress, or the critical elongational rate of strain for changes in the configuration of vWF and for selected types of cells.

vWF monomers have strong attractive interaction giving it a robust globular conformation, imparting significantly higher and well-defined thresholds for unfolding. When unfolding is started, vWF exhibits the same two types of behavior: unfolding-collapsing cycles in simple shear and abrupt but stable unfolding in extensional flow [98]. While there has been much research focusing on the effect of shear stress on the cell damage, the other component of viscous stress also plays a significant role in inducing cell damage, which is extensional stress. Apart from red blood cells, there have been other objects that have been affected by extensional stress. For example, the motion and deformation of a synthetic, liquid filled capsule that is freely suspended in hyperbolic extensional flow [109]. In fact, the shear and extensional stresses have usually combined to act on cell [84] [81, 111]. While important, the extensional stresses are often not given equal treatment in the literature for vWF. The reason might be the fact that shear stresses are more predictable than extensional stresses in a turbulent flow field, especially the shear stress at the solid boundary of a pipe or duct that can be calculated from a force balance and knowing the pressure drop in the device. However, extensional stresses can be damaging to vWF molecules at levels that may be one order of magnitude smaller than shear stresses [91] and can be seen in Table1.1. Apart from that, the detailed measurement of stresses in a hemodynamic velocity field is difficult, especially in-situ for turbulent flow conditions, since it involves the measurement of derivatives of the blood velocity in all three space directions, and in every location of the flow (not only the solid walls [80]). In such cases, the use of computational methods has become critical for both the probing of the hemodynamic conditions and for devise design [112]. In fact, Assessment of CFD performance in simulations of an idealized medical device the Food and Drug Administration (FDA) has issued challenges to the computational fluid dynamics (CFD) community for the accurate prediction of blood flow in typical blood flow devices [113-115]. From a polymer physics perspective, vWF stretching was further elaborated to prove that elongational flows were the most principal factors in the regulation of vWF and one of the prominent triggers in blood clotting. In vivo, shear force could promote conformational changes in vWF and act as a key factor in the dynamic regulation of vWF self-association [116].

Jhun et al. [117] designed two custom apparatus: a capillary tubing grader (CTD) and a Taylor-Couette-type degrader, to control the stress and exposure time to these stresses and measure the degradation of high molecular weight multimers (HMWM) in vivo in wide range of stress and exposure times but modifications of that apparatus would need to be made to control for elongational stress rather than shear stress (e.g., a parabolic channel flow or a four-roll Taylor mill, instead of Taylor-Couette viscometer) [118]. Bortot et al. also provided two microfluidic devices: a 90-degree step leading to an abrupt constriction to replicate the shear rate (SR) obtained from the computational fluid dynamics (CFD) models of normal and stenotic aortic valves [119]. Recent results utilizing Computational Fluid Dynamics to guide microfluidic experiments in parabolic channels have shown that elongational rates are one order of magnitude smaller than shear rates (10,000 $s^{-1}$ vs 1,000 $s^{-1}$), but they do not lead to significant cleavage of the vWF protein in the presence of ADAMTS13 [119]. Dong et al. [105] applied MD simulations to study force-induced unfolding of the A2 domain with and without a single N-linked glycan type on each site. The pulling force (i.e., the extensional stress) was predetermined and it changed as the simulations progressed. Zhang et al. used single-molecule experiments proving the A2 domain is unfolded by elongational forces in the range experienced by vWF in the vasculature and only the unfolded A2 domain is cleaved by ADAMTS13 [120].

In summary, the simulation of extensional stress on vWF mostly from the molecular level and in this study, the statistical values of both shear and extensional stress on vWF at larger scales have been computed to evaluate the distribution, the average values of hydrodynamic stress on vWF. Also, the obtained data could be useful to estimate the percent of vWF particles that have the stress overcome the threshold of unraveling in turbulent flow.

### 1.2.3 Critical shear and extensional stress for the unravelling of vWF

The critical value of shear stress (the stress is higher than this level then there are changes that affect the function of protein) for vWF deformation is around 5 Pa [86]. It has been found that the vWF is hemostatically active only under high shear rate, and the value of the critical activation threshold is $\gamma_{crit} \approx 5000\ \mathrm{s}^{-1}$ [100, 121]. In addition, there is a sharp, well-defined, large scale extension of vWF with end-to-end lengths up to 10 μm at shear rates > 5000 $\mathrm{s}^{-1}$ (corresponding to shear stress ~4 – 5 Pa) [92]. Investigation of vWF in solution at shear stress of 6 Pa has showed that high shear stresses and long exposure times caused loss of high molecular weight multimers of vWF, resulting in poor binding to platelets and subendothelial collagen [92]. For blood cells, both the shear and the extensional stresses combine to act on the cell [81, 84, 111, 122, 123]. Interestingly, RBCs deform at about 20 Pa in a simple shear flow, while in an extensional flow, the deformation is slightly higher (as measured by the deformation index) and occurs at much lower stress levels (about 6 Pa). Hence, the deformation of RBCs is more efficient in an extensional flow than in a simple shear flow [80], and one could examine the hypothesis that this could be the case for proteins [86, 95]. Further, the time of exposure of a cell in a stress field affects the level of cell trauma [115, 123-128]. In a combination of transient, extensional, and shear flow experimental studies, cultures of Chinese hamster ovary (CHO) showed cell damage above a critical value of turbulent kinetic energy dissipation rate [129]. Microfluidic sensing of the mechanical cell damage under an extensional stress field showed that the CHO cells were mechanically damaged when the extensional stress was greater than ~250 Pa [130]. Table 1.1 provides literature review of critical shear and extensional stresses for the deformation of vWF, cells, and capsules.

Table 1.1 Literature review of critical shear and extensional stresses for the deformation of vWF, cells, and capsules.

| Type of deformable object | Critical shear stress or rate of strain | Critical extensional stress or rate of strain | Ref. |
|---|---|---|---|
| von Willebrand Factor (vWF) | Shear rate 300-600 $s^{-1}$<br>Shear stress > 20 $dyn/cm^2$ | Elongation rate of strain 560 $s^{-1}$ | [91] |
| vWF | | Elongational strain rate < 300 $s^{-1}$ no unraveling;<br>Elongational strain rate 300 to 400 $s^{-1}$, metastable unraveling;<br>Elongational strain rate > 400 $s^{-1}$ unraveling | [131] |
| vWF fibers | Critical shear rate = 5,000 $s^{-1}$ | | [100] |
| vWF | Critical shear rate = 5,522 $s^{-1}$ | | [98] |
| vWF | Critical shear stress = 2-2.5 Pa | | [132] |
| High molecular weight multimers of vWF | Shear rate ≥ 5000 $s^{-1}$ for conformational changes;<br><br>Shear stress < 1012 $dyne/cm^2$, no molecular degradation;<br>Shear stress > 3070 $dyne/cm^2$ exposure time of 60s, 90.7% molecular degradation, while exposure time of 600s led to 96.1% molecular degradation | | [117] |
| vWF (~50nm typical vWF dimer) | Critical shear rate<br>300 to 600 $s^{-1}$ | Critical elongation rate ~560$s^{-1}$ for unfolding | [95] |
| Tethered von Willebrand Factor | Critical shear rate = 5000 $s^{-1}$<br>Critical shear stress = 2.0–2.5 Pa. | | [106] |
| Red blood cell (RBC) | Shear stress > 20 Pa | Extensional stress > 6 Pa | [80] |
| Chinese hamster ovary (CHO) cells | | Extensional stress > 250 Pa | [130] |

| | | | |
|---|---|---|---|
| vWF concatamers | Critical shear stress 50 dyn/cm$^2$ (5 Pa) | | [86] |

According to Pushin et al. [133] and Zlobina [134], the vWF molecule can undergo irreversible stretching or unfolding when it undergoes stresses even for small times (as in Figure 1.6). Therefore, the history of stresses on a molecule is important and can lead to an elongated or cleaved vWF as a result of a high stress experienced at earlier times, or as a result of low stress experienced over long times, even when the molecule at one particular snapshot in time is not stressed.

In literature [133], the cumulative effect of shear for platelet activation leading to conformational changes of vWF was calculated and compared to a critical shear stress as follows:

$$CSS = \int_{t_{in}}^{t_{out}} \tau(t)dt \geq CSS_0 \qquad (1\text{-}5)$$

where CCS is the cumulative shear stress acting on platelets with vWF, and $\tau(t)$ is the shear stress which platelets are exposed under unsteady conditions at time t.

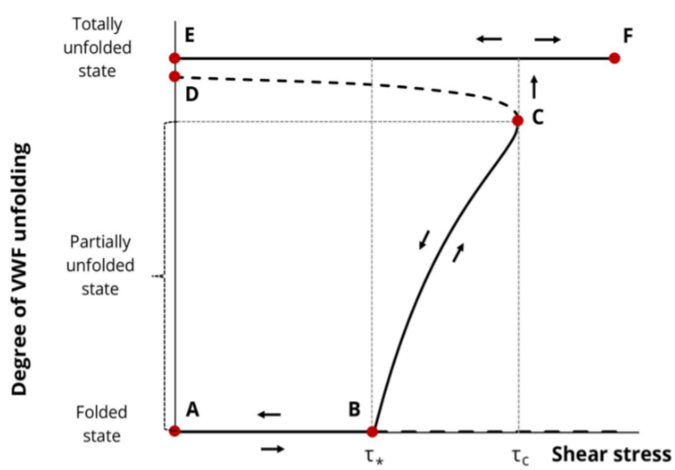


Figure 1.6 This figure from ref. [133] indicates that the folding-unfolding of the vWF on the surface of platelets depends on the shear stress values and a molecule unfolding on a surface has interactions and forces causing it is not a reversible process – it depends on the history of the stress that is experienced by the vWF molecule.

For RBC hemolysis, power law models are often used to quantify the expected hemolysis by considering both the stress level and the time of exposure,

$$HI = C\tau^{\alpha}t^{\beta} \tag{1-6}$$

where *HI* is the hemolysis index (a measure of hemolysis), $\tau$ is shear stress, *t* is length of exposure time to stress $\tau$, and the constants $\alpha$, $\beta$, and *C* are obtained through experiments.

In this study, we assume vWF degradation follows the power-law dependency which can ease the calculation process because we want to emphasize the stress component on vWF particles first. Prior research with vWF degradation with time, for example Zhussupbekov et al. [98], predicted that clearly indicate a power law model for the unfolding of vWF with shear stress in figure [98]). From their data, a constant percentage of vWF unfolding occurs either when the stress is high and the time of exposure is low, or when the inverse occurs. Another example of results where a power law model for vWF elongations appears to be valid is in the work of Kania et al.[131]. Indirect evidence that a power law applies for the change in protein conformation vs time and shear rate (which can be translated to stress using the fluid viscosity) is also offered in [132], where a normalized radius of gyration of the vWF is plotted as a function of the product of shear rate times a characteristic time. Even though the mechanisms of protein elongation and the mechanism of ADAMTS13 cleavage are complex, applying a power law as a first order approximation makes sense. When extracting the data from Figure 1.7 and the data in Figure 1.8 and the obtained plot in Figure 1.9, it has been shown that the unfolding of vWF follows the power law model but the obtained values $\alpha$ are different to 1 and varies for different cases. However, for the sake of simplification, we assumed that the constants $\alpha$, $\beta$, and *C* are close in value to one, so we made them equal to one.

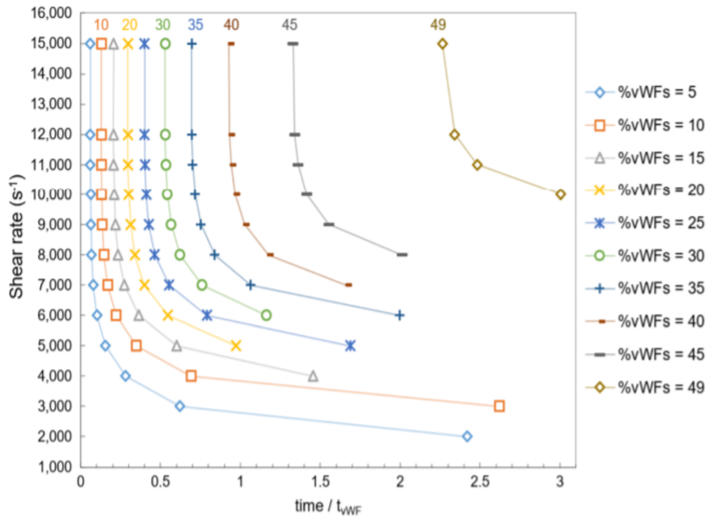


Figure 1.7 The prediction of unfolding of vWF subjected to shear. This is a copy of Fig. 4 from ref. [98] where the inverse proportionality of shear rate (and thus shear stress) with time of exposure is evident for the unfolding of vWF. Unfolding of vWF is not the same as degradation. The experiments that Antaki used to validate his work actually proves that vWF is not degraded.

**TABLE 2 Averaged exposure time required to unravel a globular vWF multimer for varied elongational rate**

| Strain rate ($s^{-1}$) | Required exposure time |
|---|---|
| 1500 | 315.2 h |
| 2000 | 1.31 h |
| 2500 | 1.03 min |
| 3000 | 5.12 s |
| 3500 | 0.75 s |
| 4000 | 0.17 s |

Figure 1.8 The Table 2 in ref. [135] provide data for averaged exposure time required to unravel a globular vWF multimer for varied elongational rate.

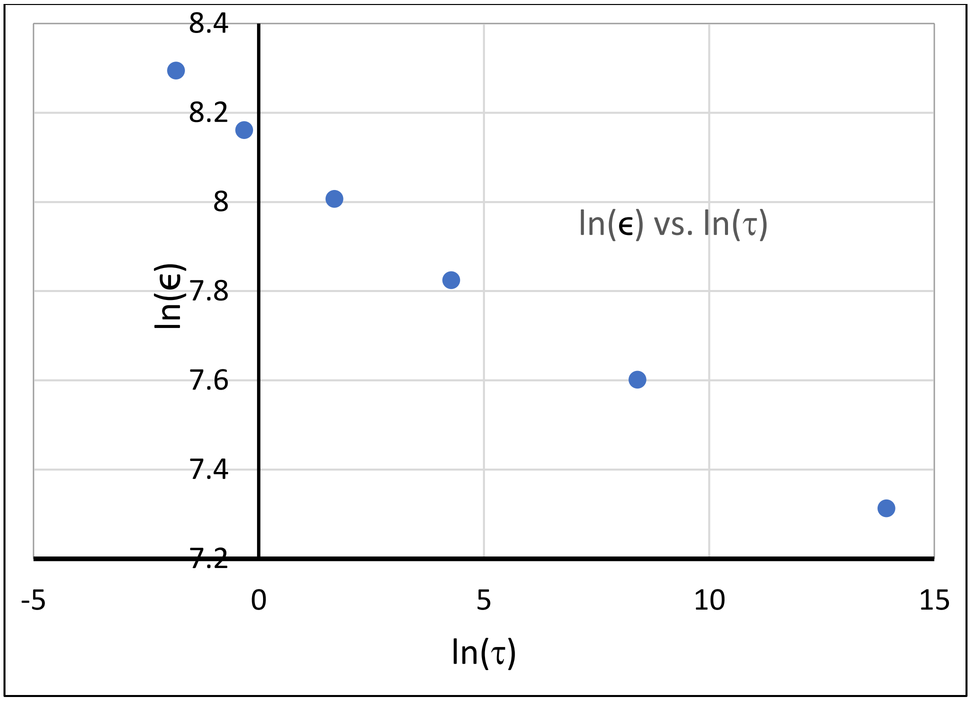


Figure 1.9 This is a plot of the logarithm of the elongational rate vs the logarithm of the exposure time using the data from Table 2 in ref.[135]. The straight line indicates the validity of a power law model. Strain rate is in $s^{-1}$ and exposure time is in seconds. The values in that Table are shown, in Figure 1.8.

Development of surrogate models for vWF degradation could be a viable alternative to the cases in which resolving fine scales of turbulent motion is infeasible [98]. Although there have been many studies on the vWF degradation, they have not fully characterized the comprehensive model for this process. High fidelity simulations, instead of turbulence modeling that is based on Reynolds Averaged Navier-Stokes (RANS) equation approaches, can provide detailed and accurate numerical predictions while avoiding empiricisms and approximations, which the FDA wanted to evaluate. Canonical flows that can be used as models for blood flow can be simulated with Direct Numerical Simulation (DNS), while flow in the complicated geometries of medical devices can be simulated with the less accurate RANS techniques. Using RANS for the calculation of extensional stresses locally in a turbulent flow field would not be feasible, since RANS provides the average velocity and not the fluctuating velocity field in 3D.

Therefore, recognizing advantages of DNS and Lagrangian Scalar Tracking (LST) we applied it to the case of vascular assist devices and indicate that (i) the development of a numerical methodology for obtaining the history of the stresses on vWF molecules as they move in a flow field; (ii) the detailed calculation of hydrodynamic stress statistical distributions on the vWF molecules showcasing the importance of the tails of the distributions in addition to average values; and (iii) the investigation of the importance of the flow field configuration and of the location of vWF injection on the distribution of stresses over time.

In addition to the flow simulation, the trajectories of particles that serve as surrogates of the vWF were modeled, and the values of the shear and extensional stresses along the individual vWF trajectories were calculated as they traveled in the flow field. Two flows, a plane Poiseuille flow (PF) and a plane Poiseuille-Couette flow (PC) were examined, and the trajectories of vWF molecules released at different locations in the PF and PC flow fields, respectively, were calculated. The history of the particles was thus computed, allowing the calculation not only of the average value of the stresses, but also of the statistical distribution of the stresses as a function of time and as a function of the location of vWF release, and of the history of the stresses as a function of time of exposure in the flow field.

## 1.3 Helicity and Dissipation and Coherent structures

Controlling turbulent flow plays a crucial role in engineering practical applications. It can be achieved only when the physical aspects of turbulence are well understood [136]. The notion of helicity was introduced about half a century ago. However, its role in the turbulence behavior and its influence on turbulence energy redistribution remains under debate until now [137]. Helicity is a topological variable, which measures the degree of the linkage of the vortex lines in a flow field, and includes linking, twisting, and writhing, degree of the knottedness and degree of broken symmetry [138-140]. Helicity plays an important role in the generation and evolution of turbulent flows, and helicity is one of only two inviscid invariants (kinetic energy and helicity) in 3D turbulence [141-143]. Helicity appears in natural phenomena such as hurricanes, tornadoes and rotating ‘supercell’ thunderstorms in the atmosphere and Langmuir circulations in the oceans [138]. It is not only important in atmospheric and geophysical flows but also is a helicity-based index which is used in biomedical research to quantify swirling motions in cardiovascular flows [144]. Helicity is also critical in characterizing complex 3D flows such as mixing, loss of stability and transition in turbulence, vortex breakdown and topology of vortices. The helical coherent structures could boost the mixing in chemical components [145]. On the other hand, helicity is also a crucial and universal property of three-dimensional coherent structures in turbulent and transitional flows [146-148]. The existence of mean of helicity could modify the values of the standard transport coefficients and introduce new effects described as ‘pseudo-transport effects [149].

Total helicity and helicity density play important roles in understanding the nonlinear dynamics, intermittency, and topology of fluid turbulence [146]. The total helicity in a flow, H, is defined as a volume integral in the flow field (H = $\int \boldsymbol{u} \cdot \boldsymbol{\omega} dV$, where $\boldsymbol{u}$ is the velocity vector and $\boldsymbol{\omega}$ is the vorticity vector. The inner product of velocity and vorticity is called the helicity density, $h$, ($h = \boldsymbol{u} \cdot \boldsymbol{\omega}$) [150, 151]. In general, there are two types of helicity studies, one is focused on exploring the emergence of helicity and the other is focused on investigating the effects of helicity on the dynamics of turbulence [152-154]. For this latter type of studies, most have concentrated on homogeneous turbulence and its effects on the turbulent kinetic energy cascade [153].

### 1.3.1 Helicity and dissipation rate

According to Moffatt, high relative helicity density should be correlated with low energy dissipation rate and vice versa [155, 156]. It has been noted that in the presence of helicity, the turbulent energy transfer may be suppressed due to the topological constraint related to the possible conservation of kinetic helicity [157]. Helicity is associated with the corkscrew motion of fluid particle and, according to some studies, the presence of helicity in isotropic turbulence does somewhat weaken the energy cascade [158]. Another study also suggested that in regions of low dissipation, which occupy a large part of the volume, there exist coherent, helical structures [159]. Orlandi at el. [136] considered a rotating pipe in which the flow symmetry was disrupted by the rotation and a mean helicity was present. They showed that when helicity increased, the dissipation was reduced [136].

From the analysis on the vector identity:

$$|\boldsymbol{u}\cdot\boldsymbol{\omega}|^2+|\boldsymbol{u}\times\boldsymbol{\omega}|^2=|\boldsymbol{u}|^2|\boldsymbol{\omega}|^2 \tag{1-7}$$

( $\boldsymbol{u}$ is velocity vector and $\boldsymbol{\omega}$ is the vorticity vector) the contributions from convection terms are small in regions of high helicity density. A high rate of energy cascade to smaller scales is indicated through large values of the term $\boldsymbol{u}\times\boldsymbol{\omega}$, hence the regions which are helical have relatively low dissipation [151, 160]. Because the nonlinear convective acceleration term in the rotational form of equation Navier-Stokes equation (the Lamb vector $\boldsymbol{\omega}\times\boldsymbol{u}$) represent for the cascade of turbulent kinetic energy. Therefore, the cascade of turbulent kinetic energy is prevented in the region with high helicity density $\boldsymbol{u}\cdot\boldsymbol{\omega}$ [156, 161]. When the velocity and vorticity vectors are aligned, the nonlinear energy transfer is inhibited [146]. For a bounded system, the helicity is a Galilean invariant quantity that is only determined by the vorticity field. However, the relative helicity density is a local quantity that depends on velocity and does not display Galilean invariance. Therefore, what velocity is used in this definition is important [141, 151].

Pelz et al. investigated the role of helicity density fluctuations using direct numerical simulation (DNS) of turbulent channel flow with the Taylor-Green vortex flow [162]. They concluded that while the vorticity is mainly in the spanwise direction near the rigid wall, towards the center of channel, the large-scale vorticity was being convected by and aligned with the mean flow. Far from the wall, the large-scale turbulent features were approximately force-free in that $\boldsymbol{u} \times \boldsymbol{\omega}$ was relatively small [162]. Leonid at el. applied DNS for a Taylor-Green vortex to test the relation between dissipation and helicity density [159]. Accounting for the normalized helicity density in selected points in the flow (i.e., only those that had small dissipation defined as a very small percent of the maximum dissipation, $\epsilon<10^{-3}\epsilon_{max}$ where $\epsilon$ is dissipation rate), it was found that the vorticity and velocity vectors were aligned with increasing probability, as the dissipation decreased. However, it was noted that this effect was observed in transitional turbulence. The alignment of $\boldsymbol{u}$ and $\boldsymbol{\omega}$ in low dissipation regions must be tested in fully developed turbulent flows [159].

By contrast, Speziale examined the role of helicity fluctuations in relationship to small scale intermittency and coherent structures in turbulent flows [163]. The author indicated that it is extremely unlikely that these helicity fluctuations can be correlated with turbulence activity such as coherent structures and small-scale intermittency [163]. Rogers and Moin used DNS of homogeneous flows and channel flows and indicated that there is no correlation between relative helicity density and the dissipation of turbulent kinetic energy in homogeneous turbulent flows. As for channel flow, the study showed that except for low dissipation regions near the outer edge of the buffer layer, there was no tendency for flow to be helical. They did not observe strong peaks in the relative helicity density probability density function (PDF) and the association of these peaks with regions of low dissipation [151]. Wallace et al. used joint probability analysis and indicated that alignment of the vectors is associated with lower turbulent kinetic energy dissipation. There has been little relationship between small instantaneous dissipation rate and large relative helicity density except in the regions of the high shear flows where all instantaneous dissipation rate amplitudes are small compared to the largest values occurring in the whole flow domain [156]. Choi et al. suggested a strong correlation between helicity and enstrophy in fluid turbulence. The intermittently large local helicity was found in the core region of the coherent rotational structures, thus showing a strong correlation with local enstrophy not dissipation [161]. Choi et al. calculated helicity in the Lagrangian sense to apply it for the study of turbulent transport and diffusion problems. Based on onset of intermittent distribution acceleration is closely related to movement of vortical structures, this study compared the helicity distribution to the intermittent distribution of Lagrangian velocity acceleration. They argued that this comparison could give a relation between helicity and turbulence transport and particle dispersion problems [164]. Biferale et al. simulated fully developed homogeneous and isotropic turbulence and investigated the transfer properties of energy and helicity fluctuation [165]. By-and-large, it appears that the interaction mechanism between energy and helicity dynamics is complex and it is often unclear, even more so in anisotropic turbulent flows [138, 140]. Nguyen and Papavassiliou applied DNS of turbulent channel flow at $Re_\tau$=300 in conjunction with Lagrangian tracking of fluid particles and passive scalar markers for $Sc$ number 0.7 and 200 to calculate local helicity along trajectories of markers and fluid particles. The Lagrangian helicity distribution indicated that a change of the alignment between velocity and vorticity vectors occurs for scalar transport markers [150].

In this study, the DNS is combined with Lagrangian scalar tracking (LST) to simulate Poiseuille and Couette flows and compute the velocity of particles at different $Sc$ [166]). The calculations provided the total helicity and the helicity of the fluctuating velocity field, as well as the dissipation of the turbulent kinetic energy (TKE) in the Lagrangian framework. Statistical analysis was used to evaluate the correlation between helicity and dissipation. In this way, one can make inferences about the use of helicity as an indicator to characterize the level of energy cascade. The two types of flow (Poiseuille and plane Couette) were chosen to gain insights for the correlation between helicity and dissipation in flows that have different structures. A plane Couette flow, where the driving force for the fluid flow is the shear effect of the two channel walls moving in opposite directions, exhibits a wider logarithmic layer than that plane channel flow [167] with the same $Re_\tau$ and thus Couette turbulent flow has a different velocity structure to the Poiseuille channel flow [168-170]. The non zero gradient in the mean velocity profile at the centerline of the Couette flow leads to the non-zero production of turbulent kinetic energy, resulting in higher turbulent velocity fluctuations at the centerline in comparison to channel flow [35, 62].

The contributions of this work are to (a) determine the correlation between helicity and dissipation in a Lagrangian framework; (b) determine the effects of helicity, if any, on scalar transport for different $Sc$ scalars; (c) probe the correlation of helicity and flow structure in different turbulent flows and how it affects turbulent transport.

### 1.3.2 Helicity and coherent structures

There have been a lot of studies focusing on various aspects of helicity. Yokoi et al. suggested that the inhomogeneity of the mean field could maintain both anisotropy and helicity of turbulence [160]. Chen et al. explained the mechanism which permits a joint forward cascade of energy and helicity in 3D turbulence. However, the role of helicity in three-dimensional turbulence is still somewhat mysterious. The detail of the interaction between energy and helicity dynamics has not been clarified [153]. Umberto et al. investigated the relationship between helical flow structures and vascular wall indexes of atherogenesis in aortocoronary bypass models and concluded that helical flow plays important role in preventing plaque deposition or in tuning the mechanotransduction pathways of cells. The authors also applied a quantitative method (Lagrangian approach) based on a mathematical description of helical motion along particles trace to evaluate the level of helicity in the flow field [171]. Choi et al. explained the cause of the intermittency of helicity in the connection with coherent vortical structures. The obtained results suggested that high helicity occurs ~~on~~ with the intensely rotating structures [161]. Biferale et al. showed that when helicity dominates, the dynamic structures are less coherent and present only on a much larger scale [165]. Li et al. studied the geometrical and vortical statistics in the small scales of both helical and nonhelical turbulences. The data of relative helicity density showed that the alignment between u and $\omega$ comes predominantly from large-scale motions. The author also observed that the intermediate eigenvalue of the vorticity strain rate tensor is more probable to take negative values when the helicity injection rate is positive and vice versa [173]. Yokoi et al. studied the effect of kinetic helicity on turbulent momentum transport. The authors suggested that the inhomogeneous turbulent helicity coupled with the mean vorticity or rotation could contribute the generation of large-scale flow [157]. Alex et al. studied the flow in 3-D cubic cavity driven by its parallel walls moving in perpendicular directions to elevate helicity. The velocity vector field, the helicity density, kinematic vorticity number and normalized helicity density were investigated at various cases of flow in lid-driven cubical cavity with the Reynolds number in the range of 100-1000 [145]. The mechanism of the mean-flow generation and its relationship to the turbulent helicity were investigated in a rotating inhomogeneous turbulence with an external force by

Kazuhiro. The obtained model indicated that the inhomogeneity of helicity plays an important role in rotating turbulence such as the momentum transport [154]. Yu et al. suggested in turbulent channel flows without rotation, the helicity spectra are chaotic. In the near wall regions, the multiscale nature of helicity is detected, which highlights the complexity of wall-bounded turbulence [140]. There are also various studies that focus on the simulation of cascade of kinetic energy and helicity in turbulent flow [174] [175], mean and fluctuate helicity budgets for evaluating the system rotation effects on flow evolutions [176].

Coherent structures in turbulent flows have been one of the most attractive topics in fluid mechanics. Coherent structures are a spatio-temporal self-organization, an order or structure that contradicts the long-held belief of the quasi-randomness of turbulence [177-179]. When the interaction term $\boldsymbol{u} \times \boldsymbol{\omega}$ is small, the energy transfer is small, and this term is minimized by the alignment of the velocity and vorticity vectors that is represented by helicity density. Therefore, the helicity density is important in evaluating coherent structures and turbulence [180]. There was an argument that coherent structures at different scales are associated with regions in which helicity is large and dissipation is low. Low dissipation means that these coherent structures could survive for a long time and therefore impose significant impacts on the flow. The sign of helicity depends on whether right-handed or left-handed helical motions are dominant in the flow. There was a hypothesis that helical behavior inhibits the nonlinear energy cascade hence the helical structures could endure coherent structures in long time [151]. Yuning et al. reviewed and listed helicity as one of methods for vortex identification in hydroturbines by which the normalized helicity can be employed to extract vortex core lines with assumption that near the vortex core regions, the angle is small, hence the maximal points of normalized helicity could be used to identify the vortex core [181]. The sign of normalized helicity is used to identify the swirling direction of the vortex [181].

Tsinober et al. indicated that the three-dimensional coherent structures possess coherent helicity. However, this assertion was carried out on transitional or rather low $Re$ number [182]. Levich et al. explored the case of homogeneous turbulence and pointed out that the existence of helical structures and fluctuations in 3-D turbulent flow are correlated to the phenomena of intermittency and coherent structures [182]. Pelz et al. investigated the local helicity fluctuations in Poiseuille and Taylor-Green vortex flow using direct numerical simulation. They suggested that the coherent structures, small-scale intermittency and helicity fluctuations are correlated [146, 162]. James et al. used a miniature multi-sensor hot-wire probe to measure vectors with a special resolution of Kolmogorov dissipation lengths for three types of turbulent flow which are turbulent boundary layer, two-stream turbulent mixing layer, turbulent grid flow [183]. The probability density distributions of the relative helicity density of the total and fluctuating velocity and vorticity were calculated at different conditions. However, their results have not elucidated whether within coherent structures, the relative density is large or not [183]. In the past, Andre et al. considered the effects of helicity on the dynamics of flows in the absence of magnetic field by energy and helicity spectra [152]. The author also referred to the result of Kraichnan that helicity increase the diffusion of a passive scalar by a factor of the order of 20% which indicated that helicity is important only in the magnetohydrodynamic context [152]. According to Roger et al., when deriving the equation governing the mean vorticity field, helicity density is related to the nonlinear vortex stretching and convective terms in the vorticity equation. Therefore, nonlinear interactions are reduced by helicity [151]. They investigated helicity in homogeneous turbulence, homogeneous irrotationally strained flows and homogeneous shear flows; and fully developed turbulent channel flow. The obtained results showed no apparent correlation of the fluctuating helicity density contours with the hairpin vortices or with strong spanwise coherent vortices [151].

However, the relation between helicity density and coherent structures has been still tenuous. The large coherent hairpin like vortices that dominate the homogeneous shear flow do not correlate with any level of helicity density. The simulations showed that there was no evidence for the association of relative helicity with low dissipation or coherent structures [151].

In fact, as described by theory suggested by Speziale, it is unlikely that these helicity fluctuations can be correlated with turbulence activity such as coherent structures and small-scale intermittency because of the nature of the velocity and pressure field fluctuations [163]. When studying experiments on helicity density of turbulent flow for mixing layer, Jame et al. [156] suggested that the streamwise vortices have significant relative helicity density and may be the source of the tendency of the alignment between total velocity vector and vorticity vectors as well as the higher rms values of streamwise fluctuating vorticity in comparison to other two components. However, their results did not clarify whether the relative helicity density should be large within coherent structures. Accordingly, coherent structures when vorticity axes nearly aligned with mean velocity will have rather high helicity densities than those that are more orthogonal to the mean velocity. As in mixing layer, the large-scale spanwise vortices have low relative helicity density [156]. Kerr et al. showed the histograms of the normalized values of helicity, the strain rate and vortex stretching and concluded that there is evidence for a various type of alignment between velocity and vorticity [141]. They also suggested that the dissipative regions or turbulence have a characteristic as a sheet-like structure. On the other hand, the regions with high value of normalized helicity, there is no evidence that these regions are involved in the turbulent cascade [141]. Shtilman et al. applied direct numerical simulations of the complex flow with no mean flow, forcing or special, deterministic initial conditions [180]. The authors argued that there was spontaneous generation and fluctuation of helicity in an unforced turbulent flow which revealed significant changes in the topological structure of the vorticity field –[180]. Wolfgang et al. studied the statistics of helicity fluctuations in homogeneous isotropic turbulent flows and from the observed fluctuations, it was expected that the invariance properties of helicity could not be related to the buildup of the correlations and whether the role of helicity fluctuations in the organization or characterization of turbulent structures is still questionable [147].

Vortices are characteristics structures that significantly influence the transport of momentum and other quantities in fluids [184]. There have been various Galilean invariant vortex identification techniques based on local analysis of velocity gradient tensor $\nabla\boldsymbol{u}$ such as Q criterion, $\lambda_2$ criterion, $\Delta$ criterion, swirling strength ($\lambda_{ci}$) criterion [185]. In this study, the method that is chosen to identify the vortices is the Q-criterion, using the second invariant Q. This method is suitable for the identification of a vortex in the incompressible fluid. The rotating force overcomes the strain force (when Q > 0) ensuring the existence of the vortex structure and protecting the vortex surface from deformation [181]. The Q values are determined as follows [186-188]:

$$S_{ij} = \frac{1}{2}\left(\frac{\partial u'_i}{\partial x_j} + \frac{\partial u'_j}{\partial x_i}\right) \tag{1-8}$$

$$\Omega_{ij} = \frac{1}{2}\left(\frac{\partial u'_i}{\partial x_j} - \frac{\partial u'_j}{\partial x_i}\right) \tag{1-9}$$

$$Q = \frac{1}{2}(\|\Omega\|^2 - \|S\|^2) \tag{1-10}$$

In this study, DNS and LST have been combined to compute the helicity at the location of passive particles that are dispersing in turbulent flow and at various Schmidt numbers, *Sc*. The flow fields for plane Poiseuille and plane Couette flow were utilized to provide insights for turbulent transport in relation to coherent flow structures. The turbulence structure of channel and

Couette flows is inherently different, since there is no turbulent kinetic energy production in the center of Poiseuille flow, while there is in the center of a plane Couette flow channel. At the same time, the Reynolds stress in the center of Poiseuille flow is zero, while it is finite for Couette flow [62]. The contributions of this study are to (i) characterize the correlation between helicity and coherent structures by examining the vorticity, the vertical velocity, the distribution of helicity conditioned on the Reynolds stress quadrant events, and the Q criterion; (ii) examine the effects of helicity on turbulent dispersion to assess the role of helicity in transport and its relevance to the coherent structures; (iii) investigate the correlation between normalized fluctuating helicity and the alignment of vorticity with the eigenvectors of the rate of strain tensors; and (iv) examine the effects of molecular dispersion, as expressed through the *Sc*, on all the above.

# CHAPTER 2: METHODOLOGY

## 2.1 Direct Numerical Simulation (DNS)

Direct numerical simulation (DNS) of turbulence is a valuable tool for the study of turbulent flows. The statistical quantities computed from DNS results are commonly utilized for both to further understand flow physics and verify hypotheses regarding turbulence, DNS data are commonly used like experimental data to calibrate and validate engineering turbulence models [13, 189]. In DNS the instantaneous, three-dimensional, Navier–Stokes equations are solved without any averaging or approximation. No modeling is needed, but it requires resolution in both space and time from the largest scales to the smallest scales at the beginning of the dissipation scales. The numerical discretization errors can be estimated and controlled by using higher order numerical schemes [2, 189].

DNS of a fully developed turbulent channel flow for various Reynolds numbers has been carried out to investigate the Reynolds number dependence by Hyroyuki et al. The turbulence statistics such as turbulence intensities, vorticity fluctuations, Reynolds stresses, their budget terms, two-point correlation coefficients, and energy spectra were obtained and discussed [53]. Robert et al. used direct numerical simulation to study fully developed turbulent channel flow at three Reynolds numbers up to $Re_\tau$=590 [190]. The effect of the domain size on the large-scale structures of the flow, as well as on the velocity and pressure statistics were investigated to determine the smallest box that reproduces across the full channel height one-point statistics identical to those in the larger domains size at $Re_\tau$=4200 [191]. A series of DNS calculations for turbulent plane Couette flow were performed with various box lengths by Takahiro et al. They examined the effect of the computational box size on the statistics, such as turbulence intensities [37]. Direct numerical simulation was applied to investigate the spatial features of very large-scale motions (VLSMs) in a turbulent channel flow with $Re_\tau$ ≈930 by Jin Lee at el. [192]. Lee et al. studied the large-scale motions in turbulent plane Couette flows at moderate friction Reynolds number up to $Re_\tau$= 500 [33]. Jukka et al. used direct numerical simulation for plane turbulent Couette flow at a Reynolds number of 750. This study focused on properties of structures and obtaining accurate turbulence statistics [38]. In Avsarkisov's study, turbulent plane Couette flow in a large box of dimension ($20\pi h$; $2\pi$h; $6\pi$h) at Reynolds number. $Re_\tau$=125, 180, 250 and 550 were simulated and compared with simulations at lower Reynolds numbers, Poiseuille flows and experiments [40]. Pirozzoli et al. investigated the behavior of the canonical turbulent Couette flow at computationally high Reynolds number through a series of large-scale direct numerical simulations [14].

From numerical simulation and physical experimental data, the turbulent structure in plane Couette flow at low Reynolds numbers was studied. It was shown that the near-wall turbulence structure is quite similar to what has previously been found in plane Poiseuille flow; however, there were also some large differences especially regarding Reynolds stress production [193]. Lee et al. explored the similarities and differences between Couette flows and Poiseuille flow by studying the production, transport, and dissipation mechanisms. They showed that the role of small-scale motions is universal in both Poiseuille and Couette flows at different Re numbers [194]. Orlandi presented an extensive compilation of DNS data for Poiseuille and Couette flows, from the laminar into the fully turbulent regime, and characterized similarities and differences [29]. DNS was also used to study drag reduction (DR) in plane Couette flow (PCF) induced by the addition of flexible polymers. The similarities and differences in the drag reduction features of PCF and plane Poiseuille flow (PPF) have been examined in detail [12]. George et al. performed the simulation of turbulent Couette flow over a backward facing step at a relatively low Reynold number using DNS to explore in detail the instantaneous vortex topology in the shear-layer and the recirculation bubble as well as in the re-development zone [195]. Myoungkyu et al. performed direct numerical simulation of incompressible channel flow at a friction Reynolds number of 5186 to investigate characteristics of high Reynolds number wall bounded turbulence [196]. Yoshinobu et al. employed large-scale DNS to study the high Prandtl number passive scalar transport of heat transfer in the turbulent channel flow imposed a wall normal magnetic field [197]. Mitali et al applied DNS to study chemical selectivity in a series of parallel reaction in a decaying homogeneous turbulent flow [198]. Yutaka et al. conducted DNS to study a turbulent channel flow having periodic pressure gradient, channel having flat plate walls, a solid one on one side and porous wall on other side [199]. Quoc et al. studied plane Poiseuille-Couette flow using direct numerical simulation to provide insights into the mechanism of turbulent drag reduction in case of specified slip at wall [200]. In summary, DNS have been one of the most effective and widespread means to simulate turbulent flow not only in channel flow but also applied to characterize the physical terms in pipe [56, 201] and boundary layer flow [201, 202].

The DNS algorithm used herein was developed by Lyons et al. [203] to simulate flow in a channel. The code is for Newtonian fluids that have constant physical properties, and it has been modified by Papavassiliou [204] to simulate Couette flow and has been extended by Kontomaris [205] to simulate the transport of particles in the Lagrangian sense. The details of this simulation have been described in reference [203] and in the dissertation by Lyons [206]. The results have been validated with experiments and with other DNS and experimental results for channel flow and plane Couette flow [35, 167, 207], as well as for particle tracking in the DNS [166, 167, 208].

In this algorithm, the rotational form of the dimensionless Navier-Stokes (N-S) equations is solved. The equations are made dimensionless using the viscous wall parameters, i.e., the kinematic viscosity, $v$, and the friction velocity $u^* = (\tau_w/\rho)^{1/2}$, where $\tau_w$ is the shear stress at the wall and $\rho$ is the fluid density. In the rotational form of the Navier-Stokes, the inertia term is replaced with the vector identity:

$$\boldsymbol{u} \cdot \nabla \boldsymbol{u} = -\boldsymbol{u} \times \boldsymbol{\omega} + \frac{1}{2} \nabla (\boldsymbol{u} \cdot \boldsymbol{u}) \tag{2-1}$$

where $\boldsymbol{u}$ is the velocity vector, and the vorticity vector is $\boldsymbol{\omega} = \nabla \times \boldsymbol{u}$.

The flow is periodic in the streamwise and spanwise directions, with no slip and no penetration boundary conditions on the channel walls. The time integration is done using the pseudospectral fractional step method developed by Orszag and Kells [209] with a pressure step field correction suggested by Marcus [210]. The velocity field advances from time step N to step N+1 by three fractional steps: in the first, the non-linear convective term and the mean pressure gradient are calculated. The second fractional step calculates the dynamic pressure head and the third fractional step solves for the viscous terms of the N-S. The convective term and the mean pressure terms are advanced in time by a second order accurate semi-implicit Adams-Bashforth-Crank-Nicholson scheme. The dynamic pressure terms and the viscous term are advanced in time with a first order accurate Euler scheme. The convective (nonlinear) term is evaluated in physical space and, thus, aliasing errors occur, which are reduced by using the two-thirds truncation rule. The velocity field is expanded in terms of truncated Fourier series in the streamwise (direction x) and spanwise (direction z) directions and Chebyshev polynomial series in the wall normal direction (direction y). The periodic boundary conditions in x and z were thus satisfied with the use of Fourier series expansions. The number of Fourier modes depends on the simulation, and it is equal to the number of mesh points in the z direction and the z direction. The number of Chebyshev nodes is equal to the number of mesh points in the wall-normal direction (direction y).

## 2.2 Lagrangian Scalar Tracking (LST)

On the other hand, turbulent flow comes from Eulerian measurements in which a frame of reference is fixed in space. However, in Lagrangian computations and measurements, the system of reference follows the motion of individual fluid elements, this can provide valuable insights about turbulent flow and about the mechanism of turbulent transport [211]. Moreover, calculating statistical properties of the scalar field from statistical properties of the velocity field is a challenging problem in developing a theory for turbulent transport of mass or heat from a wall. Another advantage of LST is that a single computation can be used to reconstruct the behavior in different problem configurations; isothermal and isoflux walls, step change in wall temperature or heat flux, continuous and instantaneous line source [212].

A Lagrangian approach provides a natural way to investigate turbulent dispersion, in general, turbulent heat/mass transport [213]. Therefore, the combination of Direct Numerical Simulation and Lagrangian scalar tracking (LST) could be beneficial in studying turbulent transport. Papavassiliou et al. utilized computations with the LST method and DNS and indicated that turbulence and molecular diffusion can lead to particle separation in anisotropic turbulence. Lagrangian techniques were used because they are very well-suited for simulating scalar transport in both low, but mainly high, $Sc$ regimes from 6 to 2400 [214]. In anisotropic turbulence, the interplay between convection and diffusion is critical. Qualitative and quantitative measures of mixing efficiency and intensity were defined, and the dynamics of mixing were investigated [215]. In prior work by Le in our laboratory, the behavior of elevated sources in turbulent channel flow and in turbulent-plane Couette flow was studied. The trajectories of heat markers were monitored in space and time as they moved in a hydrodynamic field created by a DNS. The behavior of instantaneous and continuous line sources of heat or mass at different locations of turbulent plane

Poiseuille and plane Couette flow was also investigated using LST [167]. The simulation and modeling of the dispersion from an instantaneous source of heat or mass located at the center of a turbulent flow channel were also carried out and the dispersion was modeled based on LST [216]. These methods were also utilized in infinitely long channels to study the principal direction of transport of heat (or mass) for both forwards and backwards single particle dispersion. The viscous sub-layer, the transition region (between the viscous sub-layer and the logarithmic region), and the logarithmic region of a Poiseuille flow and a plane Couette flow channel were studied [213].

Polanco et al. combined DNS with Lagrangian tracking of particle pairs to extend the observations on relative dispersion of fluid particles pair to wall-bounded turbulent flows. This work also dealt with forward and backward dispersion statistics of fluid particle pairs in a turbulent channel flow [48]. Fahimeh et al. employed DNS and LST to study dispersion and deposition mechanism of particles in Poiseuille and Couette flows the diffusional deposition mechanism for the particles in Couette flow is less efficient in than that is Poiseuille flow but the number of deposited particles in Couette flow is greater than that for Poiseuille flow [217]. Our research group also applied the integration of DNS and LST in studying chemical reaction in turbulent flow [218, 219], heat transfer [10, 55], dispersion and mixing [212, 215, 216] prediction of turbulent Prandtl number in wall flow [220] and direction of scalar transport [213] etc.

The trajectories of each marker were modeled using a Lagrangian approach, i.e., Lagrangian scalar tracking (LST) [150, 167, 200, 221]. The particles were assumed to be passive, so one-way coupling between the flow and the motion of the particles was employed. That means that drag effects were not considered, and that the presence of the particles did not affect the fluid flow. The main driving force for marker movement is the convection effect (i.e., the velocity of the fluid) and the Brownian motion that depends on the hydraulic diameter of these particles, and it is important for particles at the nano-scale. These markers were released into the simulated flow field from specified locations at one instant of the simulation (instantaneous source). The convective part of the marker motion was calculated using the fluid velocity $\boldsymbol{V}$ at the particle position and integrating in time. The Brownian motion was simulated by imposing a random jump at the end of each convection step [205, 212, 222]. This random jump took values from a normal probability density function that had a zero mean and a standard deviation that depends on the fluid properties and the molecular diffusivity of the particles. The equation of motion for each marker in each space direction *x* is given by [223]

$$x_{t+1}^{p} = x_t^p + \int_t^{t+1} V_t^p \, dt + Z\sigma \qquad (2\text{-}2)$$

where $x_{t+1}^{p}$ is the displacement of the marker relative to its source at time $t + 1$, $V_t^p$ is the velocity of the fluid in the *x* direction at position $x_t^p$, $\Delta t$ is the time step, *Z* is a random number following a standard normal distribution.

Since the markers were passive, the presence of one did not affect the trajectory of any other marker that is realistic for scalar marker and dilute solutions (small concentration). The *x* location for each marker was calculated by subtracting the initial position $x_0$ of the marker, therefore (x- $x_0$) was considered as the marker location in the streamwise direction. In vector form, the location of each marker in the Lagrangian sense, $\boldsymbol{X}(\boldsymbol{x_0}, t)$, represented the location of the marker that was released at position $\boldsymbol{x_0}$ at time $t = t_0 = 0$, and the corresponding Lagrangian velocity of the marker at that location was $\boldsymbol{V}(\boldsymbol{x_0}, t)$. Assuming that the velocity of each marker is the Eulerian velocity, $\vec{U}$, of the fluid at its location, the Lagrangian velocity was given as $\boldsymbol{V}(\boldsymbol{x_0}, t) = \boldsymbol{U}[\boldsymbol{X}(\boldsymbol{x_0}, t), t]$. The markers moved because of convection in the flow field, using the relation $\boldsymbol{V}(\boldsymbol{x_0}, t) = \frac{\partial \boldsymbol{X}(\boldsymbol{x_0}, t)}{\partial t}$, and because of molecular diffusion. The equation of particle motion was integrated using an Adams-Bashforth scheme (explicit, second-order accurate) in each space direction. By using a mixed sixth-order Lagrangian-Chebyshev interpolation scheme to calculate the velocity vector between grid points, it was possible to track mass markers [221, 222, 224]. The random molecular diffusion movement of each marker was calculated at the end of the convective motion. The particle displacement was selected randomly from a normal statistical distribution following Einstein's theory for Brownian motion. The random displacement had a mean value of zero. The standard deviation, $\sigma$, depended on the diffusivity of the particle and it was found as $\sigma = \sqrt{2\Delta t/Sc}$, in each space direction, where $\Delta t$ is the time step of the simulation and *Sc* is the Schmidt number, $Sc = \nu /D$. The illustration for the simulation is shown in Figure 2.1 and Figure 2.2.

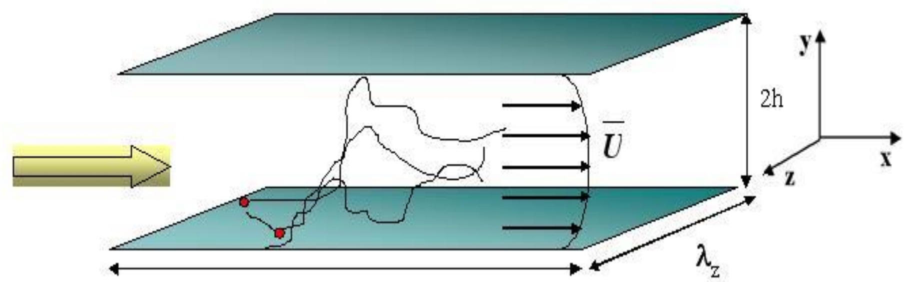


Figure 2.1 Plane channel flow configuration [225].

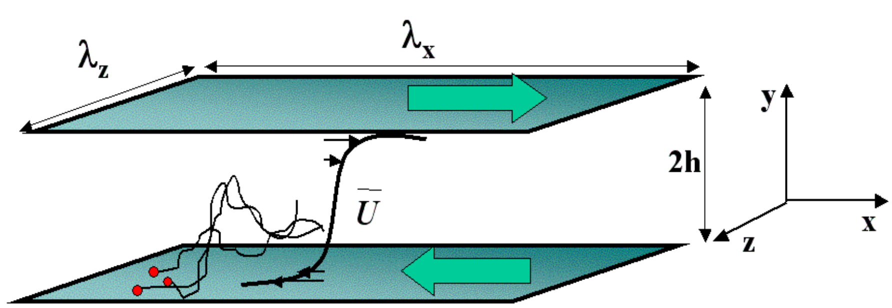


Figure 2.2 Plane Couette flow configuration[225].

# CHAPTER 3: COMPUTATIONS OF THE SHEAR STRESSES DISTRIBUTION EXPERIENCED BY PASSIVE PARTICLES AS THEY CIRCULATE IN TURBULENT FLOW: A CASE STUDY FOR VWF PROTEIN MOLECULES.

## 3.1 Methodology and parameter

In the present work, direct numerical simulation (DNS) was used to obtain the details of the flow field in biologically relevant turbulent and transitional flows. A Lagrangian method for tracking the trajectories of vWF surrogate particles in space and time was applied. It should be very clear that the molecular structure of the vWF was not obtained with this numerical approach, but the contribution of our work was to show with detailed calculations the level of hydrodynamic stresses and their distribution on particles that move the same way as vWF molecules would move in a turbulent flow field. It is not feasible to conduct molecular dynamics in Reynolds number flows comparable to the ones applied herein, which are representative of the Reynolds number in cardiovascular devices, as it is not feasible to conduct molecular computations for the time duration presented herein. We also offer result for plane Poiseuille flow and for Poiseuille-Couette flow. As Bortot et al. have pointed out, most prior studies (both experiments and computations) have been conducted under laminar flow conditions, even though turbulence is needed to cause severe damage to vWF [93]. In the present work progress toward covering this knowledge gap is reported – the shear stress along the particle trajectories was calculated providing not only average stresses, but the distribution of stresses. Further, the determination of stresses when particles were injected at different locations in the flow field was possible. While the computations were conducted using dimensionless equations, the results were related to cases of actual biomedical devices. Furthermore, the effects of the history of particle motion were explored. In prior work, the focus herein was exclusively on shear stresses and on probing the idea that in turbulent flow fields predictions of average stresses or wall shear stresses are not enough to predict the levels of protein damage due to shear stress.

The simulations were conducted in dimensionless units, using the kinematic viscosity of the fluid, $\nu$, and the friction velocity of the fluid, $u^*$, to normalize the Navier-Stokes equations. The numerical scheme has been described in detail elsewhere – it is based on a pseudospectral method that employs Fourier transforms for the velocity in the periodic streamwise and spanwise directions, and Chebyshev polynomial expansions in the wall normal direction. The rotational form of the Navier-Stokes equation is solved, with the Marcus correction for the calculation of the pressure [206, 226].

The fluid viscosity and the friction velocity at the wall allow for the definition of velocity, length and the scales; units are the viscous wall units that are typically used in the studies of wall turbulence. The friction velocity is defined based on the fluid density and the wall shear stress as follows; $\rho$ is the fluid density, $\tau_w$ is the wall shear stress, and $u^*$ is the friction velocity; as follows:

$$u^* = \sqrt{\frac{|\tau_w|}{\rho}}$$

The length scale is then $l^* = \nu/u^*$ where $\nu$ is the kinematic viscosity of the fluid and the time scale is $t^* = l^*/u^*$.

The dimensions of the computational box in the *x* (streamwise), *y* (wall-normal) and *z* (spanwise) directions were $30\pi h$ x $2h$ x $4\pi h$ for the Poiseuille-Couette (PC) flow and $16\pi h$ x $2h$ x$2\pi h$ for the fully turbulent Poiseuille (PF), where *h* was the half-channel height. The flows were periodic in *x* and *z*, with no-slip boundary conditions at the channel walls. The bottom wall of the PC flow channel was moving in the negative x direction with velocity 7.78 in wall units and the top wall was moving with the same velocity but in the positive x direction. The number of mesh points was

512x128x128 for the PC flow and 1024x256x128 for the PF. Since the goal here is not to explore the rheological behavior of blood, but the values of the stresses in a flow field, the assumption of a Newtonian fluid at high shear rates was reasonably made [115, 227, 228]. The time step for the simulations was $\Delta t = 0.075$ for the PC flow and $\Delta t = 0.1$ for PF.

The friction Reynolds number, $Re_\tau$, was 80 for the PC flow and $Re_\tau = 300$ for the fully turbulent PF. Ventricular Assist Devices (VAD) operate in rather low Reynolds numbers [229, 230] with PC flow in the annular space between the rotor and the shell of the VAD device. Typical annular spacing in axial flow VADs is in the range from 1mm to 5mm [231-234]. Choosing a PC with channel width equal to 1.5 mm for $Re_\tau = 80$ and assuming blood viscosity $\mu = 0.0035$ Pa s, the shear stress at the wall, $\tau_w$, was calculated to be 35.16 Pa, with friction velocity $u^* = 0.183$ m/s. The Reynolds number for turbulent PF can be related to the Reynolds number for flow in the typical centrifugal blood pump that was offered as part of the Food and Drug Administration critical path initiative for simulations [114, 115, 128, 235]. The case of flow of blood at 7 L/min at Re = 3661 in a 1.5mm diameter pipe corresponds to a mean velocity of 2.015 m/s, which when compared to the mean velocity of 16.68 in viscous wall units, of the $Re_\tau = 300$ simulation gives $u^* = 0.1208$ m/s and $\tau_w = 14.95$ Pa.

Lagrangian scalar tracking (LST) of mass markers that represented vWF molecules dispersing in the flow field was conducted after the flow reached stationary state using the particle tracking algorithm of Kontomaris et al. [221]. These markers were assumed to be passive, which we define as particles whose trajectories are affected by the flow field and by their Brownian motion, but their presence in the flow does not affect the velocity of the surrounding fluid. While the particles may change internal conformation under stress (such as vWF molecules would), they were assumed to continue to not affect the flow field around them.

Assuming that the flow is stationary (i.e., that the average quantities for the flow velocity do not change with time) the time of release is not important. To ensure that there are no bias effects of the locations of the release, we release along lines that span the length of the computational box. Mass markers were injected instantaneously at different locations in the flow, at $Yo$ = 0, 3, 5, 15, 80 wall units away from the bottom channel wall for the PC flow and at $Yo$ = 0, 1.5, 3, 5, 10, 15, 75, 300 for the PF simulation. Possible bias because of the initial velocity field was mitigated by releasing markers from 20 lines spanning the *x-z* plane at every $Yo$ value. These lines were placed along the $z$ direction and were uniformly spaced along the $x$ direction, with the first line starting at $x = 0$. We injected 100,000 markers at every $Yo$ from locations that were equally spaced in the spanwise direction, $z$.

The random movement was determined by random selection of the particle jump utilizing a Gaussian statistical distribution. According to the Brownian motion theory developed by Einstein, the random jump should follow a Gaussian probability density function that has an average value of zero and a variance that depends on the diffusivity coefficient of the particle. Utilizing the Schmidt number, $Sc = \nu/D$, where $D$ is the molecular diffusivity of the vWF in blood, the standard deviation, σ, for the Brownian motion in each space direction was found as ($\sigma = \sqrt{2\Delta t/Sc}$), where $\Delta t$ is the time step of the simulation.

Assuming that the hydrodynamic radius of a vWF multimer was 1.8 $\times 10^{-8}$ m (based on a molecule with molecular weight of 20,000KDa [236]), and that the dynamic viscosity of blood was 0.0035 Pa s (at 37 Celsius – the temperature of a healthy human), the Stokes-Einstein relationship produced a diffusivity coefficient $D = 3.6119\times10^{-12}$ $m^2/s$, and a Schmidt number of 914,179 (the blood kinematic viscosity was taken as $\nu = 3.30189\times10^{-6}$ $m^2/s$). In order to be able to use the Stokes-Einstein equation, the vWF particles were assumed to be spherical. Possible changes of the vWF shape in the flow field were not accounted for the diffusivity calculations. The use of a particle diameter in the Stokes-Einstein equation was justified by the assumption that the most important contributions to the motion of the vWF were convection and Brownian motion, while drag effects were not important.

Prior researchers have also assumed that the vWF can be treated as a sphere [92, 97]. Others have implied in their analysis that the vWF is spherical, for example Pushin et al. [133] assumed that the forces acting on the vWF could be calculated as stress multiplied by the area of a circle (i.e., the circle is the projected area of a sphere on the stress plane). Further, it is known that when mechanical stresses are low, interdomain attraction between the vWF molecular regions lead to a collapsed conformation [99]. Therefore, instead of updating the protein diffusivity of the trajectories of modified proteins as they might unfold in flow, it was assumed that small changes in the protein size (within an order of magnitude), would have negligible effects on the probability density functions for stresses. The justification for this was based on prior results regarding the dispersion of high *Sc* particles in turbulent flow. It has seen that particles with $Sc > 2{,}400$ behave quite the same in terms of statistical quantities, such as the mean particle velocity, the Lagrangian autocorrelation coefficient, and the rate of dispersion [167, 237].

Since the velocity of the vWF markers was assumed to be equal to the velocity of the fluid at the marker location, it was assumed that the shear stress acting on each marker was equal to the shear stress based on the Eulerian velocity, $\tau_y = \mu \partial U_x / \partial y$, at the marker's position in the Eulerian framework (the extensional stress are described in Chapter 4). This was the highest component of the stress tensor acting on the particles. Statistical analysis to find the average stress as a function of time and to calculate the probability density function followed, once the statistical sample space from the stress on each of the 100,000 individual particles was calculated at each time step and for each location of particle release.

The history of shear stresses was calculated using a Lagrangian integration of the shear stress components. The time integral of the shear stress along the trajectory of each particle was calculated, and then the distribution of the Lagrangian integral was determined as a function of time. The effects of the history of the stresses on the hemolysis of red blood cells have been calculated with the same approach [115, 125, 238]. Investigating the history of the stress on each molecule is important, since there is evidence that the vWF can stretch or unfold under stress, even when it is exposed to stress for small time intervals [133]. Small stresses applied for long time periods can result in cleaved or deformed vWF, as can high stresses experienced for shorter time periods.

## 3.2 Results and Discussion[1]

### 3.2.1 Transitional Poiseuille-Couette flow

Figure 3.1 is a display of the average location of the vWF surrogate particles as they moved in the flow field. This is the trajectory of the center of mass of the cloud of the particles as a function of time in the $X$, $Y$ space, where $X$ is the average ($x$-$x_o$) position of all particles released at the same distance $Yo$ from the channel wall, and $Y$ is the average $y$ position of these particles. The averages were calculated at each time step of the simulation, from time 0 to 300 in wall units. The bottom wall of the channel was moving in the negative $x$ direction and the top wall in the positive $x$ direction, so the average particle position was in the negative $X$ region at early times. The Poiseuille part of the motion started to be effective in moving the particle cloud as the particles

[1] The results presented in this chapter have been published in reference [74].

dispersed in the flow field at later times. For particles released at the center of the channel, the Poiseuille effect dominated, and the X values were positive. One would need to keep the data in this figure in mind when discussing the stresses, because the stress distribution was affected by the location of the particle cloud. Figure 3.2 is an illustration of the trajectories of individual particles released at different locations in the computational box.

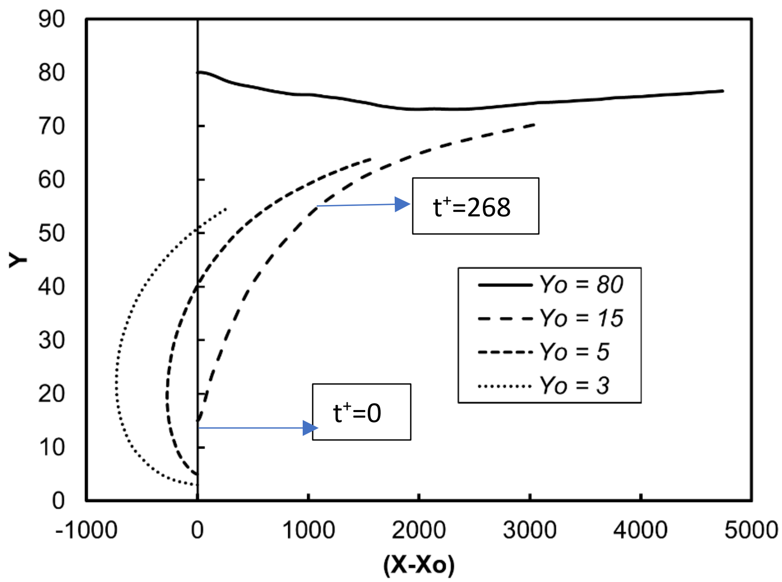


Figure 3.1 Average position of the vWF markers in the Poiseuille-Couette velocity field at each time step. Results for particles released within the viscous wall layer (Yo = 3 and 5), within the buffer region (Yo = 15) and at the center of the channel (Yo =80) are presented. Each point in the figure is the average of position of all particles per a release position at each time step.

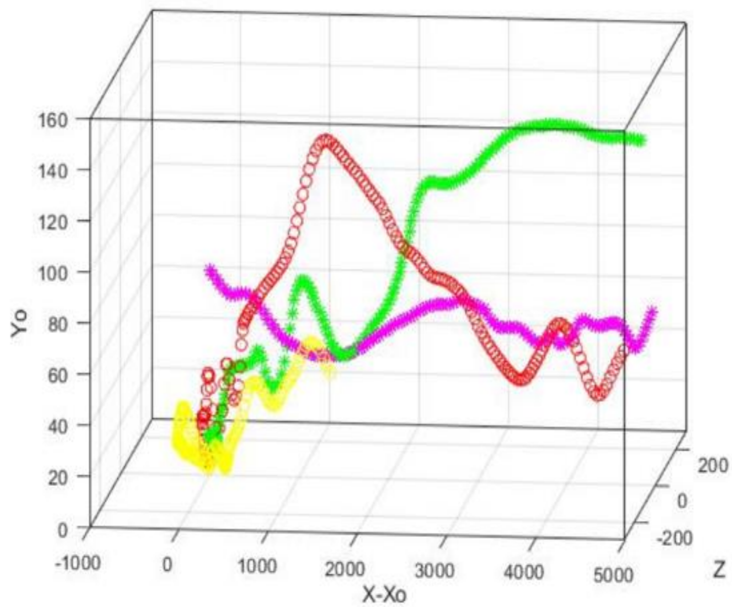


Figure 3.2 Sample trajectories of individual vWF markers in the Poiseuille-Couette velocity field. Examples of particles released at Yo = 3 (yellow circle), Yo 5(red circle), Yo = 15 (green start), Yo = 80 (pink star) are shown.

The average shear stress on the vWF particle locations as a function of time is presented in Figure 3.3 and 3.4. The stress was the highest close to the wall, as expected. The shear was dominated by the mean velocity gradient, which in viscous wall units has the value of one by definition. Since the vWF particles mostly stayed in this region, the average stress did not change dramatically over 600 time units. However, when the vWF injection was farther away from the wall, the average stress showed variation. As the average position of the particles moved away from the wall (see Figure 3.1), the average stress took lower values. For release at the buffer region, *Yo*=15, the average stress was roughly 40% of the maximum value, and for release in the center of the channel the stress was much lower – about 10% of the maximum value. However, when one considers the dimensional value of the stress, it was higher than 5 Pa – the critical stress that can cause damage to the vWF molecular configuration [86]. Figure 3.3 is a plot of the average of the absolute value of the stress. In this way, whether the vWF underwent stress in the positive or negative $x$-direction is not important. Average of stress by accounting for positive and negative stresses is shown in Figure 3.4.

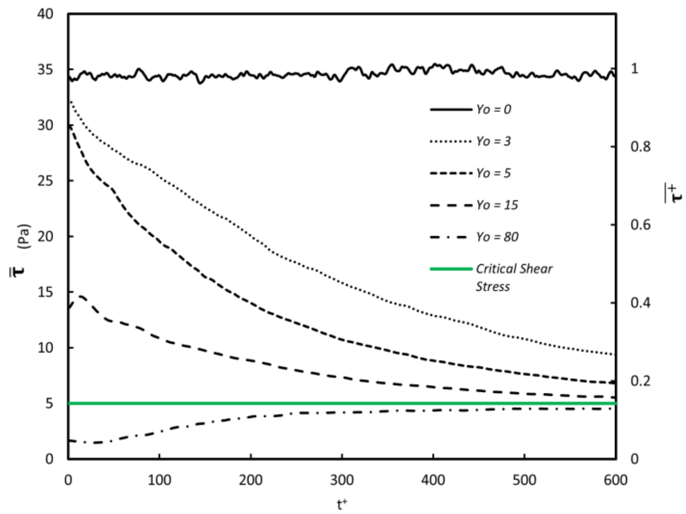


Figure 3.3 Magnitude of shear stress as a function of time for vWF particles injected at different initial locations. The abscissa in dimensionless viscous parameters and in dimensional units is shown. The critical shear stress is 5 Pa as in Ref [86]

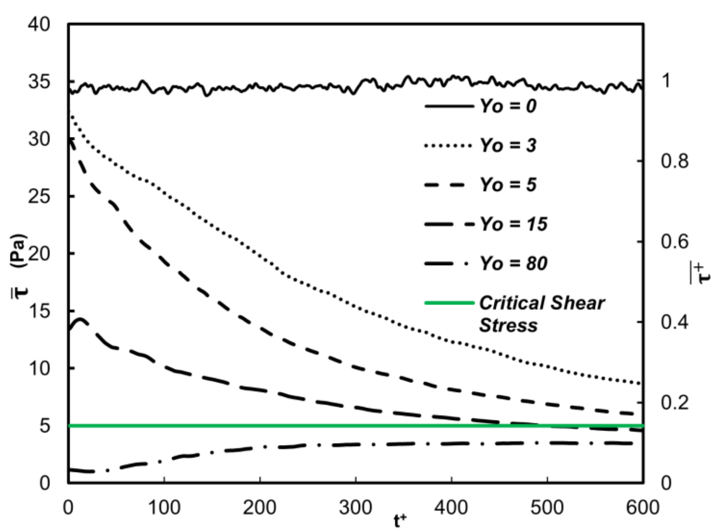


Figure 3.4 Average of actual shear stresses. The abscissa in dimensionless viscous parameters in dimensional units is shown. One can adjust the dimensional stress axis at the same Re by considering a new channel width with a new corresponding mean velocity to recalculate $\tau_w$ and $u^*$, and using the dimensionless values presented.

One of the questions that this study aims to answer is whether the average shear stress provides a complete picture of the stresses that the vWF molecules undergo in this flow field. The full distribution of stresses is presented in Figure 3.5 at specific time instances after particle injection. While the stress distribution for release at the channel bottom wall did not change much with time, as seen in Figure 3.5A, when the release point for the vWF was at a distance from the wall, the distribution changed. As the particles moved on average away from the wall after their release (see Figure 3.1), the probability density function (PDF) for the stress distribution increased its variance (it became wider). The particles did not all undergo the same stresses, but they spent some time in areas of high stress (higher than the average) and sometime in areas of low stress. The stress on particles released at the center of the channel followed a distribution that was narrower for all times. This is expected when one considers the average particle position as seen in Figure 3.1. The mean velocity gradient was not as large as in other regions of the channel, resulting in a more symmetric distribution (Figure 3.5D).

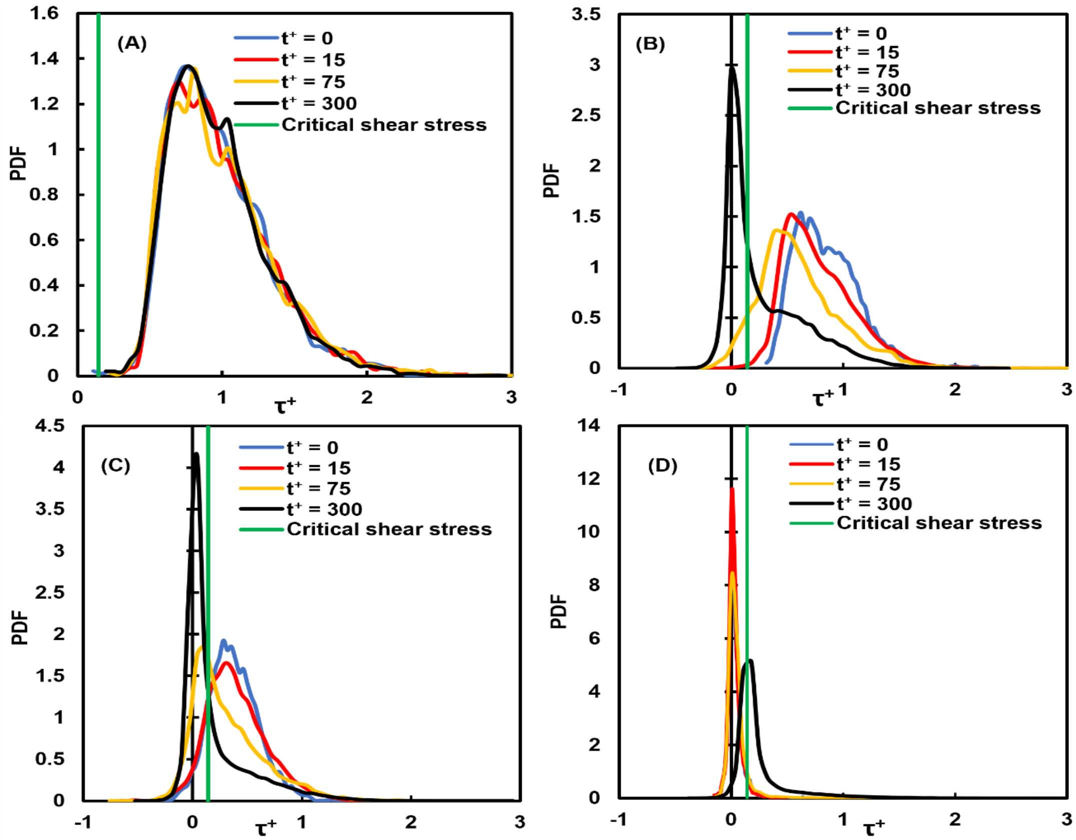


Figure 3.5 Distributions of shear stress on vWF particles at different times in viscous wall units. (A) Cloud released at the channel bottom wall, (B) release at the edge of the viscous wall subregion (Yo = 5), (C) release within the buffer region (Yo = 15) and (D) release at the channel center.

The injection location was important in determining what stress a vWF particle would undergo as it moved in the flow field. It was also apparent that a particle would experience different stresses depending on its trajectory. Thus, the history of stress was not the same for every particle in the flow. In other cases of blood flow, the history of stresses on particles, specifically red blood cells (RBCs) are important and can lead to cell trauma. The well-known phenomenon of RBC hemolysis has been modeled with power law models that incorporate the level of stress and the time of exposure of RBCs to such stresses. Furthermore, data by Zhussupbekov et al. [98] indicate that the unfolding of vWF could possibly follows the power law model. In their study, a constant percentage of vWF unfolding occurred either when the stress was high and the time of exposure was low, or when the inverse occurred.  Other indirect evidence by Heidari et al. [132] showed that the change in protein conformation with time and shear rate follows a power law model. In Figure 3 of their work, they plotted the radius of gyration of the vWF versus a characteristic time scale multiplied by the shear rate.

Our hypothesis was that the vWF undergoes a similar process – the longer it was exposed to high stresses, the higher the probability of reconfiguration and damage. It is important, therefore, to investigate the history of stress and observe the distribution of stress histories. A power law model is a reasonable approximation for modeling the effects of time of exposure to stress, even though the details of the mechanism of vWF cleavage and elongation are not explicitly modeled. The power law exponents are not known, so the calculations herein were carried out with the assumption that the exponents are equal to one. The distribution of the history of the stress on particles at two different times after their injection is presented in Figure 3.6. The integrated stress became larger over time, and the distribution was displaced to larger values as time advanced. Further, the variance of the distribution increased, indicating that there were particles that underwent much higher stresses than others. For example, there were particles that underwent much higher stresses while traveling in the same flow field, even when released from the same location. In Figure 3.6B, as an example, some particles experienced an integrated stress of 100 $\tau^+$, and others saw 500 $\tau^+$ or more (recall that multiplying by 35.16 Pa yields the integrated stress in SI units). In all instances, the vWF particles experienced high stresses, above the critical value of 5 Pa [86].

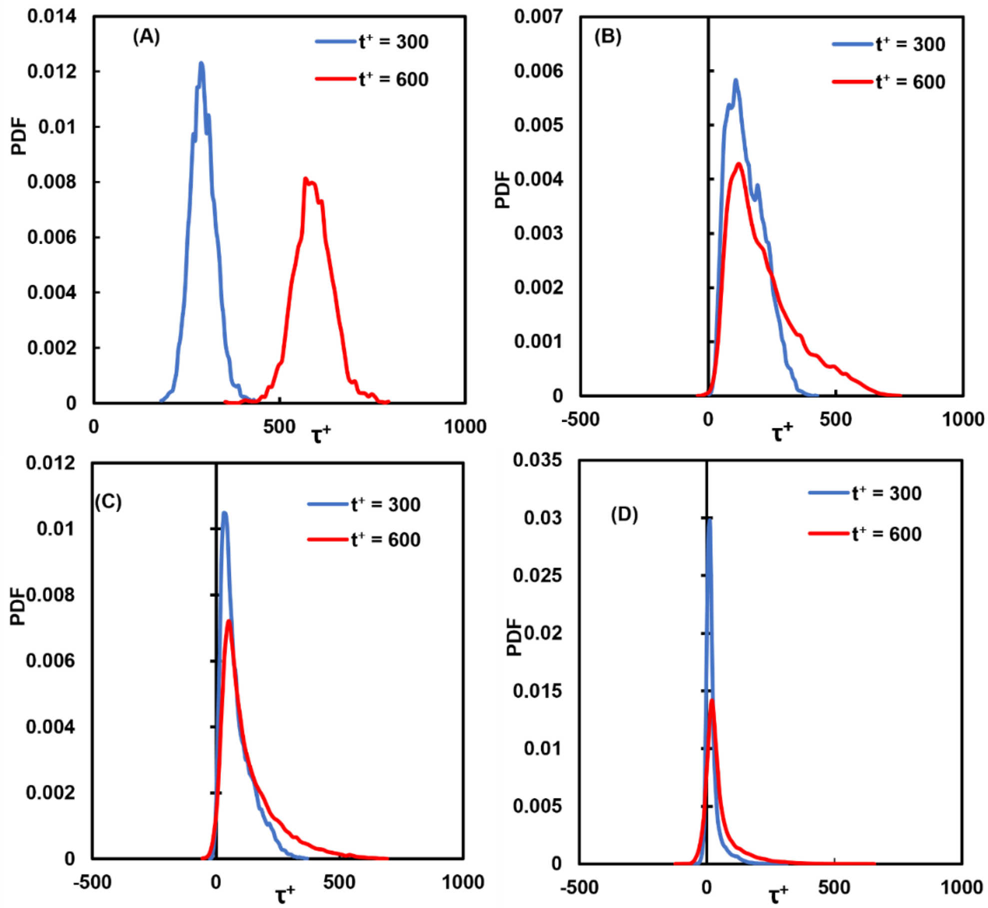


Figure 3.6 Distributions of the shear stress history for vWF particles at different times in viscous wall units. (A) Cloud released at the channel bottom wall, (B) release at the edge of the viscous wall subregion (Yo = 5), (C) release within the buffer region (Yo = 15) and (D) release at the channel center.

### 3.2.2 Fully turbulent Poiseuille flow

In medical devices that help with blood circulation outside the body, like dialysis machines, the flow can be in the turbulent regime. Figure 3.7 is a display of the average location of the vWF surrogate particles as they moved in a fully turbulent flow field and Figure 3.8 is an illustration of trajectories of individual particles released at different locations. The average position of the vWF cloud after injection at different locations in the channel provided information for the particle trajectories on average. Since there was no Couette component of the flow, the particles moved in the positive *x* direction. Particles released at the center of channel (*Yo* =300) did not have a reason to move above or below the center (on average), but particles released closer to the wall tended to move on average away from it, because of the boundary that the wall presented to them. Closer to the wall, the mean velocity of the fluid in the *x* direction was smaller, and the extent to which they moved in the *x* direction was mostly affected by the magnitude of the mean flow in the streamwise *x* direction.

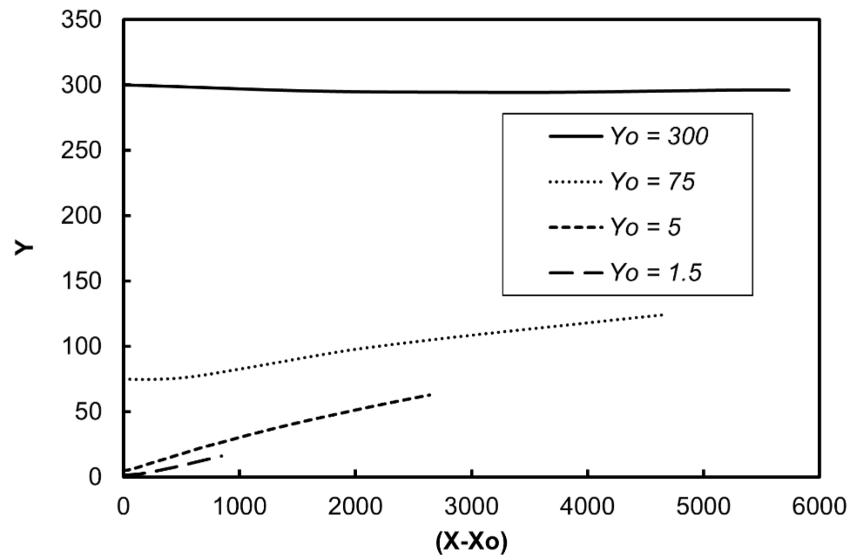


Figure 3.7 Average vWF position in fully-developed Poiseuille turbulent flow. Results for particles released within the viscous wall layer (Yo = 1.5 and 5), within the logarithmic layer (Yo = 75) and at the center of the channel (Yo = 300) are presented. Each point in the figure is the average position of all particles per release position at each time step.

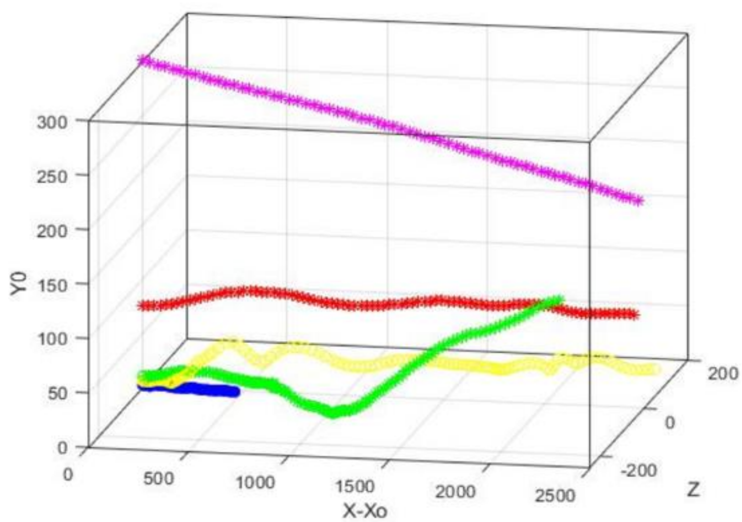


Figure 3.8 Trajectories of particles released in a Poiseuille flow field. Examples of particles released at Yo = 1.5 (blue circles), Yo = 5 (yellow circles), Yo = 10 (green stars), Yo = 75 (red stars), Yo = 300 (pink star dot).

The average of the absolute value of the shear stress on the vWF particle locations as a function of time is presented in Figure 3.9. The average of the actual shear stress is shown in Figure 3.10, while the actual stress distribution at different times is presented in Figure 3.11. The qualitative behavior of the average stresses as a function of the location of particle injection was similar to the case of Poiseuille-Couette flow. The thick green line indicating the critical shear stress for vWF damage crosses through the stress profiles. Depending on the location of release, and on the time elapsed since the release, the particles move from regions with stresses below the critical value to regions above the critical point and vice versa. This was even more pronounced when examining the full distributions of the stresses. There was a probability that a vWF particle would experience below or above critical stresses, depending on the time since release and depending on the location of release.

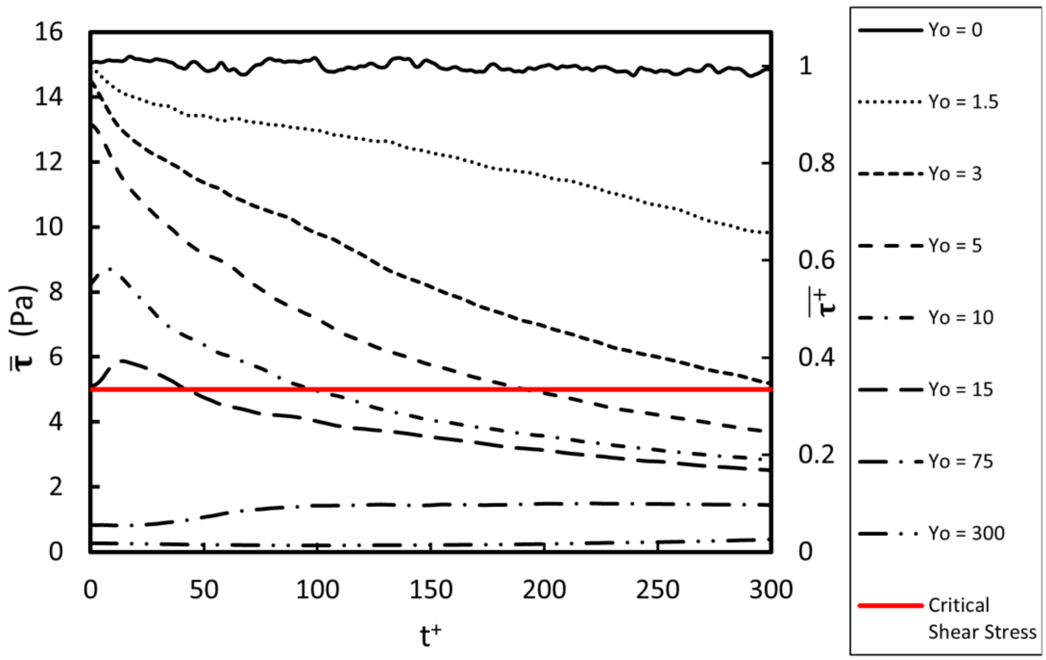


Figure 3.9 Magnitude of the shear stress as a function of time for vWF particles released at different initial locations in fully turbulent flow. The abscissa in dimensionless viscous parameters and in dimensional units is shown.

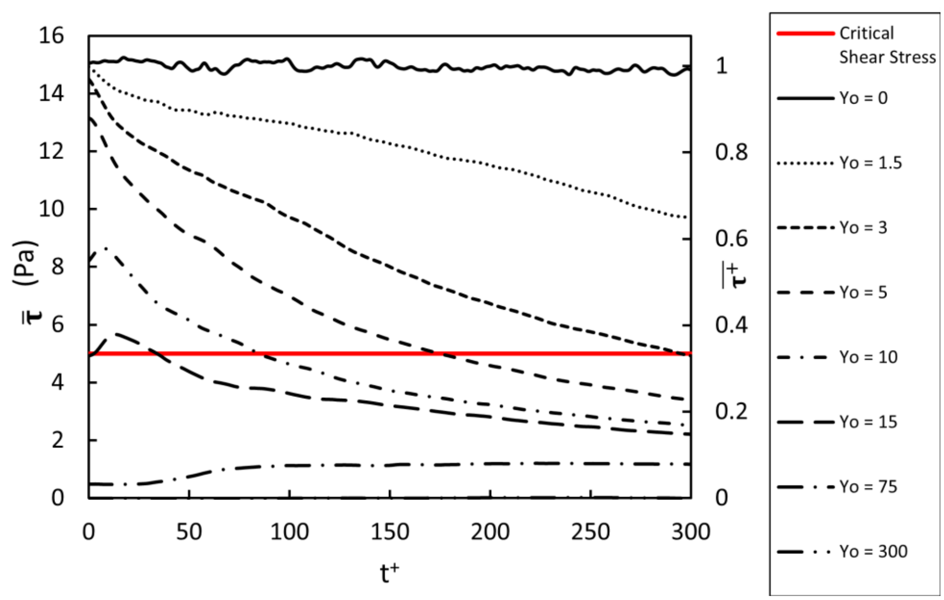


Figure 3.10 Average of actual shear stresses. The abscissa in dimensionless viscous parameters and in dimensional units is shown. The dimensional stress axis can be adjusted for a different channel when the actual mean velocity and channel size is known by using the dimensionless values presented.

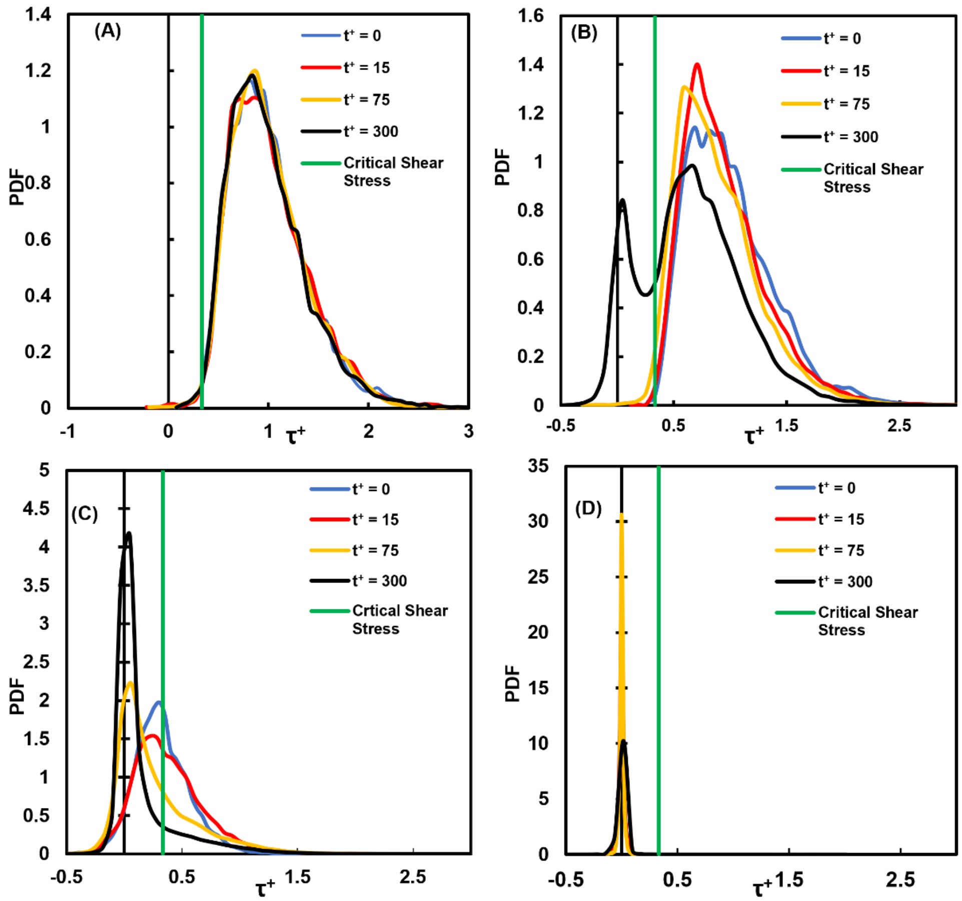


Figure 3.10 Distributions of shear stress on vWF particles at different times in viscous wall units. (A) Cloud released at the channel bottom wall, (B) release within the viscous sublayer (Yo = 1.5), (C) release within the buffer region (Yo = 15) and (D) release at the channel center.

The history of stresses on a particle was also important in this case. As seen in Figure 3.8, as time advanced, the distribution of the history of the stresses increased in its variation. The vWF particles did not all have the same exposure to damaging stress, but instead experienced a range of stresses that became wider as time advanced.

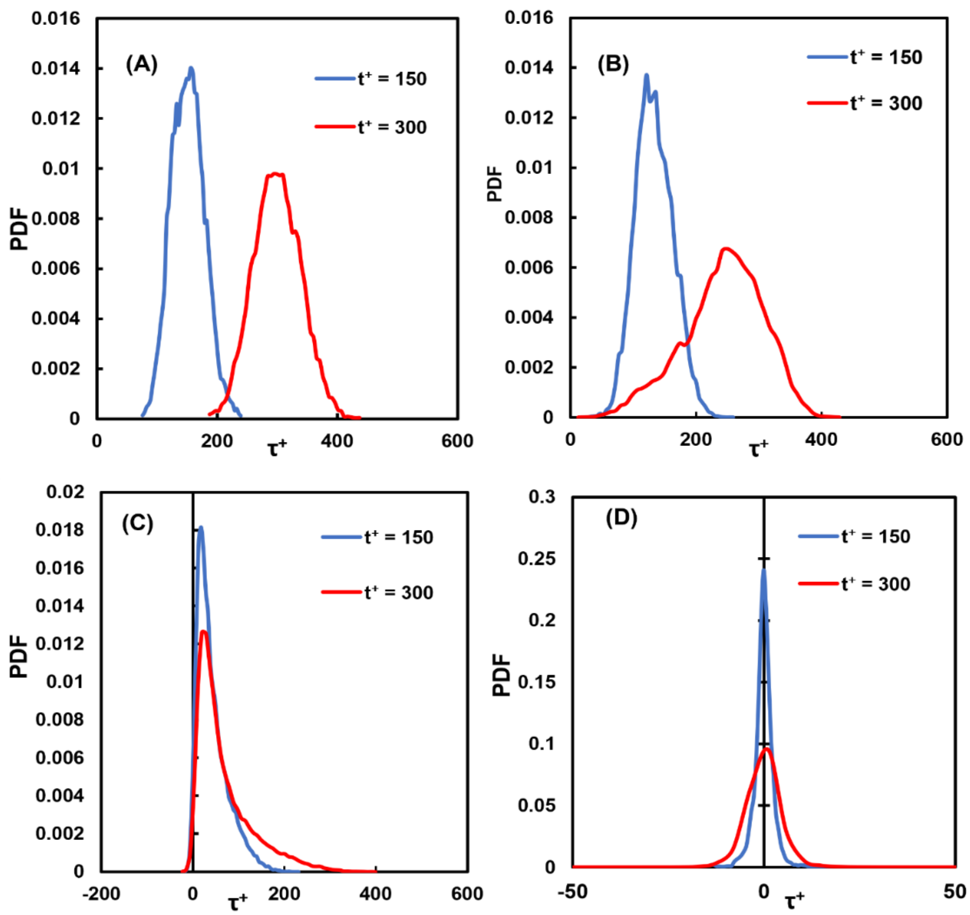


Figure 3.11 Distributions of the shear stress history for vWF particles at different times in viscous wall units. (A) Cloud released at the channel bottom wall, (B) release within the viscous wall subregion (Yo = 1.5), (C) release within the buffer region (Yo = 15) and (D) release at the channel center.

## 3.3 Conclusions

The distribution of shear stresses induced on vWF surrogate particles injected *in silico* to computationally obtained velocity fields that are found in blood flow through biomedical devices and implants was calculated in detail. A Lagrangian approach, where individual vWF particles were followed in time and space while monitoring the hydrodynamic stresses, was applied. With this approach, details on the stresses and their distribution as a function of the location of particle release and the type of flow (transitional and fully turbulent) were obtained. It should be noted here that the model for the vWF is a simplification of an actual medical device, in the sense that the interactions between the vWF molecules and the surrounding molecules ~~beyond hydrodynamics~~ are not considered, for example interactions between vWF proteins that come in proximity to each other and might get entangled. However, an interaction like that, in the framework utilized herein would mean that the Schmidt number of the entangled particle would now be different, but the trajectory that the new particle would follow, and the stresses seen by this new particle would not be different than what is reported here. One can improve upon the present model by incorporating a bead-and-spring model for the vWF molecule and modeling the configuration and orientation of the molecule under stress. Such an approach could be the subject of future study.

Both Poiseuille-Couette flow and Poiseuille flow were found to result in potentially damaging stresses. In the near wall regions, the value on shear stress of vWF distributed in wider range from -1 to 2.5 in comparison to buffer region and channel center. As for the PC flow, the history of stress some particles experienced an integrated stress of 100 $\tau^+$, and others saw 500 $\tau^+$ or more (recall that multiplying by 35.16 Pa yields the integrated stress in SI units) meanwhile the PF shows the range of history stress from 0 to 400 $\tau^+$ in near wall regions. In all instances, the vWF particles experienced high stresses, above the critical value of 5 Pa The distribution of stresses on the particles showed that particles have had a stochastic exposure to stresses and these stresses could cause damage at different times during the movement of the particles. Higher stresses were observed for particles injected close to the channel wall, and exposure to lower stresses was observed for particles released at the center of the flow field. A model for vWF damage, similar to the power law models for hemolysis [47, 49], could be developed by determining both the appropriate exponent for the dependence on the time of exposure and the exponent for dependence on the observed stress. However, using a deterministic model to predict the stresses either based on wall shear stress or based on average stresses would not be an accurate approach. Instead, a stochastic model for the level of stresses and the probability of the vWF to be in regions of low or high shear stresses would be needed, with data similar to those presented herein. Further research to predict the shear stress distribution as a function of the flow conditions on the vWF particles is necessary.

As already mentioned, the mechanism of unraveling within the protein surrogate particle in our computations was not simulated – the details of the trajectories of such surrogate particles are calculated and the shear stresses along the individual trajectories of such surrogate particles are calculated and analyzed statistically. While changes at the molecular level may occur on the vWF molecules depending on the magnitude of the hydrodynamic stresses, these changes are assumed to not affect the fluid flow around them (i.e., they are assumed to be passive throughout the calculations). The reader can use our dimensionless data to obtain dimensional distributions of stresses and use other values of critical stress, based on any molecular model, to determine the percentage of vWF that may be compromised. Since the stress distribution results presented herein would apply to other cases of proteins with similar diffusivity as the vWF, or for small colloidal particles or micelles with high enough Schmidt numbers, one could also apply the present results to more general situations. The difference would be to determine from published work in the literature the level of the critical shear stress needed to modify the structure of such small particles or macromolecules.

# CHAPTER 4: DISTRIBUTION AND HISTORY OF EXTENSIONAL STRESSES ON VWF SURROGATE MOLECULES IN TURBULENT FLOW

## 4.1 Methodology and parameter

The simulation procedure and parameters are the same as described in Chapter 3 and have been listed again in Table 4.1.

Table 4.1 The simulation parameters for Poiseuille and Poiseuille-Couette flows.

| | Poiseuille flow (PF) | Poiseuille-Couette flow (PC) |
|---|---|---|
| Dimension | $16\pi h$ x $2\pi h$ x $h$ | $30\pi h$ x $2h$ x $4\pi h$ |
| Computational box | 1024x256x128 | 512x128x128 |
| Time step $\Delta t$ | 0.1 | 0.075 |
| Friction Reynolds number $Re_{\tau,}$ | 300 | 80 |
| Wall shear stress $\tau_w$ | 14.95 | 35.16 |
| Friction velocity $u^*$ | 0.1208 m/s | 0.183 |
| Release particle positions $Y_0$ | 1.5, 3, 5, 10, 15, 75, 300 | 0, 3, 5, 15 and 80 |
| Channel width | 1.5 mm | 1.5 mm |
| Number of particles | 800000 | 500000 |

The extensional stresses were calculated in dimensionless form as follows [84, 111, 239]:

$$\sigma_{xx} = 2\frac{\partial u}{\partial x}, \sigma_{yy} = 2\frac{\partial v}{\partial y}, \sigma_{zz} = 2\frac{\partial w}{\partial z} \quad (4\text{-}1)$$

where $u$, $v$, and $w$ are the fluid velocity components in the $x$, $y$ and $z$ directions respectively. This stress was calculated at the position of each vWF marker at each time step, based on interpolation of the Eulerian velocity field at the marker location. A sixth order Legendre interpolation scheme in the *x* and *z* directions and a Chebyshev polynomial interpolation in the wall-normal direction was implemented to obtain the velocity at the markers' location [221].

## 4.2 Results and discussion[2]

### 4.2.1 Transitional Poiseuille-Couette flow

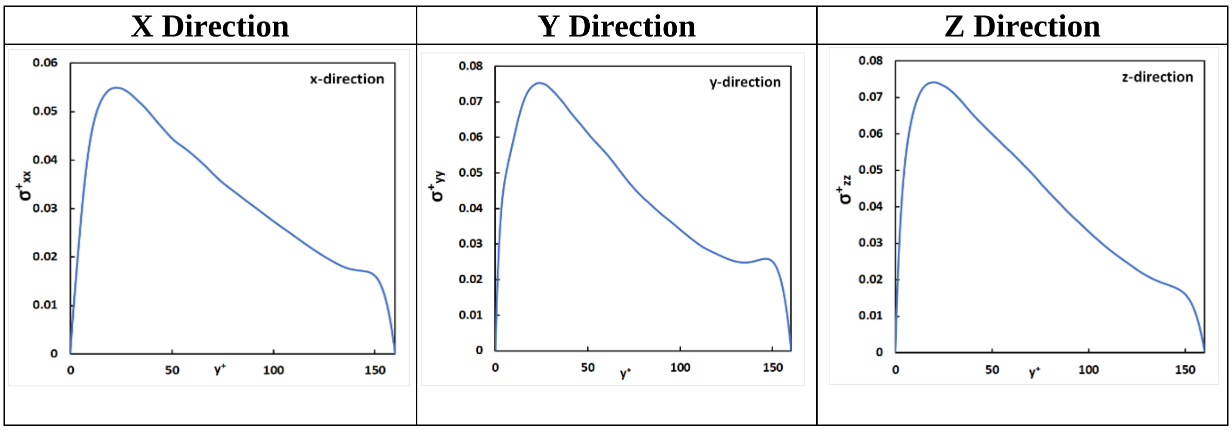


Figure 4.1 The magnitude of the extensional stress as a function of the channel height in the x, y, z directions in Poiseuille-Couette flow. These are averaged values of Eulerian velocity fields.

In Figure 4.1 the Eulerian results for the average extensional stress profile are presented as a function of the distance from the channel wall. The stress values increased dramatically from the wall to get to a maximum value at $y^+=25$ and then decreased gradually, before sharply falling to zero at the moving wall. One would expect that the extensional stress on vWF markers that are released in this flow field at $Y_0 < 25$ would start increasing as the markers move to the regions of high extensional stress, and then decrease, as the markers move farther away into the channel. For release at the center of the PC channel, one would expect a distribution with constant mean value (as markers would move closer to the top wall as well as closer to the bottom wall), but the variance of the statistical distribution of the stresses would be expected to grow with time.

[2] The results in this chapter have been published in reference [75].

The Lagrangian average of the extensional stresses over the vWF particles as a function of time is seen in Figure 4.2. We just plot the absolute value of the extensional stress because the magnitude of the stress and not its direction (compressive or extensional) is the important parameter that affects the vWF molecules. In y and z directions, the absolute values are larger than the critical extensional stress value (1.2 Pa). The change of stress value in all directions is similar each other. As expected, the vWF markers released close to the location of the Eulerian maximum (at $Y_0$ = 15) started from a higher average value at $t^+$ =0, while those released closer to the wall were initially at smaller values. For vWF released within the viscous sublayer ($Y_0$ = 3 and 5) the stress value increased until $t^+$=250 and then decreased gradually. The vWF markers released at the wall of the channel stayed in the wall region, since the molecular diffusion part of their motion was not enough to force them to leave the region very close to the wall. The particles released at the channel center (at $Y_0$ = 80) do not show significant change in the average stress over time.

| X Direction | Y Direction | Z Direction |
|---|---|---|
| 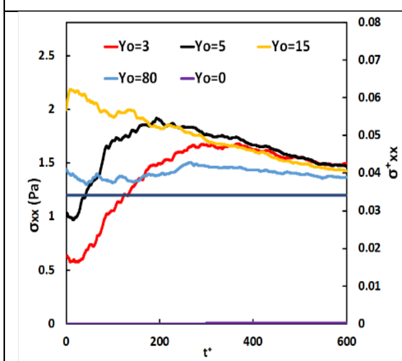 | 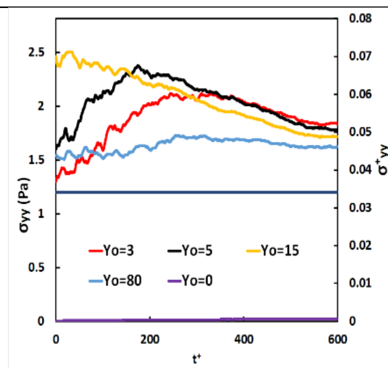 | 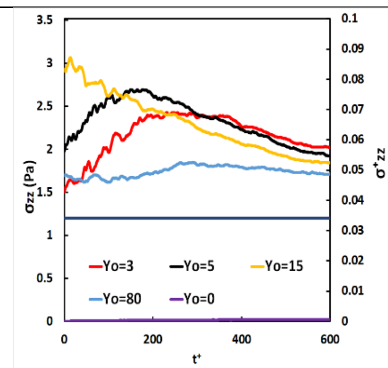 |

Figure 4.2 Mean of the absolute value of extensional stress for particles released at different positions in the Poiseuille-Couette flow field over time. The dark blue line represents the critical stress of 1.2 Pa for the case modeled herein.

In Figure 4.3 we present the probability density function (PDF) of the statistical stress distribution in all directions as a function of time and as a function of the point of release. The investigating positions are the wall of the channel, the edge of the viscous wall subregion (at $Y_0$ = 5), the buffer region and the center of the channel. For release at $Y_0$ = 5, the PDF of the stresses became wider as time passed. When the release position is farther from the wall, at $Y_0 = 15$, the PDF becomes narrower with time, showing that the markers were experiencing a smaller variation of stresses with time. In the channel center, the stress distribution remained roughly the same as a function of time. Moreover, the PDF was symmetric for that case. The critical extensional stress is also shown on the figure for the positive stress, and it is seen that those vWF molecules that experience the stress at the right and the left tail of the distribution would be damaged by extensional stress.

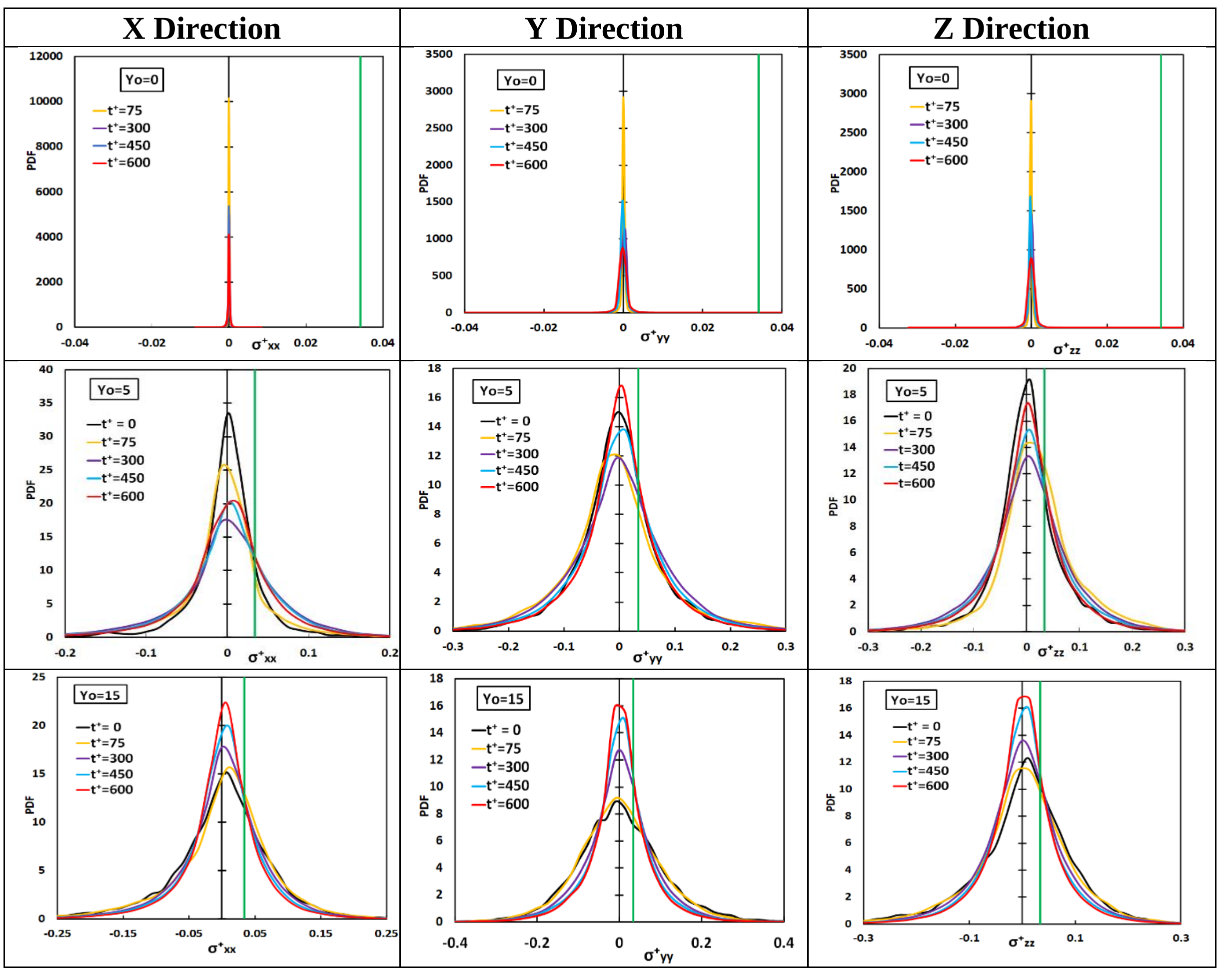

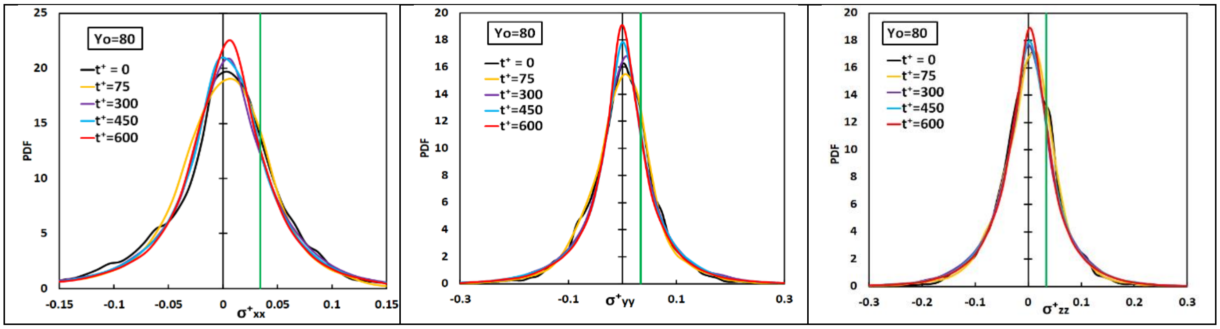


Figure 4.3 Probability density function for the extensional stress components in x, y, z directions of particles released at $Y_0 = 0, 5, 15, 80$ at different time instances Poiseuille-Couette flow field. The green line represents the critical stress of 1.2 Pa for the case modeled herein.

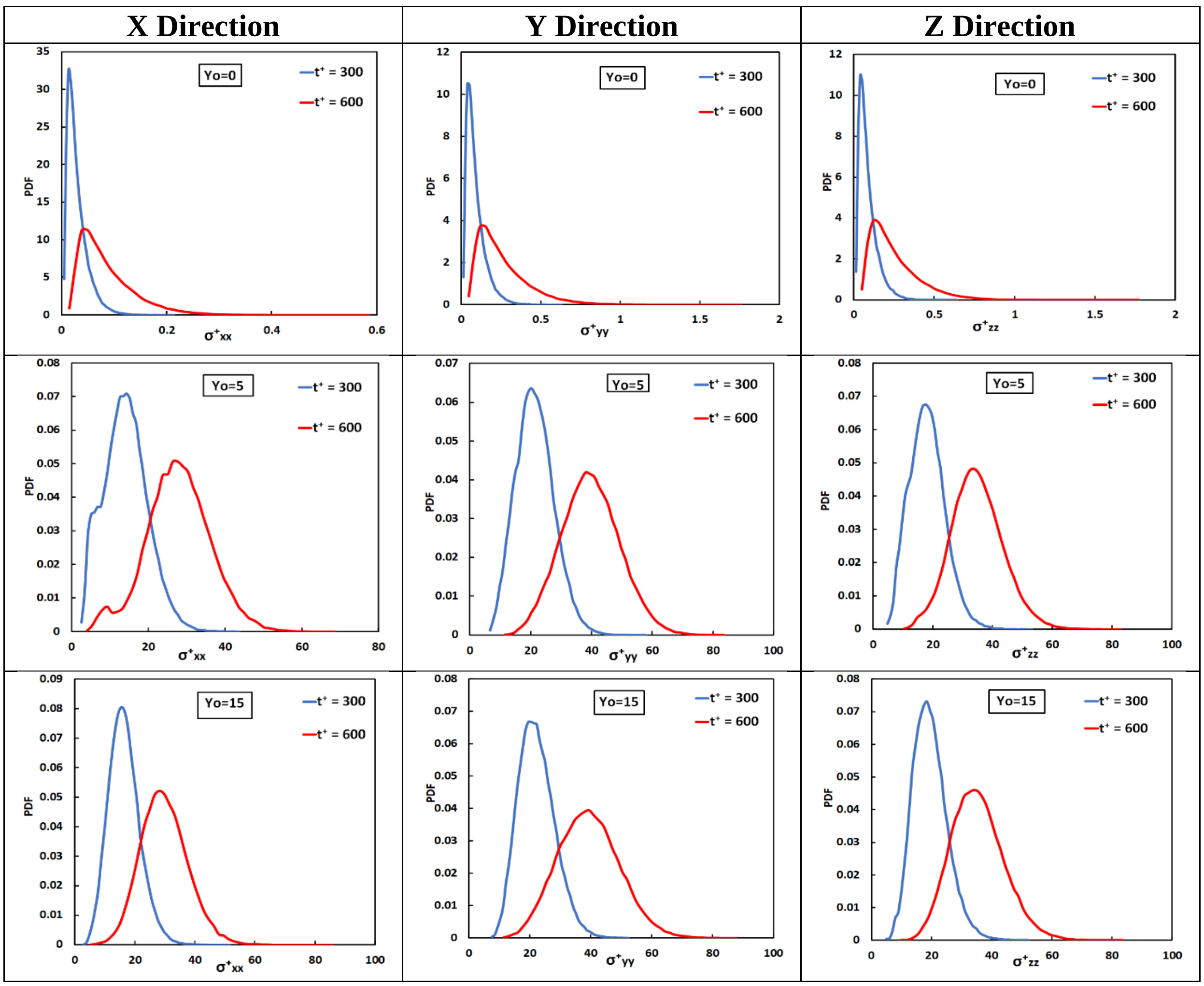

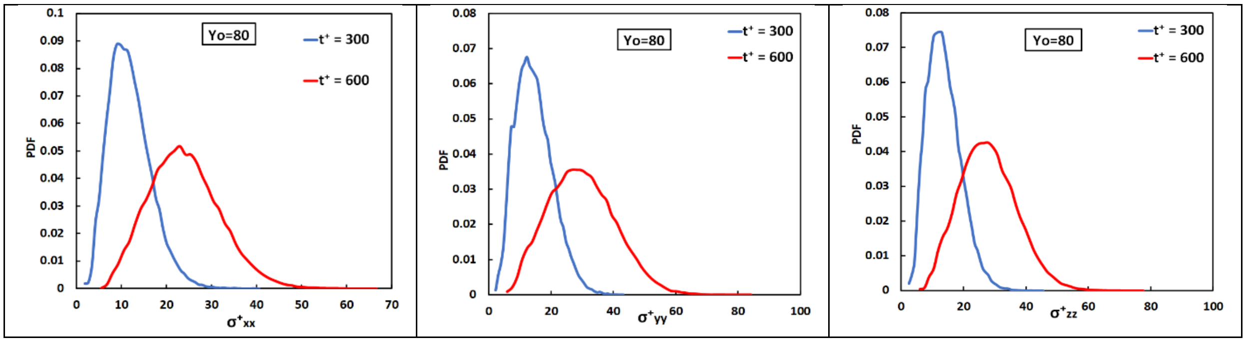

Figure 4.4 Probability density function of the extensional stress histories in x, y, z, directions for particles released at different positions at $t^{+}$=300 and 600 in the Poiseuille-Couette flow field.

Figure 4.4 is a presentation of the PDF of the distribution of the history of the stress on particles at two time instances after being released in the flow field. The distribution was displaced to larger values, since the particles experienced a stress for longer exposure times, but the variance of the distributions increased as well. The width of the distribution is an indication of the significant differences in the stress that particles underwent, and these differences seem to grow as time passed. At the release position $Y_0$=0, the integrated stress values were much smaller when compared to the other release positions. At larger times, it appears that the stress distributions tended to be more symmetric and looked more like the PDF for particles released at the channel center. This is expected, since turbulent convection would mix and distribute the particles across the channel width as time passed.

### 4.2.2 Fully developed turbulent Poiseuille flow

The average of the absolute value of the extensional stresses in the three space directions as a function of the distance from the channel wall is presented in Figure 4.5. In this case, the center *yz* plane in the channel was a plane of symmetry, so only the profile at the bottom half of the channel is shown. The stress profiles seen in Figure 4.5 are Eulerian averages and they show that there was a maximum stress at $y^{+}$=25 in the buffer layer. Farther out from the channel wall the stresses have lower values and reach a minimum at the center of the channel. The normal stress in the *y* direction, $\sigma_{yy}$, was larger than the extensional stress in the other two directions.

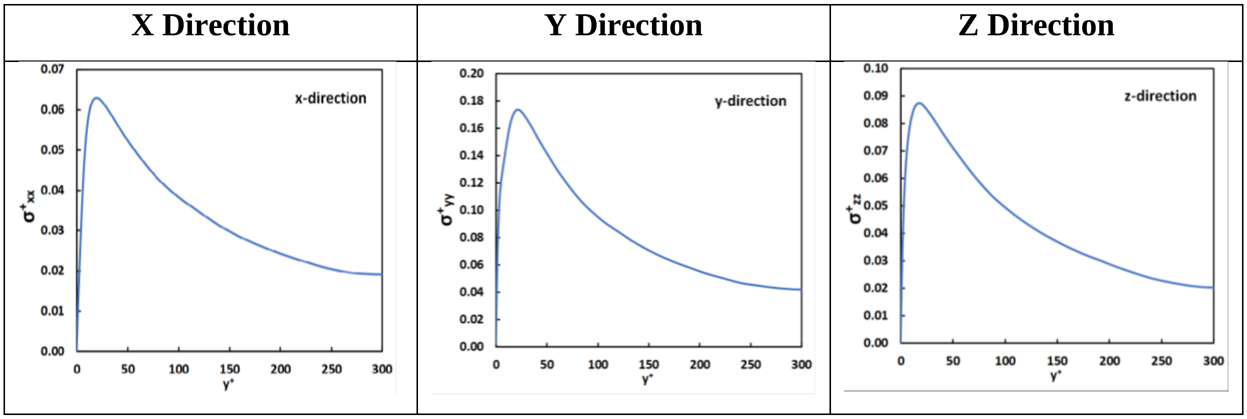


Figure 4.5 Eulerian average of the absolute value of the extensional stress as a function of the distance from the wall in plane Poiseuille flow. Since the Poiseuille flow channel is symmetric across the center place at $y^{+}$=300, only the bottom half of the stress profile is presented.

Figure 4.6 is a presentation of the Lagrangian average of the absolute value of the extensional stresses acting on the vWF model particles as a function of time. The mean value of the extensional stress in the *x* direction was smaller than the critical value for vWF deformation [131]. In the *y* and *z* directions, however, particles released at the edge of the viscous sublayer and within the buffer region (at $Y_0$ = 3, 5 and 15) appear to have experienced high stresses on average – higher than the critical value of 1.2 Pa. In general, the change of stress value followed the same trend in all directions. The average stress for vWF particles released at the center of the channel remained roughly constant, as expected based on the Eulerian stress profile and as discussed for the PC flow case. Particles released at the wall or very close to it (at $Y_0$ = 0 and 1.5) did not have a chance to disperse away from the wall and experience high stresses. As the time after particle release increased, the particles dispersed more uniformly across the channel and the average stress was expected to reach the bulk average Eulerian value across the channel.

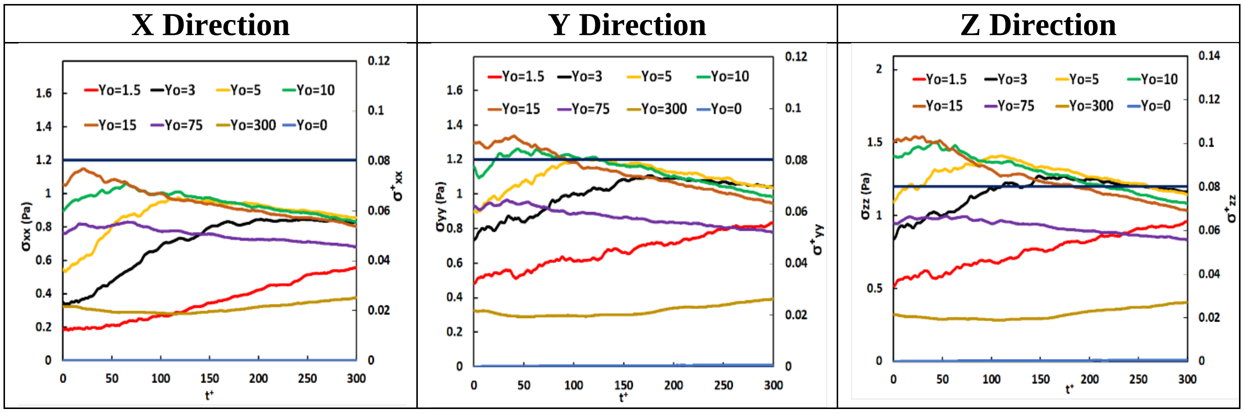


Figure 4.6 Average of the absolute value of the extensional stress on vWF model particles released at different positions in the Poiseuille flow field. The solid straight line at 1.2 Pa indicates the critical extensional stress.

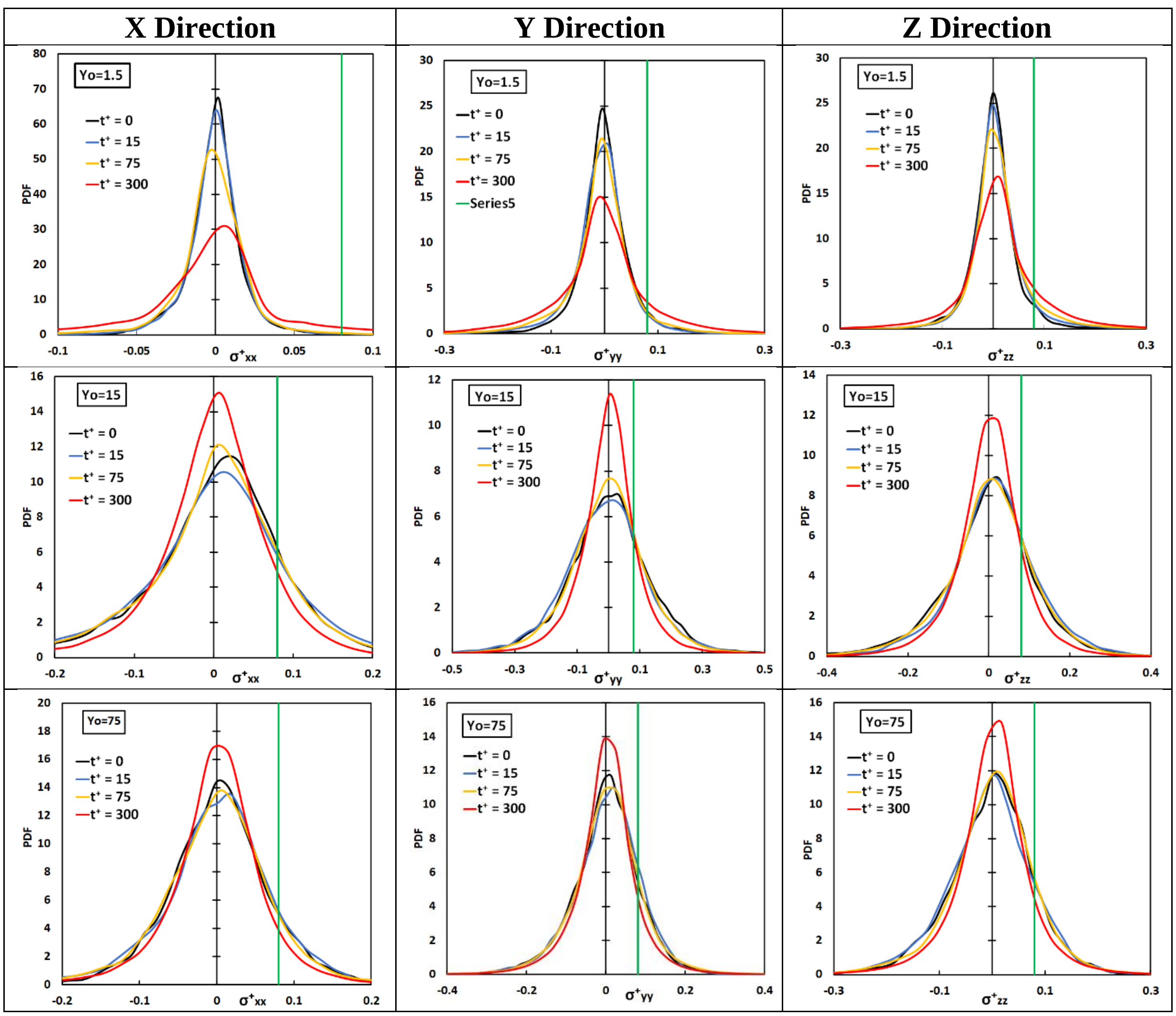

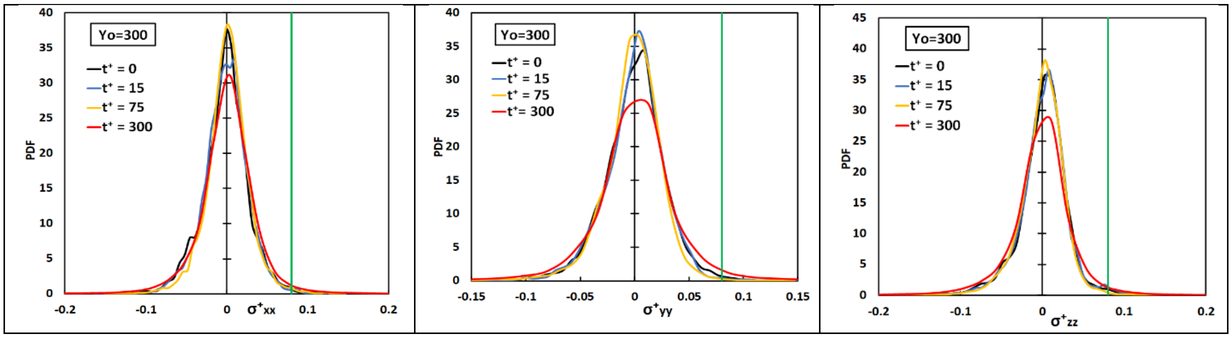


Figure 4.7 The probability density function for the extensional stress components in x, y, z directions of particles released at Yo=1.5, 15, 75, 300 at different time instances Poiseuille flow field. The solid green line depicts the critical stress value for vWF deformation.

After injecting particles, the full distribution of extensional stress was calculated at specific time instances and is presented in Figure 4.7. It appears that for all three directions *x*, *y*, *z* the extensional stress distribution for particles released within the viscous sublayer and the buffer region changed the most with time. The most dramatic change was from $t^+$=15 to $t^+$=75. The variance of the PDF for the stress distribution increased as time elapsed, as indicated by the widening of the PDFs. When particles were released in the log-layer ($Y_0$=75) and at the center of the channel the changes were moderate.

Figure 4.8 is a presentation of the PDF of the distribution of the history of the stress on particles at two time instances after being released in the flow field. The PDFs shown are for particles released at $Y_0$ =1.5, 15, 75, 300. The integrated stress on particles at $t^+$=150 shows a narrow distribution, roughly in the range from 0 to 10 for $Y_0$ =1.5 and 300 and from 0 to 25 for $Y_0$ = 5, 15, 75. This observation can be interpreted when one considers the Eulerian stress profile depicted in Figure 4.5 and the high *Sc* for the vWF particles. For particle release close to the wall of the channel one would expect that a high *Sc* particle would have small diffusion both by molecular means (the standard deviation of the Brownian motion displacement is very low) and by turbulent convection (the turbulent velocity fluctuations that can carry vWF particles away from the wall are very small for $y^+$ between 0 and 1.5). At the channel center, as seen in Figure 4.5, the average stresses did not vary much between a quarter of the channel height (which is the edge of the log-layer and the beginning of the outer region of the flow, at $y^+$=150) and the channel center at $y^+$=300. For release at other locations, in the buffer layer and the viscous sublayer, the vWF particles could diffuse by molecular means and mostly by turbulent convection. In this way they could disperse in the wall-normal direction *y* and would experience a variety of stress values, leading to wider distributions of stress. At later times, as expected, the peaks of the stress history PDFs shifted to the right and the PDFs widened, while the stress distributions tended to be less skewed.

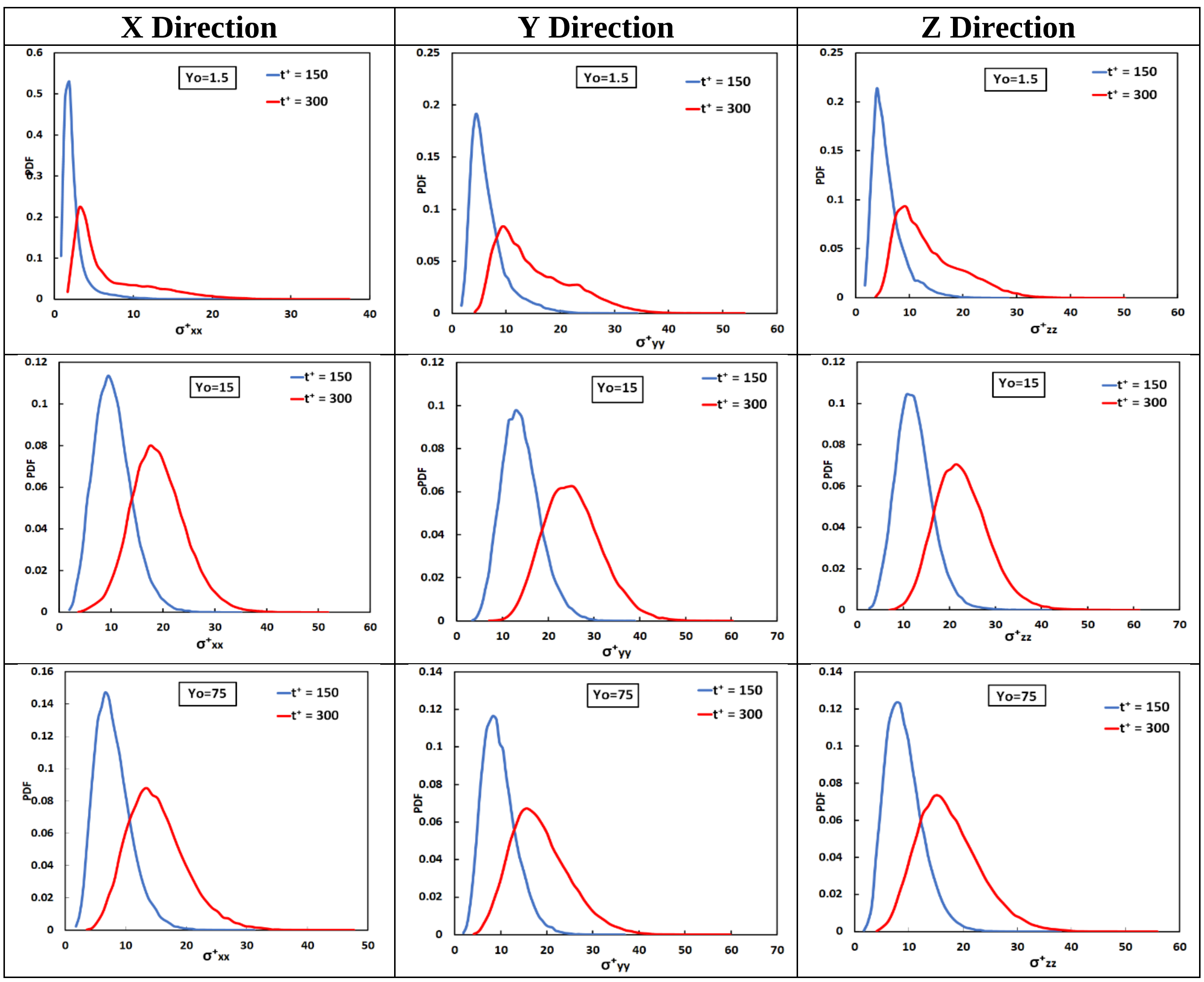

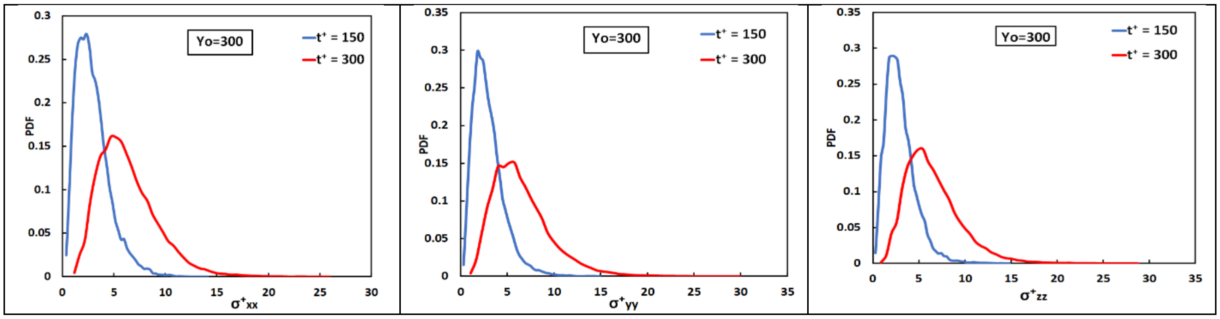


Figure 4.8 The PDF of the extensional stress histories in x, y, z, directions for particles released at different positions at $t^+$=150 and 300 in the Poiseuille flow field.

### 4.2.3 Conclusions

In this study, direct numerical simulations and Lagrangian scalar tracking methods were applied to compute the extensional stress of vWF surrogate particles in different flow configurations (plane Poiseuille-Couette and plane Poiseuille). The vWF particles were assumed to be spherical, in order to obtain a diffusion coefficient. The changes in the shape of the vWF under stress were not taken into account in the calculation of the diffusivity. The drag forces were assumed to be negligible, while Brownian motion was assumed to be the most dominant contributor to the vWF movement after convection. Following this approach, the three components of the extensional stress were monitored for individual vWF particles over time, enabling calculations of the detailed statistical distributions of the stresses. Such calculations are not trivial for either experimental approaches or computational approaches using turbulence modeling with other low-order numerical methods. On the other hand, these computations are not designed to provide structural information for the vWF or for vWF interactions, such as end-to-end-distance of the protein molecule or adherence and adsorption.

The Eulerian results for the average extensional stress showed that the highest average stress was about 0.055-0.075 at the position $y^+$=48 for PC flow meanwhile the PF flow has the maximum values about 0.06, 0.17 and 0.09 at $y^+$=45 for x, y and z directions, respectively. The results of the simulation show that the distribution of stress was a function of both time and release position. It was found that both flow conditions lead to a percentage of vWF particles experiencing damaging stresses. The maximum percentage of particles would be damaged by extensional stress is about 25-30% for Poiseuille flow meanwhile Poiseuille Couette flow has the maximum percentage of particles that could be damaged is more than 50%. The most unpredictable cases were the ones when the vWF were released in the viscous sublayer or in the buffer region of the turbulent flow field. In addition, it is highly probable that particles were exposed to different stresses as they dispersed in the flow field, and these stresses were potentially damaging for a portion of the time they spent in the flow. Injections at the center of the flow field, rather than closer to the wall, would be preferred, as they result in exposure to lower and more predictable stress.

The time history of the stress distribution revealed a similar picture. There are stochastic effects that determine the stress that different particles experience, and the history of stress exposure can vary by multiple times depending on the trajectories of each particle. One would need to develop a power law model for vWF damage, in analogy to power law models for cell trauma [33], but the exponents of the power law model would need to be determined with experimental methods or molecular level computations (e.g., molecular dynamics or coarse-grained techniques). Finally, it is apparent that extensional stresses, which can cause clotting or damage to the vWF functionality at levels lower than the shear stresses, should be accounted in predictions of AcWF syndrome, and the whole distribution of stresses should be determined when designing cardiovascular devises. Future research should include the development of stochastic models for estimating the probability of the vWF to be in regions of high or low extensional stresses in turbulent flow fields.

The trajectories of the particles tracked in the present work are representative of vWF particles only based on the diffusivity of these particles as calculated with the Stokes-Einstein relationship. Solid particles, or other protein molecules of the same diffusivity would follow (according to our modeling assumptions) similar trajectories and would undergo similar levels of stresses in the statistical sense, i.e., the distribution of stresses on any such particles released in these flow fields at the same locations would be subject to the same probability distributions for stresses.

# CHAPTER 5: HELICITY AND DISSIPATION CORRELATION IN ANISOTROPIC TURBULENT FLOW FIELDS.

## 5.1 Methodology and Parameters

The data generated by DNS and LST could allow the investigation of various major issues in turbulent transport for example the transport of scalar dissipation [240, 241] and the role of dynamics of vortex tubes in scalar transport. Our LST provides the fluid velocity at each marker location with time. Assuming that during the small time step of the simulation turbulence is "frozen" (*i.e.,* assuming that *Taylor's frozen turbulence hypothesis [242]* holds over 0.1 viscous time units) one can obtain the space and time derivatives of the fluid velocity along marker trajectories, thus generating data for dissipation, vorticity and helicity (the dot product of velocity and vorticity) along these trajectories. A very recent *Science* article [243] showed for the first time that experimental measurements of helicity are possible, opening up opportunities to revisit the role of helicity in turbulence with new investigative tools. "Helicity is of key importance in turbulent thermal convection …. it is vital to understand how helicity inhibits the energy cascade to small scales at which turbulent energy is dissipated as heat," as stated in the *Perspectives* section of the same issue of *Science [244].* We will use our LST data to calculate the helicity of scalar transporting fluid structures to explore the question of whether scalar transport is promoted due to invariant helicity or not. We can compare the helicity for scalar transport to that for momentum transfer along fluid particle trajectories released at the same location in the channel (note that in our analysis framework fluid particles are LST particles with $Sc \rightarrow \infty$). The data allow calculations of writhe and twist, and the integration of helicity along marker trajectories to explore the invariance of the helicity.

In this study, the DNS is combined with Lagrangian scalar tracking (LST) to simulate Poiseuille and Couette flows and compute the velocity of particles at different Schmidt number, *Sc*. The calculations provided the total helicity and the helicity of the fluctuating velocity field, as well as the dissipation of the turbulent kinetic energy (TKE) in the Lagrangian framework. Statistical analysis was used to evaluate the correlation between helicity and dissipation. In this way, one can make inferences about the use of helicity as an indicator to characterize the level of energy cascade. The two types of flow (Poiseuille and plane Couette) were chosen to gain insights for the correlation between helicity and dissipation in flows that have different structures. The contributions of this work are to (a) determine the correlation between helicity and dissipation in a Lagrangian framework; (b) determine the effects of helicity, if any, on scalar transport for different *Sc* scalars; (c) probe the correlation of helicity and flow structure in different turbulent flows and how it affects turbulent transport.

In this study, the pseudospectral DNS algorithm presented by Lyons et al. [203, 245] and validated by the experiments of Gunther et al. [207] was applied to simulate turbulent channel flow. This algorithm has been modified and used to simulate plane Couette flow [58, 167, 224, 246]. The dimensions of computational box were$16\pi h \times 2h \times 2\pi h$ for both Poiseuille and Couette flow in the streamwise x, normal y, and spanwise z directions, respectively. The half channel height was $h$ = 300, so that the friction Reynolds number was also $Re_\tau = h$ = 300. The number of grid points was 1024x128x256 for Poiseuille and 1024x256x256 for Couette flow in the x, y and z directions.

As for Couette flow, the walls of the channel moved relative to each other, while there was no mean pressure gradient. Therefore, in Couette flow the code was modified by changing the Dirichlet boundary conditions, so that the streamwise velocity at the wall $U_w$ was:

$$U_w = \pm Gh \quad (5\text{-}1)$$

and G was constant (G=0.064). The top wall of the channel moved in the negative x direction and the bottom wall moved in the positive x direction. The Reynolds number defined for Poiseuille flow based on the mean centerline velocity and the half channel height, $Re=(U_c h/v)$ and for Couette flow as $Re=(U_w h/v)$, was 5,700. The fluid was assumed to be an incompressible Newtonian fluid with constant properties. At the channel walls the no-slip, no-penetration boundary condition was utilized, while periodic boundary conditions were applied in the streamwise and spanwise directions. The transport equations in these two directions were expanded by Fourier series and the vertical velocity and pressure head were expanded in terms of a Chebyshev polynomial series which provided adequate resolution to satisfy rigid boundary condition [247]. The time step for the simulation of Poiseuille flow was $\Delta t = 0.1$, and for Couette flow it was $\Delta t = 0.05$.

In a Lagrangian framework, the system of reference moves with fluid particles [166]. In Lagrangian scalar tracking (LST), the trajectories of individual scalar markers were monitored as described in a thesis by Kontomaris [166, 205, 248, 249]. Scalar markers were released into the flow after the channel and Couette flow reached stationary state. Simulations were conducted for different cases of *Sc*: *Sc* = 0.7, 6 and the case of fluid particles.

Scalar markers were released at given distances $Y_o$ from the bottom wall of the computational channel, $Y_o$ =0, 1.5, 3, 5, 10, 15, 75, 300 for both Poiseuille and Couette flow. These release positions represent the channel wall, the viscous wall sublayer, the buffer region, the logarithmic layer and the channel center. At each $Y_o$, 100,000 particles were released from 20 lines that were uniformly spaced in the *x* direction while spanning the width of the channel in the *z* direction. This was done to avoid bias that could be potentially caused by the turbulent velocity field at the instant of marker release. Therefore, the total number of particles released in the flow filed was 800,000 for either Couette or Poiseuille flow.

### *Post Processing*

Using LST, data for position, velocity, vorticity and for the derivative of the velocity in each of the three directions were obtained along the trajectory of each particle in the flow. To calculate the fluctuating velocity and the derivatives of the fluctuating velocity at each time step, the mean velocity **U** and the derivative of the mean velocity dU/dy in the Eulerian framework were used to obtain the mean velocity and its derivative at each particle position in the y direction. A weighted average of the two values connected by a straight line was used [250].

The fluctuating velocity vector, $u'$, and its derivatives in the three space directions was used to calculate the vorticity vector for the fluctuating velocity, $\omega'$. The relative normalized helicity density is defined as $h' = cos\theta'$, where $\theta'$ is the angle between the fluctuating velocity and vorticity vectors [162].

$$h' = \ cos\theta' = \frac{u'.\omega'}{(|u'||\omega'|)} \tag{5-2}$$

where $u' = u - \mathrm{U}$ and $\omega' = \nabla \times u'$. When the velocity and vorticity vectors align with each other, then $h' = 1$ and when they are perpendicular to each other, $h' = 0$.

The turbulent dissipation rate along the trajectories of each marker was calculated as [251]:

$$\epsilon = 2\left(\frac{\partial u\prime}{\partial x}\right)^2 + 2\left(\frac{\partial v\prime}{\partial y}\right)^2 + 2\left(\frac{\partial w\prime}{\partial z}\right)^2 + \left(\frac{\partial u\prime}{\partial y} + \frac{\partial v\prime}{\partial x}\right)^2 + \left(\frac{\partial u\prime}{\partial z} + \frac{\partial w\prime}{\partial x}\right)^2 + \left(\frac{\partial v\prime}{\partial z} + \frac{\partial w\prime}{\partial y}\right)^2 \tag{5-3}$$

The statistical analysis was based on calculations of correlation coefficients and joint pdfs (JPDF). The joint pdf P($\epsilon, h'$) can demonstrate how $h'$ is distributed for all values of $\epsilon$ and is a useful tool to define what conditions on $\epsilon$ yield regions that are helical in nature [151]. In this case, a 2D array of bins were generated that represented different values of $\epsilon$ and $h'$. The number of scalar markers that had values within the range of each bin was counted and then the probability was calculated by diving for total number of particles.

The autocorrelation for relative helicity density and dissipation was evaluated as follows [252]:

$$R_{h'-h'(t)} = \frac{\overline{h'(t_0)h'(t_0+t)}}{\overline{h'(t_0)^2}} \tag{5-4}$$

$$R_{\epsilon-\epsilon(t)} = \frac{\overline{\epsilon(t_0)\epsilon(t_0+t)}}{\overline{\epsilon(t_0)^2}} \tag{5-5}$$

The cross-correlation between relative helicity density and dissipation was calculated by the Pearson cross-correlation formula as follows:

$$R_{h'-\epsilon} = \frac{\sum_{i=1}^{n}(h'_i - \overline{h'})(\epsilon_i - \bar{\epsilon})}{\sqrt{\sum_{i=1}^{n}(h'_i - \overline{h'})^2}\sqrt{\sum_{i=1}^{n}(\epsilon_i - \bar{\epsilon})^2}} \tag{5-6}$$

The overbars above represent the ensemble average over all *n* scalar particles, while the index i designates individual particles.

## 5.2 Results and Discussion

### 5.2.1 Eulerian mean of helicity in Poiuseuille and Couette flow

The profiles of the mean of the absolute value of the helicity of the fluctuating velocity field, $|H'|$, and the absolute value of the relative helicity density for Poiseuille and Couette flow are presented in Figure 5.1. The absolute value is used instead of the actual value, to make sure that positive and negative helicity do not cancel out because of changes in the value of the cosine. For Poiseuille flow, the mean of the absolute helicity increases from 0 at the wall to a maximum at a position within the buffer layer, at about 20 viscous wall units away from the wall. The absolute helicity then declines gradually to reach a local minimum at the center of the channel. The absolute values of the relative helicity density ($h' = cos\theta'$) increase from the channel wall to about 0.5 at $Y^+$=50, and then appear to be almost constant with distance from the wall. The velocity and vorticity vectors tend to be at about 60° from each other beyond $Y^+$=50, while they were perpendicular to each other at very low $Y^+$. Meanwhile, when it comes to Couette flow, the profile of $|H'|$ and $h'$ exhibit a trend like Poiseuille flow but $|H'|$ has higher values than for Poiseuille flow. The alignment of velocity and vorticity on average (as seen by $h'$) is the same in Poiseuille and in Couette flow.

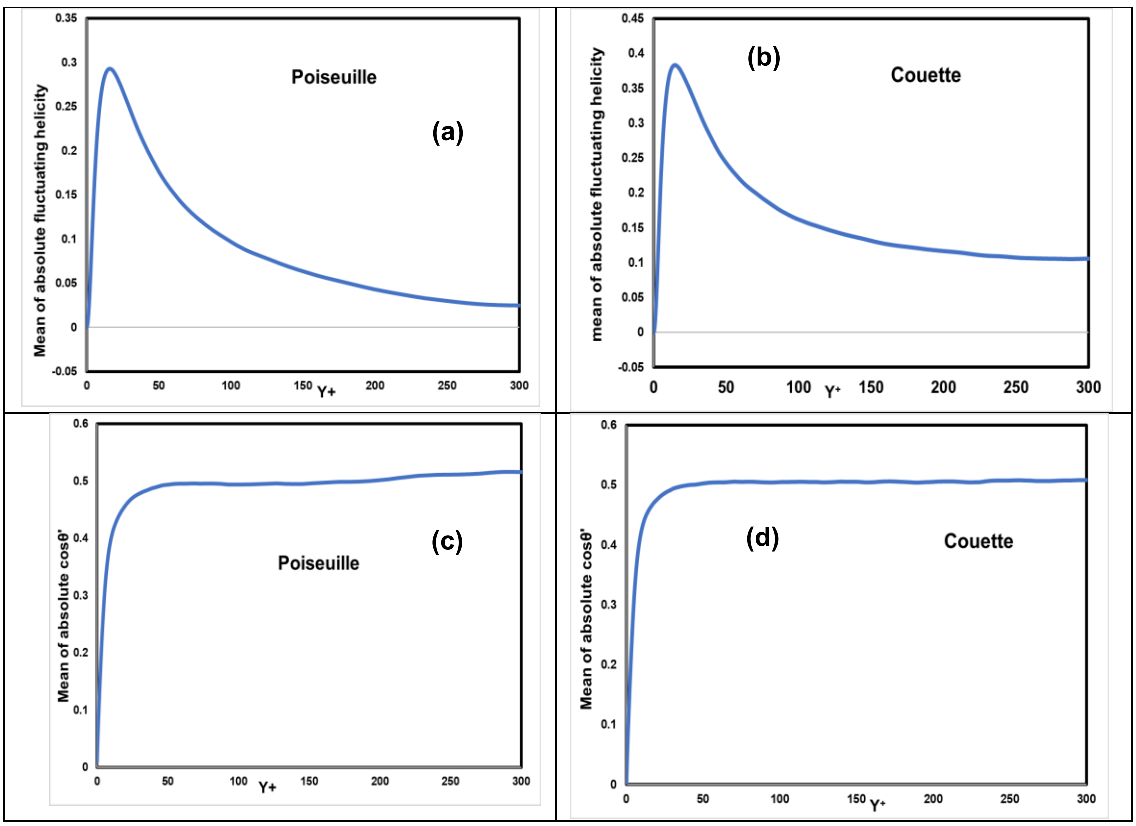


Figure 5.1 The Eulerian mean of the absolute values of fluctuating helicity density ($|H'| = |\boldsymbol{u}'.\boldsymbol{\omega}'|$) for (a) Poiseuille flow and (b) for Couette flow. Mean absolute value of the relative helicity density ($|h'| = |cos\theta'|$) calculated as a function of distance from the wall for (c) Poiseuille flow and (d) Couette flow.

### 5.2.2 The average position of particles at various release position and Sc numbers

Two types of flow, Couette and Poiseuille flow, were chosen to investigate the interaction between helicity and dissipation as well the effect of position of release particles on the change of helicity with time. The average positions of particles released at Yo = 1.5, 3, 5, 75 of Couette flow and Poiseuille flow at various *Sc* number are presented in Figure 5.2. The markers moved farther from the wall and the average position of particles increased faster for Couette and Poiseuille flows at *Sc* = 0.7 than Poiseuille at *Sc* = 6 and for fluid particles. This can be explained based on the fact that the particles with smaller *Sc* have larger Brownian motion, so that they can escape the viscous wall region faster and then diffuse with larger displacement.

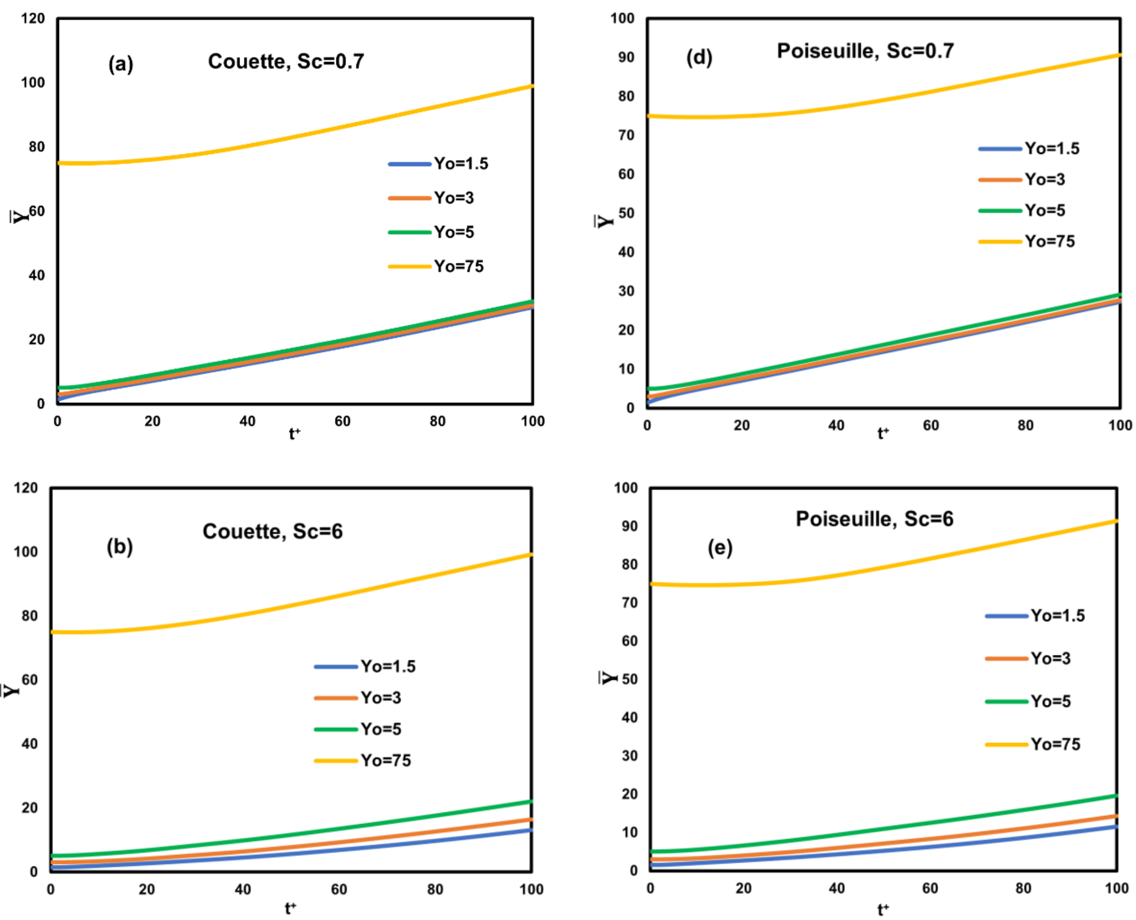

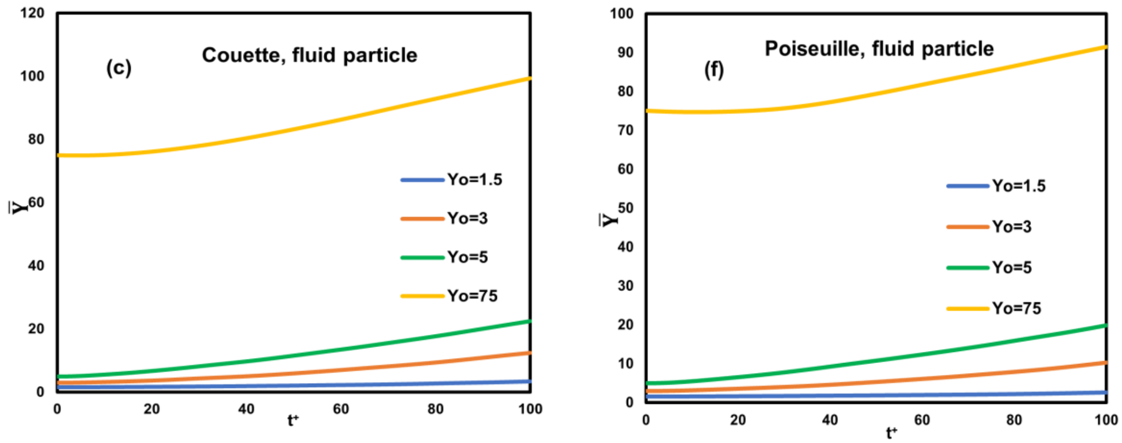


Figure 5.2 The average position of particles at release positions Yo =1.5, 3, 5, 75 of Couette flow and Poiseuille flow at various $Sc$ number. Couette flow (a) $Sc$=0.7, (b) $Sc$ =6, (c) fluid particle; Poiseuille flow (d) $Sc$ =0.7, (e) $Sc$ =6, (f) fluid particle.

### 5.2.3 Autocorrelation of helicity and dissipation in Poiseuille and Couette flow at different $Sc$ number

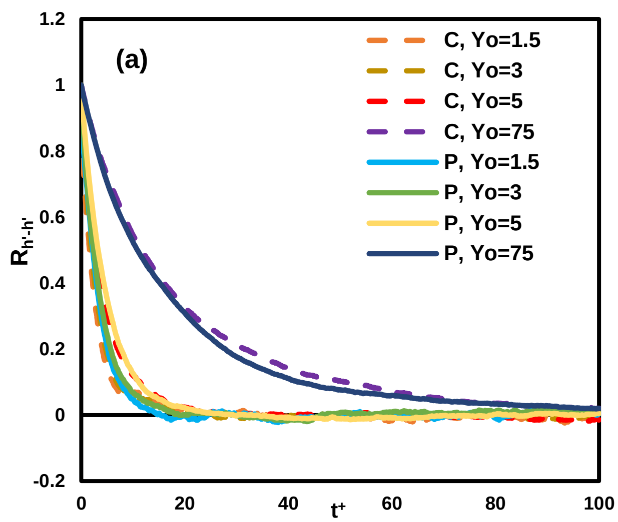

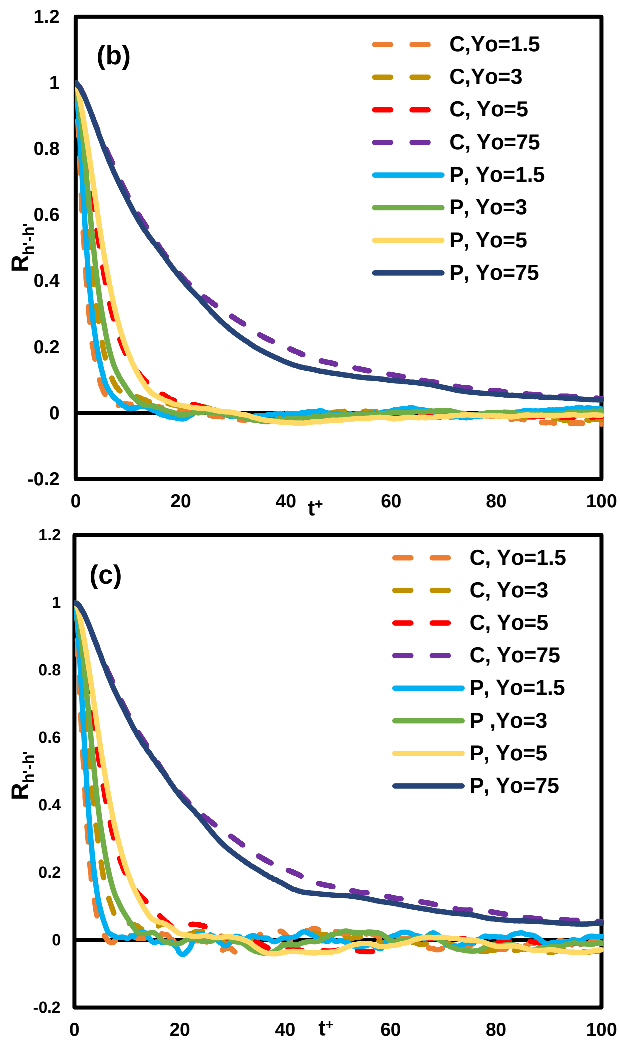


Figure 5.3 The autocorrelation of relative helicity density $h' = cos\theta'$ for Poiseuille flow and Couette flow at (a) $Sc$ = 0.7, (b) $Sc$ = 6 and (c) fluid particles. The symbol P on the legend represents results for Poiseuille flow and the symbol C represents Couette flow.

The effect of *Sc* on the autocorrelation coefficient of the relative helicity density of the fluctuating velocity can be seen in Figure 5.3. The coefficient decreased most significantly after 20 time units for $Y_o$=1.5,3,5 for both Couette and Poiseuille flows. As can be seen, the autocorrelation decreases slower when the position of marker release ($Y_o$) is farther from the wall. In particular, these values decreased to about zero after 30 dimensionless time units. However, when the particles were released in the logarithmic layer at $Y_o$ = 75, the autocorrelation remained larger than zero for 100 time units. This trend is significant for the case of fluid particles (see

Figure 5.3c) and following that is the case of *Sc* = 6. For *Sc* = 0.7 there seems to be minimal change in the autocorrelation profile at Yo =1.5, 3, 5 for both Couette and Poiseuille flows. In general, the autocorrelation of the relative helicity density depends on the release positions and on the *Sc* rather than the configuration of the flow.

### 5.2.4 Cross correlation of helicity and dissipation rate conditioned on kinetic energy

In order to examine the correlation of $h'$ to the dissipation of the turbulent kinetic energy $\epsilon$, the cross-correlation coefficient was determined along the trajectories of the passive markers in the flow as presented in Figure 5.4. It is apparent that the correlation values fluctuate within a very small range around the value of zero, and do not show any trend with time in all cases. This leads to the suggestion that there was no correlation between $\epsilon$ and $h'$. Regions of low (or high) helicity do not correspond to regions of low (or high) dissipation, indicating that the energy cascade to very small scales is not related to the relative alignment of the velocity and vorticity vectors along the trajectories of scalar particles in the flow.

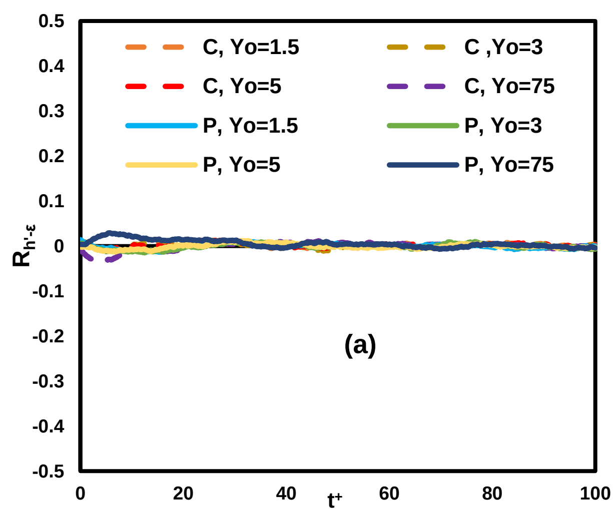

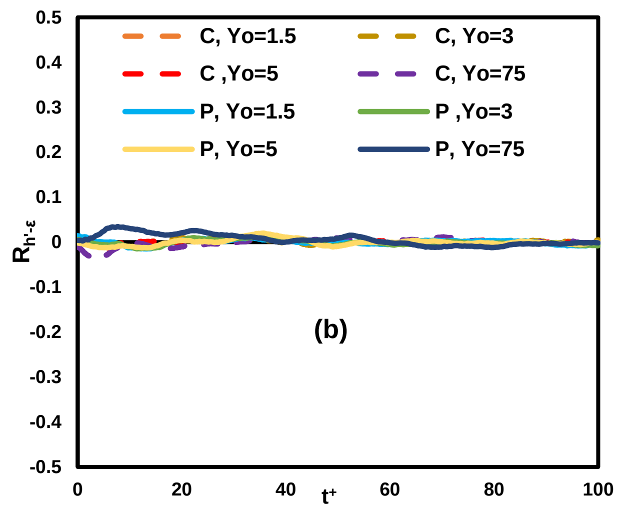


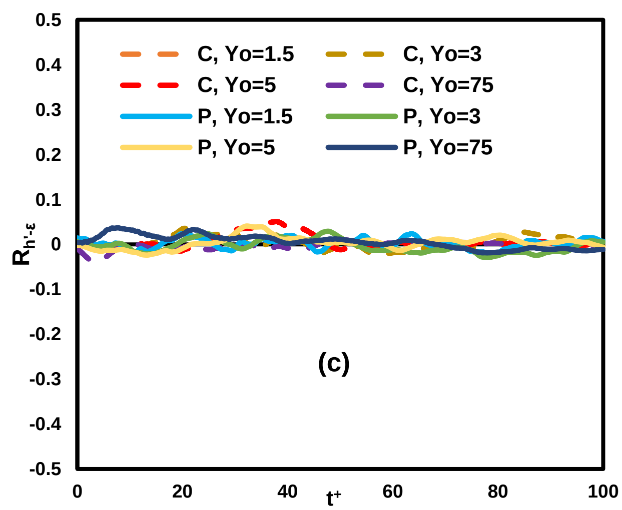


Figure 5.4 The Pearson cross-correlation between the relative helicity density $h' = cos\theta'$ and the dissipation for Poiseuille flow and Couette flow at (a) $Sc$=0.7, (b) $Sc$= 6, (c) fluid particles.

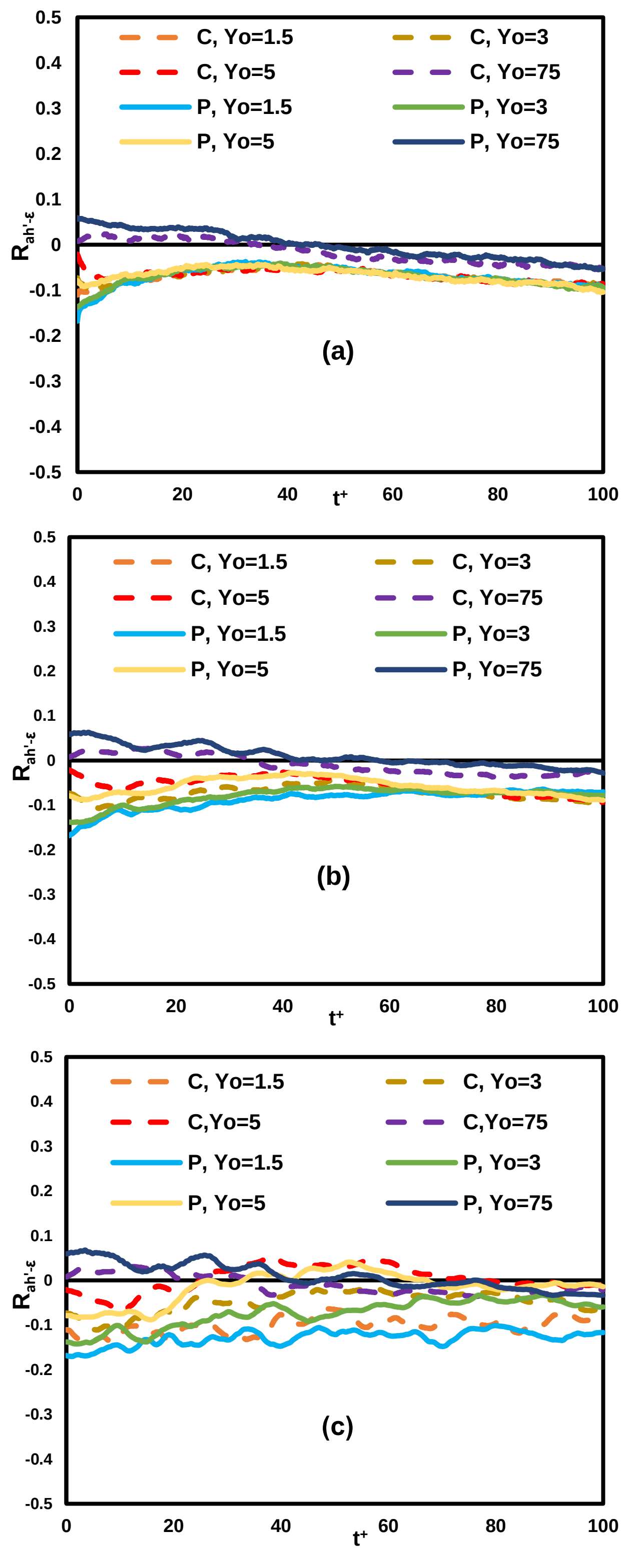


Figure 5.5 The Pearson cross-correlation between $\epsilon$ and absolute value of $h'$ for Poiseuille flow and Couette flow at different $Sc$: (a) $Sc$ =0.7, (b) $Sc$ =6, (c) fluid particles.

The Pearson cross-correlation between $\epsilon$ and the absolute value of $h'$ is represented in Figure 5.5. The results are interesting; consider the case of fluid particles where the lowest values of the cross-correlation appear for fluid particles released within the viscous wall sublayer, at the position $Y_o$ =1.5 and for both types of flow. For release farther from the wall, the correlation gets higher values but is still negative, except for $Y_o$ =75, where cross-correlation values are positive during the initial time units after particle release, but then fall to less than 0. This is similar to the case for $Sc$ = 6. When $Sc$=0.7, the values of $R_{h'-\epsilon}$ were negative but not significantly different between $Y_o$ =1.5,3 and 5. From these figures, one may-conclude that the relative helicity density and the dissipation are anticorrelated. This anticorrelation is not complete since the values of the cross-correlation do not go as low as -1. There are many particles that have dissipation larger than average, the corresponding $h'$ is smaller than average, but this does not occur with all particles.

### 5.2.5 Correlation of helicity and dissipation of particle moving farthest and closest

Whether helicity can be used to identify flow structures that are major contributors to turbulent dispersion has been explored in the past. The hypothesis was that regions with high values of helicity, if they also exhibited low dissipation, could indicate flow structures that would tend to persist in time, making them candidates for strong contributors to turbulent transport [150]. In order to examine this relationship between helicity and turbulent transport further, we now focus on the particles that are transported the farthest from the wall in the normal direction, y. These were the scalar markers that were released at Yo = 3. The particles that did not disperse far are also examined, to differentiate between high dispersion and low dispersion. The results are seen in Figure 5.6. We chose the top quartile, i.e., the 25% of the particles that moved the farthest away from the wall at the end of the simulation and compared their behavior to the bottom quartile, i.e., the 25% of the particles that remained close to the wall at the end of the simulation. The relation between h′ and ϵ for particles that dispersed farthest and closest to the wall was also evaluated. As can be seen, the autocorrelation of h' followed the same trend in all cases. This coefficient remains positive, but it declines slowly with time for the top quartile of dispersing particles. It tends to stay constant at long times for the particles that were closer to the wall (see the bottom raw of Figure 5.6). Therefore, particles that stayed in flow structures of similar h′ and did not go through flow regions where the alignment of velocity and vorticity changed, remained closer to the wall.

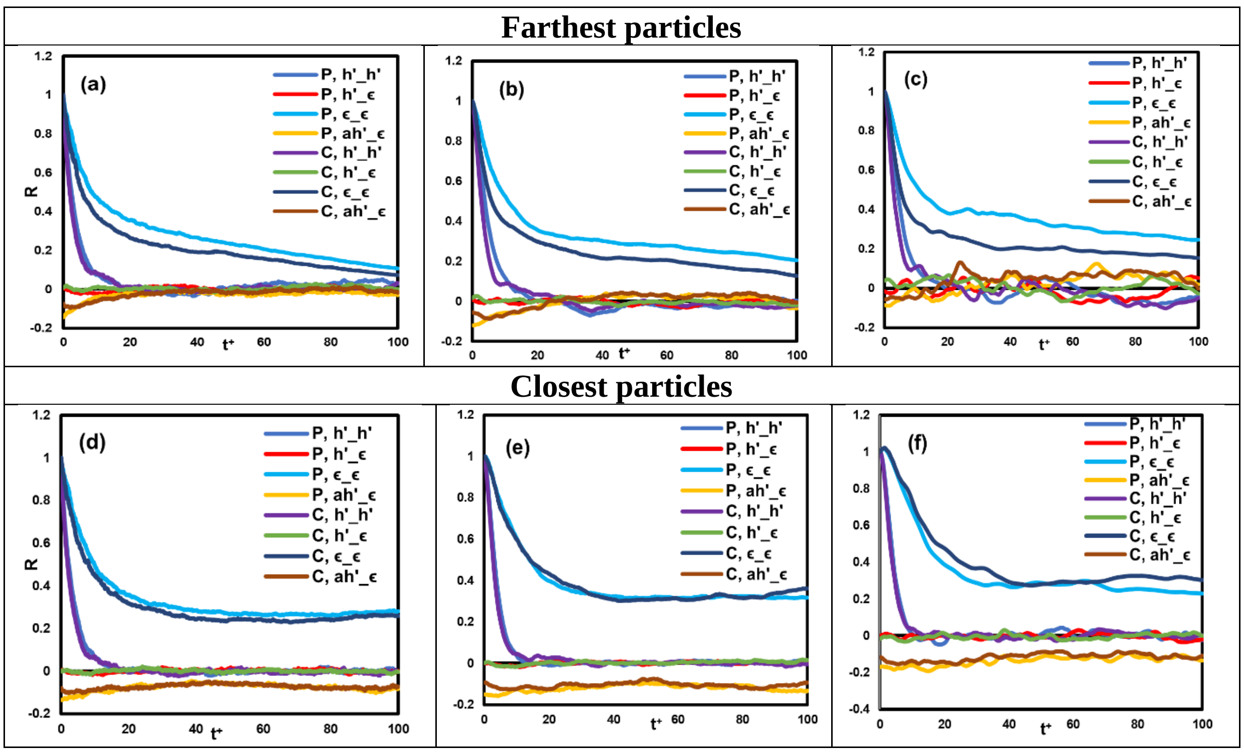


Figure 5.6 Profiles of the autocorrelation of $h'$ with time, $h'\_h'$; the autocorrelation of dissipation with time, $\epsilon\_\epsilon$ ; the Pearson cross-correlation between $h'$ and dissipation $h'\_\epsilon$ ; and the Pearson cross-correlation of the absolute value of $|h'|$ with dissipation, $ah'\_\epsilon$. The correlations for the 25% of the particles that were found to be the farthest from the wall at $t^+=100$ are shown in the top raw: (a) $Sc$ = 0.7, (b) $Sc$ = 6, (c) fluid particles. The correlations for the 25% of the particles that were found to be the closest to the wall at $t^+$=100 is shown in the bottom raw: (d) $Sc$ = 0.7, (e) $Sc$ = 6, (f) fluid particles. The particles that were released at $Y_o$ = 3 for both Poiseuille and Couette flow.

The Pearson cross-correlation between $h'$ and $\epsilon$ is very small for the cases of $Sc$ = 0.7 and 6, but this value fluctuates more for fluid particles. There are no differences between the top and bottom quartiles of particles. When it comes to the autocorrelation of $\epsilon$, this value decreased within the first 20 time units and then gradually declined with time for all cases, but with different slope for various *Sc* and for the farthest and closest particles. The autocorrelations and the Pearson cross-correlations for Poiseuille and Couette flow at *Sc* = 0.7 and 6 also display the same trends for the particles closer to the wall, while the particles that transport the farthest in Poiseuille flow showed a decrease in helicity correlation that is slower than that of Couette flow. The dissipation correlation shows a faster decline for Couette flow in comparison to Poiseuille flow. However, there is a difference in the Pearson cross-correlation of the absolute value of the relative helicity density $h'$ and $\epsilon$ for the farthest and closest particles. The particles close to the wall have constant values around -0.2 for both types of flows and different *Sc* number, while for the farthest particles, the value of the cross-correlation started at about -0.2 and then approached zero for all cases. This leads to the question of whether scalar transport in the flow has been affected by helicity.

### 5.2.6 Lagragian timescale as a function of source for dispersion

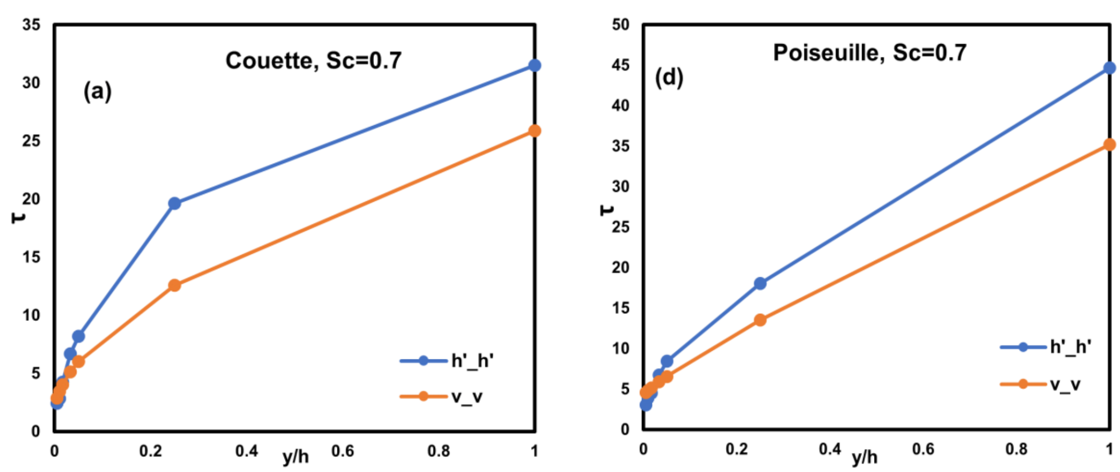

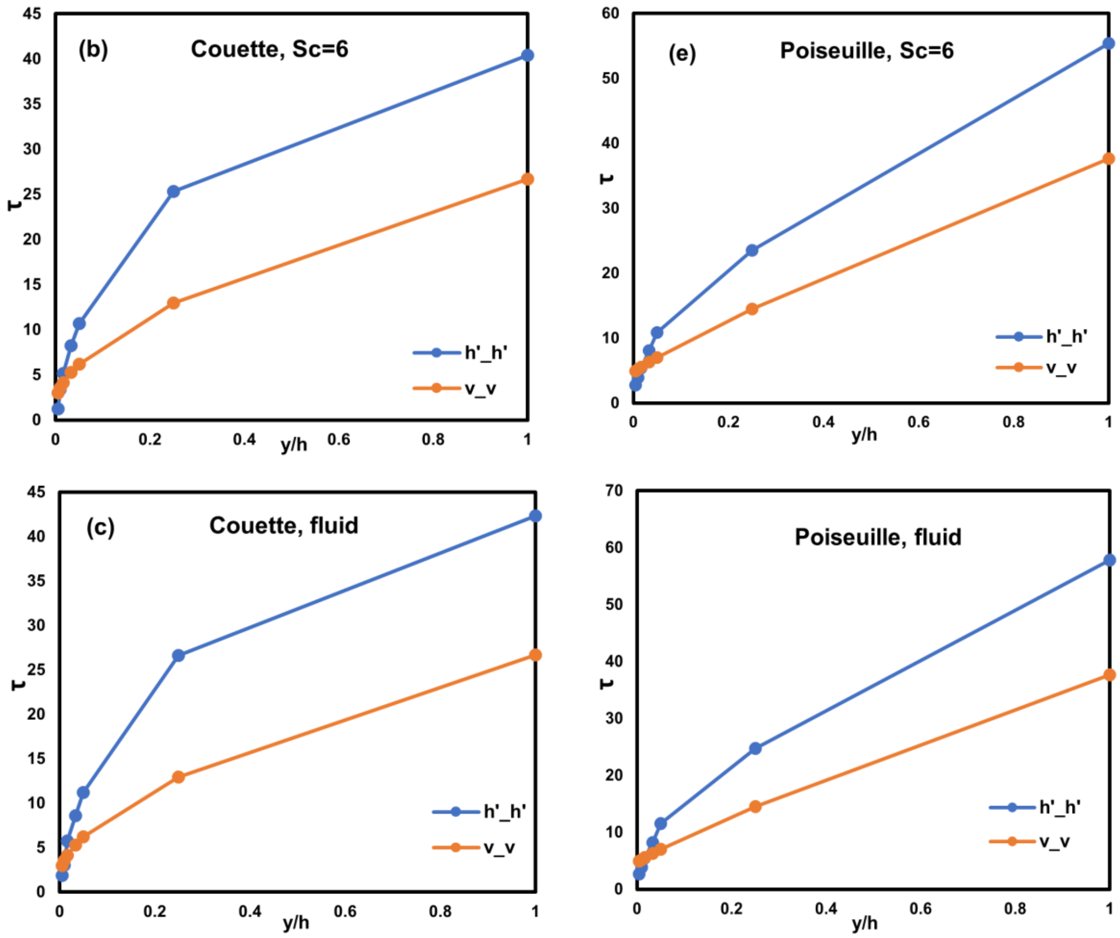


Figure 5.7 The Lagrangian timescale as a function of source elevation for dispersion in the y-direction for different $Sc$ number and types of flow where the vertical axis is timescale and the horizontal axis is $\frac{Y_o}{h}$ ($Y_0$ is the initial position of release particles) for the relative helicity density $h' = cos\theta'$ (h'_h') and velocity from prior results (v_v, from ref [167]) for Couette flow at (a) $Sc$ = 0.7, (b) $Sc$ = 6, (c) fluid particles and for Poiseuille flow at (d) $Sc$ = 0.7, (e) $Sc$ = 6 and (f) fluid particles.

The autocorrelation coefficients can be used to define characteristic timescales for the dispersion of the scalar. The dispersion Lagrangian timescale that can be obtained as a function of the elevation from the wall of the scalar source, $Y_o$, in the *y*-direction that can be calculated as [167]:

$$\tau_{Ly} = \int_{t_o}^{\infty} R_{h'h'}(t, t_o)dt \qquad (5\text{-}7)$$

As can be seen from Figure 5.7, the newly defined timescale was a function of the position of scalar release and the timescale increased to get its highest value for scalar release at the center of the channel. For the Couette flow, the largest time scale was in the range from 30-45 viscous time units, meanwhile that of Poiseuille flow was higher in the range of 45-55. This shows that Poiseuille flow exhibits a larger characteristic timescale than Couette flow. Comparing this timescale with the Lagrangian timescale for the fluctuating velocity, which has been reported in a prior study from our laboratory [167], it is found to be larger.

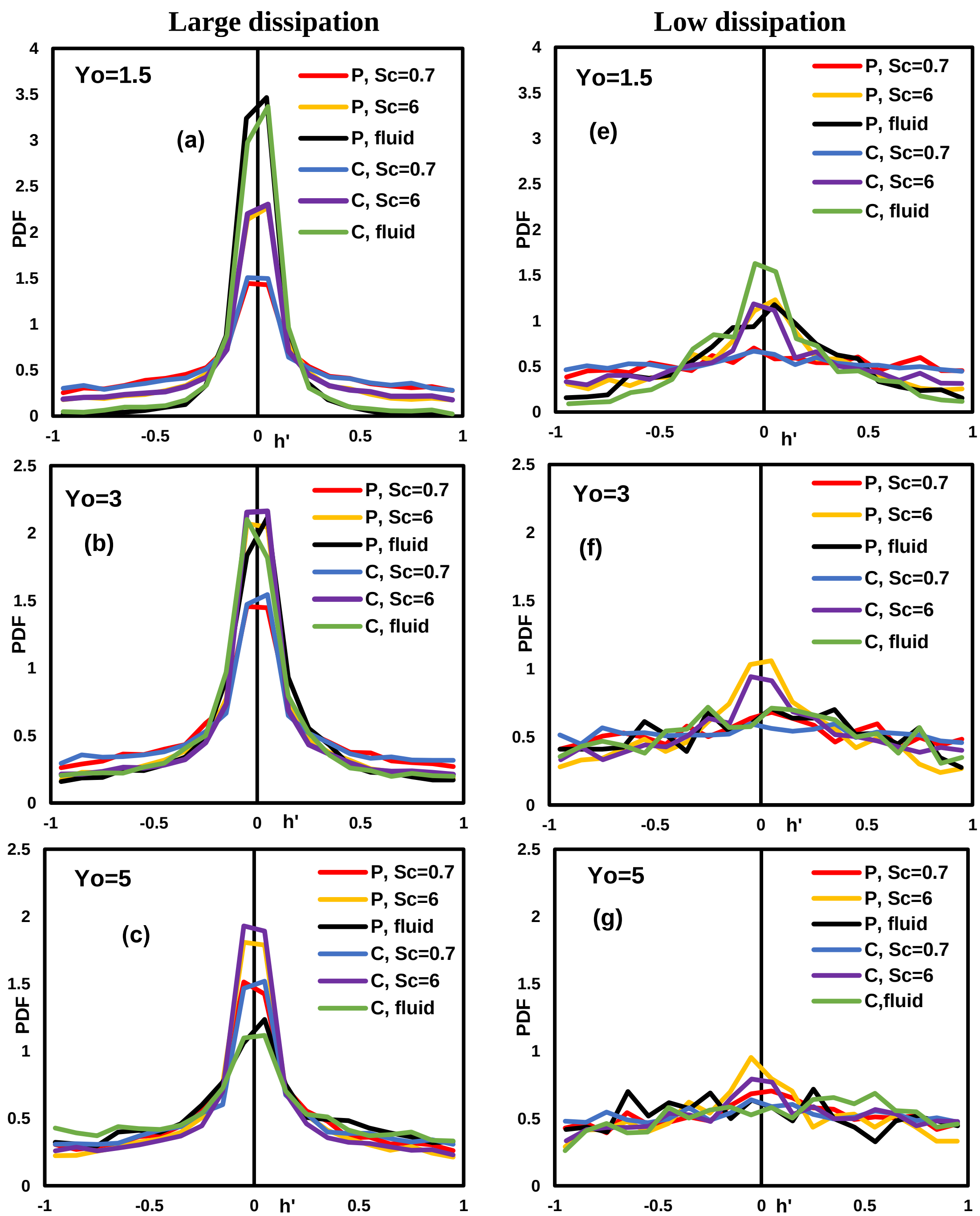

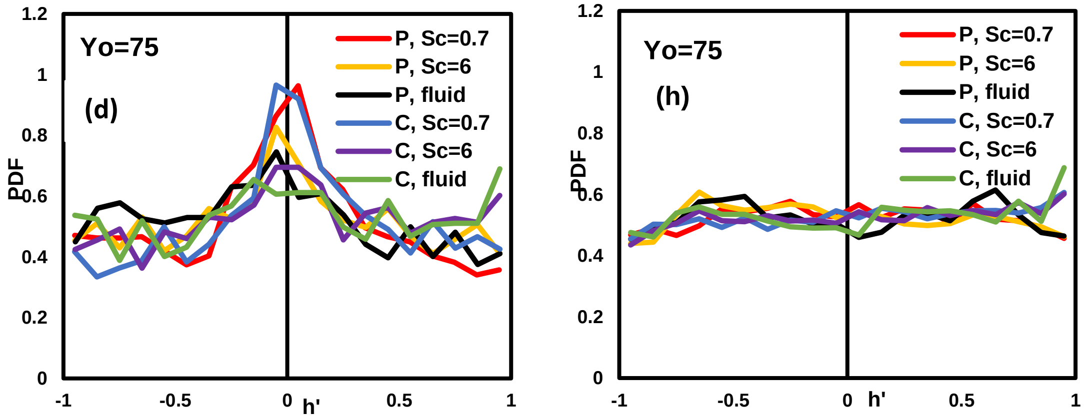


Figure 5.8 The distribution of relative helicity density $h' = cos\theta'$ conditional on high (left column) at (a) Yo = 3, (b) Yo = 10, (c) Yo =15, (d) Yo =75 and low dissipation (right column) at (e) Yo =3, (f) Yo = 10, (g) Yo = 15, (h) Yo =75 at $t^+$=100 for Poiseuille and Couette flow. For both Couette and Poiseuille flow, the high dissipation is more than 8 times and 10 times the average dissipation respectively, and the low dissipation is less than 0.25 times the average dissipation.

The probability density functions (PDFs) for $h'$ have been calculated and displayed in Figure 5.8. A distinction between the particles that were found in areas of low and high dissipation was made. The PDF for particles that have the highest $\epsilon$ show a peak around the value of zero. This indicates that the velocity and the vorticity vectors for particles in areas of high dissipation of TKE tend to be perpendicular to each other. Far from the wall the PDFs appear to be flatter, so the probability of having velocity and vorticity vectors to align in areas of high dissipation is smaller than closer to the wall. However, when considering the *Sc,* it is seen that the lower the *Sc* the flatter the PDFs are (meaning that the tails of the PDFs are higher and the peaks are lower as Sc decreases). On the other hand, the PDF for the helicity $h'$ of particles that are in locations of low $\epsilon$ are much flatter in comparison. This shows that for regions with low dissipation, the distribution of $h'$ is more uniform. The vorticity and velocity vectors do not have an alignment that favors a $90^o$ angle – which was the case for high dissipation. The alignment seems to be more random. Further, there does not appear to be a *Sc* effect on flatness of the PDF. On the other hand, for the particles with high dissipation, their $h'$ distribution has been affected by *Sc* and the position of release rather than the flow configuration.

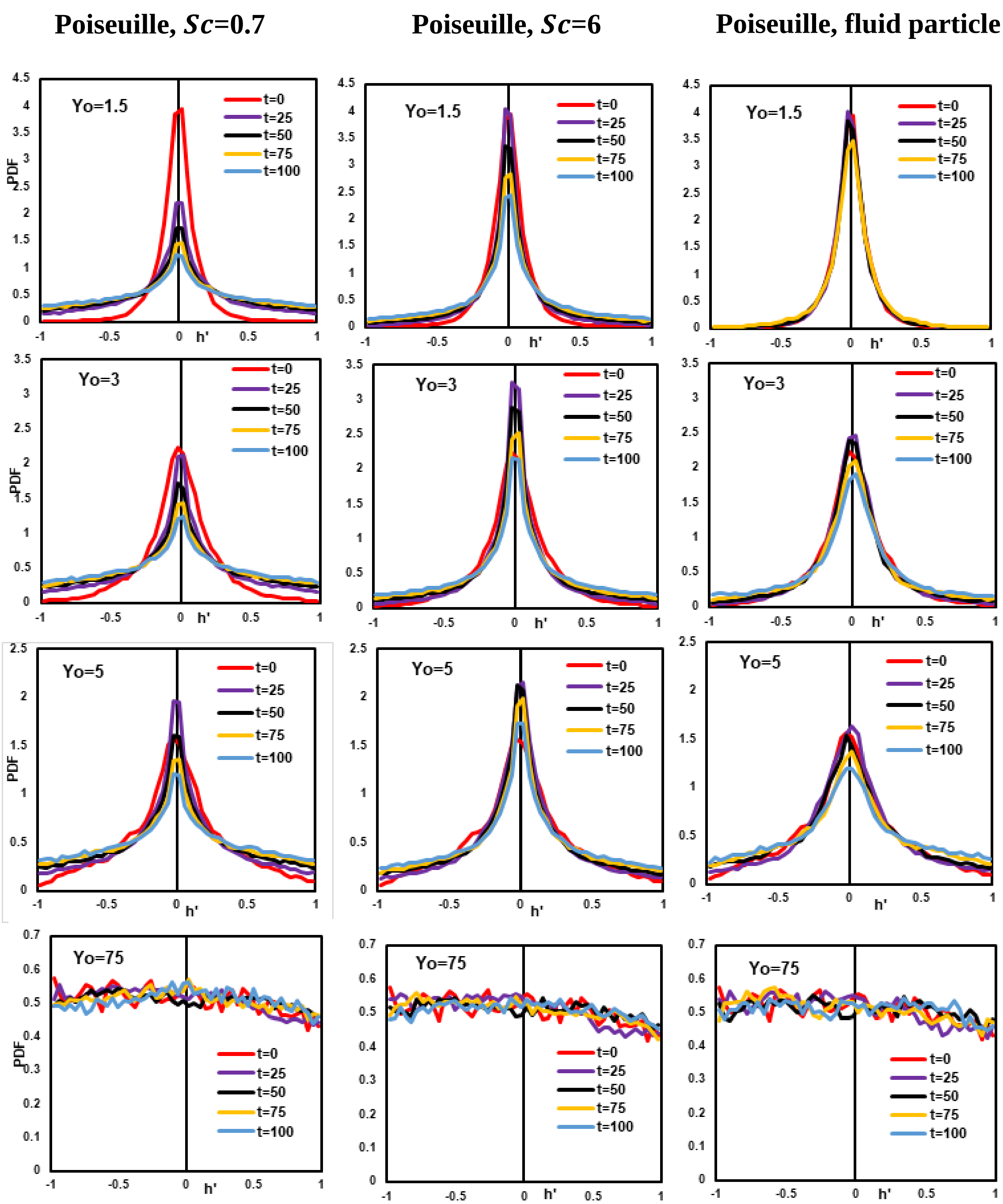


Figure 5.9 The distribution of relative helicity density $h' = cos\theta'$ at various times for a release position at $Y_0$ = 1.5, 3, 5, 75 of Poiseuille flow with Sc = 0.7, 6, and fluid particles. Columns correspond to Sc and rows to positions of release.

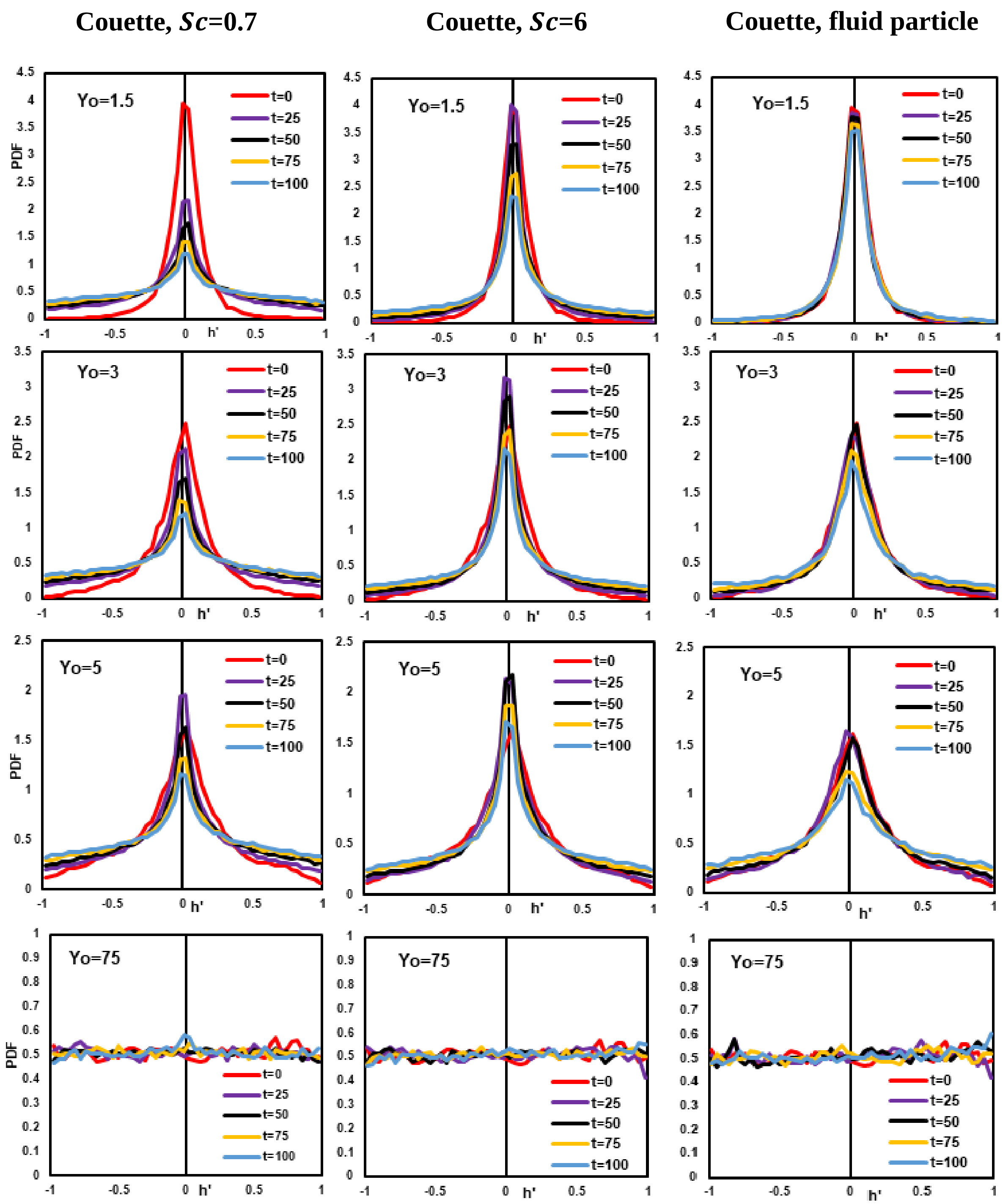


Figure 5.10 The distribution of relative fluctuating helicity density $h' = cos\theta'$ at various times for release position Yo = 1.5, 3, 5, 75 for Couette flow with Sc = 0.7, 6, and fluid particles. Columns correspond to Sc and rows to positions of release.

Figure 5.9 and Figure 5.10 show the distribution of $h'$ at various times for different release positions and *Sc* for Poiseuille and Couette flow, respectively. For both Couette and Poiseuille flows, it can be seen that at $Y_o$ =1.5, 3 and 5, at t=0 the PDF is narrow around low helicity value and then it widens as time advanced. Moreover, the *Sc* = 0.7 case showed the most dramatic decrease in the intensity of the PDF peaks with time, the *Sc* = 6 exhibited the same trend but with less pronounced peaks. The profiles of the PDF for fluid particles did not change much with time. This can be explained by considering the Brownian motion of particles at low *Sc.* These particles have large Brownian motion and could disperse faster to regions farther from the wall. For $Y_o$ =75, the distribution of helicity is flat and does not change with time or *Sc*. Therefore, it can be concluded that farther from the wall, the values of normalized fluctuating helicity were larger, and the velocity and vorticity vectors were more aligned to each other rather than being perpendicular to each other.

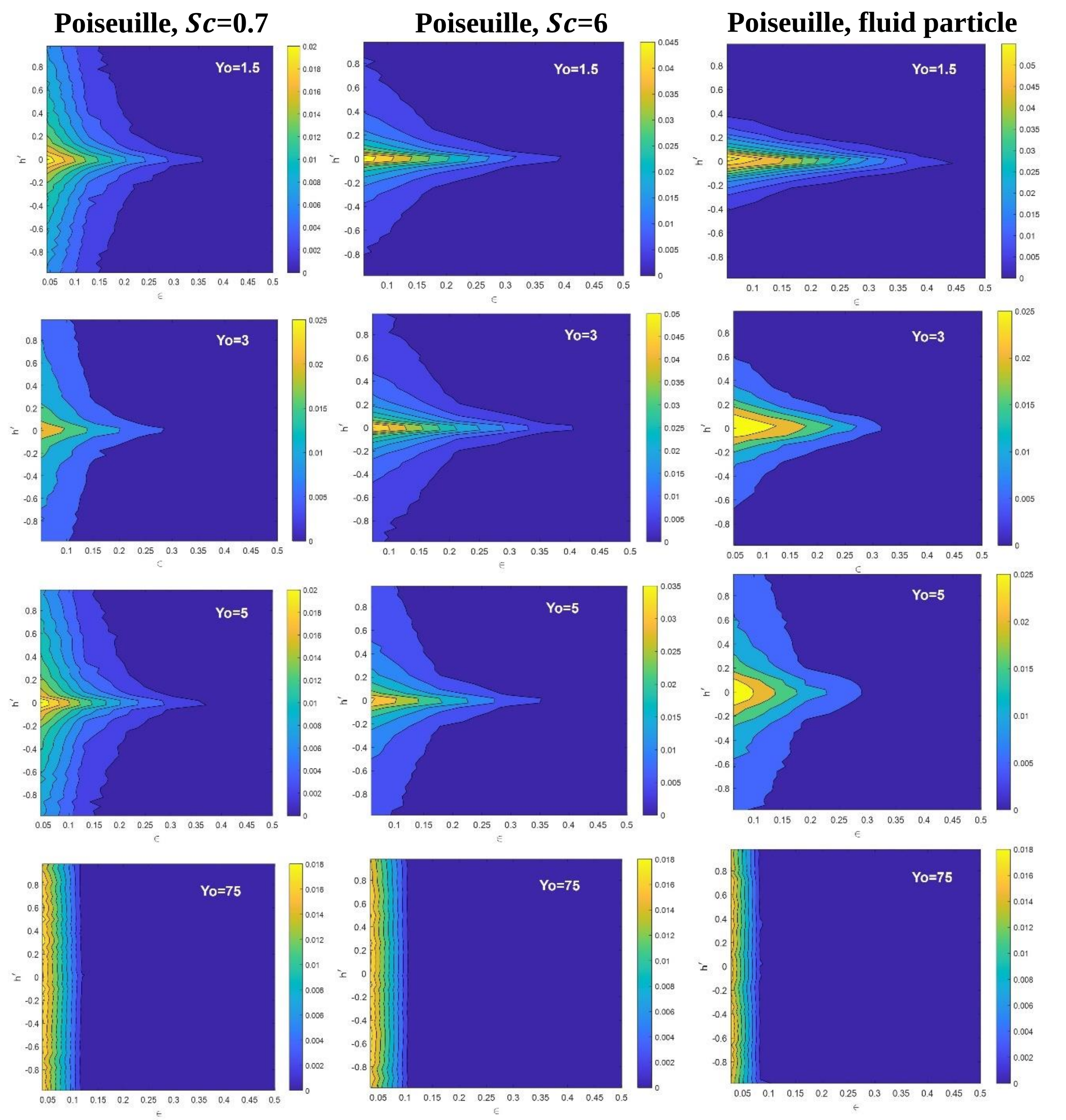


Figure 5.11 Joint PDF of relative helicity density $h' = cos\theta'$ and fluctuating dissipation for all particle of Poiseuille flow for different $Sc$ numbers at time $t^+$=100.

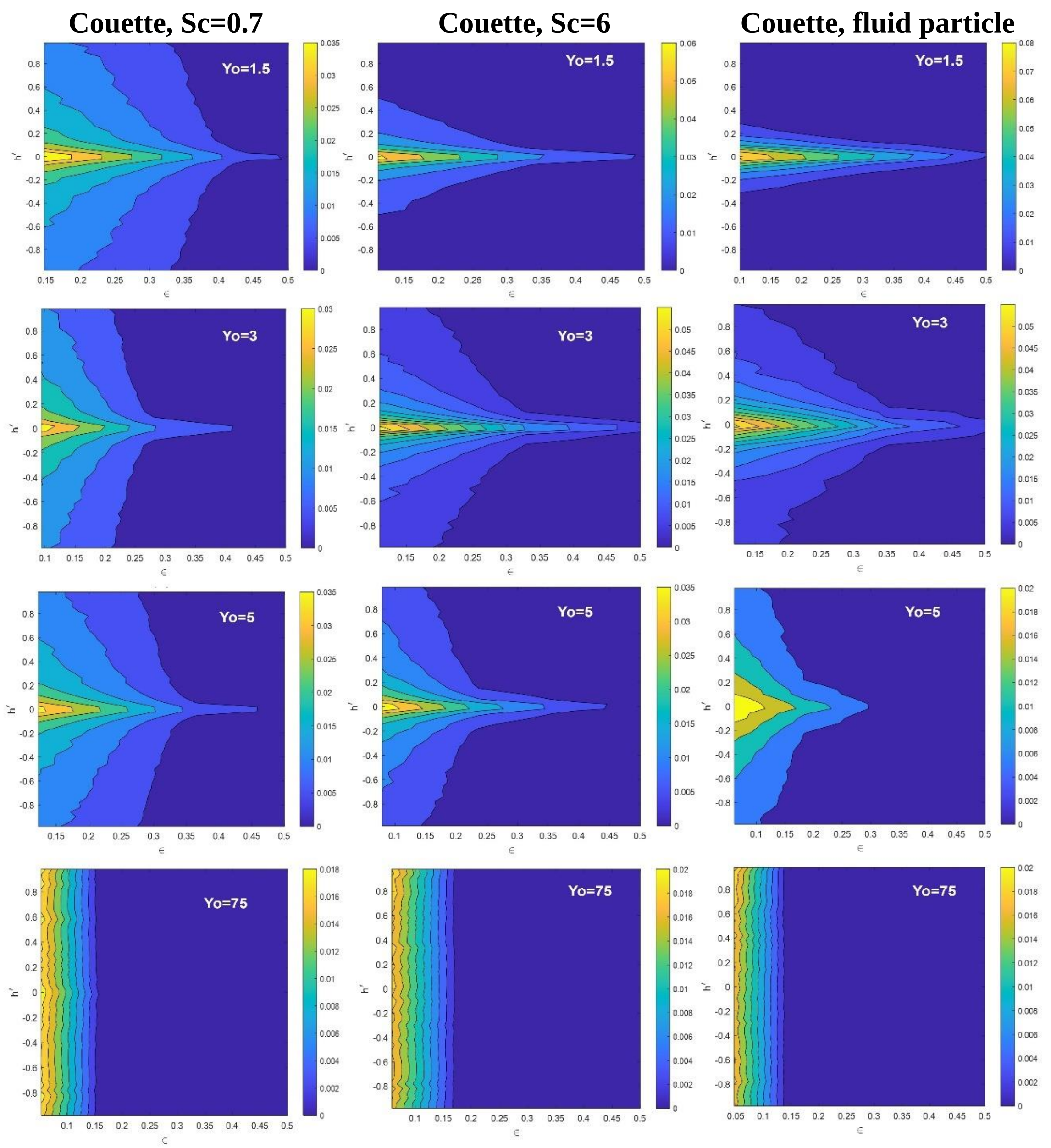


Figure 5.12 Joint PDF of relative helicity density $h' = cos\theta'$ and fluctuating dissipation for all particle of Couette flow for different $Sc$ numbers at time $t^{+}$=100.

The joint PDF between the relative helicity density and the dissipation for Poiseuille flow and Couette flow at $Sc$ = 0.7, 6 and fluid particles is shown in Figure 5.11 and Figure 5.12, respectively. At the release position $Y_0$ =1.5, the case for fluid particles has the narrowest range of distribution of $h'$ from -0.4 to 0.4 for Poiseuille flow and -0.3 to 0.3 for Couette flow, while $Sc$ = 6 has the wider range from -0.8 to 0.8 for Poiseuille flow and -0.7 to 0.7 for Couette flow. For $Sc$

= 0.7 the values are in range of -1 to 1 for both types of flow. Farther from the wall, the distribution of $h'$ is wider, from -1 to 1. From $Y_0$ =1.5 to $Y_0$ =5 the probability of particles that are in locations where the fluctuating velocity and vorticity vectors are perpendicular is high. However, this value is evenly distributed from -1 to 1 for a scalar release position within the log layer region. More importantly, from these patterns, it is seen that the low $h'$ does not necessarily associate with high dissipation and vice versa. These results are in agreement with Rogers et al. [151] that there is no obvious relation between helicity of the fluctuating velocity field and the dissipation of TKE.

## 5.3 Conclusions

In this study, the relative helicity and the dissipation of turbulent kinetic along passive particle trajectories were tracked in a Poiseuille channel and a plane Couette flow using direct numerical simulation and Lagrangian scalar tracking. The changes of helicity and dissipation were monitored along the trajectories of scalar markers as a function of time. The autocorrelation of fluctuating relative helicity density and the Pearson cross-correlation between helicity and dissipation were computed. The autocorrelation of $h'$ decrease from 1 to zeros after 20 time units for release position close to the wall meanwhile the value for release at Y0=75 remain larger than zero. The joint PDF between relative helicity density and dissipation was also presented.

It is found that there is no positive correlation between helicity and dissipation, and flow regions with low dissipation do not necessarily indicate regions of high helicity. This result is in agreement to the previous study of Rogers and Moin [151] and the theory of Speziale [253]. In fact, an anticorrelation between helicity density and dissipation is observed, which is more pronounced in the viscous sublayer and becomes very weak in the logarithmic layer. In low dissipation regions, the distribution of the helicity density is more uniform than in high dissipation, indicating that a more random alignment between fluctuating velocity and vorticity vectors. On the other hand, both the position of release of the particles and the *Sc* number have noticeable effects on the helicity experienced by a passive particle. The type of flow, whether it is Couette or Poiseuille, does not appear to play a significant role.

Regarding turbulent transport, there appears to be an effect of helicity, but not because of an association of helical flow structures to low TKE dissipation. The Lagrangian time scale for helicity density is longer than the Lagrangian time scale for velocity, showing that the alignment of the vorticity and velocity vectors relative to each other is important for long times. The particles that disperse less over the simulation period are those that exhibit a strong anticorrelation between the helicity density and dissipation, while the helicity autocorrelation coefficient is positive and larger than for particles that disperse the most. For Couette flow, the largest time scale had values between 30 to 45 viscous time units, meanwhile that of Poiseuille flow was higher, in the range of 45-55. In this respect, helicity can be an indicator of low turbulent dispersion. The PDFs of the helicity density indicate that as particles transport away from the channel walls, they tend to follow flow structures where the vorticity and velocity vectors tend to align with each other, rather than staying perpendicular to each other. The relationship between helicity and turbulent scalar transport needs further evaluation in the future.

# CHAPTER 6: THE ROLE OF HELICITY IN TURBULENT TRANSPORT AND COHERENT STRUCTURES.

## 6.1 Methodology and Parameters

The data generated by DNS and LST could allow the investigation of various major issues in turbulent transport for example the transport of scalar dissipation [240, 241] and the role of dynamics of vortex tubes in scalar transport. Our LST provides provides the fluid velocity at each marker location with time. Assuming that during the small time step of the simulation turbulence is "frozen" (*i.e.,* assuming that *Taylor's frozen turbulence hypothesis* [242] holds over 0.1 viscous time units) one can obtain the space and time derivatives of the fluid velocity along marker trajectories, thus generating data for dissipation, vorticity and helicity (the dot product of velocity and vorticity) along these trajectories. A very recent *Science* article [243] showed for the first time that experimental measurements of helicity are possible, opening up opportunities to revisit the role of helicity in turbulence with new investigative tools. "Helicity is of key importance in turbulent thermal convection …. it is vital to understand how helicity inhibits the energy cascade to small scales at which turbulent energy is dissipated as heat," as stated in the *Perspectives* section of the same issue of *Science* [244]. We will use our LST data to calculate the helicity of scalar transporting fluid structures to explore the question of whether scalar transport is promoted due to invariant helicity or not. We can compare the helicity for scalar transport to that for momentum transfer along fluid particle trajectories released at the same location in the channel (note that in our analysis framework fluid particles are LST particles with $Pr \rightarrow \infty$). The data allow calculations of writhe and twist, and the integration of helicity along marker trajectories to explore the invariance of the helicity. Based on prior results that show specific flow structures play different roles in transport with *Pr,* we expect to see that turbulent transport does not occur on invariant helicity structures.

The dimensions of computational box were $16\pi h \times 2h \times 2\pi h$ for Poiseuille flow and $16\pi h \times 2h \times 2\pi h$ for Couette flow in the streamwise x, normal y and spanwise z directions, respectively. The half channel height was $h$ = 300, so that the friction Reynolds number as also $Re_\tau$ = $h$ = 300. The number of grid points was 1024x128x256 for Poiseuille and 1024x256x256 for Couette flow in the x, y and z directions.

As for Couette flow, the walls of the channel moved relative to each other, while there was no mean pressure gradient. Therefore, in Couette flow the code was modified by changing the Dirichlet boundary conditions, so that the streamwise velocity at the wall $U_w$ was $U_w = \pm Gh$ and G was constant (G=0.064). The top wall of the channel moved in the negative x direction and the bottom wall moved in the positive x direction. The Reynolds number defined for Poiseuille flow based on the mean centerline velocity and the half channel height, $Re$=($U_c h/\nu$) and for Couette flow as $Re$=($U_w h/\nu$), was 5,700. The fluid was assumed to be an incompressible Newtonian fluid with constant properties. The time step for the simulation of Poiseuille flow was Δt = 0.1, and for Couette flow it was Δt = 0.05.

The markers were released into the flow after the channel and Couette flow reached stationary state. The simulation cases are for different $Sc$ number $Sc$ = 0.7, 6 and for the case of fluid particles. Markers were released at given distances $Y_o$ from the bottom wall of the computational channel, $Y_o$ =0, 1.5, 3, 5, 10, 15, 75, 300 for both Poiseuille and Couette flow. These release positions represent the channel wall, viscous wall sublayer, the buffer region, the log layer, and the channel center. At each $Y_o$, 100 000 particles were evenly released in 20 lines which uniformly spaced in x direction and spanning the width of channel in z direction, this can contribute to avoiding the bias caused by the initial velocity field. Therefore, the total number of particles was 800000 for both Couette and Poiseuille flow.

***Post Processing***

The data for particle position, velocity, vorticity and the derivative of the fluid velocity at the particle location in three directions were obtained and recorded for every particle in the flow at every time step. To calculate the fluctuating velocity and the derivative of the fluctuating velocity at each time step, the profile of the mean velocity $U$ and the derivative of this velocity d$U$/dy in the Eulerian frame were used to interpolate at each particle and at the corresponding Y position using linear interpolation. Then the fluctuating velocity was calculated by the total velocity minus the mean velocity, and the same was applied for the derivative of the mean velocity. The relative normalized helicity density $h' = cos\theta'$, where $\theta'$ is the angle between the fluctuating velocity and vorticity vectors [162] was calculated as

$$cos\theta' = \frac{\boldsymbol{u}'.\boldsymbol{\omega}'}{(|\boldsymbol{u}'||\boldsymbol{\omega}'|)} \qquad (6-1)$$

$\boldsymbol{u}' = \boldsymbol{u} - \boldsymbol{U}$ and $\boldsymbol{\omega}' = \boldsymbol{\nabla} \times \boldsymbol{u}'$

The statistical analysis was based on calculations of correlation coefficients and joint probability density functions (JPDF) to demonstrate how $h'$ was distributed for all values of v$'$. In this case, to calculate the joint PDF, P(v$', h'$) and P(cos $(\omega_y, z), h'$), a 2D array of bins was generated that represented different values of v$'$ and $h'$. The number of scalar markers that had values within the range of each bin was counted and then the probability was calculated by diving with total number of particles.

## 6.2 Results and Discussion

### 6.2.1 Helicity and verical velocity

In a previous study, we have analyzed subsets of the scalar markers that have positive vertical velocity component, so these that moved far from the wall, and the markers that have negative vertical velocity and move towards the wall to consider their difference in heat or mass transfer.[3] In general, these markers could contribute to the generation of turbulent heat or mass flux – the markers moving toward the wall could transfer mass from the channel center to the wall, while the markers that move away from the wall transfer mass from the bottom channel wall region to the outer region of the flow [10].

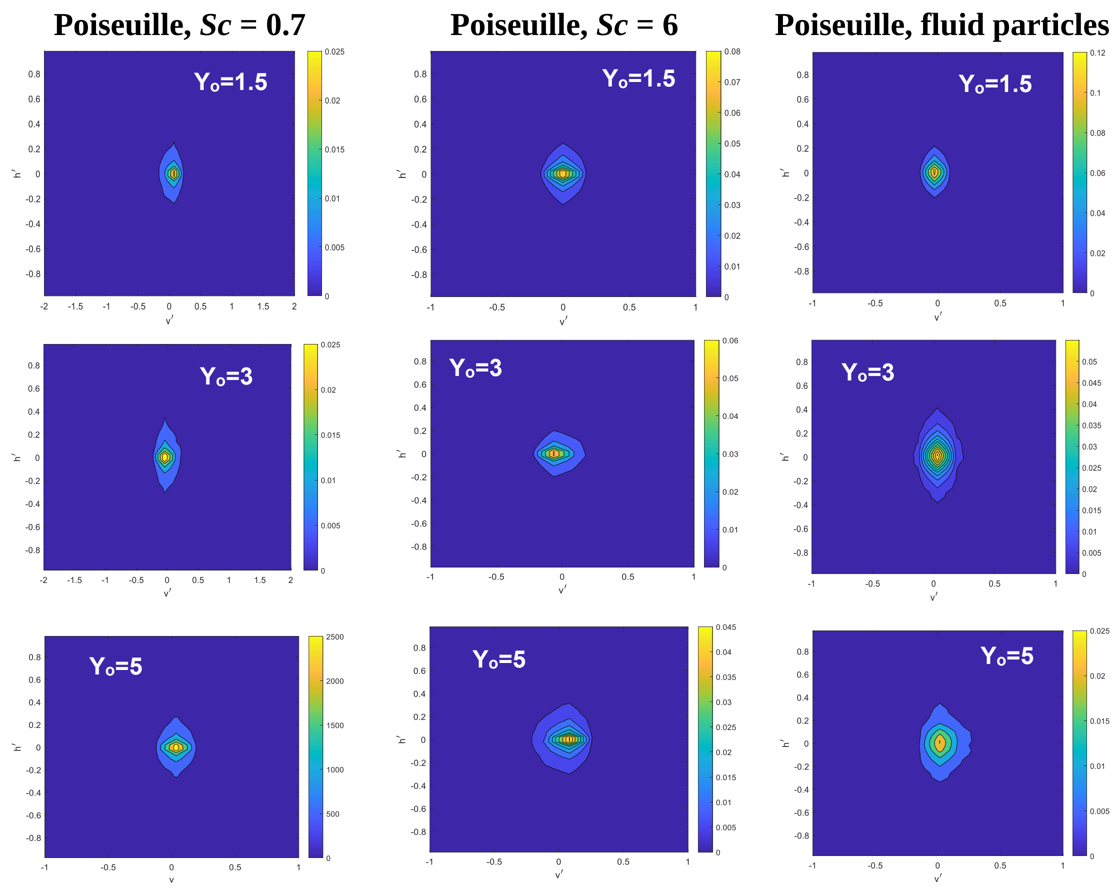


[3] From this point on, in this Chapter we will use mass transfer terminology and the *Sc*, even though all results are applicable for heat transfer expressed by the Prandtl number, *Pr,* of the dispersing scalar markers.

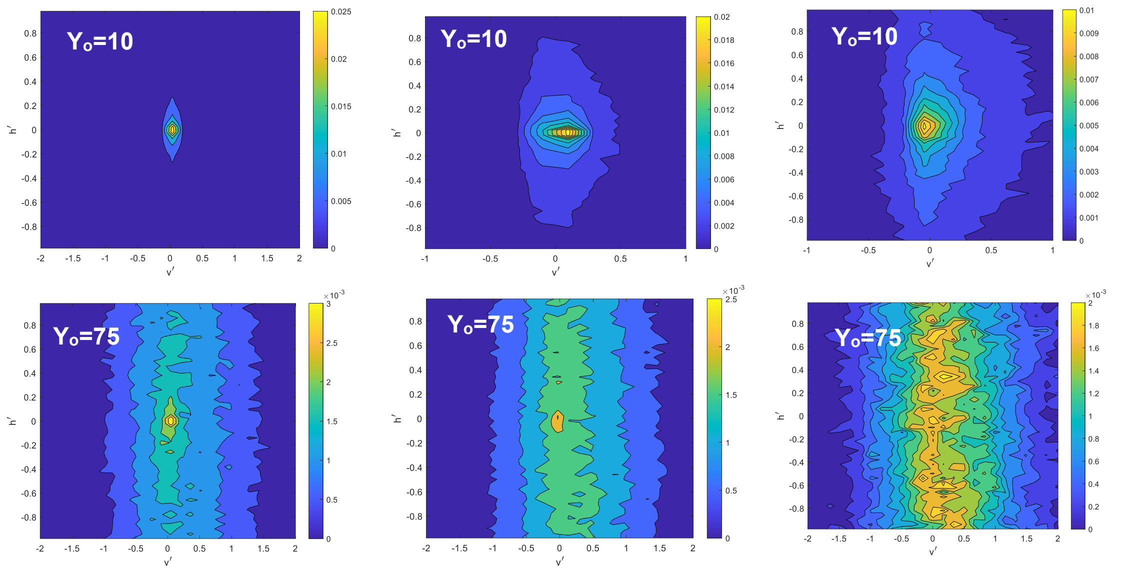


Figure 6.1 JPDF of relative helicity density $h' = cos\theta'\ and$ vertical velocity v′ of all particles, at time $t^+$=100 for Poiseuille flow at *Sc* = 0.7, 6 and fluid particles. Rows correspond to different location of marker release in the y direction, indicated by the value of $Y_0$, shown in the plots, and columns correspond to markers of different *Sc*, as indicated at the top of the figure.

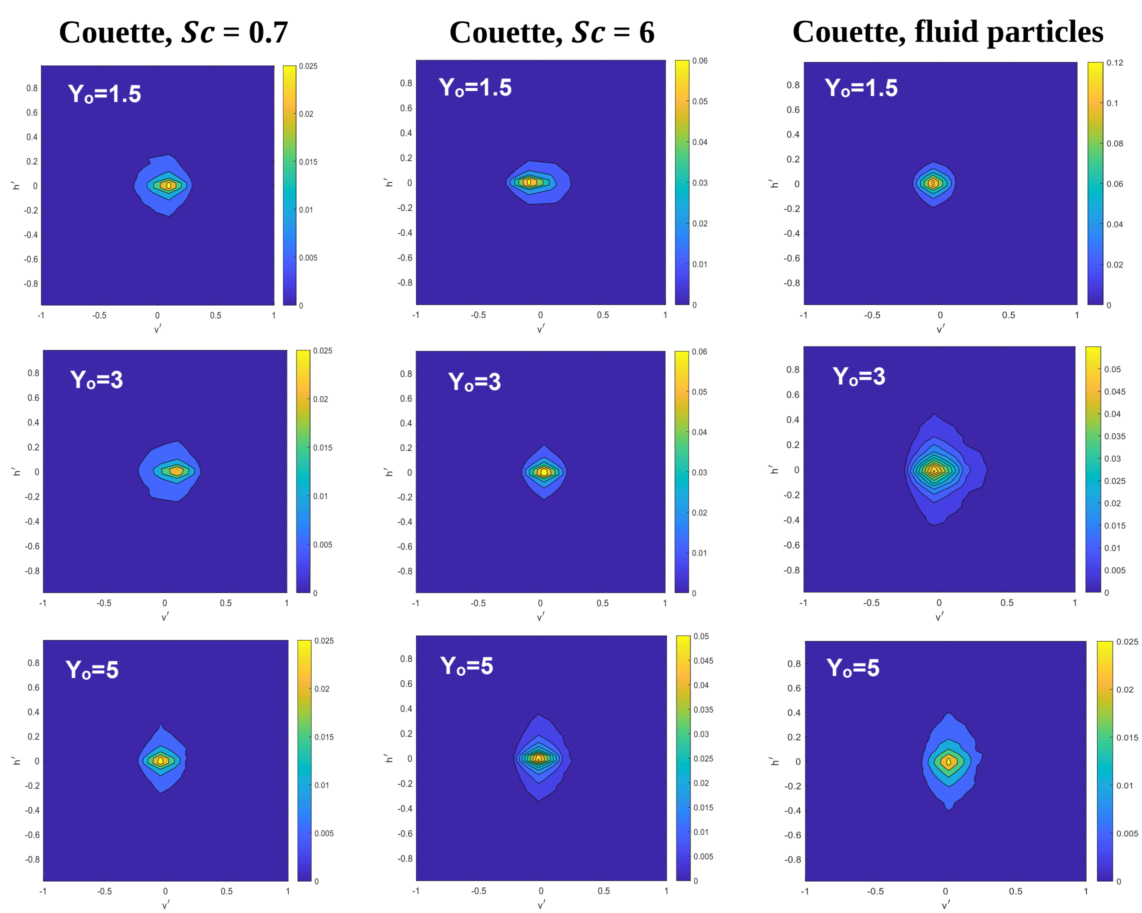

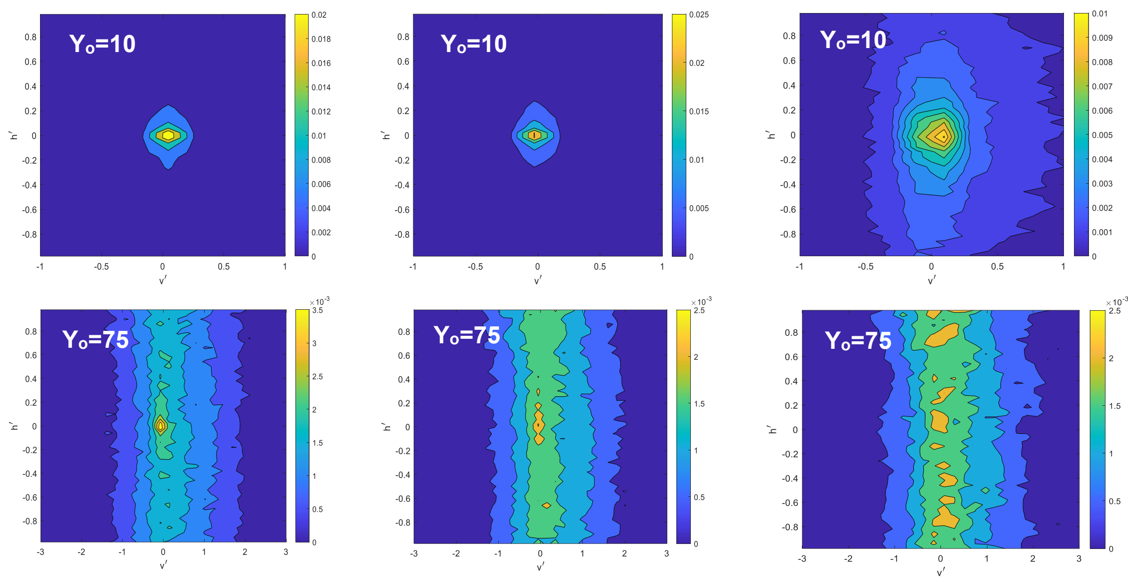


Figure 6.2 JPDF of relative helicity density $h' = cos\theta'$ and vertical velocity v′ of all particles, at time t+=100 for Couette flow at Sc = 0.7, 6 and fluid particles. Rows correspond to different location of marker release in the y direction, indicated by the value of $Y_0$, shown in the plots, and columns correspond to markers of different *Sc*, as indicated at the top of the figure.

Therefore, to investigate the role of helicity in transport in turbulent flow, the correlation between helicity and vertical velocity needs to be considered. The joint PDF (JPDF) between the relative helicity density and vertical fluctuating velocity of all particles that are released at $Y_0$ =1.5, 3, 5, 10, 75 of Poiseuille and Couette flow at *Sc* = 0.7, 6 and fluid particles are shown in Figures 6.1 and 6.2, respectively. As release positions get closer to the wall and inside the viscous wall sublayer, i.e., for $Y_0$ = 1.5, 3 and 5, the values of both $h'$ and v′ is small, this mean that near wall region the fluctuating velocity vector and the fluctuating vorticity vector seem to be perpendicular to each other as the simulation time passes. Further, the value of the vertical velocity is not yet significant to drive the particles away from the wall. However, when the release position is $Y_0$ =10 and 15, the distribution of $h'$ and v′ extended to larger values than that of particles released close to the wall, and the extension is most significant from the position inside the outer region from the log-layer at $Y_0$ =75 to the channel center. In general, the distribution is relatively symmetric, suggesting that particles are equally distributed in the four quadrants of sign of $h'$ and $v'$. From this evidence, it could be concluded that there is a correlation between the vertical velocity and helicity and this correlation is affected by *Sc* number and the various regions of particle release in the flow.

To provide more evidence about the correlation between helicity and vertical velocity, the JPDF of quadrant percentile of particle moving farthest and closest are investigated. Figures 6.3 and 6.4 show the JPDF of $h'$and $v'$ at $t^+$=100 of 25000 particles that have moved the farthest and the closest from the release position $Y_0$ = 3 for Poiseuille and Couette flow at various *Sc* numbers. As for the closest particles, both $h'$ and $v'$ have small magnitude that is less than 0.1 for velocity and 0.2 for helicity density. After released, particles that move the slower have been around the near wall region and in this region the velocity vector and vorticity vector are nearly perpendicular to each other, while for the farthest particles, the distribution of velocity and helicity has been widened and symmetric but there is not particular tendency in the alignment between velocity and vorticity. The large positive $v'$ could drive particles to move farther, and the negative velocity could bring particles back to the wall, but the distribution of $h'$ is uniform from -1 to 1.

**Closest particles**

**Poiseuille, *Sc*=0.7** | **Poiseuille, *Sc*=6** | **Poiseuille, fluid**

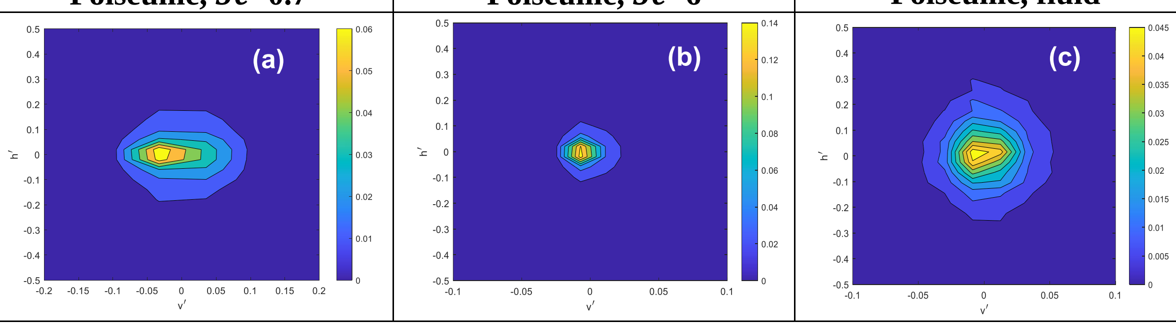


**Farthest particles**

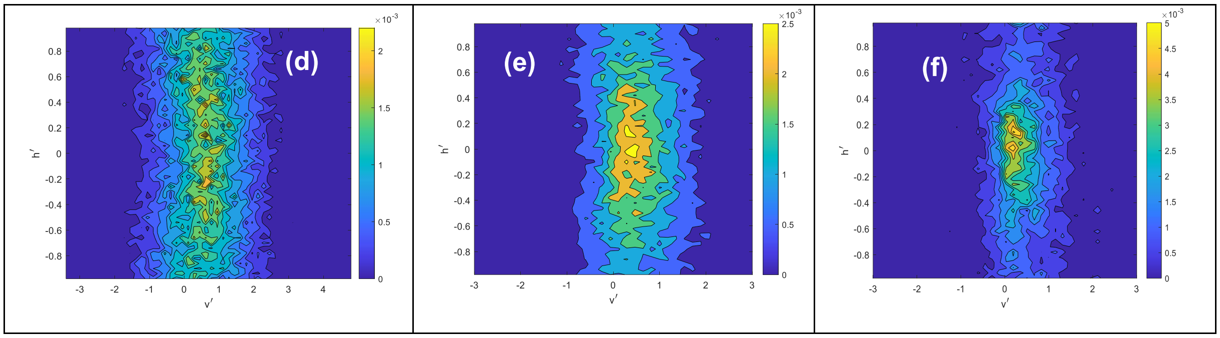


Figure 6.3 JPDF of relative helicity density $h' = cos\ \theta'$ and vertical velocity v′ at $t^+$=100 for only the 25000 particles in Poiseuille flow that are the closest to the channel wall (a) *Sc* = 0.7, (b) *Sc* = 6 and (c) fluid particles and for the 2,500 particles that are the farthest from the wall (d) *Sc* = 0.7, (e) *Sc* = 6 and (f) fluid particles in Poiseuille flow from initial position $Y_0 = 3$.

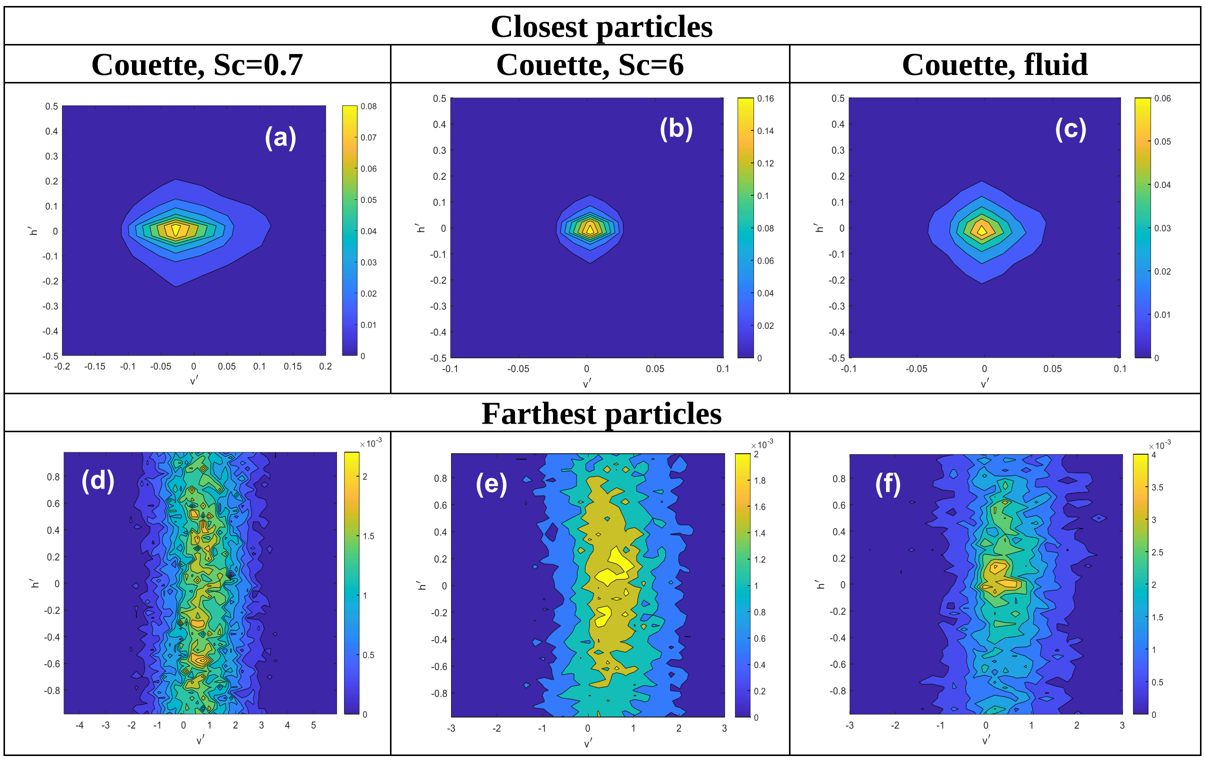


Figure 6.4 JPDF of relative helicity density $h' = cos\ \theta'$ and vertical velocity v′ at $t^+$=100 for only the 25000 particles in Couette flow that are the closest to the channel wall (a) *Sc* = 0.7, (b) *Sc* = 6 and (c) fluid particles and for the 2,500 particles that are the farthest from the wall (d) *Sc* = 0.7, (e) *Sc* = 6 and (f) fluid particles in Poiseuille flow from initial position $Y_0 = 3$.

### 6.2.2 Helicity and vorticity

Apart from investigating the correlation between vertical velocity and helicity, the correlation between helicity and the projection of the vorticity vector on the vertical direction (cosω) is also considered ($w_i$ is the vorticity component in x, y, z directions as indicated by the index $i$)

$$cos\omega = \frac{w_y}{\sqrt{|w_x|^2+|w_y|^2+|w_z|^2}} \tag{6-2}$$

**Poiseuille, $Sc$=0.7** **Poiseuille, $Sc$=6** **Poiseuille, fluid**

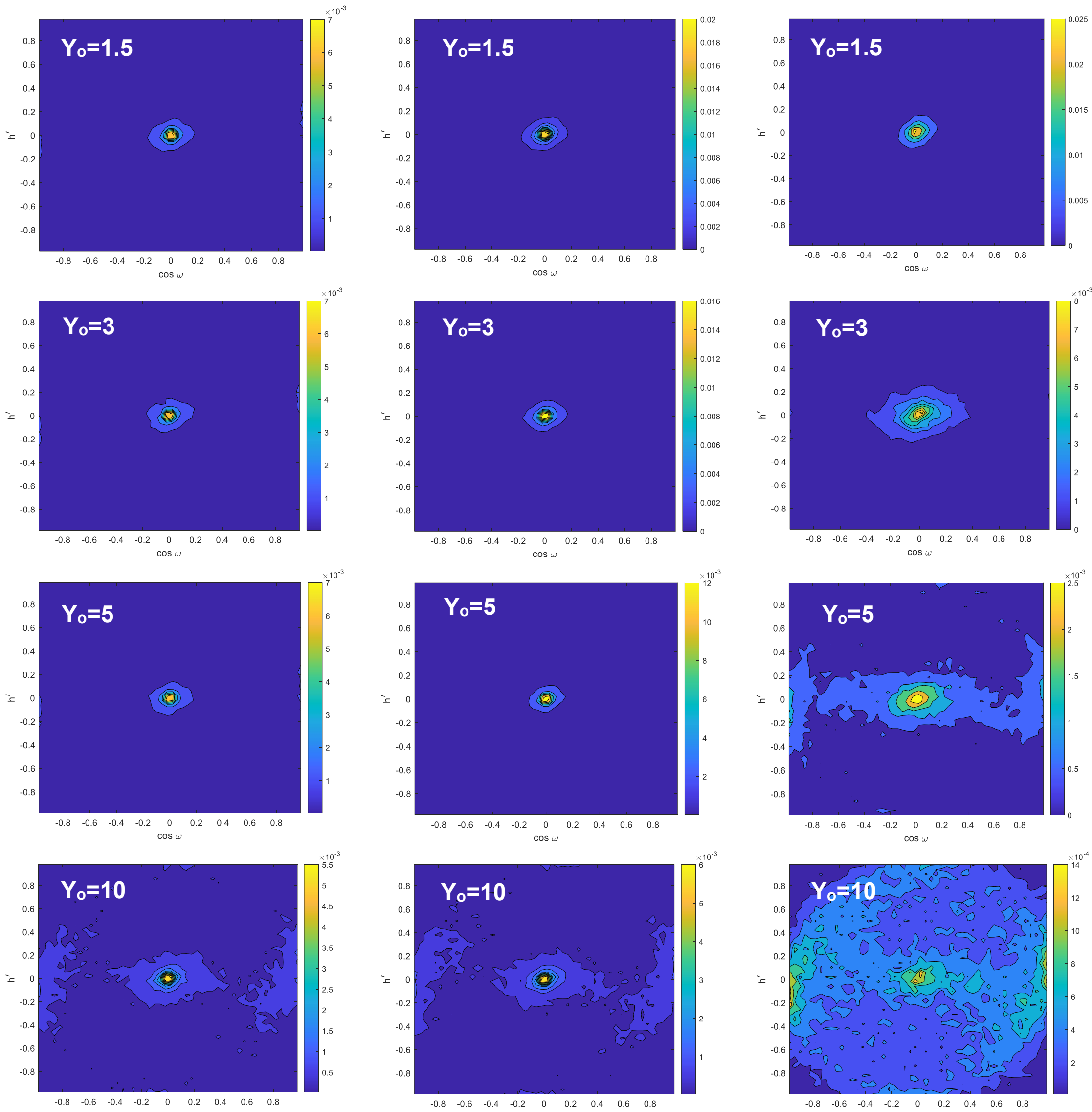

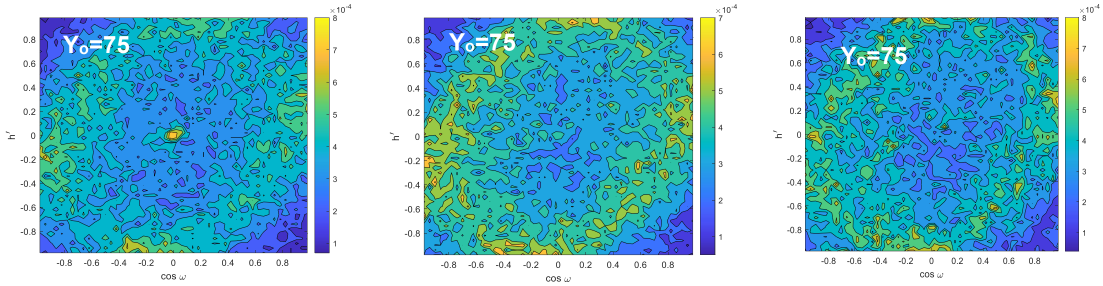


Figure 6.5 the JPDF of relative helicity density $h' = cos\ \theta'$ and the cosine of vorticity in the normal direction cos$\omega$ of all particles and Poiseuille flow at $t^+$=100. Rows correspond to different locations of marker release in the y direction, indicated by the value of $Y_0$, shown in the plots, and columns correspond to markers of different *Sc*, as indicated at the top of the figure.

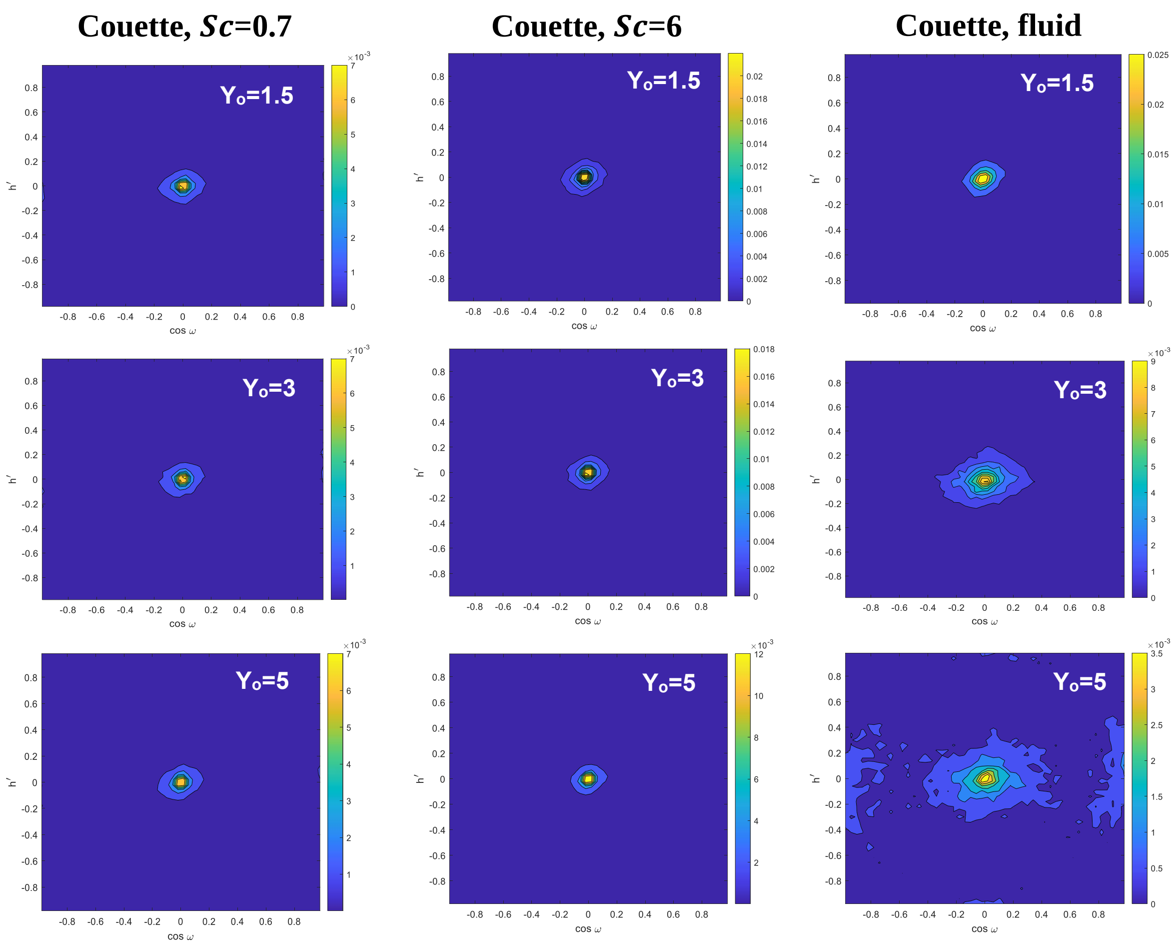

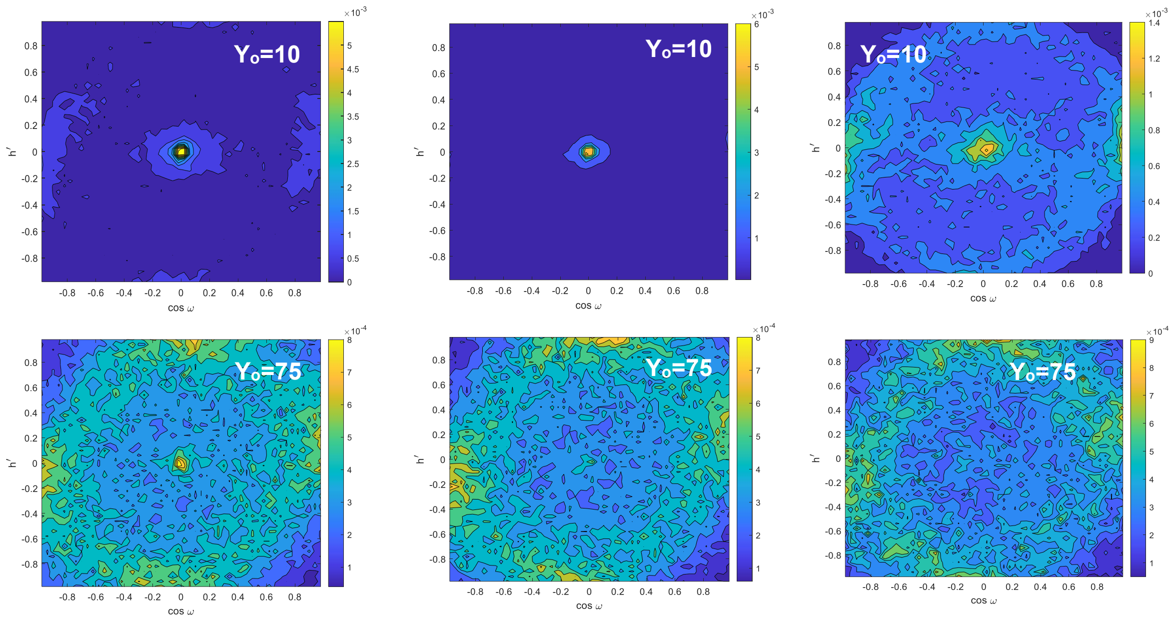


Figure 6.6 the JPDF of relative helicity density $h' = cos\ \theta'$ and cosine of vorticity in the normal direction cos$\omega$ of all particles and Couette flow at $t^+$=100. Rows correspond to different locations of marker release in the y direction, indicated by the value of $Y_0$, shown in the plots, and columns correspond to markers of different *Sc*, as indicated at the top of the figure.

Figures 6.5 and 6.6 present the JPDF of relative helicity density $h' = cos\ \theta'$ and projection of vorticity in z direction of all particles of Poiseuille and Couette flow for *Sc* = 0.7, 6 and the fluid particles. Particles released within the near wall region show a distribution of $cos\ \theta'$ and cos$\omega$ just in a small range between -0.2 and 0.2. The small values of cos$\omega$ and $cos\ \theta'$ indicated that the vorticity is perpendicular to the vertical axis of the channel and is also perpendicular to the velocity vector, indicating that the fluctuating velocity vector of markers released in the near wall region tends to align with the direction that is normal the wall. This means that while in the near wall region the flow vortices tend to move along streamwise or spanwise direction, the particles would displace along the vertical direction. The shape of distribution is symmetric and nearly like a circle. Farther from the wall, the distribution extended for both $cos\ \theta'$ and cos$\omega$ and the fluid particles witness the farthest extension.

For release within the log-layer region and channel center (not shown here), the distribution looks more uniform and there is no certain shape for the joint PDF. Once more, this is evidence that the distribution profiles of $h'$ change with the change of position of particle release and of the *Sc*, but the flow configuration (Poiseuille or Couette) does not have a significant effect on this. The relative helicity density and the alignment of vorticity with vertical direction just have correlation in the near wall regions.

### 6.2.3 Helicity distribution conditioned on Reynold stress quadrants

Quadrant analysis of the Reynold shear stress is employed for the identification of coherent structures, and to separate ejection from sweep events. The ejection and sweep events are coherent vortical structures that are generated in the near wall region and extend towards the logarithmic layer [254]. These structures extend to the edge of the logarithmic region and become scarce at the center of the channel for Poiseuille flow [168]. For Couette flow they can extend farther out, since the Couette flow channel exhibits a log layer that extends from one wall to the other, across the channel center. Turbulent events associated with each quadrant are called outward interactions (Q1, u'>0 and v'>0), ejections (Q2, u'<0 and v'>0), downward interactions (Q3, u'<0 and v'<0) and sweeps (Q4, u'>0 and v'<0) [255]. The forward dispersion in time through the viscous sub-layer (i.e., dispersion from a point towards other regions of the turbulent flow) has behavior associated with transport due to quadrant 2 (Q2) or quadrant 4 (Q4) flow events. For backwards dispersion in time (i.e., when one examines where particles were before arriving at a specific location in the turbulent flow field), the markers seem to be carried towards the viscous sub-layer by quadrant 1 (Q1) or quadrant 3(Q3) events at large times and by Q2/Q4 events at small times. Kahler showed that the probability of finding high momentum fluid moving towards the wall (Q4-sweep events) is quite high when compared to high-speed fluid moving away from the wall, and the largest flow angles are often associated with Q2 and Q4 events [256].

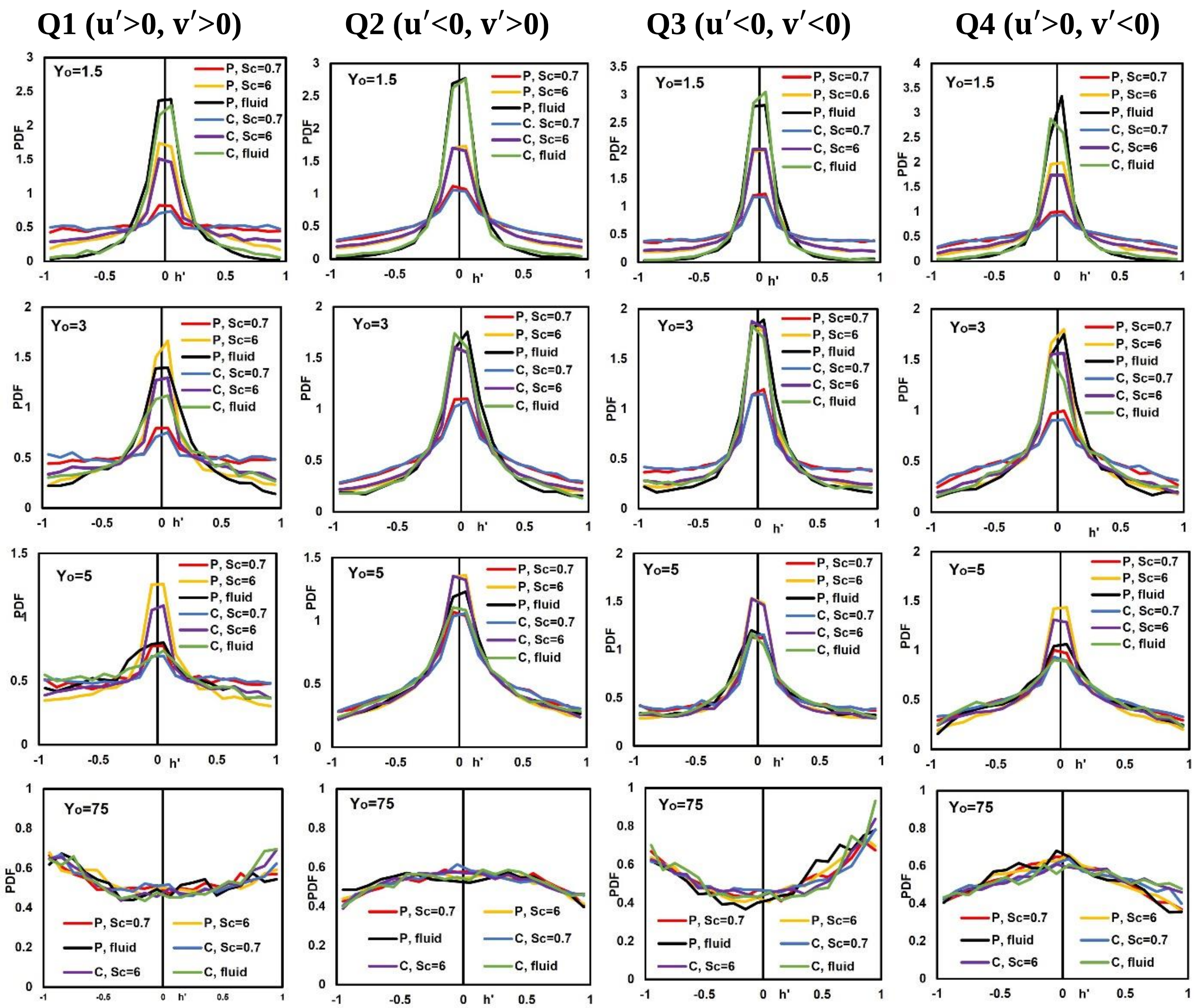


Figure 6.7 Conditional distribution of relative helicity density $h' = cos\ \theta'$ for particles within each of the 4 quadrants of Reynolds stress (u′v′) at $t^+$=100. Rows correspond to different locations of marker release in the y direction, indicated by the value of $Y_0$, shown in the plots, and columns correspond to markers at different Reynolds stress quadrants at time $t^+$ =100. The type of low, Poiseuille or Couette, is indicated by P or C respectively and the *Sc* is also indicated in the figure legends for each curve.

In this study, the distribution of relative helicity density conditioned on each of the 4 Reynolds stress quadrants for Poiseuille and Couette flow at different *Sc* numbers at time $t^+$=100 is investigated to probe further the relation between helicity and coherent structures in anisotropic turbulent flow. It can be seen from Figure 6.7 that there is no significant difference of distribution of $h'$ across the four quadrants, except for the release position at $Y_0$ = 75. The cosine of velocity and vorticity is mainly distributed close to the value of zero, indicating that the two vectors are perpendicular to each other in the near wall region. The distributions have been more flatness when the releasing position farther from the wall. The highest probability of low value of $h'$ is from the fluid particles and when the *Sc* number decreases, the peaks appear to widen. This means that distribution of $h'$ does not depend on the Reynolds stress quadrant, but it depends on the particle position in the channel and on the molecular diffusivity of the particles. At release position at $Y_0$ = 75, there is the difference between quadrants Q2, Q4 and Q1, Q3. Although the distribution is quite flat in this region, there are more particles in quadrants Q2, Q4 that have values of $h'$ close to zero, while the number of particles that have large $h'$ is more significant in cases of Q1 and Q3. Alignment of vorticity and velocity, indicated by values of $h'$ close to 1 or -1, is taking place along the trajectories of particles in the log layer and beyond. In general, helicity density appears to be independent of the coherent structures determined by quadrant events.

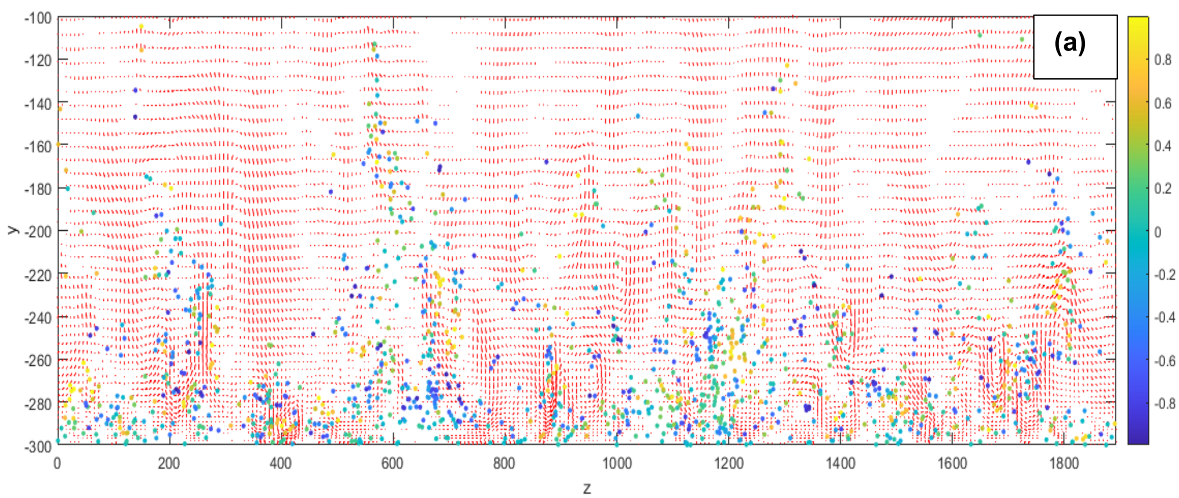

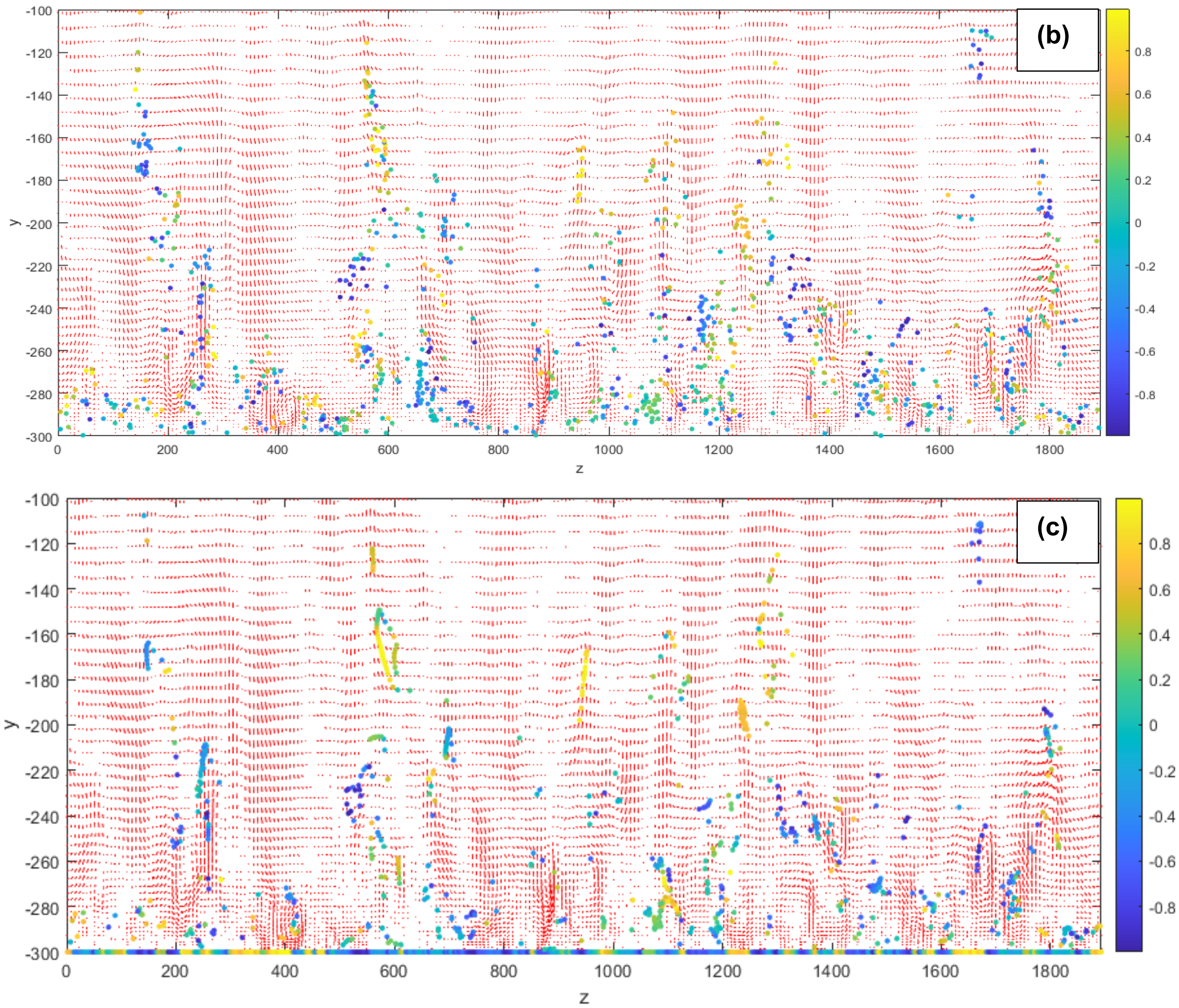


Figure 6.8 The contour plot of velocity field and the particles with their relative helicity density magnitude at yz plane at $254\,\Delta x \le x \le 256\,\Delta x$ time $t=100^{+}$ for Poiseuille flow at various *Sc* numbers (a) *Sc* = 0.7, (b) *Sc* = 6 and (c) fluid particles. The center of the channel is at y = 0 and the bottom wall is at y = -300.

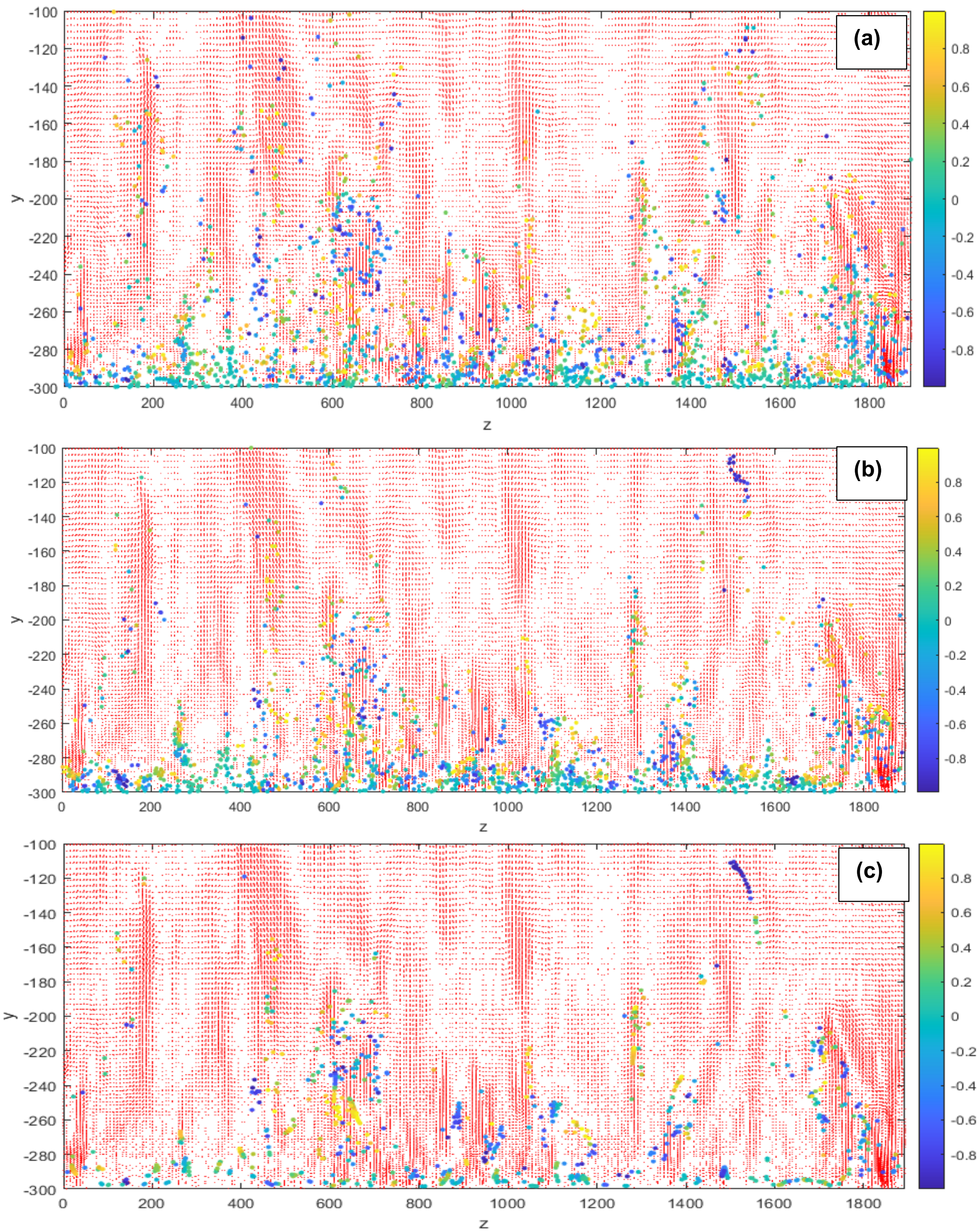


Figure 6.9 Vector plot of velocity field with the particles and their relative helicity density magnitude on a yz plane. The particles shown are for $254\,\Delta x \le x \le 256\,\Delta x$ at time t=100$^+$ for Couette flow at various *Sc* numbers (a) *Sc* = 0.7, (b) *Sc* = 6 and (c) fluid particles. The center of the channel is at y = 0 and the bottom wall is at y = -300.

The fluctuating velocity vector in a typical yz plane of the simulated flow is shown in Figures 6.8 and 6.9. The particle positions are superimposed, colored with the value of $h'$. As can be seen, the particles appear to concentrate at the edges of vortical structures. This is more obvious in the case of *Sc* = 6, while the *Sc* = 0.7 particles disperse more uniformly. More importantly, near the wall region, the color of the particles shows that they reside in locations where the value of $h'$ is around zero, and farther from the wall their color is blue or yellow, which indicates that the value of $h'$ is distributed towards -1 or 1. Around vortices in the near wall region, most particles have green color that corresponds to values near zero.

### 6.2.4 Helicity and Q-criterion

One of the criteria typically used to identify vortices is the Q-criterion that is based on the invariants of the rate of strain tensor and the vorticity tensor. The value of Q is determined as follows [186]:

$$S_{ij} = \frac{1}{2}\left(\frac{\partial u'_i}{\partial x_j} + \frac{\partial u'_j}{\partial x_i}\right) \tag{6-3}$$

$$\Omega_{ij} = \frac{1}{2}\left(\frac{\partial u'_i}{\partial x_j} - \frac{\partial u'_j}{\partial x_i}\right) \tag{6-4}$$

$$Q = \frac{1}{2}(\|\Omega\|^2 - \|S\|^2) \tag{6-5}$$

where $S_{ij}$ is the ij component of the rate of strain tensor and $\Omega_{ij}$ is the ij component of the vorticity tensor. The use of the Q value is suitable for the identification of vortices, since a value of Q > 0 indicates that rotation overcomes strain, ensuring the existence of a vortex structure that is protected from deformation [181].

Herein, the Lagrangian autocorrelation coefficient for Q is calculated for particles released at different distances from the channel wall. This coefficient, along the trajectories of particles, can be used to determine the time scales associated with particle transport in vortical structures and compare it to the time scales in the rest of the fluid. The Lagrangian autocorrelation is calculated as follows [211]:

$$R_{Q-Q(t)} = \frac{\overline{Q(t_0)Q(t_0+t)}}{\overline{Q(t_0)^2}^{1/2}\overline{Q(t_0+t)^2}^{1/2}} \tag{6-6}$$

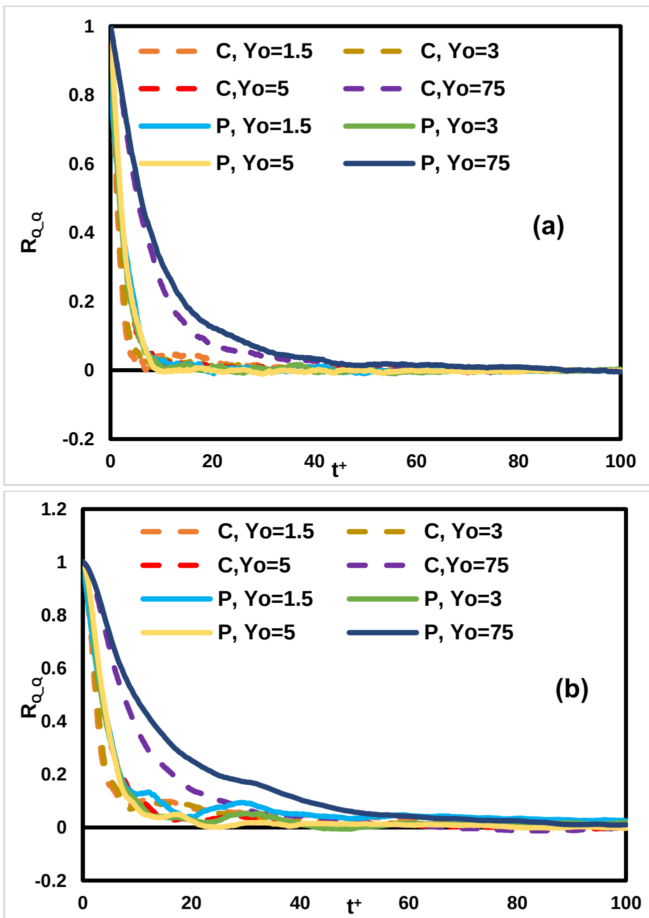

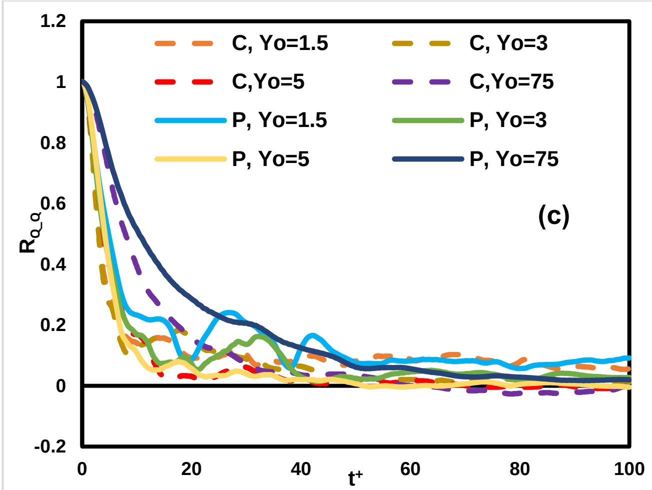


Figure 6.10 The autocorrelation coefficient for the Q values as a function of time for Poiseuille and Couette flow (indicated as P and C on the legend) at various *Sc* numbers and for different positions of particle release (a) *Sc* = 0.7, (b) *Sc* = 6, (c) fluid particles.

Figure 6.10 is a presentation of the autocorrelation for the Q values in Poiseuille and Couette flow at various *Sc* numbers and particle release positions. The correlation coefficients remain larger than zero in the case of fluid particles and the values are around 0.1 at $t^+$=100. The values of the correlation coefficient for Poiseuille flow are greater than those for Couette flow. Father from the wall, the correlation decreases at a lower rate, as seen for particle release at $Y_0$ = 75. The correlation values decrease dramatically from initial time to $t^+$=10 for the case of *Sc* = 0.7 and to $t^+$=20 for *Sc* = 6 and fluid particles. The larger molecular dispersion for low Sc is the reason for this observation – the particles jump away from convective flow structures and disperse faster, forgetting the structure at which they were released at time zero. Note that the value of the correlation coefficient approaches zero for *Sc* = 0.7 at time $t^+$=100. The fluid particles exhibit the longest correlation with time. Therefore, the Q values are correlated longer for Poiseuille flow and for larger Sc numbers.

While the results appearing on Figure 6.10 provide general information for all particles, showing that low *Sc* results in enhanced transfer, Figure 6.11 is focused on discriminating between the particles that disperse the most compared to the particles that disperse the least. To probe differences in the flow structures that move particles away from the wall, the correlation of Q values for the particles that are found the farther away and those that are found the closer to their release location at $Y_0$ = 3 are shown in Figure 6.11. In general, the correlation coefficient values are larger than zero, and the correlation profile looks more stable for the particles that do not disperse far in the y direction. As expected, the particles of Poiseuille and Couette flow at *Sc* = 0.7 have the fastest decrease in the correlation coefficient value, followed by the *Sc* = 6 and the fluid particles. The fluid particles present some periodicity in the values of the correlation both in Couette and Poiseuille flow. More importantly, it can be concluded that the particles that have the least dispersion for the same *Sc* are those that have the longer correlation of the Q criterion values. This is because they remain within flow structures that are still in the near wall region, where coherent structures dominate, while the particles that disperse the most leave these coherent structures and move farther from the wall.

**Quartile of particles the closest to wall**

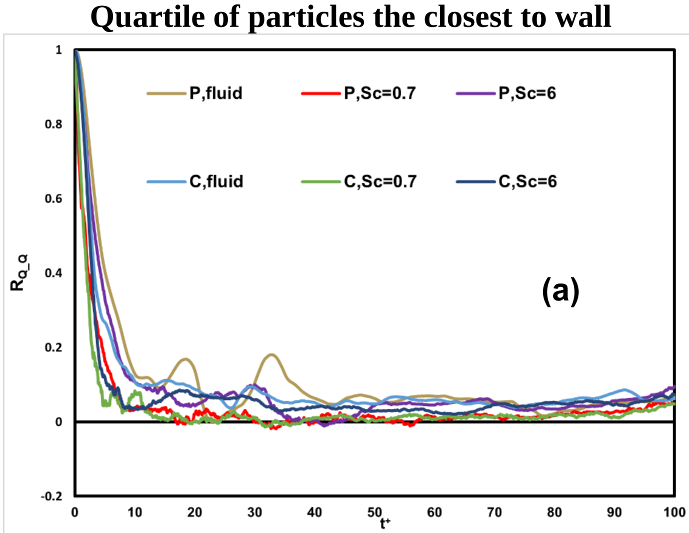


**Quartile of particles the farthest from wall**

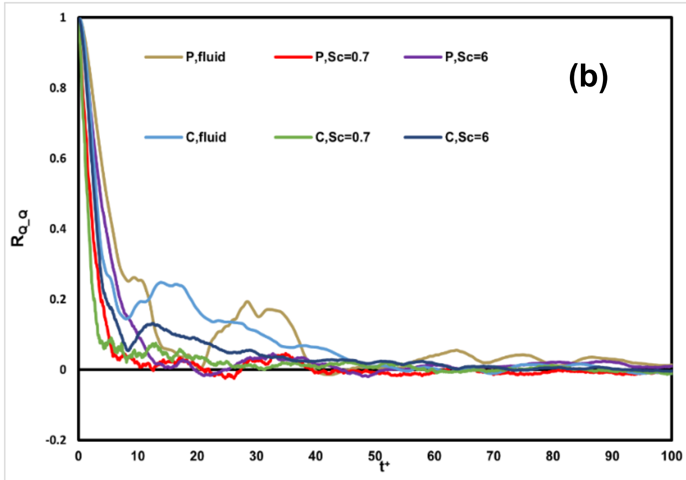


Figure 6.11 The correlation of Q values with time for particles conditional on their location relative to the wall at time $t^+ = 100$: (a) The 25% of all particles that are closer to the wall, (b) 25% of particles that are the farthest from their initial position at $Y_0 = 3$ for Poiseuille and Couette flow and for various *Sc* numbers.

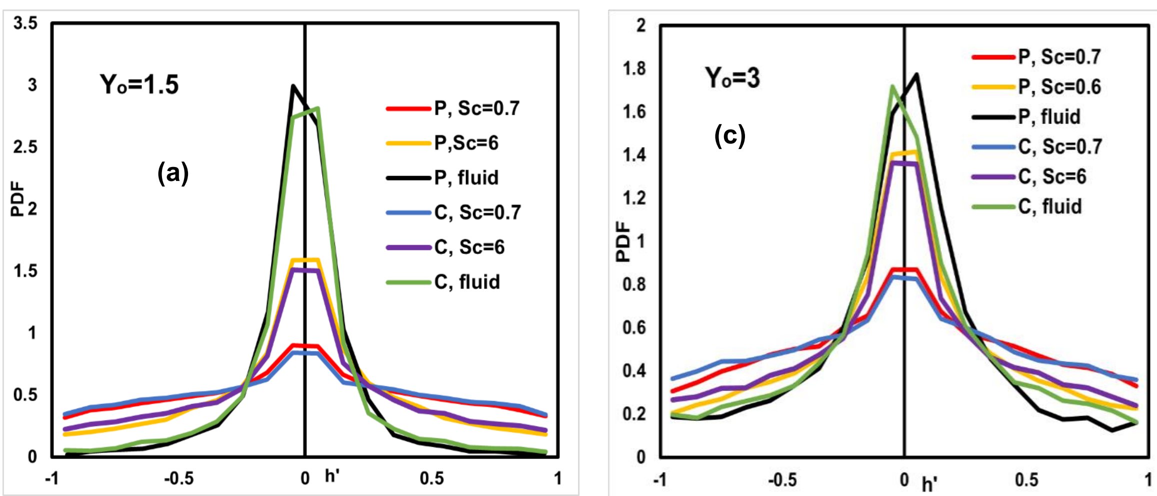

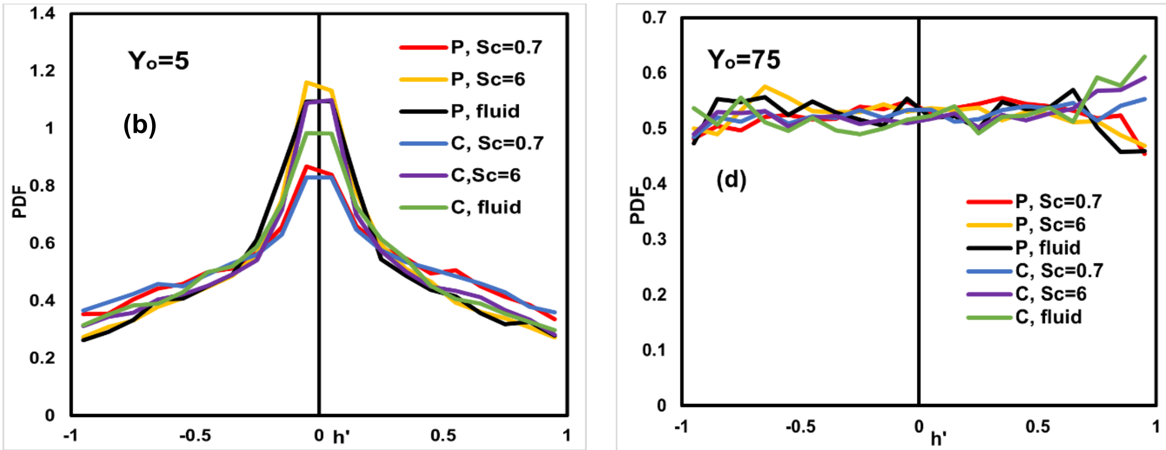


Figure 6.12 The distribution of relative helicity density $h'$ conditioned for Q > 0 for Poiseuille and Couette flow at various *Sc* numbers and for release positions (a) $Y_0$ = 1.5, (b) $Y_0$ = 3, (c) $Y_0$ = 5, (d) $Y_0$ = 75 at time $t^+$=100.

The distribution of relative helicity density conditioned on Q > 0 is analyzed at different release positions and *Sc* numbers. In general, the distribution of $h'$ varies with the change of *Sc* numbers and position of release particles. The fluid particles have the highest probability of zero value of $h'$ at the release position $Y_0$ = 1.5 and then the peak decreases gradually with the distance from the wall. Following this, the particles with *Sc* = 6 exhibit similar trends, as do fluid particles. The case of *Sc* = 0.7 also witnesses the change with the position of release but the distribution is flatter in comparison to the distributions for *Sc* = 6 and fluid particles. On the other hand, the distribution of $h'$ is almost a uniform distribution at $Y_0$ = 75, which means that there is no representative characteristic of helicity in this region despite the fact that the particles are within vortex regions (Q>0). Once again, there appears to be no clear correlation between the values of helicity density and the vortex structure. The alignment of vorticity and velocity vector, expressed by the helicity density, depends mainly on the regions within which particles disperse. At release positions close to the wall, vorticity and velocity are perpendicular to each other, and as the particles disperse away from the wall the vorticity and velocity tend to become parallel to each other. At the same time, whether helicity could be considered as a factor to mark vortex structures in anisotropic turbulence is questionable.

### 6.2.5 Helicity and eigenvetors of rate of strain tensor

According to Zhang et al., helicity density has been considered as a vortex identifier, however, it is not Galilean invariant, which becomes the main criticism for this approach, since the concept is not applicable for general nonhomogeneous turbulent flows. When analyzing the eigen system associated with a vortex, the rate of strain tensor has been a used because it always produces real eigenvalues and eigenvectors [257, 258]. The rate of strain tensor and its three eigenvalues could be derived from the spatial derivatives of the velocity field. The eigenvalues are ordered in size as $\alpha \geq \beta \geq \gamma$ and have the restriction that they sum to zero for incompressible flow [259]. In three-dimensional incompressible flows, the principal directions consist of one extensive and one compressive direction, and an intermediate direction, which can be either extensive or compressive. Vorticity is preferentially aligned with the intermediate direction, misaligned with the compressive direction and the orientation of the extensive direction [260]. Arhurst et al. studied the probability of vorticity alignment in isotropic flow and showed that vorticity is most likely to point in the $\beta$ direction, and least likely to point in the most compressive direction $\gamma$. The author also investigated the correlation between rate of strain tensor with respect to vorticity and helicity and showed that there is a slight dependence in the shape of relative helicity PDFs when conditioned on $\beta$ [259]. The $\alpha$ component of the rate of strain is always positive and $\gamma$ is always negative, therefore the sign of $\beta$ could determine whether the local structure of turbulence is sheetlike or tubelike. If $\beta > 0$, there are two components of the rate of strain along which the fluid is stretching, and one component along which it is compressed suggesting that the local structure will be sheetlike. Meanwhile, if $\beta < 0$ there will be two compressive components and one stretching component of the rate of strain, which suggests tubelike structures. On the other hand, this study showed that the dissipative structures of turbulence are sheets and when sheetlike structure is strongest, the influence of helicity is even smaller. The sheetlike structure is related to the nonlinear terms responsible for vortex stretching and the cascade of energy to small scales [258]. As described by Arhust et al., there is a correlation between a diffusing scalar and the strain field when studying two-dimensional mixing flows. Fluctuations in strain rate and vorticity couple to produce a stretching vortex filament that conserves angular momentum but increases dissipation [259]. The PDF of the alignment between ω and eigenvectors $e_i$, $\cos(\omega, e_i)$, in Nakamura et al. [261], indicated that the shapes of the PDF do not depend much on time and regions and these shaped PDFs of the alignment have been observed in many turbulent flows. The intermediate vector tends to be parallel to the vorticity vector [261].

In present study, the largest eigenvalue α of the rate of strain tensor, $S_{ij} = \frac{1}{2}(\frac{\partial u_i}{\partial x_j} + \frac{\partial u_j}{\partial x_i})$, corresponds to eigenvector $e_1$ and is related to extension, γ corresponds to eigenvector $e_3$ and is related to compression, and β corresponds to eigenvector $e_2$ and is related to either extension or compression [260-262].

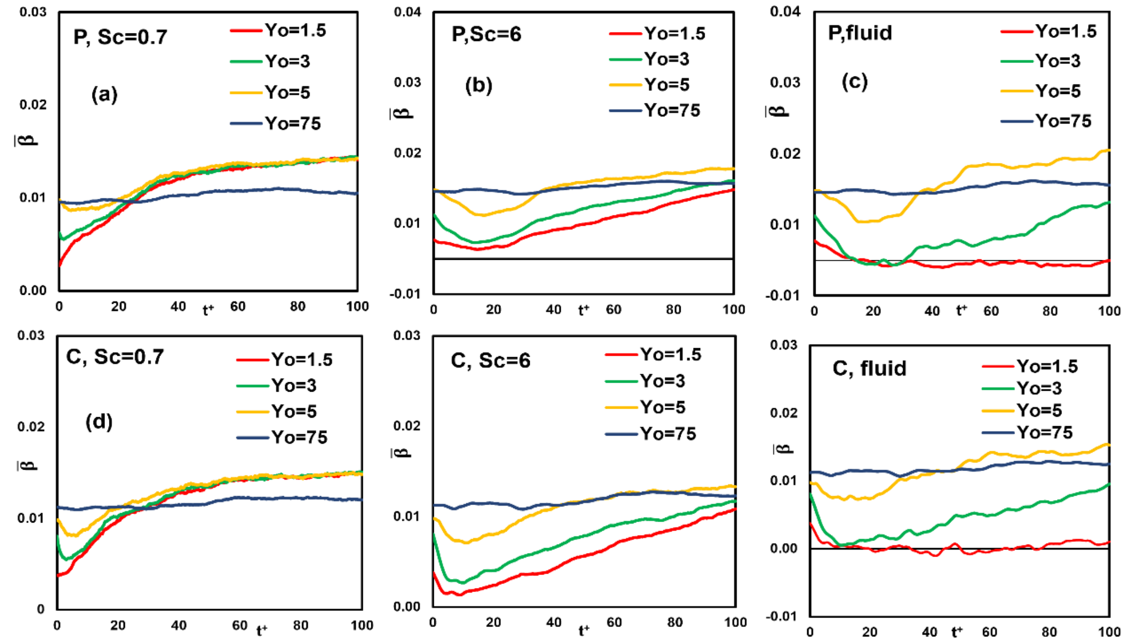


Figure 6.13 The average value of the second largest eigenvalues β of strain rate tensor for Poiseuille and Couette flows at various *Sc* numbers and release positions.

As discussed above, the value of β is directly related to the dissipative structures and, thus, it is important to evaluate the average value of β for passive markers moving in the flow field to understand further the effects of flow in enhancing turbulent transport. As can be seen from Figure 6.13, the average value of β is larger than 0 with time for both Couette and Poiseuille flow. As for the case of fluid particles, the average value of β does not show significant change with time, while at $Sc$ = 0.7 and 6, it increases for particle release in the viscous sublayer, $Y_0$ =1.5, 3, and 5. Particles released at $Y_0$ = 75 the average β values do not seem to change for all cases from the value of β = 0.01. The smallest values are observed when the release position was $Y_0$ =1.5, and these values increase with the distance from the wall at $Y_0$ = 3 and $Y_0$ = 5. The positive β values can be explained based on angular momentum conservation arguments. Arhust et al. used the ice skater who starts to spin as an illustration of this explanation. Indeed, for long times, the vorticity field is stretched out in the direction of the intermediate strain, which is positive and the other two vorticity components go to zero [259].

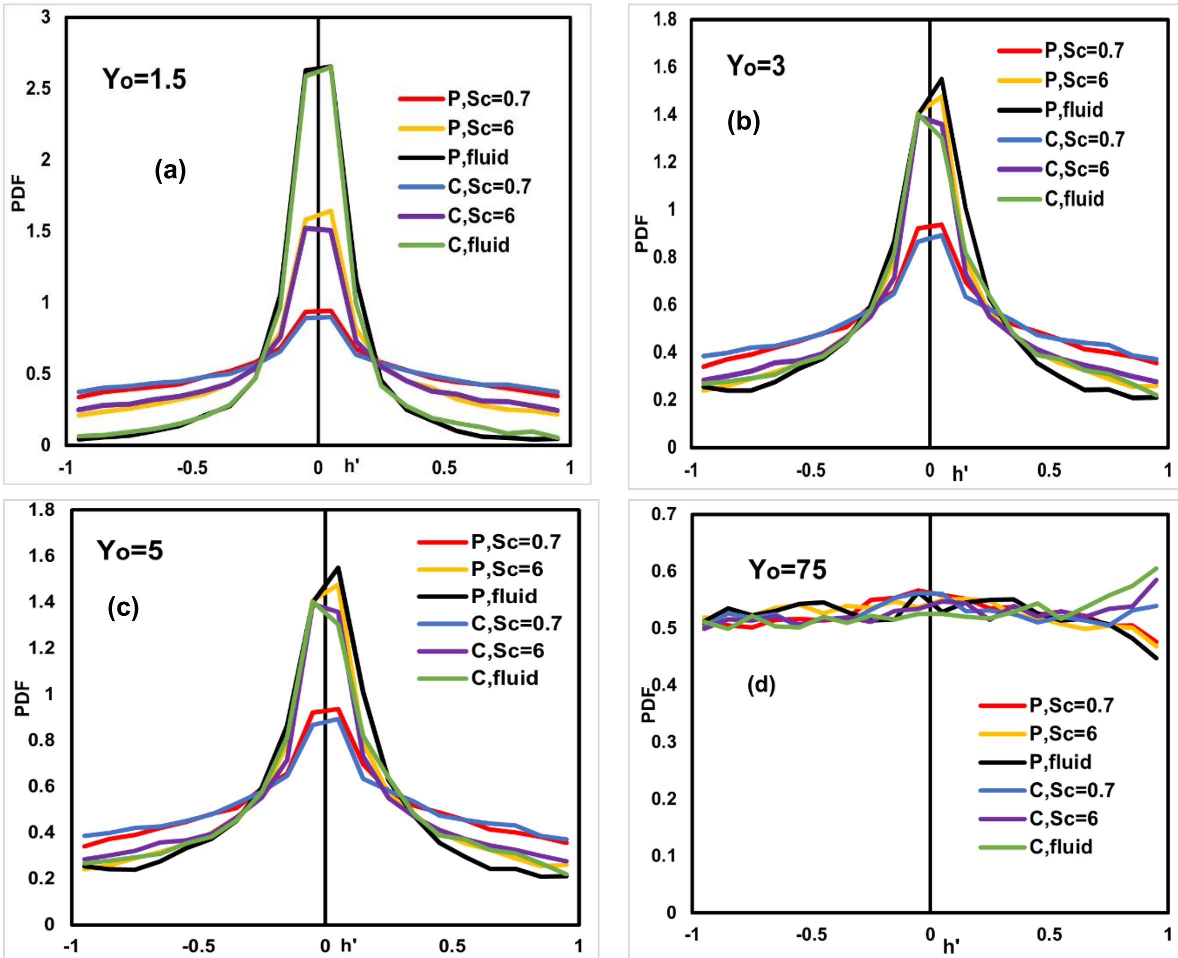


Figure 6.14 Distribution of relative helicity density $h'$ conditioned on $\beta > 0$ at various position of release (a) $Y_0$ =1.5, (b) $Y_0$ =3, (c) $Y_0$ =5 and (d) $Y_0$ =75 and $Sc$ numbers.

While the average of β is positive, as indicated in Figure 6.13, there are negative β values for some of the dispersing particles. Focusing on the distribution of relative helicity conditioned on β > 0, Figure 6.14 was generated. The distribution curves depend on release positions and on $Sc$ numbers, which is a similar result when considering unconditioned distributions and the distributions of $h'$ conditioned on the Q criterion.

As discussed earlier, the β condition, or the Q criterion, or the Reynolds stress quadrants have been used to indicate the existence of coherent structures. The distribution profiles reveal that there is not a distinction between conditioned or unconditioned distribution of relative helicity.

Near to the channel wall, the peak of the PDF for $h'$ is in values around zero, and father from the wall the values of $h'$ start to become more uniform, leading to the flattening (widening) of the PDF peaks. On the other hand, the distribution of $h'$ is affected by *Sc* numbers, the smaller *Sc* numbers contribute to stronger dispersion of particles that make the peaks of the distribution become flatter. Therefore, it is not accurate to conclude that helicity has a certain correlation to coherent structures characteristics. It is questionable to conclude that helicity could be considered as an indicator of coherent structures.

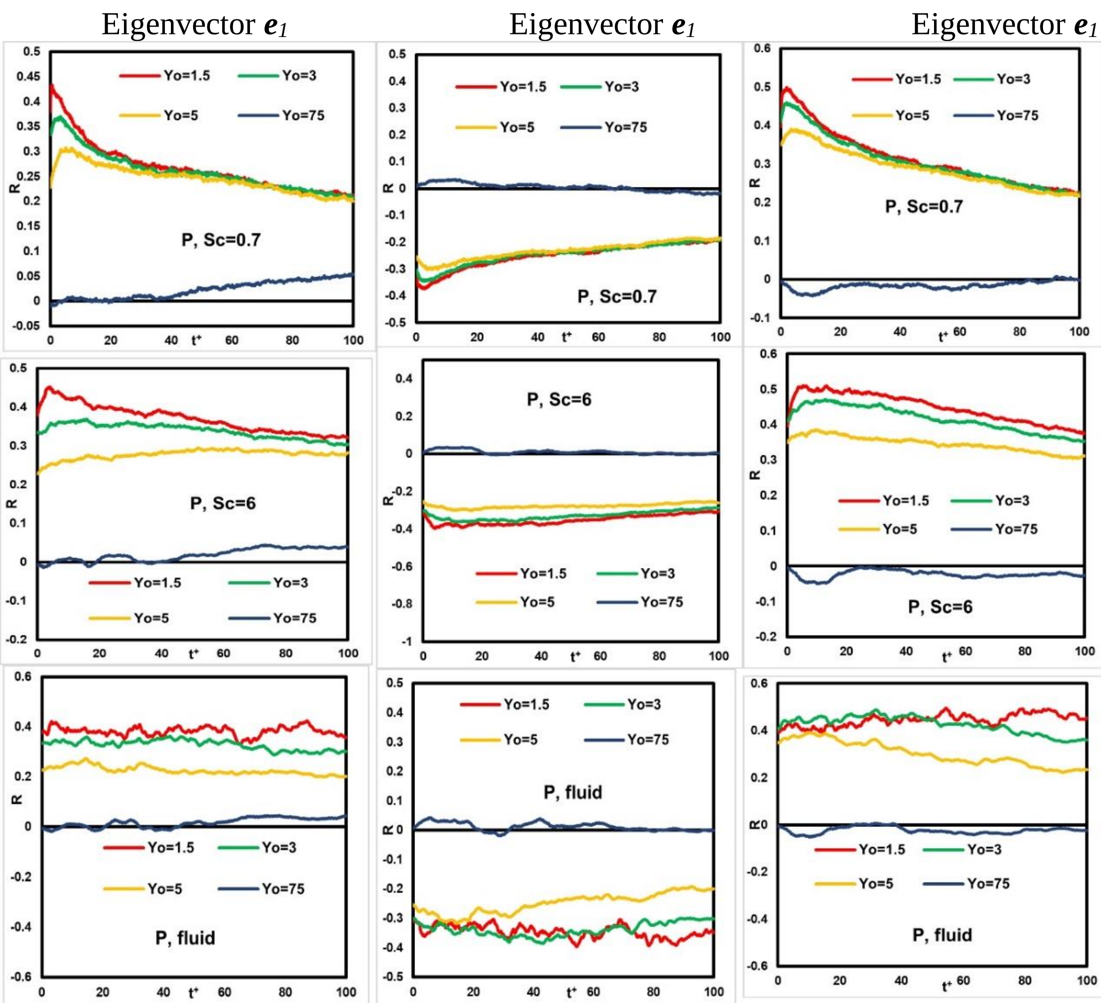


Figure 6.15 Cross correlation between absolute value of relative helicity $h' = cos\theta'$ and absolute value of the cosine between vorticity and the eigenvectors of the rate of strain tensor, cos(ω, $\boldsymbol{e}_i$). $\boldsymbol{e}_i$ with i=1-3 corresponds to eigenvectors with eigenvalues α>β>γ, for Poiseuille flow and various *Sc* numbers.

Eigenvector $\boldsymbol{e}_1$ Eigenvector $\boldsymbol{e}_2$ Eigenvector $\boldsymbol{e}_3$

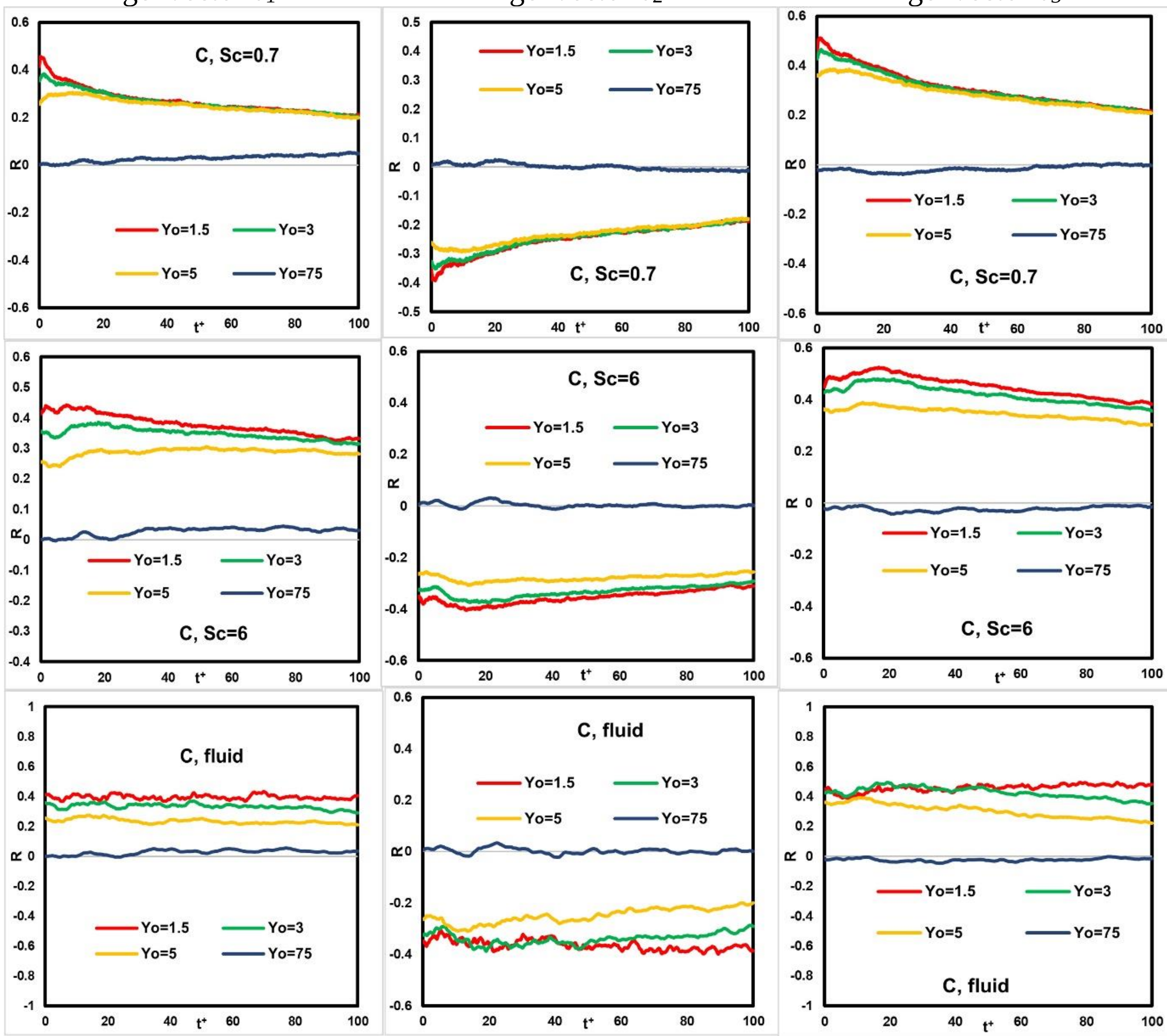


Figure 6.16 Cross correlation between absolute value of relative helicity $h' = cos\theta'$ and absolute value of the cosine between vorticity and the eigenvectors of the rate of strain tensor, cos(ω, $\boldsymbol{e}_i$). $\boldsymbol{e}_i$ with i=1-3 corresponds to eigenvectors with eigenvalues α>β>γ, for Couette flow and various *Sc* numbers.

The cross-correlation between relative helicity density $h'$ and $\epsilon_i = \cos(\omega, \boldsymbol{e}_i)$ was calculated by the Pearson cross-correlation formula as follows:

$$R_{h'-\epsilon} = \frac{\sum_{i=1}^{n}(h'_i - \overline{h'})(\epsilon_i - \bar{\epsilon})}{\sqrt{\sum_{i=1}^{n}(h'_i - \overline{h'})^2}\sqrt{\sum_{i=1}^{n}(\epsilon_i - \bar{\epsilon})^2}} \tag{6-7}$$

Figures 6.15 and 6.16 are presentations of the cross correlation between the absolute value of $cos\theta'$ and cos(ω,$\boldsymbol{e}_i$) in the case of Poiseuille and Couette flow at *Sc* = 0.7, 6 and fluid particles. The absolute value is used, since the important issue here is the alignment between the vectors, not which one is first or second. It can be seen that the cross-correlation coefficients do not show significant change with time for $Sc$ = 6 and the case of fluid particles, meanwhile the case of $Sc$ = 0.7 has a remarkable change within the first 50 time units. The correlation coefficient generally decreases with the release position located farther from the wall, and its value for release at $Y_0$ = 75 is approximately zero. This indicates that there is a correlation between the angle of vorticity projected on the eigenvectors of the rate of strain tensor, and that this correlation is different than zero for the duration of the simulations. More importantly, it is interesting that the values of the correlation between the absolute value of $h'$ and $\cos(\omega,\boldsymbol{e}_2)$ (corresponding to the intermediate eigenvector) are negative, while the cross correlations with $\cos(\omega,\boldsymbol{e}_1)$ and $\cos(\omega,\boldsymbol{e}_3)$ are always positive for both Couette and Poiseuille flows. This is in agreement with previous studies that showed that the probability of large value of $\cos(\omega,\boldsymbol{e}_2)$ is highest for any region [259-261]. Other studies also revealed that for near wall region, the value of relative helicity density is distributed around zero. Therefore, when the vorticity aligns to the intermediate eigenvector, it tends to be perpendicular to the velocity vector.

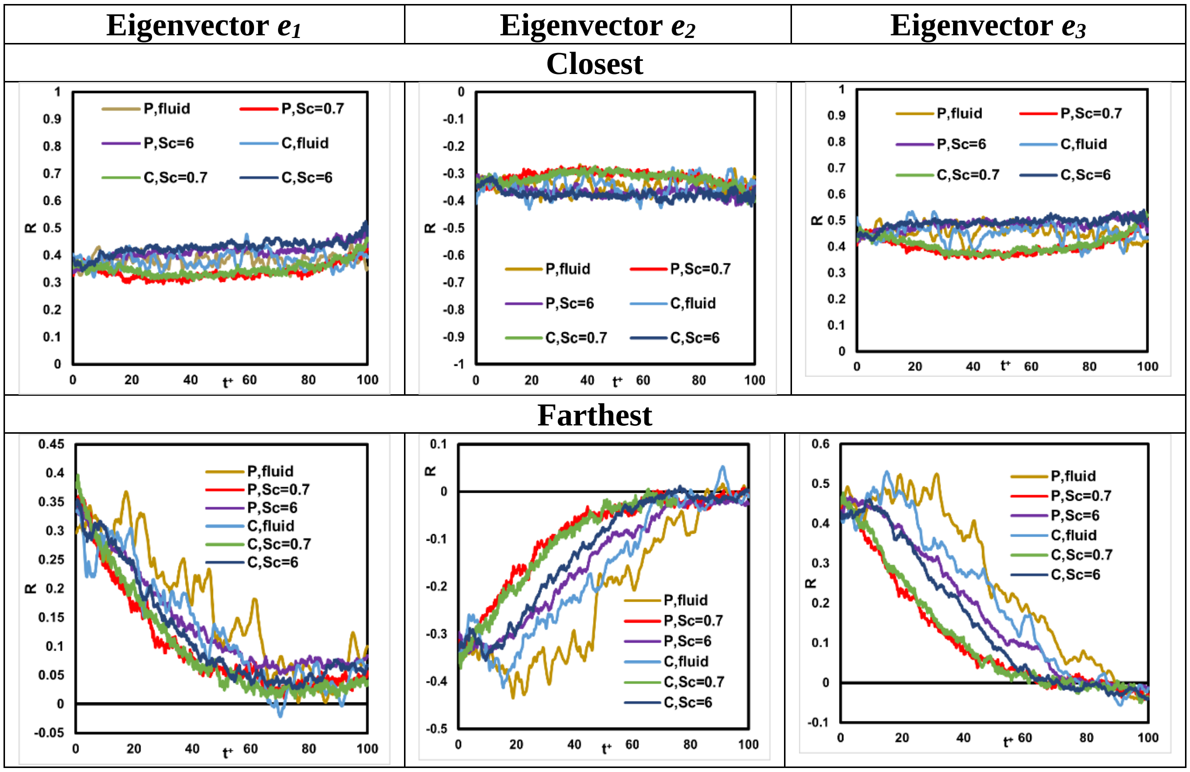


Figure 6.17 Cross correlation between the absolute value of relative helicity $h' = cos\theta'$ and absolute value of cosine between vorticity and eigenvectors cos(ω, $\boldsymbol{e}_i$). $\boldsymbol{e}_i$ with i=1-3corresponds to eigenvectors of eigenvalues α > β > γ) for the 25% of particles that are located closer and farther from the initial position $Y_0 = 3$ for Couette and Poiseuille flows at various $Sc$ numbers.

The cross correlation for the absolute value of $cos\theta'$ and cos(ω, $\boldsymbol{e}_i$) for the quartiles of the particles that disperse the least in the y direction and those that disperse the most at time $t^+ = 100$ for release position at $Y_0 = 3$ are shown in Figure 6.17 . There is a remarkable difference between the data for the particles located closest and farthest away from the wall. The value of the cross correlation does not change a lot during the time of simulation for the particles moving closest, meanwhile the particles that disperse the most witness a dramatic decrease in the value of the cross-correlation coefficient to the value of zero. This can be explained by considering that the particles that are closer to the wall are those that are still located in the near wall region, being trapped in flow structures that are keeping them there. When they can escape these structures, then they can be transferred away from the wall by taking advantage of synergisms between difference structures [263]. For the particles that are the farthest away from the wall, the cross-correlation in these regions is nearly zero.

### 6.3 Conclusions

This study explored the relation between relative helicity density and the physical characteristics of turbulence in channel and Couette flow using Lagrangian methods applied to a Direct Numerical Simulation. The joint probability density function between relative helicity and vertical fluctuating velocity shows that in the near wall region both $h'$ and $v'$ have small value but farther from the wall the vertical velocity and relative helicity density have larger values. This similarity could reflect the correlation of relative helicity density and normal velocity that directly affect transport of particles in the flow field. The JPDF between relative helicity and the alignment of the vorticity vector with the vertical direction indicate that in the near wall region, vorticity tends to misalign with the vertical direction and velocity vector but from the log layer region, there is no correlation between these alignments. The distribution of helicity conditioned on coherent structure identification indices, such as the Q-criterion, the second largest eigenvalue of the rate of strain tensor and the Reynold stress quadrants showed that the alignment between vorticity and velocity depends on the region of the flow from where the particles were released and on the effects of molecular diffusivity, expressed through the *Sc* numbers. The same conclusion can be drawn when considering the vector plot of instantaneous fluctuating velocity and the magnitude of relative helicity density for particles in both Poiseuille and Couette flows. In the near wall region, the relative helicity of particles has small values, meaning that the velocity and vorticity vectors are perpendicular to each other. Within the log layer region, the values of relative helicity have been distributed in broader values, extending in a more uniform fashion from -1 to 1. These distribution profiles are similar regardless of whether the distribution is conditioned on any criterion used herein for identifying coherent structures. This indicates that the vorticity and velocity vectors tend to align as particles move farther form the wall, in agreement with prior findings [150]. The Lagrangian autocorrelation coefficient for Q values along particle trajectories was computed and the obtained results suggest that this autocorrelation coefficient is larger than zero for at least 100 viscous time units, while its values depend on *Sc* number and the release position and the type of flow. When it comes to the relation between relative helicity and the alignment of vorticity with eigenvectors of the rate of strain tensor, there is an important finding that the value of the relative helicity has an anti-correlation to the projection of vorticity on the intermediate eigenvectors of rate of strain tensor. There is a difference in the cross correlation between relative helicity density and the alignment of vorticity with the three eigenvectors of the rate of strain tensor at various *Sc* numbers, release position and the farthest and closest particles. Summarily, it is found that helicity plays a role in the transport of particles, if cannot be considered an indicator for the coherent structures in anisotropic turbulence flow.

# CHAPTER 7: CONCLUSIONS AND FUTURE WORKS

## 7.1 Conclusions

- The distribution of shear stress and extensional stress induced on vWF surrogate particles injected *in silico* to computationally obtained velocity fields that are found in blood flow through regions of biomedical devices and implants was calculated in detail.
- Both Poiseuille-Couette flow and Poiseuille flow were found to result in potentially damaging stresses. The distribution of stresses on the particles showed that particles have had a stochastic exposure to stresses and these stresses could cause damage at different times during the movement of the particles.
- The most unpredictable cases were the ones when the vWF were released in the viscous sublayer or in the buffer region of the turbulent flow field. In addition, it is highly probable that particles were exposed to different stresses as they dispersed in the flow field, and these stresses were potentially damaging for a portion of the time they spent in the flow. Injections at the center of the flow field, rather than closer to the wall, would be preferred, as they result in exposure to lower and more predictable stress.
- The relative helicity and dissipation along passive particle trajectories were tracked in a Poiseuille channel and a plane Couette flow using Direct Numerical Simulation and Lagrangian Scalar tracking.
- It has been concluded that there was an ambiguous anti-correlation between helicity and dissipation, some particles could have high helicity and low dissipation, but some did not. The position of release of the particles and the *Sc* number has noticeable effects on the helicity experienced by a passive particle rather than the type of flow. In the near wall region, the anticorrelation between the helicity and dissipation is more obvious, while the

log-layer region does not show these correlations. However, whether helicity could be used as an indicator of dissipation has still been questionable.

- The joint probability density function between relative helicity and vertical fluctuating velocity shows that in near wall region both have small value but farther from the wall the vertical velocity and relative helicity density have larger values. This similarity could reflect the correlation of relative helicity density and normal velocity that directly affect transport of particles in the flow field.
- The distribution of helicity conditioned on vortex identification indices such as the Q-criterion, the second largest eigenvalue of strain rate tensors, the Reynold stress quadrants, the vector plot of fluctuating velocity and the magnitude of relative helicity density of particles in Poiseuille and Couette flows showed that the alignment between vorticity and velocity depends on the regions of that particles moving in and the $Sc$ numbers.
- In the near wall regions, the relative helicity of particles has small values, indicating that the velocity and vorticity vectors are perpendicular to each other. From the log layer region, the values of relative helicity have been distributed in wider values from -1 to 1 and these distribution profiles are similar regardless of whether the distribution is conditioned on any criterion of coherent structures.
- The correlation of Q values with time is computed and the obtained results suggest that this autocorrelation coefficient is larger than zero during the simulation time and its values depend on $Sc$ number, release positions and type of flow. When it comes to the relation between relative helicity and the alignment of vorticity with eigenvectors of rate of strain tensor, there is an important conclusion that magnitude of relative helicity has the anti-correlation to the projection of vorticity on the intermediate eigenvectors of strain rate

tensor. There is a difference in the cross correlation between relative helicity density and the alignment of vorticity with the three eigenvectors of strain rate tensor at various $Sc$ number, release position and the most and least dispersed particles.

- In summary, helicity plays a role in the transport of particles but could not be seen as an indicator for the coherent structures in anisotropic turbulence flow.

## 7.2 Future works

- Investigate structures and correlation between physical quantities and determine the existence of coherent structure which indicates the large-scale motion in Couette flow for h=450.
- The code of Couette flow at h=450 will be integrated to Lagrangian Scalar Tracking algorithm to investigate the turbulent transport of heat and scalar marker from which illustrate the effects of large-scale motion on the turbulent transport in buffer layer, viscous sublayer, channel center, near wall region. This can be useful and significant in controlling the turbulent flow with high Reynold number especially in the presence of large-scale motion or coherent structures.
- The DNS and Lagrangian scalar tracking have been used to estimate the shear and extensional stress on vWF in channel flow. However, this work still lacks the comprehensive modelling for unfolding of vWF in turbulent flow and the change in shape of this protein could result in the variance of diffusivity coefficients. Building a stochastic model for vWF in turbulent flow is important in calculating the probability density function of stresses on vWF marker.
- Extending the application of Direct Numerical Simulation and Lagrangian scalar tracking to different fields in chemical engineering and biological engineering.

- Parallelize the Direct Numerical Simulation code under the support of supercomputer to optimize the run time to make this code applicable to larger Reynolds numbers with high resolution.
- Apply Machine Learning (ML) to turbulent transport that could provide predictive model and optimization for the transport of a scalar in turbulent flow using the high-fidelity turbulence data generated from DNS and LST for training and testing data. We hope ML could be an efficient and accurate tool to support the development of turbulent stresses and heat/mass transfer or to estimate turbulence coefficients for the scalar transport.

# APPENDIX A: INVESTIGATE THE COUETTE FLOW USING DIRECT NUMERICAL SIMULATION

## 1. Methodology and Parameters

In the Couette flow, the walls are moving relative each other, and this is taken into account by changing Dirichlet boundary conditions. For Couette flow the streamwise velocity at the wall $U_w$=±Gh. where G is a constant (G =0.04123 for current study), which specifies the Reynolds number of the simulated field. The choice of G is such that the dimensionless variables calculated in the code have values as close as possible to their values in wall units. The top wall of the channel moves in the minus x-direction, and the bottom wall moves in the positive x-direction. The detail of running DNS code for Couette flow was described in literature [7].

The Couette flow was simulated in computational box 11200x5600x450 in x,y, and z directions. The flow was assumed to be periodic in the streamwise, *x*, and spanwise, *z*, directions with lengths of periodicity equal to the box size in those two directions. Plane Couette flow of an incompressible and Newtonian fluid was simulated at frictional Reynolds numbers of 450, corresponding to the Reynold number about 8000, based on half of channel height and the wall velocity. The computational box has a resolution 512x512x768 in *x*, *y*, *z* directions.

A uniform mesh was used in $x$ and $z$, while a non-uniform mesh based on Chebyshev collocation points was used in the $y$ direction. The DNS code was parallelized using OpenMP and run on the supercomputer with 16 number of threads. The code is run every 500 time steps and the duration for each run is 21 hrs. Until now, this run reached the total time step about 293000 corresponding to $t^+$=14650 (with time step $\Delta t = 0.05$).

The obtained results have been averaged for every 2500 steps from step 257000 to step 293000 (total 36000 steps) for Reynolds stress, the mean square of velocity, mean velocity and mean of viscous stress.

## 2. Results

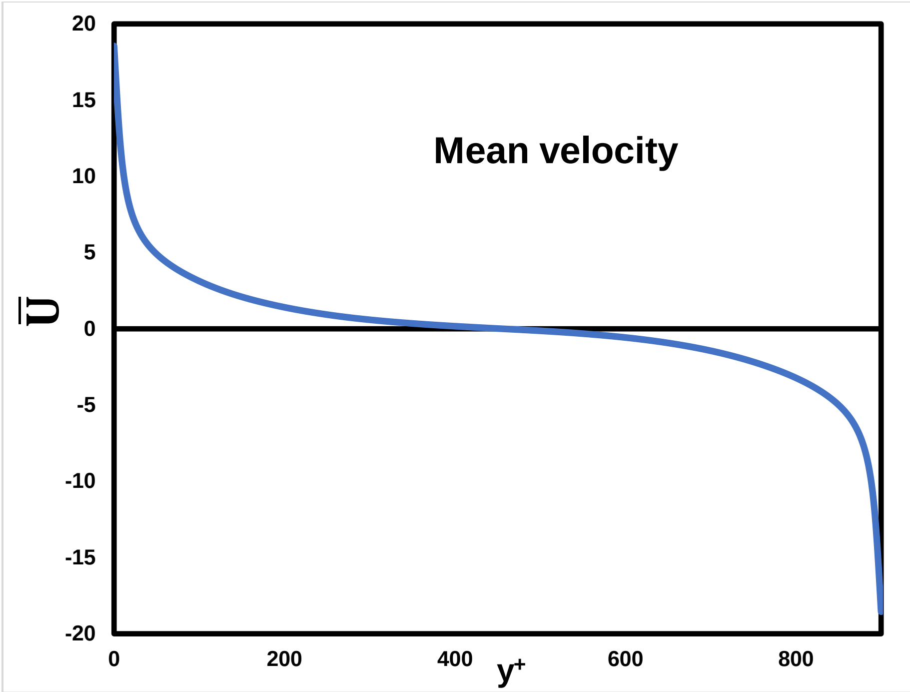


Figure A. 1 Mean of velocity profile of Couette flow in wall units.

Figure A.1 is the mean velocity distributions that are presented by wall units. The obtained profile is similar to the one in Ref [37]. The profile shows a non-zero mean velocity gradient at the centerline. The maximum value of velocity is at the wall and then decreases with the distance from the wall. The velocity profile is in the S-shape and antisymmetric about the horizontal centerline which are similar to the obtained results from Ref [37, 41].

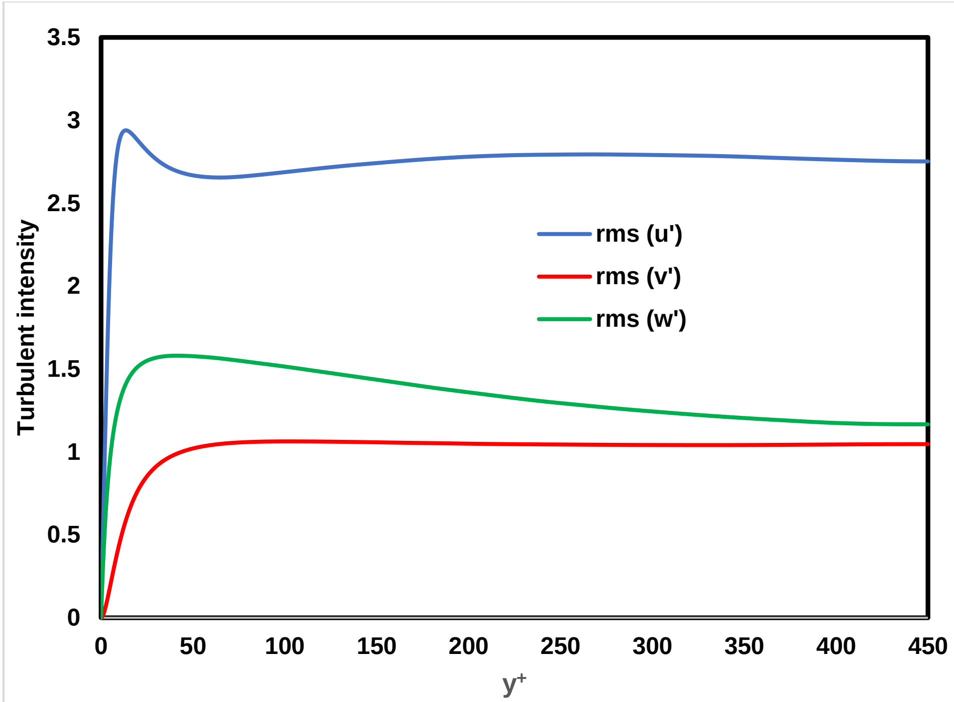


Figure A. 2 Root mean square of fluctuating streamwise (rms (u’)), spanwise (rms (w’)) and vertical (rms(v’)) velocity in wall units.

The root mean square (rms) of three total velocity components is shown in Figures A.2. The rms values of streamwise velocity ($u$) is smallest at channel wall and then increase dramatically to maximum value of about 2.9 at $y^+$=12. Afterward, the rms of u decrease slightly and does not change a lot at centerline. Meanwhile, the profile of rms of spanwise velocity shows that the value increases to get maximum at $y^+$=35 then decreases to minimum at centerline. The rms of vertical velocity increases significantly from channel wall to $y^+$=65 then levelling off to channel center.

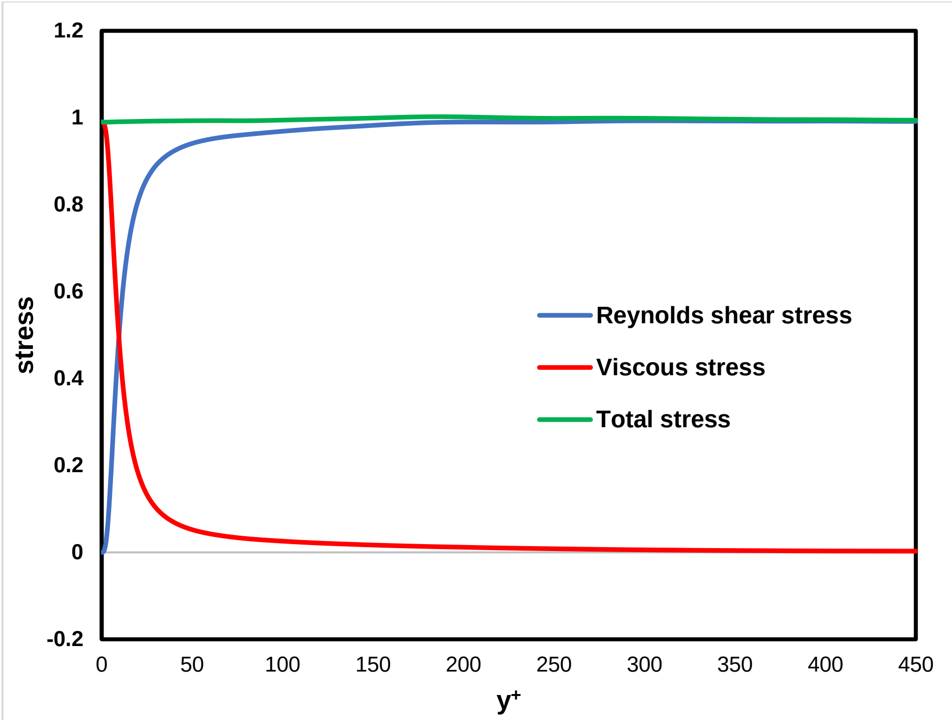


Figure A. 3 The total stress and mean of Reynolds stress for plane Couette flow in wall units.

The distribution of the Reynolds and viscous stress are symmetrical. From the conservation of mean momentum, the stationary turbulent Couette flow, the total shear stress $\tau_{total}$ is the sum of Reynolds stress $\overline{u'v'}$ and viscous stress $d\bar{U}/dy$. [193]

$$\tau_{total} = -\overline{u'v'} + \frac{d\bar{U}}{dy} = 1 \qquad \text{(A-1)}$$

Therefore, to ensure the simulation reaches statistical stationary, the total stress, Reynolds shear stress and viscous stress need to be monitored to evaluate the stationary status. From the Figure A.5, the obtained Reynolds shear stress profile is similar to the one from Ref [40] and show that the value of Reynolds shear stress increase dramatically from zero to high value at $y^+$=35 and then gradually going up to nearly 1 value at channel center. Meanwhile, the viscous stress witnesses the contrast trend, and the total stress profile is kept constant at approximate 1 through the channel. The profile of turbulent intensities and Reynolds stress obtained from this work are similar to the one from previous studies in Ref [35, 37, 41, 62]

In the future, the two-point autocorrelation coefficient, the animation of coherent structures in flow field, spectra energy, instantaneous velocity field needs to be investigated to provide the structural information on the flow [38, 40]. The turbulent budgets such as production, dissipation, turbulent diffusion, pressure strain, pressure diffusion and viscous diffusion [40] are also taken into account for the simulation of Couette flow. Our purpose is to check whether the computational box is large enough to accommodate the largest scales of turbulence with good accuracy.

## REFERENCES


1. Harun, Z. and E. Reda Lotfy, *Generation, Evolution, and Characterization of Turbulence Coherent Structures*, in *Turbulence and Related Phenomena*. 2019.
2. Dewan, A., *Tackling Turbulent Flows in Engineering*. 2011.
3. Frans T.M. Nieuwstadt , B.J.B., Jerry Westerweel, *Turbulence:Introduction to Theory and Applications of Turbulent Flows.*
4. Christophe Bailly , G.C.-B., *Turbulence.* 2015.
5. Ozturk, M., E. O'Rear, and D. Papavassiliou, *Reynolds Stresses and Hemolysis in Turbulent Flow Examined by Threshold Analysis.* Fluids, 2016. **1**(4).
6. Vartdal, M., *Computing turbulence structure tensors in plane channel flow.* Computers & Fluids, 2016. **136**: p. 207-211.
7. Davies, J.T., *Turbulence Phenomena: An Introduction to the Eddy Transfer of Momentum, Mass, and Heat, Particularly at Interfaces.* 1972.
8. P. A. Durbin, B.A.P.R., *Statistical Theory and Modeling for Turbulent Flows.* 2011
9. Argyropoulos, C.D. and N.C. Markatos, *Recent advances on the numerical modelling of turbulent flows.* Applied Mathematical Modelling, 2015. **39**(2): p. 693-732.
10. Le, P.M. and D.V. Papavassiliou, *A physical picture of the mechanism of turbulent heat transfer from the wall.* International Journal of Heat and Mass Transfer, 2009. **52**(21-22): p. 4873-4882.
11. Borrell, G., J.A. Sillero, and J. Jiménez, *A code for direct numerical simulation of turbulent boundary layers at high Reynolds numbers in BG/P supercomputers.* Computers & Fluids, 2013. **80**: p. 37-43.
12. Teng, H., et al., *Turbulent drag reduction in plane Couette flow with polymer additives: a direct numerical simulation study.* Journal of Fluid Mechanics, 2018. **846**: p. 482-507.
13. Oliver, T.A., et al., *Estimating uncertainties in statistics computed from direct numerical simulation.* Physics of Fluids, 2014. **26**(3).
14. Pirozzoli, S., M. Bernardini, and P. Orlandi, *Turbulence statistics in Couette flow at high Reynolds number.* Journal of Fluid Mechanics, 2014. **758**: p. 327-343.
15. Marusic, I., et al., *Wall-bounded turbulent flows at high Reynolds numbers: Recent advances and key issues.* Physics of Fluids, 2010. **22**(6).
16. Bernardini, M., S. Pirozzoli, and P. Orlandi, *Velocity statistics in turbulent channel flow up to.* Journal of Fluid Mechanics, 2014. **742**: p. 171-191.
17. Baltzer, J.R., R.J. Adrian, and X. Wu, *Structural organization of large and very large scales in turbulent pipe flow simulation.* Journal of Fluid Mechanics, 2013. **720**: p. 236-279.
18. Schlatter, P., et al., *Simulations of spatially evolving turbulent boundary layers up to.* International Journal of Heat and Fluid Flow, 2010. **31**(3): p. 251-261.
19. Smits, A.J., B.J. McKeon, and I. Marusic, *High–Reynolds Number Wall Turbulence.* Annual Review of Fluid Mechanics, 2011. **43**(1): p. 353-375.
20. Harun, Z., et al., *Pressure gradient effects on the large-scale structure of turbulent boundary layers.* Journal of Fluid Mechanics, 2013. **715**: p. 477-498.
21. Balakumar, B.J. and R.J. Adrian, *Large- and very-large-scale motions in channel and boundary-layer flows.* Philos Trans A Math Phys Eng Sci, 2007. **365**(1852): p. 665-81.
22. Lee, J.H. and H.J. Sung, *Comparison of very-large-scale motions of turbulent pipe and boundary layer simulations.* Physics of Fluids, 2013. **25**(4).
23. Solak, I. and J.-P. Laval, *Large-scale motions from a direct numerical simulation of a turbulent boundary layer.* Physical Review E, 2018. **98**(3).

24. Marusic, I., et al., *On the logarithmic region in wall turbulence.* Journal of Fluid Mechanics, 2013. **716**.
25. Guala, M., S.E. Hommema, and R.J. Adrian, *Large-scale and very-large-scale motions in turbulent pipe flow.* Journal of Fluid Mechanics, 2006. **554**(-1).
26. V. Berdichevsky, A.F., and V. Sutyrin, *Prediction of Turbulent Velocity Profile in Couette and Poiseuille Flows from First Principles.* Physical Review Letters, 1996. **76**: p. 3967-3970.
27. Yoon, M., et al., *Large-scale motions in a turbulent channel flow with the slip boundary condition.* International Journal of Heat and Fluid Flow, 2016. **61**: p. 96-107.
28. Alfonsi, G., et al., *Hairpin vortices in turbulent channel flow.* Procedia Computer Science, 2011. **4**: p. 801-810.
29. Orlandi, P., M. Bernardini, and S. Pirozzoli, *Poiseuille and Couette flows in the transitional and fully turbulent regime.* Journal of Fluid Mechanics, 2015. **770**: p. 424-441.
30. Eitel-Amor, G., R. Örlü, and P. Schlatter, *Simulation and validation of a spatially evolving turbulent boundary layer up to.* International Journal of Heat and Fluid Flow, 2014. **47**: p. 57-69.
31. Hiroyuki Abe, H.K., Haecheon Choi, *Very Large-Scale Structures and Their Effects on the Wall Shear-Stress Fluctuations in a Turbulent Channel Flow up to $Re_t$=640.* Journal of Fluids Engineering, 2004. **126**: p. 835-843.
32. Tiselj, I., *Tracking of large-scale structures in turbulent channel with direct numerical simulation of low Prandtl number passive scalar.* Physics of Fluids, 2014. **26**(12).
33. Lee, M. and R.D. Moser, *Extreme-scale motions in turbulent plane Couette flows.* Journal of Fluid Mechanics, 2018. **842**: p. 128-145.
34. Schneider, T.M., et al., *Transient turbulence in plane Couette flow.* Phys Rev E Stat Nonlin Soft Matter Phys, 2010. **81**(1 Pt 2): p. 015301.
35. Hanratty, D.V.P.a.T.J., *Interpretation of large-scale structures observed in a turbulent plane Couette flow.* Int. J. Heat and Fluid Flow, 1997. **18**: p. 55-69.
36. W. Gretler, W.M., *Calculation of plane turbulent Couette-Poiseuille flows with a modified k-e model.* Fluid Dynamics Research, 1997. **21**: p. 263-283.
37. Tsukahara, T., H. Kawamura, and K. Shingai, *DNS of turbulent Couette flow with emphasis on the large-scale structure in the core region.* Journal of Turbulence, 2006. **7**.
38. Komminaho, J., A. Lundbladh, and A.V. Johansson, *Very large structures in plane turbulent Couette flow.* Journal of Fluid Mechanics, 1996. **320**(-1).
39. R. Kristoffersen, K.H.B.A.H.I.A., *Numerical Study of Turbulent Plane Couette Flow at Low Reynolds Number.* Applied Scientific Research, 1993. **51**: p. 337-343.
40. Avsarkisov, V., et al., *Turbulent plane Couette flow at moderately high Reynolds number.* Journal of Fluid Mechanics, 2014. **751**.
41. Liu, C.-H., *Turbulent Plane Couette Flow and Scalar Transport at Low Reynolds Number.* Transactions of the ASME, 2003. **125**: p. 988-998.
42. N Kasagi, Y., Tomita, A. Kuroda, *Direct Numerical Simulation of Passive Scalar Field in a Turbulent Channel Flow.* Transactions of the ASME, 1992. **114**: p. 598-606.
43. Li, F., et al., *Predicting contaminant dispersion using modified turbulent Schmidt numbers from different vortex structures.* Build Environ, 2018. **130**: p. 120-127.
44. Chauchat, J., et al., *Controversial turbulent Schmidt number value in particle-laden boundary layer flows.* Physical Review Fluids, 2022. **7**(1).

45. Menon, V.K.C.a.S., *Linear eddy simulations of Reynolds number and Schmidt number effects on turbulent scalar mixing.* Physics Of Fluids, 2001. **13**(2).
46. Jean-Baptiste Lagaert, G.B., Georges-Henri Cottet, Patrick Bégou, *Particle method: an efficient tool for direct numerical simulations of a high Schmidt number passive scalar in turbulent flow.* Center of Turbulence Research Proceedings of the Summer Program, 2012. **hal-00748132**: p. 167-176.
47. Bourgoin, M., et al., *Turbulent transport of finite sized material particles.* Journal of Physics: Conference Series, 2011. **318**(1).
48. Polanco, J.I., et al., *Relative dispersion of particle pairs in turbulent channel flow.* International Journal of Heat and Fluid Flow, 2018. **71**: p. 231-245.
49. Warnecke, H.B.D.M.W.P.H.-J., *Micro and Macro Mixing:Analysis, Simulation and Numerical Calculation.* 2010 **Springer-Verlag Berlin Heidelberg**(1860-4846).
50. Calmet, I. and J. Magnaudet, *Large-eddy simulation of high-Schmidt number mass transfer in a turbulent channel flow.* Physics of Fluids, 1997. **9**(2): p. 438-455.
51. Yu-Hong Dong, X.-Y.L., Li-Xian Zhuang, *Large eddy simulation of turbulent channel flow with mass transfer at high-Schmidt numbers.* International Journal of Heat and Mass Transfer 2003. **46**: p. 1529–1539.
52. den Toonder, J.M.J. and F.T.M. Nieuwstadt, *Reynolds number effects in a turbulent pipe flow for low to moderate Re.* Physics of Fluids, 1997. **9**(11): p. 3398-3409.
53. Hiroyuki Abe, H.K., Yuichi Matsuo, *Direct Numerical Simulation of a Fully Developed Turbulent Channel Flow With Respect to the Reynolds Number Dependence.* Transactions of the ASME, 2001 **123**: p. 382-393.
54. Shih, T.-H. and J.L. Lumley, *Kolmogorov Behavior of near-Wall Turbulence and Its Application in Turbulence Modeling.* International Journal of Computational Fluid Dynamics, 1993. **1**(1): p. 43-56.
55. Le, P.M. and D.V. Papavassiliou, *On the scaling of heat transfer using thermal flux gradients for fully developed turbulent channel and Couette flows.* International Communications in Heat and Mass Transfer, 2008. **35**(4): p. 404-412.
56. Redjem-Saad, L., M. Ould-Rouiss, and G. Lauriat, *Direct numerical simulation of turbulent heat transfer in pipe flows: Effect of Prandtl number.* International Journal of Heat and Fluid Flow, 2007. **28**(5): p. 847-861.
57. Pham, O.L., et al., *Computations of the shear stresses distribution experienced by passive particles as they circulate in turbulent flow: A case study for vWF protein molecules.* PLoS One, 2022. **17**(8): p. e0273312.
58. Pham, O.L., et al., *Distribution and history of extensional stresses on vWF surrogate molecules in turbulent flow.* Sci Rep, 2022. **12**(1): p. 171.
59. Cazalbou, J.B. and P. Bradshaw, *Turbulent transport in wall-bounded flows. Evaluation of model coefficients using direct numerical simulation.* Physics of Fluids A: Fluid Dynamics, 1993. **5**(12): p. 3233-3239.
60. Henning Reinken, S.H.L.K., and Michael Wilczek, *Optimal Turbulent Transport in Microswimmer Suspensions.* Phys. Rev. Fluids, 2022. **7**: p. 084501
61. Xu, P.K.Y.a.S., *Schmidt number effects on turbulent transport with uniform mean scalar gradient.* Physics Of Fluids, 2002. **14**(12).
62. Debusschere, B. and C.J. Rutland, *Turbulent scalar transport mechanisms in plane channel and Couette flows.* International Journal of Heat and Mass Transfer, 2004. **47**(8-9): p. 1771-1781.

63. Garcia-Ybarra, P.L. and A. Pinelli, *Turbulent channel flow concentration profile and wall deposition of a large Schmidt number passive scalar.* Comptes Rendus Mécanique, 2006. **334**(8-9): p. 531-538.
64. Tominaga, Y. and T. Stathopoulos, *Turbulent Schmidt numbers for CFD analysis with various types of flowfield.* Atmospheric Environment, 2007. **41**(37): p. 8091-8099.
65. Schwertfirm, F. and M. Manhart, *DNS of passive scalar transport in turbulent channel flow at high Schmidt numbers.* International Journal of Heat and Fluid Flow, 2007. **28**(6): p. 1204-1214.
66. Garcia-Ybarra, P.L., *Near-wall turbulent transport of large-Schmidt-number passive scalars.* Phys Rev E Stat Nonlin Soft Matter Phys, 2009. **79**(6 Pt 2): p. 067302.
67. Salhi, Y., et al., *Numerical Investigations of Passive Scalar Transport in Turbulent Taylor-Couette Flows: Large Eddy Simulation Versus Direct Numerical Simulations.* Journal of Fluids Engineering, 2012. **134**(4).
68. Wang, L., et al., *Turbulent Transport of Momentum and Scalars Above an Urban Canopy.* Boundary-Layer Meteorology, 2013. **150**(3): p. 485-511.
69. Rasthofer, U., et al., *Multifractal subgrid-scale modeling within a variational multiscale method for large-eddy simulation of passive-scalar mixing in turbulent flow at low and high Schmidt numbers.* Physics of Fluids, 2014. **26**(5).
70. Watanabe, T., et al., *Mixing and chemical reaction at high Schmidt number near turbulent/nonturbulent interface in planar liquid jet.* Physics of Fluids, 2015. **27**(3).
71. Pirozzoli, S., M. Bernardini, and P. Orlandi, *Passive scalars in turbulent channel flow at high Reynolds number.* Journal of Fluid Mechanics, 2016. **788**: p. 614-639.
72. Brethouwer, G., *Passive scalar transport in rotating turbulent channel flow.* Journal of Fluid Mechanics, 2018. **844**: p. 297-322.
73. Mohaghar, M., L.P. Dasi, and D.R. Webster, *Scalar power spectra and turbulent scalar length scales of high-Schmidt-number passive scalar fields in turbulent boundary layers.* Physical Review Fluids, 2020. **5**(8).
74. Ranjan, R. and S. Menon, *Two level simulation of Schmidt number effect on passive scalar transport in wall-bounded turbulent flows.* Physics of Fluids, 2021. **33**(3).
75. J´er´emie Bec, C.B., and Christophe Henr, *Enhanced transport of flexible fibers by pole vaulting in turbulent wall-bounded flow.* 2023.
76. Mielck F, Q.M., *Extracorporeal membrane oxygenation.* Curr Opin Crit Care, 2005. **11**: p. 87-93.
77. Trost JC, H.L., *Intra-aortic balloon counterpulsation.* Am J Cardiol, 2006. **97(9)**: p. 1391-8.
78. Sotiropoulos, F., T.B. Le, and A. Gilmanov, *Fluid Mechanics of Heart Valves and Their Replacements.* Annual Review of Fluid Mechanics, 2016. **48**(1): p. 259-283.
79. Kameneva, M.V., et al., *Effects of turbulent stresses upon mechanical hemolysis: experimental and computational analysis.* ASAIO J, 2004. **50**(5): p. 418-23.
80. Lee, S.S., et al., *Extensional flow-based assessment of red blood cell deformability using hyperbolic converging microchannel.* Biomed Microdevices, 2009. **11**(5): p. 1021-7.
81. Down, L.A., D.V. Papavassiliou, and E.A. O'Rear, *Significance of extensional stresses to red blood cell lysis in a shearing flow.* Ann Biomed Eng, 2011. **39**(6): p. 1632-42.
82. Vitale, F., et al., *A multiscale, biophysical model of flow-induced red blood cell damage.* AIChE Journal, 2014. **60**(4): p. 1509-1516.

83. Bento, D., et al., *Deformation of Red Blood Cells, Air Bubbles, and Droplets in Microfluidic Devices: Flow Visualizations and Measurements.* Micromachines (Basel), 2018. **9**(4).
84. Faghih, M.M. and M.K. Sharp, *Modeling and prediction of flow-induced hemolysis: a review.* Biomech Model Mechanobiol, 2019. **18**(4): p. 845-881.
85. Di Stasio, E. and R. De Cristofaro, *The effect of shear stress on protein conformation: Physical forces operating on biochemical systems: The case of von Willebrand factor.* Biophys Chem, 2010. **153**(1): p. 1-8.
86. Springer, T.A., *Biology and physics of von Willebrand factor concatamers.* J Thromb Haemost, 2011. **9 Suppl 1**: p. 130-43.
87. Federici, A.B., et al., *Current diagnostic and therapeutic approaches to patients with acquired von Willebrand syndrome: a 2013 update.* Semin Thromb Hemost, 2013. **39**(2): p. 191-201.
88. Chan, C.H., et al., *The effect of shear stress on the size, structure, and function of human von Willebrand factor.* Artif Organs, 2014. **38**(9): p. 741-50.
89. Fu, H., et al., *Flow-induced elongation of von Willebrand factor precedes tension-dependent activation.* Nat Commun, 2017. **8**(1): p. 324.
90. Coghill, P.A., et al., *Benchtop von Willebrand Factor Testing: Comparison of Commercially Available Ventricular Assist Devices and Evaluation of Variables for a Standardized Test Method.* ASAIO J, 2019. **65**(5): p. 481-488.
91. Lancellotti, S., et al., *Mechanochemistry of von Willebrand factor.* Biomol Concepts, 2019. **10**(1): p. 194-208.
92. Gogia, S. and S. Neelamegham, *Role of fluid shear stress in regulating VWF structure, function and related blood disorders.* Biorheology, 2015. **52**(5-6): p. 319-35.
93. Bortot, M., et al., *Turbulent Flow Promotes Cleavage of VWF (von Willebrand Factor) by ADAMTS13 (A Disintegrin and Metalloproteinase With a Thrombospondin Type-1 Motif, Member 13).* Arterioscler Thromb Vasc Biol, 2019. **39**(9): p. 1831-1842.
94. S. Kania, A.O., X. Cheng, X. F. Zhang and E. B. Webb III, *Long time-scale study of von Willebrand factor multimers in extensional flow.* 2020. **bioRxiv** p. 290304.
95. Sing, C.E. and A. Alexander-Katz, *Elongational flow induces the unfolding of von Willebrand factor at physiological flow rates.* Biophys J, 2010. **98**(9): p. L35-7.
96. RONG, X., *Conformational changes of von Willebrand Factor multimer subject to extensional flows.* Theses and Dissertations, 2015.
97. Sharifi, A. and D. Bark, *Mechanical Forces Impacting Cleavage of Von Willebrand Factor in Laminar and Turbulent Blood Flow.* Fluids, 2021. **6**(2).
98. Mansur Zhussupbekov, R.M.n.R., Wei-Tao Wu, Mehrdad Massoudi, James F. Antaki, *A continuum model for the unfolding of von Willebrand Factor.* Ann Biomed Eng, 2021. **49(9)**: p. 2646–2658.
99. Belyaev, A., *Intradimer forces and their implication for conformations of von Willebrand factor multimers.* Biophysical journal, 2021. **120**(5).
100. S. W. Schneider, S.N., A. Wixforth, C. Gorzelanny, A. Alexander-Katz, R. R. Netz, and M. F. Schneider, *Shear-induced unfolding triggers adhesion of von Willebrand factor fibers.* Proceedings of the National Academy of Sciences, May 2007. **vol. 104**: p. 7899–7903.
101. Rack, K., et al., *Margination and stretching of von Willebrand factor in the blood stream enable adhesion.* Sci Rep, 2017. **7**(1): p. 14278.

102. Lippok, S., et al., *Exponential size distribution of von Willebrand factor.* Biophys J, 2013. **105**(5): p. 1208-16.
103. Bartoli, C.R., et al., *Pathologic von Willebrand factor degradation with a left ventricular assist device occurs via two distinct mechanisms: mechanical demolition and enzymatic cleavage.* J Thorac Cardiovasc Surg, 2015. **149**(1): p. 281-9.
104. Aponte-Santamaria, C., et al., *Force-sensitive autoinhibition of the von Willebrand factor is mediated by interdomain interactions.* Biophys J, 2015. **108**(9): p. 2312-21.
105. Dong, C., et al., *Long-ranged Protein-glycan Interactions Stabilize von Willebrand Factor A2 Domain from Mechanical Unfolding.* Sci Rep, 2018. **8**(1): p. 16017.
106. Wang, Y., et al., *Shear-Induced Extensional Response Behaviors of Tethered von Willebrand Factor.* Biophys J, 2019. **116**(11): p. 2092-2102.
107. Baldauf, C., et al., *Shear-induced unfolding activates von Willebrand factor A2 domain for proteolysis.* J Thromb Haemost, 2009. **7**(12): p. 2096-105.
108. Morabito, M., et al., *Internal Tensile Force and A2 Domain Unfolding of von Willebrand Factor Multimers in Shear Flow.* 2018.
109. Chang, K.S. and W.L. Olbricht, *Experimental studies of the deformation of a synthetic capsule in extensional flow.* Journal of Fluid Mechanics, 2006. **250**: p. 587-608.
110. Fife, J.P., et al., *Evaluation of a contraction flow field on hydrodynamic damage to entomopathogenic nematodes-A biological pest control agent.* Biotechnol Bioeng, 2004. **86**(1): p. 96-107.
111. Jen-Hong Yen, S.-F.C., Ming-Kai Chern, Po-Chien Lu, *The Effects Of Extensional Stress On Red Blood Cell Hemolysis.* Biomedical Engineering: Applications, Basis and Communications, 2015. **27**(05): p. 1550042.
112. Zhang, J., et al., *Computational and Experimental Evaluation of the Fluid Dynamics and Hemocompatibility of the CentriMag Blood Pump.* Artificial Organs, 2006. **30**(3): p. 168-177.
113. Stewart, S.F.C., Paterson, E.G., Burgreen, G.W., *Assessment of CFD Performance in Simulations of an Idealized Medical Device: Results of FDA's First Computational Interlaboratory Study.* Cardiovasc Eng Technol, 2012. **3**: p. 139–160.
114. Malinauskas RA, S.A., Sheldon MI, *Working with the Food and Drug Administration's Center for Devices to Advance Regulatory Science and Medical Device Innovation.* Artif Organs., 2015. **39(4)**: p. 293-9.
115. Heck, M.L., et al., *Flow-Field Simulations and Hemolysis Estimates for the Food and Drug Administration Critical Path Initiative Centrifugal Blood Pump.* Artif Organs, 2017. **41**(10): p. E129-e140.
116. Hailong Yuan, N.D., Songmei Zhang, Yange Cao, Qiong Wang, Xin Liu and Qing Zhang, *The unfolded von Willebrand factor response in bloodstream: the self-association perspective.* 2012. **5**(65).
117. Jhun, C.-S., et al., *Stress and Exposure Time on von Willebrand Factor Degradation.* Artificial Organs, 2019. **43**(2): p. 199-206.
118. Foster, K.M., D.V. Papavassiliou, and E.A. O'Rear, *Elongational Stresses and Cells.* Cells, 2021. **10**(9).
119. Bortot, M., et al., *Pathologic Shear and Elongation Rates Do Not Cause Cleavage of Von Willebrand Factor by ADAMTS13 in a Purified System.* Cell Mol Bioeng, 2020. **13**(4): p. 379-390.

120. Zhang, X., et al., *Mechanoenzymatic cleavage of the ultralarge vascular protein von Willebrand factor.* Science, 2009. **324**(5932): p. 1330-4.
121. Levente Nova´k, H.D., Sa´ndor Damjanovich, and Jola´n Ha´ rsfalvi, *Shear-dependent morphology of vonWillebrand factor bound to immobilized collagen.* Hemostasis, Thrombosis, And Vascular Biology, 15 MARCH 2002. **volume 99**.
122. Khoo, D.P., et al., *Normal fluid stresses are prevalent in rotary ventricular assist devices: A computational fluid dynamics analysis.* The International Journal of Artificial Organs, 2018. **41**(11): p. 738-751.
123. Buerck, J.P., et al., *A Flow Induced Autoimmune Response and Accelerated Senescence of Red Blood Cells in Cardiovascular Devices.* Sci Rep, 2019. **9**(1): p. 19443.
124. Blackshear, P.L., Jr., Dorman, F. D., Steinbach, J. H., *Some Mechanical Effects That Influence Hemolysis.* Trans Am Soc Artif Intern Organs, 1965. **11**: p. 112-7.
125. Fraser, K.H., et al., *A quantitative comparison of mechanical blood damage parameters in rotary ventricular assist devices: shear stress, exposure time and hemolysis index.* J Biomech Eng, 2012. **134**(8): p. 081002.
126. Grigioni, M., et al., *Prosthetic heart valves' mechanical loading of red blood cells in patients with hereditary membrane defects.* J Biomech, 2005. **38**(8): p. 1557-65.
127. Taskin, M.E., et al., *Evaluation of Eulerian and Lagrangian models for hemolysis estimation.* Asaio j, 2012. **58**(4): p. 363-72.
128. Hariharan, P., et al., *Verification Benchmarks to Assess the Implementation of Computational Fluid Dynamics Based Hemolysis Prediction Models.* Journal of Biomechanical Engineering, 2015. **137**(9).
129. Niki Gregoriades, J.C., Ningning Ma, Kurt Koelling, Jeffrey J. Chalmers, *Cell Damage of Microcarrier Cultures as a Function of Local Energy Dissipation Created by a Rapid Extensional Flow.* Biotechnology And Bioengineering, JULY 20, 2000. **VOL. 69**(NO. 2): p. 171-182.
130. Bae, Y.B., et al., *Microfluidic assessment of mechanical cell damage by extensional stress.* Lab Chip, 2016. **16**(1): p. 96-103.
131. Kania, S., *Predicting pathological von Willebrand factor unraveling in elongational flow.*
132. Heidari, M., et al., *Cooperation within von Willebrand factors enhances adsorption mechanism.* J R Soc Interface, 2015. **12**(109): p. 20150334.
133. Pushin, D.M., et al., *Platelet activation via dynamic conformational changes of von Willebrand factor under shear.* PLoS One, 2020. **15**(6): p. e0234501.
134. Zlobina, K.E. and G.T. Guria, *Platelet activation risk index as a prognostic thrombosis indicator.* Sci Rep, 2016. **6**: p. 30508.
135. Kania, S., Oztekin, A., Cheng, X., Zhang, X. F. Webb, E.,, *Predicting pathological von Willebrand factor unraveling in elongational flow.* Biophys J, 2021. **120**(10): p. 1903-1915.
136. Orlandi, P., *Helicity fluctuations and turbulent energy production in rotating and non-rotating pipes.* Physics of Fluids, 1997. **9**(7): p. 2045-2056.
137. Chkhetiani, O.G. and E. Golbraikh, *Turbulent field helicity fluctuations and mean helicity appearance.* International Journal of Non-Linear Mechanics, 2012. **47**(3): p. 113-117.
138. Yan, Z., et al., *Dual channels of helicity cascade in turbulent flows.* Journal of Fluid Mechanics, 2020. **894**.
139. Moffatt, H.K., *Helicity and singular structures in fluid dynamics.* Proc Natl Acad Sci U S A, 2014. **111**(10): p. 3663-70.

140. Yu, C., et al., *Helicity distributions and transfer in turbulent channel flows with streamwise rotation.* Journal of Fluid Mechanics, 2022. **940**.
141. Kerr, R.M., *Histograms of Helicity and Strain in Numerical Turbulence.* Physical Review Letters, 1987. **59**(7).
142. D. D. Holm, a.R.M.K., *Helicity in the formation of turbulence.* Physics of fluids, 2007. **19**.
143. H. K. Moffatt, A.T., *Helicity in laminar and turbulent flow.* Annu. Rev. Fluid Mech. , 1992. **24**: p. 281-312.
144. Capuano, F. and D. Vallefuoco, *Effects of Discrete Energy and Helicity Conservation in Numerical Simulations of Helical Turbulence.* Flow, Turbulence and Combustion, 2018. **101**(2): p. 343-364.
145. Povitsky, A., *Three-dimensional flow with elevated helicity in driven cavity by parallel walls moving in perpendicular directions.* Physics Of Fluids 2017. **29**.
146. Pelz, R.B., L. Shtilman, and A. Tsinober, *The helical nature of unforced turbulent flows.* Physics of Fluids, 1986. **29**(11).
147. Polifke, W., *Statistics of helicity fluctuations in homogeneous turbulence.* Physics of Fluids A: Fluid Dynamics, 1991. **3**(1): p. 115-129.
148. Seginer, A. and D. Degani, *Graphical representation of three-dimensional vortical flows by means of helicity density and normalized helicity*, in *6th Applied Aerodynamics Conference*. 1988.
149. Moffatt, H.K., *Transport effects associated with turbulence with particular attention to the influence of helicity.* Rep. Prog. Phys., 1983. **46**: p. 621-664,.
150. Nguyen, Q. and D.V. Papavassiliou, *Using helicity to investigate scalar transport in wall turbulence.* Physical Review Fluids, 2020. **5**(6): p. 062601.
151. Rogers, M.M. and P. Moin, *Helicity fluctuations in incompressible turbulent flows.* Physics of Fluids, 1987. **30**(9): p. 2662-2671.
152. André, J.C. and M. Lesieur, *Influence of helicity on the evolution of isotropic turbulence at high Reynolds number.* Journal of Fluid Mechanics, 2006. **81**(01).
153. Qiaoning Chen, S.C., and Gregory L. Eyink, *The joint cascade of energy and helicity in three-dimensional turbulence.* Physics Of Fluids. **15**(2): p. 361-374.
154. Kazuhiro Inagaki, N.Y., and Fujihiro Hamba, *Mechanism of mean flow generation in rotating turbulence through inhomogeneous helicity.* Phys. Rev. Fluids, 2017. **2**.
155. Moffatt, H.K., *Magnetostatic equilibria and analogous Euler flows of arbitrarily complex topology. Part 1. Fundamentals.* Journal of Fluid Mechanics, 2006. **159**(-1).
156. Wallace, J.M., J.L. Balint, and L. Ong, *An experimental study of helicity density in turbulent flows.* Physics of Fluids A: Fluid Dynamics, 1992. **4**(9): p. 2013-2026.
157. Yokoi, N. and A. Brandenburg, *Large-scale flow generation by inhomogeneous helicity.* Phys Rev E, 2016. **93**(3): p. 033125.
158. Agoua, W., et al., *Spontaneous generation and reversal of helicity in anisotropic turbulence.* Phys Rev E, 2021. **103**(6): p. L061101.
159. Leonid Shtilman , E.L., Steven A. Orszag, Richard B. Pelz and Arkady Tsinober *On the role of helicity in complex fluid flows.* PHYSICS LETTERS, 1985. **113A**.
160. Yokoi, N. and A. Yoshizawa, *Statistical analysis of the effects of helicity in inhomogeneous turbulence.* Physics of Fluids A: Fluid Dynamics, 1993. **5**(2): p. 464-477.
161. Choi, Y., B.G. Kim, and C. Lee, *Alignment of velocity and vorticity and the intermittent distribution of helicity in isotropic turbulence.* Phys Rev E Stat Nonlin Soft Matter Phys, 2009. **80**(1 Pt 2): p. 017301.

162. Pelz, R.B., *Velocity-Vorticity Patterns in Turbulent Flow.* Physical Review Letters, 1985. **54**.
163. Speziale, C.g., *On helicity fluctuations in turbulence.* Quart. Appl. Math. , 1987. **45**: p. 123-129.
164. Yeontaek Choi, C.L., *A Role Of Helicity In Turbulent Diffusion.* Sixth International Symposium on Turbulence and Shear Flow Phenomena. Seoul, Korea, 2009: p. 105-107.
165. Biferale, L., S. Musacchio, and F. Toschi, *Split energy–helicity cascades in three-dimensional homogeneous and isotropic turbulence.* Journal of Fluid Mechanics, 2013. **730**: p. 309-327.
166. Papavassiliou, D.V., *Turbulent transport from continuous sources at the wall of a channel.* International Journal of Heat and Mass Transfer, 2002. **45**: p. 3571–3583.
167. Le, P.M. and D.V. Papavassiliou, *Turbulent dispersion from elevated line sources in channel and couette flow.* AIChE Journal, 2005. **51**(9): p. 2402-2414.
168. Srinivasan, C. and D.V. Papavassiliou, *Comparison of backwards and forwards scalar relative dispersion in turbulent shear flow.* International Journal of Heat and Mass Transfer, 2012. **55**(21-22): p. 5650-5664.
169. Barkley, D. and L.S. Tuckerman, *Computational study of turbulent laminar patterns in couette flow.* Phys Rev Lett, 2005. **94**(1): p. 014502.
170. Barkley, D. and L.S. Tuckerman, *Mean flow of turbulent–laminar patterns in plane Couette flow.* Journal of Fluid Mechanics, 2007. **576**: p. 109-137.
171. Morbiducci, U., et al., *Helical flow as fluid dynamic signature for atherogenesis risk in aortocoronary bypass. A numeric study.* J Biomech, 2007. **40**(3): p. 519-34.
172. Olshanskii, M.A. and L.G. Rebholz, *Velocity–vorticity–helicity formulation and a solver for the Navier–Stokes equations.* Journal of Computational Physics, 2010. **229**(11): p. 4291-4303.
173. Li, Y., *Geometrical statistics and vortex structures in helical and nonhelical turbulences.* Physics of Fluids, 2010. **22**(3).
174. Yan, Z., et al., *Effect of pressure on joint cascade of kinetic energy and helicity in compressible helical turbulence.* Phys Rev E, 2019. **99**(3-1): p. 033114.
175. Zheng Yan, X.L., Changping Yu, *Scale locality of helicity cascade in physical space.* Phys. Fluids, 2020. **32**: p. 061705.
176. Yan, Z., X. Li, and C. Yu, *Helicity budget in turbulent channel flows with streamwise rotation.* Physics of Fluids, 2022. **34**(6).
177. Jeong, J., et al., *Coherent structures near the wall in a turbulent channel flow.* Journal of Fluid Mechanics, 1997. **332**: p. 185-214.
178. Robinson, S.K., *Coherent Motions In The Turbulent Boundary Layer.* Annu. Rev. Fluid Mech., 1991. **23**: p. 601-39.
179. Jiménez, J., *Coherent structures in wall-bounded turbulence.* Journal of Fluid Mechanics, 2018. **842**.
180. Leonid Shtilman, R.B.P.a.A.T., *Numerical investigation of helicity in turbulent flow.* Computers & Fluids, 1988. **16**(3): p. 341-347.
181. Zhang, Y., et al., *A review of methods for vortex identification in hydroturbines.* Renewable and Sustainable Energy Reviews, 2018. **81**: p. 1269-1285.
182. Tsinober, E.L.a.A., *On the role of helical structures in three-dimensional turbulent flow.* Physics Letters, 1982. **93A**(6).

183. Balint, J.M.W.a.J.-L., *An Experimental Study of Helicity and Related Properties in Turbulent Flows.* Paper presented at the 1UTAM Symposium: Topologieal Fluid Mechanics, Cambridge, England., August, 1989.
184. Lenhard, R., et al., *Vortex Identification in a Free-Surface Flow Problem Solved Using SPH.* MATEC Web of Conferences, 2022. **369**.
185. Chakraborty, P., S. Balachandar, and R.J. Adrian, *On the relationships between local vortex identification schemes.* Journal of Fluid Mechanics, 2005. **535**: p. 189-214.
186. Yangzi Huang, M.R., & Melissa A. Green, *Tracking Coherent Structures In Massively-Separated And Turbulent Flows.* International Symposium On Turbulence and Shear Flow Phenomena (TSFP-9), 2015. **3D-2**.
187. Haller, G., *An objective definition of a vortex.* Journal of Fluid Mechanics, 2005. **525**: p. 1-26.
188. Jie-min Zhan, Y.-t.L., Wing-hong Onyx Wai , Wen-qing Hu, *Comparison between the Q criterion and Rortex in the application of an in-stream structure.* Physics of Fluids, 2019. **31**(12).
189. Klein, M., H. Schmidt, and D.O. Lignell, *Stochastic modeling of surface scalar-flux fluctuations in turbulent channel flow using one-dimensional turbulence.* International Journal of Heat and Fluid Flow, 2022. **93**.
190. Moser, R.D., J. Kim, and N.N. Mansour, *Direct numerical simulation of turbulent channel flow up to Reτ=590.* Physics of Fluids, 1999. **11**(4): p. 943-945.
191. Lozano-Durán, A. and J. Jiménez, *Effect of the computational domain on direct simulations of turbulent channels up to Reτ = 4200.* Physics of Fluids, 2014. **26**(1).
192. Jin Lee, J.H.L., Jung-il Choi, Hyung Jin Sung, *Very-Large-Scale Motions In A Turbulent Channel Flow.* International Symposium On Turbulence and Shear Flow Phenomena, 2013.
193. Bech, K.H., et al., *An investigation of turbulent plane Couette flow at low Reynolds numbers.* Journal of Fluid Mechanics, 2006. **286**: p. 291-325.
194. Myoungkyu Lee, R.D.M., *Role of large scale motions in turbulent poiseuille and couette flows.* 10th International Symposium on Turbulence and Shear Flow Phenomena (TSFP10), Chicago, USA, July, 2017.
195. El Khoury, G.K., et al., *Massive separation of turbulent Couette flow in a one-sided expansion channel.* International Journal of Heat and Fluid Flow, 2010. **31**(3): p. 274-283.
196. Lee, M. and R.D. Moser, *Direct numerical simulation of turbulent channel flow up to.* Journal of Fluid Mechanics, 2015. **774**: p. 395-415.
197. Yamamoto, Y. and T. Kunugi, *Direct numerical simulation of MHD heat transfer in high Reynolds number turbulent channel flows for Prandtl number of 25.* Fusion Engineering and Design, 2015. **90**: p. 17-22.
198. Mitali Chakrabarti, R.M.K., and James C. Hill, *Direct Numerical Simulation of Chemical Selectivity in Homogenous Turbulence.* AIChE Journal, 1995. **41**: p. 2356-2370.
199. Yutaka Miyake, K.T., and Hideki Beppu, *Direct numerical simulation of a turbulent flow in a channel having periodic pressure gradient.* Int. J. Heat and Fluid Flow, 1995. **16**: p. 333-340.
200. Nguyen, Q.T. and D.V. Papavassiliou, *Turbulent plane Poiseuille-Couette flow as a model for fluid slip over superhydrophobic surfaces.* Physical Review E, 2013. **88**(6): p. 063015.
201. Wu, X. and P. Moin, *A direct numerical simulation study on the mean velocity characteristics in turbulent pipe flow.* Journal of Fluid Mechanics, 2008. **608**: p. 81-112.

202. Lee, J.H. and H.J. Sung, *Direct numerical simulation of a turbulent boundary layer up to $Re_\theta$=2500.* International Journal of Heat and Fluid Flow, 2011. **32**(1): p. 1-10.
203. Lyons, S.L., T.J. Hanratty, and J.B. McLaughlin, *Large-scale computer simulation of fully developed turbulent channel flow with heat transfer.* International Journal for Numerical Methods in Fluids, 1991. **13**(8): p. 999-1028.
204. Papavassiliou, D., *Structure And Transport In Wall Turbulence.* Dissertation, 1996.
205. Kontomaris, K., *Point source dispersion in a direct numerical simulation of turbulent channel flow.* PhD Dissertation, University of Illinois, 1991.
206. S.L., L., *A direct numerical simulation of fully developed turbulent channel flow with passive heat transfer.* PhD Dissertation, University of Illinois, 1989.
207. Günther, A., Papavassiliou, D., Warholic, M, *Turbulent flow in a channel at a low Reynolds number.* Experiments in Fluids, 1998. **25**: p. 503–511.
208. Bojan M. Mitrovic, P.M.L., Dimitrios V. Papavassiliou, *On the Prandtl or Schmidt number dependence of the turbulent heat or mass transfer coefficient.* Chemical Engineering Science, 2004. **59**(3): p. 543-555.
209. Steven a. Orszag , l.c.K., *Transition to turbulence in plane Poiseuille and plane Couette flow.* J. Fluid Mech., 1980. **96**: p. 159-205.
210. Marcus, P.s., *Simulation-of-Taylor-Couette-Flow-Part-I-Numerical-Methods-and-Comparison-with-Experiment.* d. Fluid Mech., 1984. **146**: p. 4.564.
211. Srinivasan, C. and D.V. Papavassiliou, *Backwards and forwards dispersion of a scalar in turbulent wall flows.* International Journal of Heat and Mass Transfer, 2010. **53**(5-6): p. 1023-1035.
212. Papavassiliou, D.V., *Scalar dispersion from an instantaneous line source at the wall of a turbulent channel for medium and high Prandtl number fluids.* International Journal of Heat and Fluid Flow, 2002. **23**: p. 161-172.
213. Srinivasan, C. and D.V. Papavassiliou, *Direction of scalar transport in turbulent channel flow.* Physics of Fluids, 2011. **23**(11).
214. Nguyen, Q. and D.V. Papavassiliou, *A statistical model to predict streamwise turbulent dispersion from the wall at small times.* Physics of Fluids, 2016. **28**(12).
215. Nguyen, Q. and D.V. Papavassiliou, *Scalar mixing in anisotropic turbulent flow.* AIChE Journal, 2018. **64**(7): p. 2803-2815.
216. Nguyen, Q., S. Feher, and D. Papavassiliou, *Lagrangian Modeling of Turbulent Dispersion from Instantaneous Point Sources at the Center of a Turbulent Flow Channel.* Fluids, 2017. **2**(3).
217. Hosseiniebalam, F., S. Hassanzadeh, and O. Ghaffarpasand, *Dispersion and deposition mechanisms of particles suspended in a turbulent plane Couette flow.* Applied Mathematical Modelling, 2013. **37**(4): p. 2417-2429.
218. Mitrovic, B.M. and D.V. Papavassiliou, *Effects of a first-order chemical reaction on turbulent mass transfer.* International Journal of Heat and Mass Transfer, 2004. **47**(1): p. 43-61.
219. Nguyen, K.T. and D.V. Papavassiliou, *Effects of a reacting channel wall on turbulent mass transfer.* International Journal of Heat and Mass Transfer, 2008. **51**(11-12): p. 2940-2949.
220. Srinivasan, C. and D.V. Papavassiliou, *Prediction of the Turbulent Prandtl Number in Wall Flows with Lagrangian Simulations.* Industrial & Engineering Chemistry Research, 2010. **50**(15): p. 8881-8891.

221. Kontomaris, K., T.J. Hanratty, and J.B. McLaughlin, *An algorithm for tracking fluid particles in a spectral simulation of turbulent channel flow.* Journal of Computational Physics, 1992. **103**(2): p. 231-242.
222. Hanratty, D.V.P.a.T.J., *The Use of Lagrangian Methods To Describe Turbulent Transport of Heat from a Wall.* Ind. Eng. Chem. Res., 1995. **34**: p. 3359-3367.
223. Papavassiliou, D.V., *Understanding macroscopic heat/mass transfer using meso- and macro-scale simulations .( Model Reduction and Coarse-Graining Approaches for Multiscale Phenomena).* Springer-Verlag, 2006: p. 489-515.
224. Hanratty, D.v.P.a.T.j., *Transport of a passive scalar in a turbulent channel flow.* Int. J. Heat Mass Transfer., 1997. **40**(6): p. 130~1311.
225. Le, P.M., *Turbulent Heat Transport In Plane Channel Flow And Plane Couette Flow Using Direct Numerical Simulation In Conjunction With Lagrangian Scalar Tracking.* Dissertation, 2009.
226. Hanratty, S.L.L.a.T.J., *Large-Scale Computer Simulation Of Fully Developed Turbulent Channel Flow With Heat Transfer.* International Journal For Numerical Methods In Fluids, 1991. **12**: p. 999-1028
227. Tobin, N. and K.B. Manning, *Large-Eddy Simulations of Flow in the FDA Benchmark Nozzle Geometry to Predict Hemolysis.* Cardiovascular Engineering and Technology, 2020. **11**(3): p. 254-267.
228. Silvia Bozzi, S.V., Marco Santus, Nicola Ghelli, Paolo Fontanili, Marco Corbelli, Gianfranco B. Fiore, Alberto C.L. Redaelli, *Fluid dynamics characterization and thrombogenicity assessment of a levitating centrifugal pump with different impeller designs.* Medical Engineering & Physics, 2020. **83**: p. 26-33.
229. Park SJ, K.S., McGregor CG, *State-of-the-art implantable cardiac assist device therapy for heart failure: bridge to transplant and destination therapy.* Clin Pharmacol Ther., 2012. **91(1):94-100**.
230. R, W., *Heart Assist Device.* United States Patent US 9,737,651 B2, 2017.
231. Chua, L.P., et al., *Numerical simulation of an axial blood pump.* Artif Organs, 2007. **31**(7): p. 560-70.
232. Throckmorton, A.L. and A. Untaroiu, *CFD analysis of a Mag-Lev ventricular assist device for infants and children: fourth generation design.* Asaio j, 2008. **54**(4): p. 423-31.
233. Zhang, Y., et al., *Design Optimization of an Axial Blood Pump With Computational Fluid Dynamics.* ASAIO Journal, 2008. **54**(2): p. 150-155.
234. Yano, T., E. Okamoto, and Y. Mitamura, *Computational fluid dynamics based design of artificial heart - An axial flow pump as a right ventricular assist device.* Transactions of Japanese Society for Medical and Biological Engineering, 2017. **55Annual**(Proc): p. 518-519.
235. Good, B.C. and K.B. Manning, *Computational modeling of the Food and Drug Administration's benchmark centrifugal blood pump.* Artificial Organs, 2020. **44**(7): p. E263-E276.
236. Furlan, M., *Von Willebrand factor: molecular size and functional activity.* Ann Hematol, 1996. **72**: p. 341–348.
237. Nguyen, Q., C. Srinivasan, and D.V. Papavassiliou, *Flow-induced separation in wall turbulence.* Phys Rev E Stat Nonlin Soft Matter Phys, 2015. **91**(3): p. 033019.
238. Fraser, K.H., et al., *The use of computational fluid dynamics in the development of ventricular assist devices.* Med Eng Phys, 2011. **33**(3): p. 263-80.

239. Faghih, M.M. and M.K. Sharp, *Evaluation of energy dissipation rate as a predictor of mechanical blood damage.* Artif Organs, 2019. **43**(7): p. 666-676.
240. Drivas, T., & Eyink, G., *A Lagrangian fluctuation–dissipation relation for scalar turbulence. Part I. Flows with no bounding walls.* Journal of Fluid Mechanics, 2017. **829**: p. 153-189.
241. Huang, Y., & Schmitt, F., *Lagrangian cascade in three-dimensional homogeneous and isotropic turbulence.* Journal of Fluid Mechanics, 2014. **741**.
242. Tennekes, H., and Lumley, John L., *A First Course in Turbulence.* Mass.: MIT, 1972. **Cambridge**.
243. Scheeler, M.W., *Complete measurement of helicity and its dynamics in vortex tubes.* Science, 2017. **357**: p. 487-491.
244. Moffatt, H.K., *Helicity—invariant even in a viscous fluid.* Science, 2017. **357**(6350).
245. Orszag, S.A., *On the elimination of aliasing in finite-difference schemes by filtering high-wavenumber components.* J. Atmos. Sci., 1971. **28**.
246. Le, P.M. and D.V. Papavassiliou, *Turbulent Heat Transfer in Plane Couette Flow.* Journal of Heat Transfer, 2006. **128**(1): p. 53-62.
247. Gottlieb, D., Orszag, Steven A and Society for Industrial Applied Mathematics, *Numerical Analysis of Spectral Methods Theory and Applications* Philadelphia, Society for Industrial and Applied Mathematics, 1977. **Monograph 26**.
248. K. Kontomaris, T.J.H., *Effect of molecular diffusivity on point source diffusion in the center of a numerically simulated turbulent channel flow.* Int. J. Heat Mass Transfer., 1994. **37**: p. 1817–1828.
249. Shom S. Ponoth, J.B.M., *Numerical simulation of mass transfer for bubbles in water.* Chemical Engineering Science, 2000. **55**(7): p. 1237-1255.
250. Chapra, S.C., *Applied Numerical Methods with MATLAB® for Engineers and Scientists.* 2012.
251. Wang, G., et al., *Estimation of the dissipation rate of turbulent kinetic energy: A review.* Chemical Engineering Science, 2021. **229**.
252. Choi, Y., Y. Park, and C. Lee, *Helicity and geometric nature of particle trajectories in homogeneous isotropic turbulence.* International Journal of Heat and Fluid Flow, 2010. **31**(3): p. 482-487.
253. Speziale, C.G., *On helicity fluctuations and the energy cascade in turbulence.* Recent Advances in Engineering Science. Lecture Notes in Engineering, 1987. **39**.
254. Dritselis, C.D. and N.S. Vlachos, *Numerical investigation of momentum exchange between particles and coherent structures in low Re turbulent channel flow.* Physics of Fluids, 2011. **23**(2).
255. Vinkovic, I., et al., *Direct numerical simulation of particle interaction with ejections in turbulent channel flows.* International Journal of Multiphase Flow, 2011. **37**(2): p. 187-197.
256. Kähler, C.J., *Investigation of the spatio-temporal flow structure in the buffer region of a turbulent boundary layer by means of multiplane stereo PIV.* Experiments in Fluids, 2003. **36**(1): p. 114-130.
257. Shuang Zhanga, D.C., *Eigen helicity density: A new vortex identification scheme and its application in accelerated inhomogeneous flows.* Physics Of Fluids 2006. **18**.
258. Kerr, R.M., *Histograms of helicity and strain in numerical turbulence.* Phys Rev Lett, 1987. **59**(7): p. 783-786.

259. Ashurst, W.T., et al., *Alignment of vorticity and scalar gradient with strain rate in simulated Navier–Stokes turbulence.* Physics of Fluids, 1987. **30**(8).
260. Gomes-Fernandes, R., B. Ganapathisubramani, and J.C. Vassilicos, *Evolution of the velocity-gradient tensor in a spatially developing turbulent flow.* Journal of Fluid Mechanics, 2014. **756**: p. 252-292.
261. Nakamura, K., et al., *Large- and small-scale characteristics in a temporally developing shearless turbulent mixing layer.* Physics of Fluids, 2022. **34**(11).
262. Danish, M. and C. Meneveau, *Multiscale analysis of the invariants of the velocity gradient tensor in isotropic turbulence.* Physical Review Fluids, 2018. **3**(4).
263. Karna, A.K. and D.V. Papavassiliou, *Near-wall velocity structures that drive turbulent transport from a line source at the wall.* Physics of Fluids, 2012. **24**(3).